AUSTRALIAN NATIONAL ANTARCTIC RESEARCH EXPEDITIONS

ANARE RESEARCH NOTES 88

Australian upper atmospheric and space physics research in Antarctica, 1992

Edited by G. Burns and M. Duldig

ANTARCTIC DIVISION
DEPARTMENT OF THE ARTS, SPORT,
THE ENVIRONMENT AND TERRITORIES

ANARE RESEARCH NOTES (ISSN 0729-6533)

This series allows rapid publication in a wide range of disciplines. Copies of this and other *ANARE Research Notes* are available from the Antarctic Division. Any person who has participated in Australian National Antarctic Research Expeditions is invited to publish through this series. Before submitting manuscripts authors should obtain a style guide from:

The Publications Office
Antarctic Division
Channel Highway
Kingston
Tasmania 7050
Australia

Published November 1992
ISBN: 0 642 18570 0

CONTENTS

AUSTRALIAN UPPER ATMOSPHERIC AND SPACE PHYSICS RESEARCH IN ANTARCTICA, 1992

Edited by Gary Burns and Marc Duldig

Antarctic Division
Department of the Arts, Sport, the Environment and Territories
Kingston, Tasmania, Australia

PREFACE

The papers in this collection were presented at the Tenth National Congress of the Australian Institute of Physics held at Melbourne University, Victoria between 10 and 14 February 1992. This anthology consists of papers the authors considered relevant to Australian Antarctic research which were presented in sessions on Solar-Terrestrial and Space Physics (South Pacific STEP Workshop), *papers 1–21*, and Astrophysics, *papers 22–32*.

The majority of the papers are preliminary and are intended as an indication of some of the current directions of Australian upper atmospheric and space physics research in Antarctica. It is anticipated that final results will appear in appropriate journals.

The editors wish to thank those researchers who have availed themselves of this opportunity to publish their research in this collective form. The editors are particularly grateful to Judy Whelan for the difficult and time-consuming task of transcription and preparation of all the manuscripts in a uniform format and to Sandra Potter for organization of the final publication.

1. ULF MAGNETIC PULSATION STUDIES IN ANTARCTICA

H.J. Hansen[1], B.J. Fraser[1], F.W. Menk[1] and R.J. Morris[2]

[1] Department of Physics
University of Newcastle
Newcastle NSW 2308
Australia

[2] Auroral and Space Physics
Antarctic Division
Kingston Tasmania 7050
Australia

ABSTRACT

The complete spectrum of ULF waves, from ion cyclotron waves (f ~ few Hz) down to hydromagnetic and other waves (with periods of minutes) plays an important role in dissipating energy involved in the solar terrestrial interaction. These waves cause oscillations in the ionospheric current systems and ground based magnetometers are sensitive to the magnetic field variations associated with these perturbations. The Space Plasma Waves Group at Newcastle University in conjunction with the Antarctic Division operates an Antarctic network of induction magnetometers in order to study these processes. This review presents an overview of these activities.

1.1 INTRODUCTION

The magnetopause is continually buffeted by the shocked solar wind in the magnetosheath. It is subjected to the stresses and flows of reconnection which results in a complete spectrum of magnetic pulsations (0.001 to 10 Hz) being observed in the polar cleft and cusp regions. Figure 1 (Glassmeier 1989) summarises the processes responsible for pulsations on field lines above the high latitude ionosphere at noon. These are listed below.

1.1.1 *Long Period Pc3 -5 (5 – 1 00 mHz) Hydromagnetic Waves*

Three different processes are responsible for these pulsations; unsteady patchy reconnection, solar wind pressure variations and the Kelvin-Helmholtz Instability. Continuous activity is often associated with standing waves in the magnetopause and low latitude boundary layer (LLBL) (Chen and Hasegawa 1974). Impulsive signals have been related to 'travelling' vortices or current patterns convecting through the polar cap (Glassmeier 1989).

1.1.2 *Pc3 (30 – 70 mHz) Solar Wind Associated Waves*

The interplanetary medium and associated magnetic field (IMF) upstream of the bowshock is a source of pulsations generated by the ion cyclotron resonance instability. Under the condition of small cone angle between the IMF and sun-earth line, compressional wave energy from the

upstream region may enter the magnetosphere, exciting harmonics of standing waves (Wolfe and Kaufmann 1975).

1.1.3 Pc1 (0.1 – 10 Hz) Ion Cyclotron Waves

Hot trapped ions from the plasmasheet (which maps down to the auroral oval) provide a free energy source for ion cyclotron wavegrowth in the equatorial magnetosphere (Kennel and Petschek 1966).

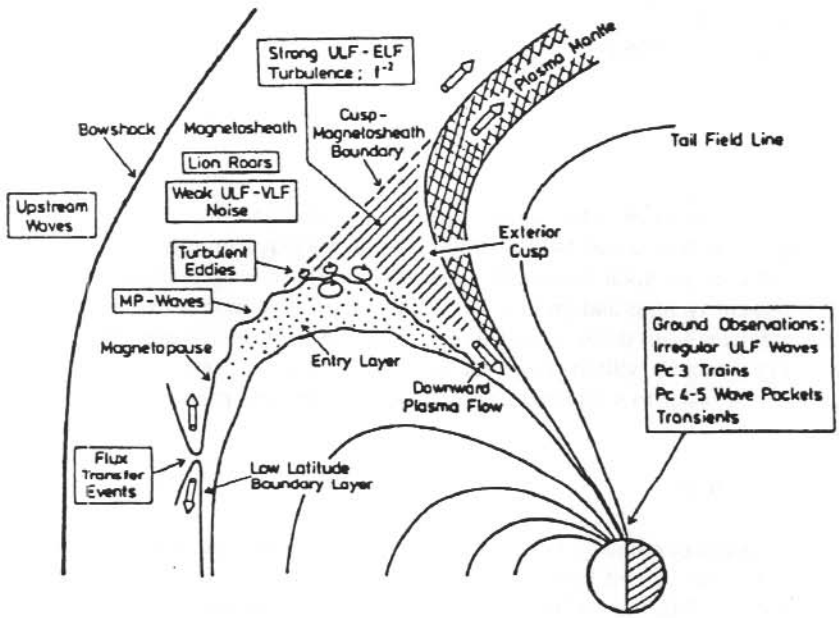

Figure 1. Schematic view of the polar cusp illustrating important space plasma physical features of this region (after Glassmeier 1989).

1.2 ANTARCTIC MAGNETOMETER ARRAY

A unique Antarctic induction magnetometer network comprising six stations at Casey, Davis, Mawson, Macquarie Island, Heard Island and Scott Base is utilised to record magnetic pulsations relating to the magnetospheric wave processes. Figure 2 is a map displaying these magnetometer sites. Clearly, the advantages of this network include widespread longitudinal and latitudinal coverage. The longitudinal spread of ~100° allows spatial and temporal ambiguities in magnetospheric wave activity to be resolved. The latitudinal spread allows the different sources of pulsations to be identified. These include the plasmapause (Heard Island – L = 4.7; Macquarie Island – L = 5.3), the auroral oval (Mawson – L = 8.7), the dayside cusp (Davis – L = 14) and the polar cap (Casey – L = 38 and Scott Base – L = 31).

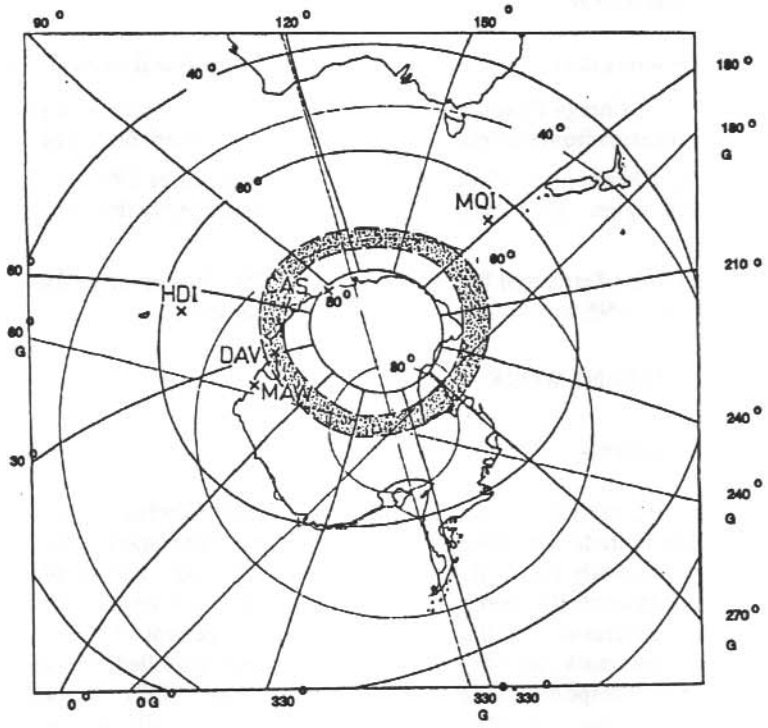

Figure 2. The locations of Casey (CAS), Davis (DAV), Mawson (MAW), Macquarie Island (MQI) and Heard Island (HDI). The bold/fine curves indicate geomagnetic/geographic coordinates. The speckled region indicates those locations on earth that rotate beneath the average location of the dayside cusp.

The instrumentation is operated in two modes; one a campaign mode where high resolution data (t = 0.5 s; f_N = 1 Hz) are gathered three to four times a year over intervals of about two weeks, and a synoptic mode recording Pc3-5 continuously (t = 4 s; f_N = 125 mHz). The timing of campaigns is planned to provide information on seasonal variations and will be coordinated with campaigns under international programs such as STEP and GEM.

1.3 ANALYSIS

The Antarctic stations use two-component induction magnetometer systems to record Pc1-5 activity over the 3 mHz – 2 Hz band down to a noise level of 5 pT. Data are logged digitally on PC XT/AT microcomputers (Fraser et al. 1991). Sometimes, Antarctic Division records digitally onto a PDP-11 computer. At Newcastle, the data are converted to a common format using a customised Data Based Management System and accessed through a dedicated LAN with six PC286/386 microcomputers. Currently, the data are analysed using multi-channel time series and cross-spectral analysis procedures.

1.4 INTERNATIONAL COOPERATION

The Antarctic plasma waves data is available for a number of international studies. These include:

1. The Solar Terrestrial Energy Program (STEP) over 1990 – 1995 which is a global study of energy dissipation processes from the solar wind into the magnetospheric/ionospheric system.

2. The Geomagnetic Environment Modelling (GEM) program. Over 1991 – 1993 this project will focus on the cusp region. The Newcastle group is involved directly through NSF sponsored research.

3. The International Solar Terrestrial Physics program (ISTP). This involves four spacecraft to be launched over 1992 – 1995, and other ground based observatories.

1.5 DETAILS OF CURRENT WORK

1.5.1 *Long Period Transients*

At cusp latitudes, these pulsations are particularly important as they relate to the electrodynamic coupling of the high latitude ionosphere with the outer magnetosphere/solar wind and the system's response to unsteady convection rather than reconnection. The coupling establishes field aligned currents through the ionosphere and the ground based magnetometers respond to magnetic variations associated with the ionospheric Hall component of these currents. The different current systems which relate to reconnection have been modelled, thus allowing for the associated magnetometer responses to be predicted (Chaston et al. 1992). In addition, it is now understood that many of the ground magnetometer signals originally associated with FTE (reconnection) current systems are merely the response to impulsive and breathing motions of the magnetosphere (Farrugia et al. 1989), viz., compressions due to solar wind variations. Dunlop et al. (1992) have identified such transient pulses of global scale propagating across the array.

1.5.2 *Pc3-5 Pulsations*

Surface waves associated with the inner edge of the magnetospheric boundary layer are known to give rise to standing waves, between 1 – 10 mHz (Olson and Rostoker 1978), which cause daily pulsation activity on ground based magnetometers (Dunlop et al. 1992). Solar wind associated Pc3 (30 – 70 mHz) waves have been shown to spread into the magnetosphere through dayside boundary layer field lines which map down to the auroral oval (Hansen et al. 1992b).

1.5.3 *Pc1 Pulsations*

It has been shown how different frequency-time characteristics of ground based high latitude Pc1 activity relate to the different magnetospheric regions which map down to the ionospheric cleft and cusp (Menk et al. 1992, Morris et al. 1992). In addition, there is a close association between Pc1 wave packets observed just equatorward of the cleft and low frequency pulses in the 1 – 10 mHz band (Hansen et al. 1992). Currently studies (Hansen et al. 1991, Francke et al. 1992, Hansen et al. 1992a) are addressing the propagation of Pc1 wave energy to higher and lower latitudes from the auroral oval region.

1.6 ACKNOWLEDGMENTS

Thanks are due to the Antarctic Division for providing the field logistics for this research. The authors also acknowledge the Australian Research Council (ARC) and the Antarctic Science Advisory Committee (ASAC) for financial support.

REFERENCES

Chaston, C.C., Hansen, H.J., Menk, F.W. *and* Fraser, B.J. (1992). Modelled ground magnetic signatures of flux transfer events. In: Burns, G.B. *and* Duldig, M.L. (Eds). *ANARE Research Notes Number 88*. Australian Antarctic Division.

Chen, L. *and* Hasegawa, A. (1974). A theory of long-period magnetic pulsations, 1. Steady state excitation of field line resonance. *Journal of Geophysical Research 79*:1024 – 1032.

Dunlop, I.S., Menk, F.W., Hansen, H.J., Fraser, B.J. *and* Morris, R.J. (1992). A multistation study of long period geomagnetic pulsations in the polar cleft and cusp. In: Burns, G.B. *and* Duldig, M.L. (Eds). *ANARE Research Notes Number 88*. Australian Antarctic Division.

Farrugia, C.J., Freeman, M.P., Cowley, S.W.H., Southwood, D.J., Lockwood, M. *and* Etemadi, A. (1989). Pressure driven magnetopause motions and attendent response on the ground. *Planetary and Space Science 37*:589 – 607.

Franke, M.H., Hansen, H.J., Menk, F.W., Fraser, B.J. *and* Morris, R.J. (1992). The propagation of Pc1 magnetic bursts across the polar cap region. In: Burns, G.B. *and* Duldig, M.L. (Eds). *ANARE Research Notes Number 88*. Australian Antarctic Division.

Glassmeier, K.H. (1989). ULF pulsations in the polar cusp and cap. In: Sandholt, F. (Ed.). *EM Coupling in Polar Clefts and Caps*. Kluwer Academic Publishers, Dordrecht. Pp. 167 – 186.

Fraser, B.J., McNabb, P., Menk, F.W. *and* Waters, C.L. (1991). A personal computer induction magnetometer system for recording geomagnetic pulsations. In: Burns, G.B. (Ed.). *ANARE Research Notes Number 80*. Pp. 83 – 92.

Hansen, H.J., Fraser, B.J., Menk, F.W., Hu, Y.D., Newell, P.T. *and* Meng, C.-I. (1991). High latitude unstructured Pc1 emissions generated in the vicinity of the dayside auroral oval. *Planetary and Space Science 39*:709 – 719.

Hansen, H.J., Fraser, B.J., Menk, F.W., Hu, Y.D., Newell, P.T., Meng, C.-I. *and* Morris, R.J. (1992). High latitude Pc1 bursts arising in the vicinity of the dayside boundary layer region. *Journal of Geophysical Research 97*:3993 – 4008.

Hansen, H.J., Fraser, B.J., Menk, F.W. *and* Erlandson, R.E. (1992a). Ground satellite observations of high latitude Pc1-2 pulsations. In: Burns, G.B. *and* Duldig, M.L. (Eds). *ANARE Research Notes Number 88*. Australian Antarctic Division.

Hansen, H.J., Fraser, B.J., Menk, F.W., Newell, P.T., Meng, C.-I. *and* Morris, R.J. (1992b). Sources of solar wind associated Pc3-5 magnetic pulsations in the magnetosphere. In: Burns, G.B. *and* Duldig, M.L. (Eds). *ANARE Research Notes Number 88*. Australian Antarctic Division.

Kennel, C.F. *and* Petschek, H.E. (1966). The limit of stably trapped particle fluxes. *Journal of Geophysical Research 71*:1 – 28.

Menk, F.W., Fraser, B.J., Hansen, H.J., Newell, P.T., Meng, C.-I *and* Morris, R.J. (1992). Multistation observations of Pc1-2 ULF pulsations between the plasmapause and the polar cap. *Journal of Geophysical Research* (in press).

Olson, J.V. *and* Rostoker, G. (1978). Longitudinal phase variation of Pc4-5 micropulsations. *Journal of Geophysical Research 83*:2481 – 2488.

Wolfe, A. *and* Kaufmann, R.L. (1975). MHD wave transmission and production near the magnetopause. *Journal of Geophysical Research 80*:1764 – 1775.

2. THE US NATIONAL SCIENCE FOUNDATION'S GEOSPACE ENVIRONMENTAL MODELLING (GEM) PROGRAM, 1990–1995

B.J. Fraser

Department of Physics
University of Newcastle
Newcastle NSW 2308
Australia

ABSTRACT

The Geospace Environment Modelling Program (GEM) is a NSF initiative to produce a comprehensive model of the interactions of the solar wind with the earth's magnetosphere and ionosphere. The scientific goal of GEM is to understand the solar-terrestrial system well enough to be able to formulate a mathematical framework that can predict the deterministic properties of geospace ('weather in space') and the statistical characteristics of its stochastic properties ('climate in space'). The approach taken was to identify the problems requiring solution and place these in a framework that would be most likely to produce the global geospace circulation model. As a consequence the program consists of a series of overlapping and integrated efforts to address predetermined problems which are supported by a synchronised series of both theory and observational campaigns. The first campaign will work on magnetopause and boundary layer physics. The specific aims of this campaign will be introduced.

2.1 THE PROGRAM

Under the sponsorship of the National Science Foundation, the US geospace research community has developed the Geospace Environment Modelling (GEM) program. The GEM program supports basic research into the dynamics and structural properties of geospace. The ultimate goal is to produce a global geospace circulation model (GGCM) with a predictive capability (Dusenbury and Siscoe 1992). This may be considered as a forecasting model for 'space weather' and is an important component of the wider US Global Change Research Program. GEM is a goal-directed, ordered sequence of coordinated theory and observing campaigns, focused on major components of the geospace program, namely, boundary and cusp, global fields and currents, magnetotail and substorms, convection and coupling, global plasmas, and ultimately geospace itself as represented by an integration of the campaign results into the GGCM. This strategy is outlined in Figure 1 and was formulated at a workshop held at the University of Washington in August 1987. A steering committee oversees the program in which the geospace community concentrates its resources on major magnetospheric problems, one at a time. The objectives of each campaign are determined by community-wide pre-campaign workshops, and campaign coordinators facilitate interaction between campaign participants and have responsibility for the success of their particular campaign. Details of the workshops leading to the first campaign are included in the reference list.

The complexity of a GGCM is shown in the prototype in Figure 1. Processes occurring near the magnetospheric boundary extract energy from the solar wind and distribute it over geospace, and,

directly or indirectly, drive magnetospheric and ionospheric processes. These complex processes can profoundly affect the upper atmosphere which is a sensitive measure for long and short term changes in the lower atmosphere.

The first campaign covers the first boxes in the theory and observing columns in Figure 2, and the objectives are to:

1. Establish the mapping of boundary processes through the magnetosphere to the dayside ionosphere.
2. Identify or verify the ionospheric signatures of these processes.
3. Advance to an operational-level understanding of the dynamics and structure of the magnetospheric boundary.
4. Extend, test, and apply magnetosheath models to determine magnetospheric boundary conditions.

In November 1990 the NSF earmarked US$1.2M for the first campaign and twenty projects were selected for funding. Four principal investigators were selected as campaign coordinators and coordination is being implemented through workshops.

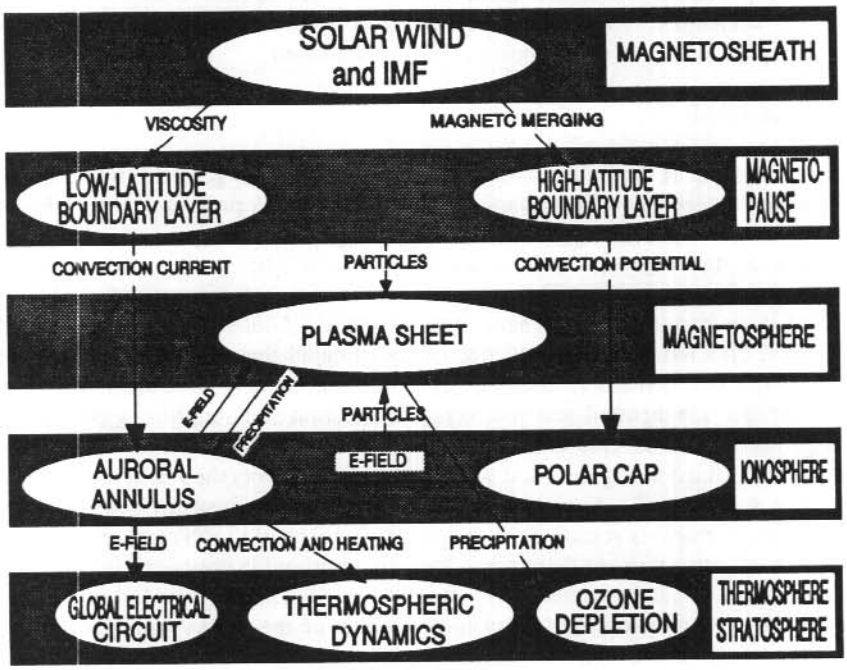

Figure 1. A coupled geospace model.

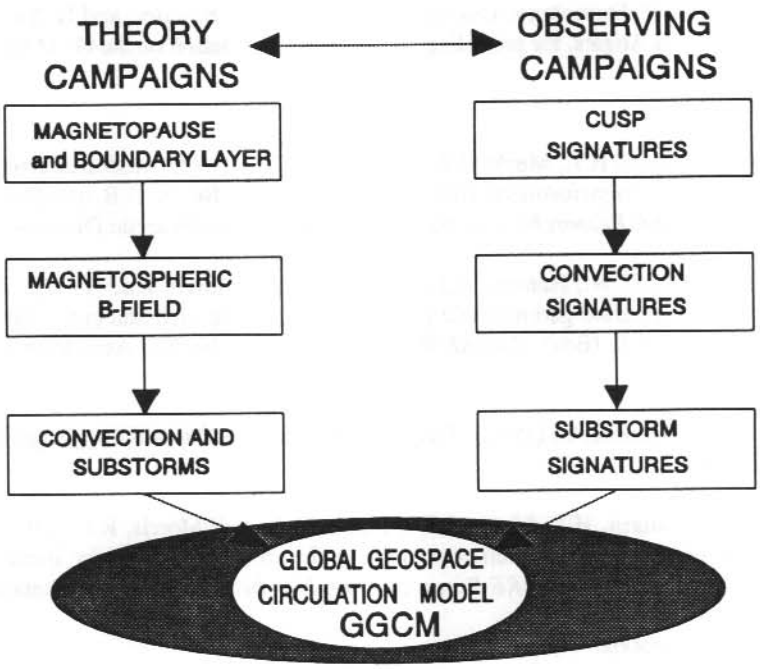

Figure 2. Major GEM campaigns.

GEM is a global program and from the beginning, the GEM workshops have been well attended by international scientists. This has been consolidated by the inclusion of international liaison members on the steering committee. The international component of GEM includes both theorists and modellers and the contribution to their own national programs provides important input to GEM. It is important that data are collected from many high latitude stations in the polar regions. The GEM program will also make an important contribution to the international Solar Terrestrial Energy Program (STEP).

On the Australian scene, important input to the GEM program is provided by the Australian Antarctic upper atmosphere research program. At this stage magnetospheric and ionospheric research in progress at the Universities of Newcastle and La Trobe, and the Australian Antarctic Division, is concentrating on the topology and dynamics of the high latitude cusp/cleft and boundary regions. Emphasis has been on transient and continuous geomagnetic pulsation signatures as indicators of the microstructure and dynamics in the high latitude regions (see for examples papers by Hansen et al. (1992), Dunlop et al. (1992), Francke et al. (1992), Chaston et al. (1992) and Morris et al. (1992). The research in Antarctica has been supported by the Australian Research Council, the Antarctic Science Advisory Committee and the participating universities and government departments. The GEM program will continue until 1995 and it is hoped that the Australian commitment will continue over this time.

2.2 ACKNOWLEDGMENTS

Thanks are due to P. Dusenbury, University of Colorado at Boulder, and G. Siscoe, University of California at Los Angles, for providing background information on the GEM program.

REFERENCES

Chaston, C.C, Hansen, H.J., Menk, F.W. *and* Fraser, B.J. (1992) Modelled ground magnetic signatures of magnetospheric flux transfer events. In: Burns, G.B. *and* Duldig, M.L. (Eds). *ANARE Research Notes Number 88*. Australian Antarctic Division.

Dunlop, I.S., Menk, F.W., Hansen, H.J., Fraser, B.J. *and* Morris, R.J. (1992). A multistation study of long period geomagnetic pulsations in the polar cleft and cusp. In: Burns, G.B. *and* Duldig, M.L. (Eds). *ANARE Research Notes Number 88*. Australian Antarctic Division.

Dusenbury, P. *and* Siscoe, G. (1992). Geospace environmental modelling program. *EOS 73*:83 – 84.

Francke, M.H., Hansen, H.J., Menk, F.W., Fraser, B.J. *and* Morris, R.J. (1992). The propagation of Pc1-2 magnetic bursts across the polar cap region. In: Burns, G.B. *and* Duldig, M.L. (Eds). *ANARE Research Notes Number 88*. Australian Antarctic Division.

GEM Workshop Reports:

The geospace environment modelling program (GEM). GEM Steering Committee (Ed.). University of Washington, August 1987.

Theory campaign on the magnetopause and boundary layer physics. Ashour-Abdalla, M. (Ed.). San Diego Supercomputing Centre, February 1989.

Ionosphere signatures of cusp magnetopause and boundary layer processes . Rosenberg, T.J. (Ed.). University of Maryland, October 1989.

Intercalibrating cusp signatures. Crooker, N. (Ed.). Weston Massachussetts, October 1990.

Hansen, H.J., Fraser, B.J., Menk, F.W., Newell, P.T., Meng, C.-I. *and* Morris, R.J. (1992). Solar wind associated Pc3 pulsations. In: Burns, G.B. *and* Duldig, M.L. (Eds). *ANARE Research Notes Number 88*. Australian Antarctic Division.

Morris, R.J., Cole, K.D., Troitskaya, V.A., Fraser, B.J., Hansen, H.J. *and* Menk, F.W. (1992). Multi-site high-latitude ULF magnetic pulsation studies. In: Burns, G.B. *and* Duldig, M.L. (Eds). *ANARE Research Notes Number 88*. Australian Antarctic Division.

3. MULTI-SITE HIGH-LATITUDE ULF MAGNETIC PULSATION STUDIES

R.J. Morris[1], K.D. Cole[2], V.A. Troitskaya[2], B.J. Fraser[3], H.J. Hansen[3] and F.W. Menk[3]

[1] Auroral and Space Physics
Antarctic Division
Kingston Tasmania 7050
Australia

[2] Department of Physics
La Trobe University
Bundoora Victoria 3083
Australia

[3] Department of Physics
University of Newcastle
Shortland NSW 2308
Australia

ABSTRACT

A case study of Pc1-2 and Pc3 magnetic pulsation events, recorded on the Australian Antarctic (Mawson, Davis and Casey) and sub-Antarctic (Macquarie Island) digital array of induction magnetometers is presented. The data base comprised of three fortnightly digital campaigns conducted during the 1990 austral winter and the 1991 austral summer, respectively. The summer campaign was augmented by a traverse which supported the operation of a field induction magnetometer at Law Dome, some 130 km inland of Casey. The ULF waves presented appear to maximise in occurrence frequency and amplitude under the projection of the dayside polar cusp and polar cleft. The propagation characteristics of these emissions over the widely spaced array (Inv. 64–80.6°S) are reported. The study focuses on whether aspects of the reported high-latitude magnetic pulsation events and their reported propagation characteristics, provide a ground diagnostic for estimating the location of the projection of the polar cusp and adjacent magnetospheric regions.

3.1 INTRODUCTION

Despite the somewhat limited high-latitude ground-based research conducted on the spectrum of pulsations emanating from the polar cusp/cleft, several new pulsation regimes in the Pc1-2 (0.2–10 s) and Pc3 (1–45 s) range have been reported in the last decade, viz., IPRP (Matveeva et al. 1976, Morris et al. 1982, Cole et al. 1982, Morris and Cole 1985), Pc1b (Matveeva et al. 1978) or IPCP (Morris and Cole 1985), Pc1 structured (Heacock et al. 1970), Pc1-2 non-structured (Bolshakova et al. 1980), serpentine emission (SE) (Gul'elmi and Dovbnya 1974, Morris and Cole 1987a) and Pc3 (Morris and Cole 1987b). The paucity of scientific literature on polar cusp/cleft and polar cap magnetic pulsations can most likely be attributed to some extent, to logistical difficulties restricting the number of suitable Arctic and Antarctic observatories.

Investigations of high-latitude magnetic pulsation regimes, i.e. Pc1-2 and Pc3, have revealed a possible connection between their morphological characteristics and the location of the projection of the polar cusp/cleft regions (Bolshakova et al. 1980, Morris and Cole 1985, 1987b). Such observations are extremely significant since ground signatures of magnetic pulsation emissions could provide a continuous monitor of the ground projection of the polar cusp and cleft, and thus afford a ground diagnostic tool on aspects of the magnetosphere. To our knowledge negligible research has been conducted on the propagation characteristics of high latitude ULF waves, in particular those emanating from the polar cusp and cleft regions of the magnetosphere.

3.2 EXPERIMENT

The installation of new ANARE induction magnetometers at Casey, Davis, Mawson and Macquarie Island was completed during early 1991, with data acquisition on chart, slow frequency-modulated audio tape and on PDP11/23+ computers for campaign intervals. Recently audio tape recording was superseded by digital acquisition using XT PCs developed at the University of Newcastle. The current research program is conducted by Antarctic Division expeditioners for: (i) Auroral and Space Physics Section, Antarctic Division, (ii) Newcastle University, and (iii) La Trobe University (Fraser and Morris 1987). In addition to the permanent stations, from time to time, field site observations have been conducted at Law Dome, Browning Peninsula near Casey (1991 summer), Heard Island (1992) and at the Law Base–Davis–inland ice depot triangulation sites (1992 winter campaign).

3.3 MULTI-SITE MAGNETIC PULSATION STUDIES

Previous studies have identified the characteristics of several high-latitude regimes of magnetic pulsations including: Pc1-2 discrete (Morris and Cole 1985, Hansen et al. 1992), Pc1-2 continuous (Morris and Cole 1991, Hansen et al. 1991, Menk et al. 1992) and Pc3 (Morris and Cole 1987b) emissions in particular, from a myriad of such phenomena as reported in the literature. Figure 1(a) illustrates multi-station amplitude-time records for typical Pc3 emissions and Figure 1(b) illustrates multi-station frequency-time dynamic spectra of Pc1 discrete emissions observed across the Antarctic induction magnetometer array.

Our research aims to advance knowledge of physical processes in the geomagnetic plasma through analysis and interpretation of campaign based magnetic pulsation data sets acquired at ANARE stations.

Campaign 1. 4 -- 18 April 1990	@ 0.3 Hz
Campaign 2. 10 – 24 July 1990	@ 5.0 Hz
Campaign 3. 14 January – 2 February 1991	@ 5.0 Hz

Such analysis will examine properties such as polarisation, dispersion, amplitude-time variations, cross correlations, correlation with other appropriate data (eg. auroral images, electromagnetic signals measured on board satellites, solar wind parameters, normal magnetograms).

This investigation will include:

1. the various classes of magnetic pulsations observable in the polar cap and in particular with a view to drawing inferences about their source mechanisms;

2. the correlation of pulsations at the various stations will be examined with the view to understanding the detailed evolution in time and space of pulsation events and to make inferences about the propagation of hydromagnetic waves in the magnetosphere and ionosphere.

In particular we wish:

1. to examine the data for evidence of ion cyclotron waves coming from the interaction region of the solar wind and the geomagnetic field;

2. to infer from the dispersion of the pulsations, bulk motions of the plasma source of the pulsations;

3. relationships of the pulsations to field aligned currents.

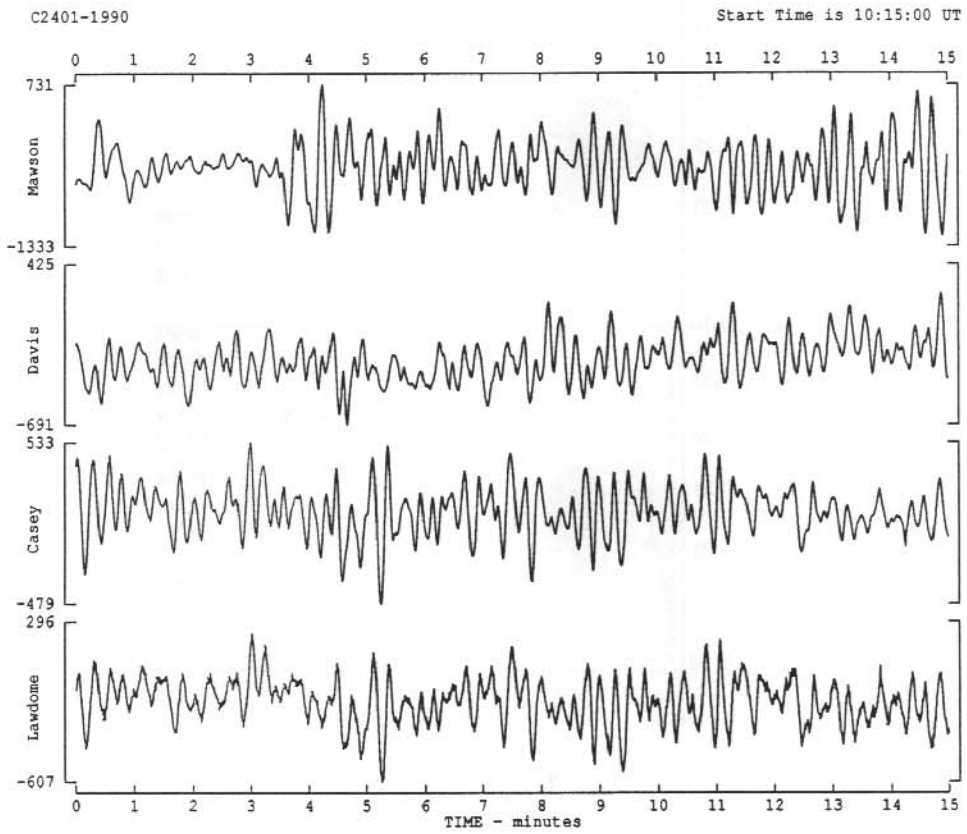

Figure 1a. Multi-station amplitude-time records of Pc3 (T ~ 20 s) emissions.

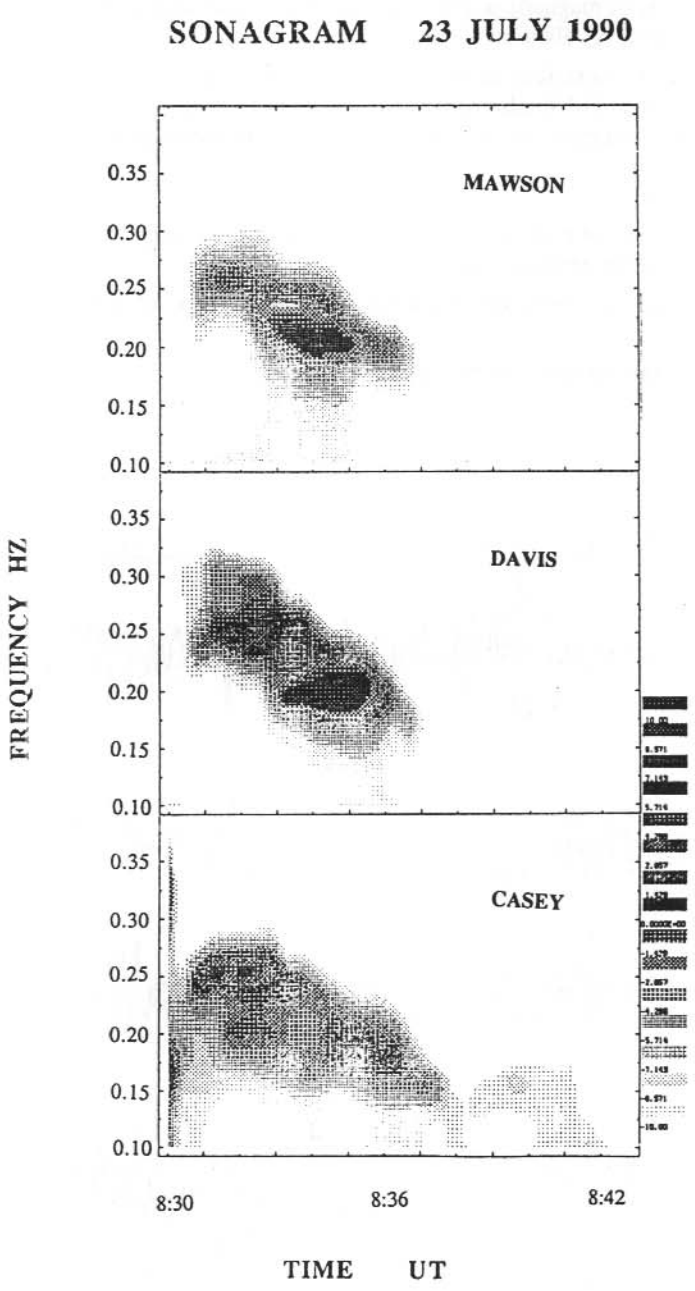

Figure 1b. Multi-station frequency-time dynamic spectra of a Pc1 discrete (IPRP) event, observed across the Antarctic induction magnetometer array.

This theoretical approach is anticipated to shed considerable light on the dynamics of energy transfer from the solar wind into the magnetosphere/ionosphere system. Where possible simultaneous measurements of the solar wind and observations of electromagnetic signals by satellites in the outer magnetosphere will be collated with ground-based data to aid inferences about the source and propagation of hydromagnetic waves, whether in the ionosphere or the outer magnetosphere. The relationship of the pulsations to source regions as determined by data from the DMSP satellite will be determined.

3.4 CONCLUSION

The objectives strike at one of the forefront's of magnetospheric research via solar wind-magnetosphere-ionosphere coupling at high latitudes. Hydromagnetic waves are the agent of such coupling and they manifest themselves as magnetic pulsations. Magnetic pulsations bring information to the ground about the kind and state of the plasma in deep space. They form a powerful data set to complement *in situ* observations by satellites. Proper interpretation of magnetic pulsations can be useful as diagnostics of this distant plasma.

3.5 ACKNOWLEDGMENT

We thank Dr Andrew Klekociuk and Mr Howie Burton for the development of the logging routines utilised in the campaigns, Mr Nico Jones for traverse logistics support at Law Dome, and the wintering Auroral and Space Physics (ASP) expeditioners for their efforts with data collection.

REFERENCES

Bolshakova, O.V., Troitskaya, V.A. *and* Ivanov, K.G. (1980). High-latitude Pc1-2 geomagnetic pulsations and their connection with location of the dayside polar cusp. *Planetary and Space Science 28*:1–7.

Cole, K.D., Morris, R.J., Matveeva, E.T., Troitskaya, V.A. *and* Pokhotelov, O.A. (1982). The relationship of the boundary layer of the magnetosphere to IPRP events. *Planetary and Space Science 30*:129–136.

Fraser, B.J. *and* Morris, R.J. (1987). Australia's magnetospheric research in Antarctica. In: Burns, G.B. *and* Craven, M. (Eds). *ANARE Research Notes Number 48*. Pp. 236–245.

Gul'elmi, A.V. *and* Dovbnya, B.V. (1974). Hydromagnetic emissions of the interplanetary plasma. *Astrophysics and Space Science 31*:21–29.

Hansen, H.J., Fraser, B.J., Menk, F.W., Hu, Y.D., Newell, P.T. *and* Meng, C.-I. (1991). High latitude unstructured Pc1 emissions generated in the vicinity of the dayside auroral oval. *Planetary and Space Science 39*:709–719

Hansen, H.J., Fraser, B.J., Menk, F.W., Hu, Y.D., Newell, P.T., Meng, C.-I. *and* Morris, R.J. (1992). High latitude Pc1 bursts arising in the vicinity of the dayside boundary layer region. *Journal of Geophysical Research 97*:3993–4008.

Heacock, R.R., Hessler, V.P. *and* Olesen, J.K. (1970). The 2–0.1 Hz polar cap micropulsation activity. *Journal of Atmospheric and Terrestrial Physics 32*:129 –138.

Matveeva, E.T., Troitskaya, V.A. *and* Feygin, F.Z. (1976). Intervals of pulsations with rising periods (IPRP) in polar caps. *Planetary and Space Science 24*:673 –678.

Matveeva, E.T., Troitskaya, V.A. *and* Feygin, F.Z. (1978). Isolated bursts of type Pc1b geomagnetic pulsations at high latitudes. *Geomagnetism and Aeronomy (English Edn) 18*:75–78.

Menk, F.W., Fraser, B.J., Hansen, H.J., Newell, P.T., Meng, C.-I. *and* Morris, R.J. (1992). Identification of the magnetospheric cusp and cleft using Pc1-2 ULF pulsations. *Journal of Atmospheric and Terrestrial Physics*. In press.

Morris, R.J. *and* Cole, K.D. (1985). Pc1-2 discrete regular daytime pulsation bursts at high latitudes. *Planetary and Space Science 33*:53 –67.

Morris, R.J. *and* Cole, K.D. (1987a). 'Serpentine emission' at the high latitude Antarctic station, Davis. *Planetary and Space Science 35*:313 –328.

Morris, R.J. *and* Cole, K.D. (1987b). Pc3 magnetic pulsations at Davis, Antarctica. *Planetary and Space Science 35*:1437 – 1447.

Morris, R.J. *and* Cole, K.D. (1991). High-latitude day-time Pc1-2 magnetic pulsations: a ground signature of the polar cusp and cleft projection. *Planetary and Space Science 39*:1473 – 1491.

Morris, R.J., Cole, K.D., Matveeva, E.T. *and* Troitskaya, V.A. (1982). Hydromagnetic 'whistles' at the dayside cusps: IPRP events. *Planetary and Space Science 30*:113 – 127.

4. MODELLED GROUND MAGNETIC SIGNATURES OF MAGNETOSPHERIC FLUX TRANSFER EVENTS

C.C. Chaston, H.J. Hansen, F.W. Menk and B.J. Fraser

Department of Physics
University of Newcastle
Newcastle NSW 2308
Australia

ABSTRACT

The ground magnetic signatures of magnetospheric flux transfer events are modelled based on small-scale field aligned current systems. The current configurations studied include the Southwood (1987) twin vortex and the Saunders et al. (1984) / Lee (1986) central vortex models. In addition two further patterns have been formulated; an elliptical one and a system of current sheets. This paper demonstrates how the phase and amplitude of each magnetic signature is dependent on the path of its associated current system with respect to a ground magnetometer. It is shown that the effective study of ionospheric FTE current configurations from the ground requires an array of closely spaced magnetometers separated by less than 500 km.

4.1 INTRODUCTION

The reconnection and convection of flux tubes at the magnetopause generates distinct current patterns in the polar ionosphere whose associated magnetic field may be measured by ground based magnetometers. A description of the essential features of the models invoked to describe these patterns follows.

4.1.1 *The Twin Vortex Model*

The solar wind provides the momentum to drive reconnected flux tubes through the ionosphere. Southwood and Hughes (1983) proposed that the momentum transfer necessary is achieved through currents aligned with the flux tube as illustrated in Figure 1. This current configuration leads to the formation of two oppositely oriented convection vortices corresponding to the upward and downward current filaments on either side of the reconnected flux tube.

4.1.2 *The Central Vortex Model*

The observed twisting of the magnetic field within a reconnected flux tube led Saunders et al. (1984) to suggest that a core field-aligned current exists through the flux tube's centre. Lee (1986) then showed that a large central convection vortex should exist inside the flux tube due to the propagation of Alfven waves from the magnetopause which carry field-aligned currents to the ionosphere. This central vortex is accompanied by two smaller vortices rotating in opposite directions to provide the necessary $\mathbf{j} \times \mathbf{B}$ force to overcome collisional losses in the ionosphere.

The ionospheric footprint of an FTE, based on the injection of the field-aligned currents through the core of the flux tube and their closure with return currents along the boundary of the flux tube, is illustrated in Figure 2.

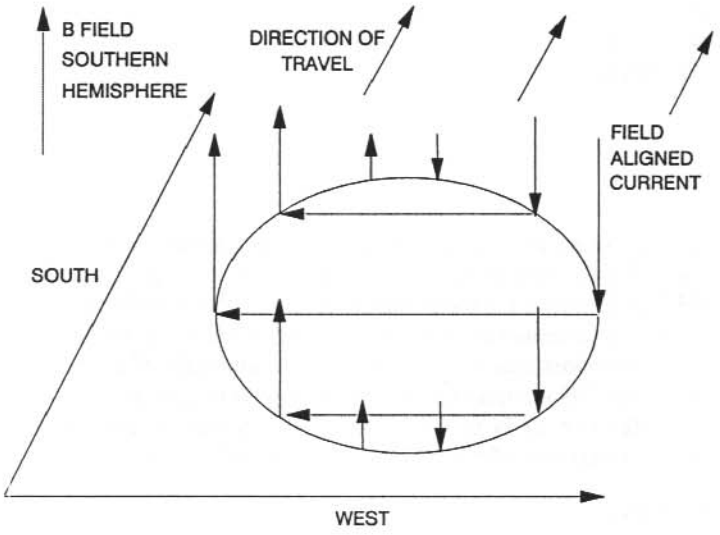

Figure 1. Field-aligned current configuration for Southwood's (1987) twin vortex model.

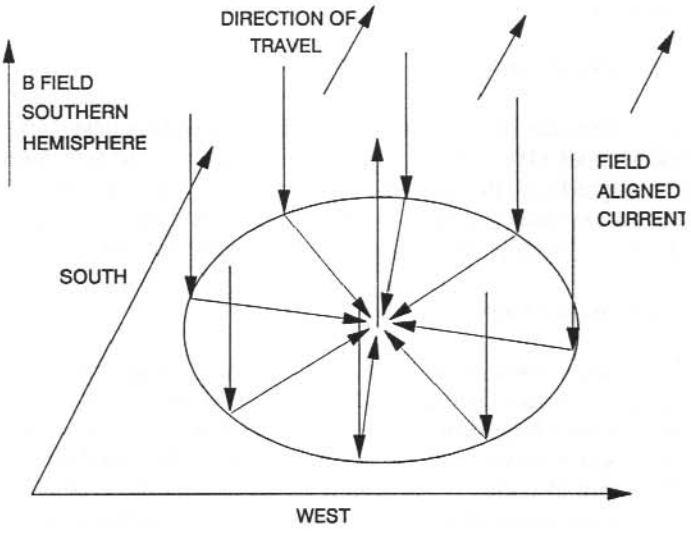

Figure 2. Field-aligned current configuration for Saunders' et al. (1984) / Lee's (1986) central vortex model.

4.1.3 *The Current Sheet Model*

Multiple field-aligned current sheets may be produced along convection channels arising from impulsive patchy reconnection (Kan 1988). The field-aligned currents, which close in the ionosphere, have opposite polarity on either side of the flux tube footprint which is elongated in the direction of convection. Each flux tube footprint leads to an individual current sheet so that several reconnection events lead to multiple field-aligned current sheets. This current configuration is modelled by an array of field-aligned current filaments oriented as shown in Figure 3.

4.1.4 *The Elliptical Twin Vortex Model*

Whilst the reconnected flux tube at the magnetopause may be circular in cross-section, its footprint on the ionosphere is unlikely to be so. The variation in the cross-section of the flux tube footprint as it convects tailward has been investigated by Crooker and Siscoe (1990). They showed that the flux tube should be roughly elliptical and should become more eccentric as the flux tube convects across the polar cap. The current configuration appropriate for this model is illustrated in Figure 4.

4.2 THE ELECTRIC AND MAGNETIC FIELD OF A SMALL-SCALE FIELD-ALIGNED CURRENT SYSTEM

4.2.1 *Field Calculation*

The approach adopted here is essentially that followed by McHenry and Clauer (1987) adapted for the southern hemisphere. The electric potential, Φ, established by a given field-aligned current distribution incident on a two-dimensional ionosphere was determined from the application of the continuity equation and Ohm's law. This yielded a Poisson-like equation in Φ. The induced electric field was then found by solving this equation for Φ and taking $-\nabla\Phi$. Applying Ohm's law to this result provided the height integrated current density. Use of the Biot-Savart law then yielded the field established on the ground as an integral over the field-aligned current distribution.

Since the electric field established in the ionosphere by the field-aligned current (FAC) induces Hall and Pedersen currents the total magnetic field established on the ground is the sum of the fields induced by each current, i.e.

$$\mathbf{B} = \mathbf{B}_{FAC} + \mathbf{B}_{Pedersen} + \mathbf{B}_{Hall}$$

However, at polar latitudes the FAC and Pedersen fields cancel (McHenry and Clauer 1987). For this reason it is only necessary to calculate the Hall field.

In all the cases which follow we consider the conducting layer of the ionosphere to be 100 km above the ground. Further, it is assumed that the ratio of the height-integrated Hall and Pedersen conductivities is ~2 in the vicinity of the cusp for the southern hemisphere, consistent with that employed by McHenry and Clauer (1987). The total current carried by each configuration is 2×10^5A as predicted by Saunders et al. (1984) and the coordinate system is such that X points southward, Y points westward and Z completes the orthogonal set.

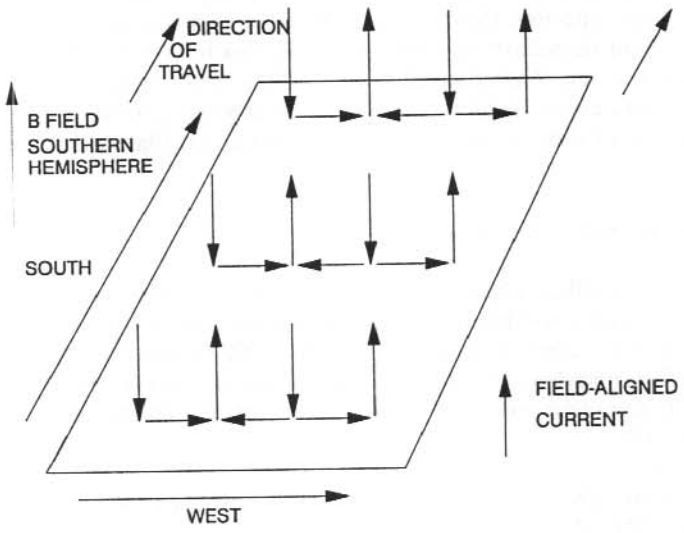

Figure 3. Field-aligned current configuration for the current sheet model.

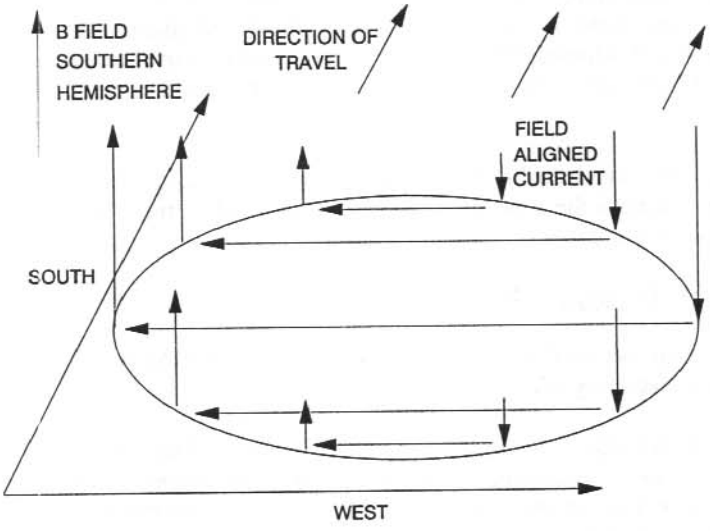

Figure 4. Field-aligned current configuration for the elongated twin vortex model.

4.3 GROUND MAGNETIC SIGNATURES

Figure 5 demonstrates that the field distribution established on the ground by each current system differ distinctly. This however is not necessarily true of the magnetic signatures which may be recorded as these distributions pass overhead.

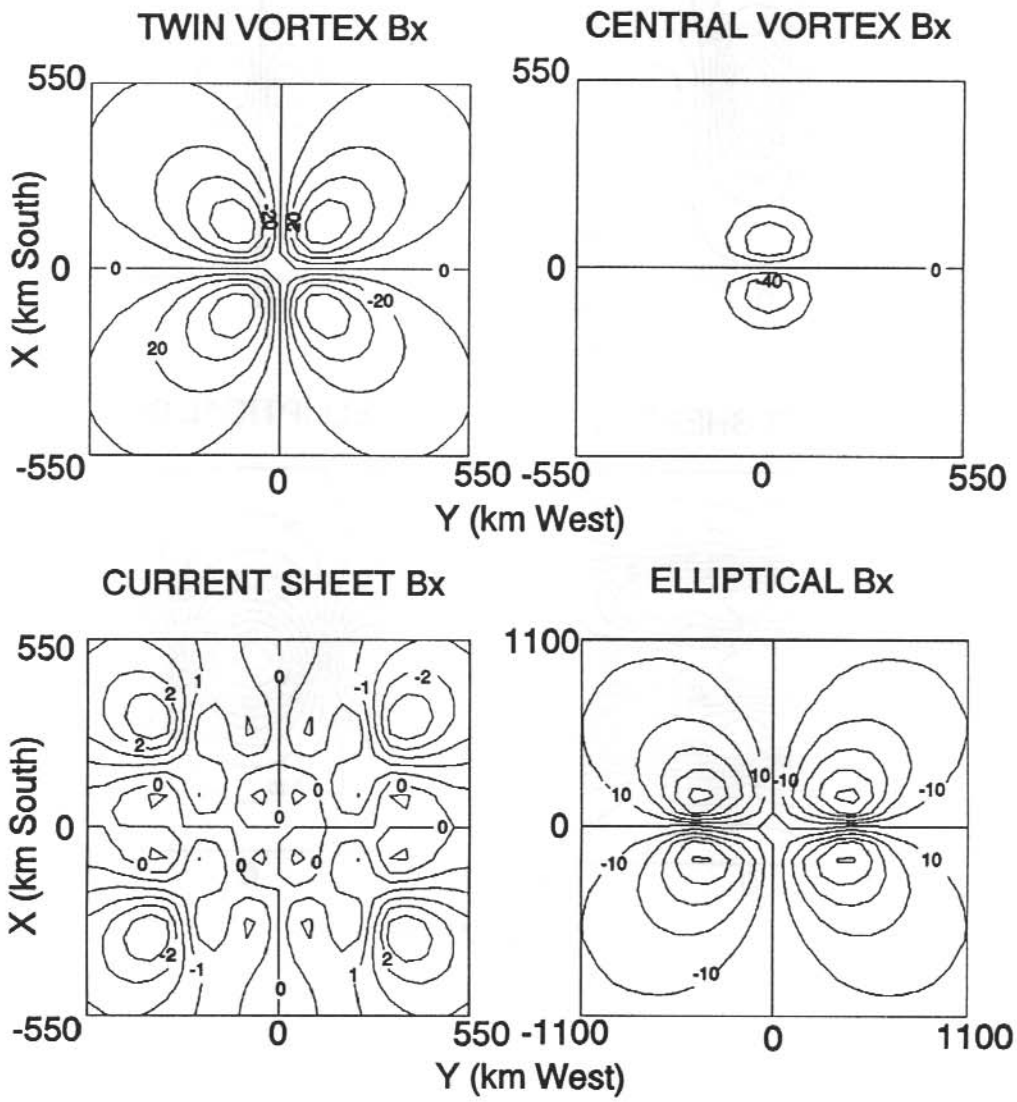

Figure 5a. X-component ground field distribution established by field-aligned current models in the southern hemisphere. Contours represent lines of equal field strength in nanoteslas.

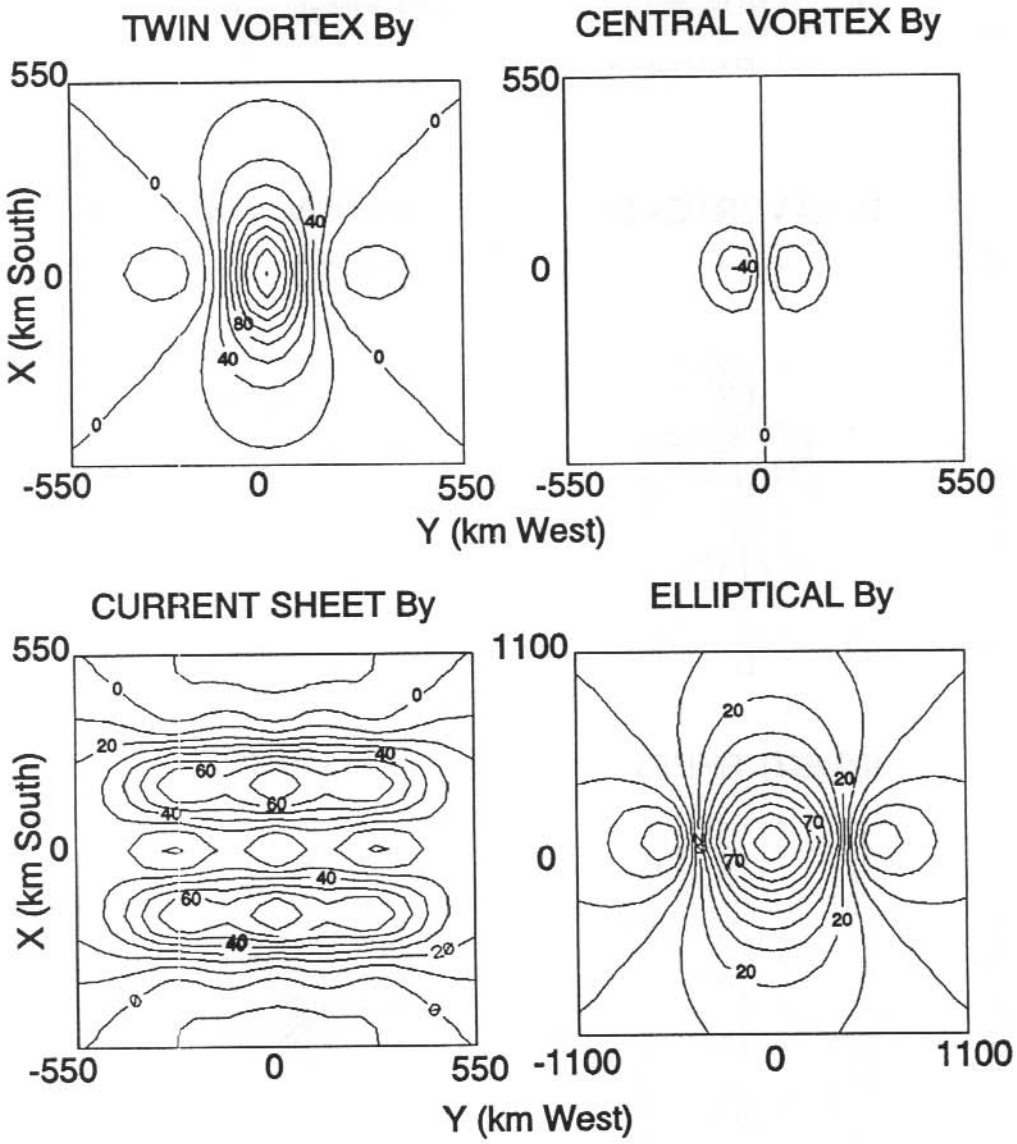

Figure 5b. Y-component ground field distribution established by field-aligned current models in the southern hemisphere. Contours represent lines of equal field strength in nanoteslas.

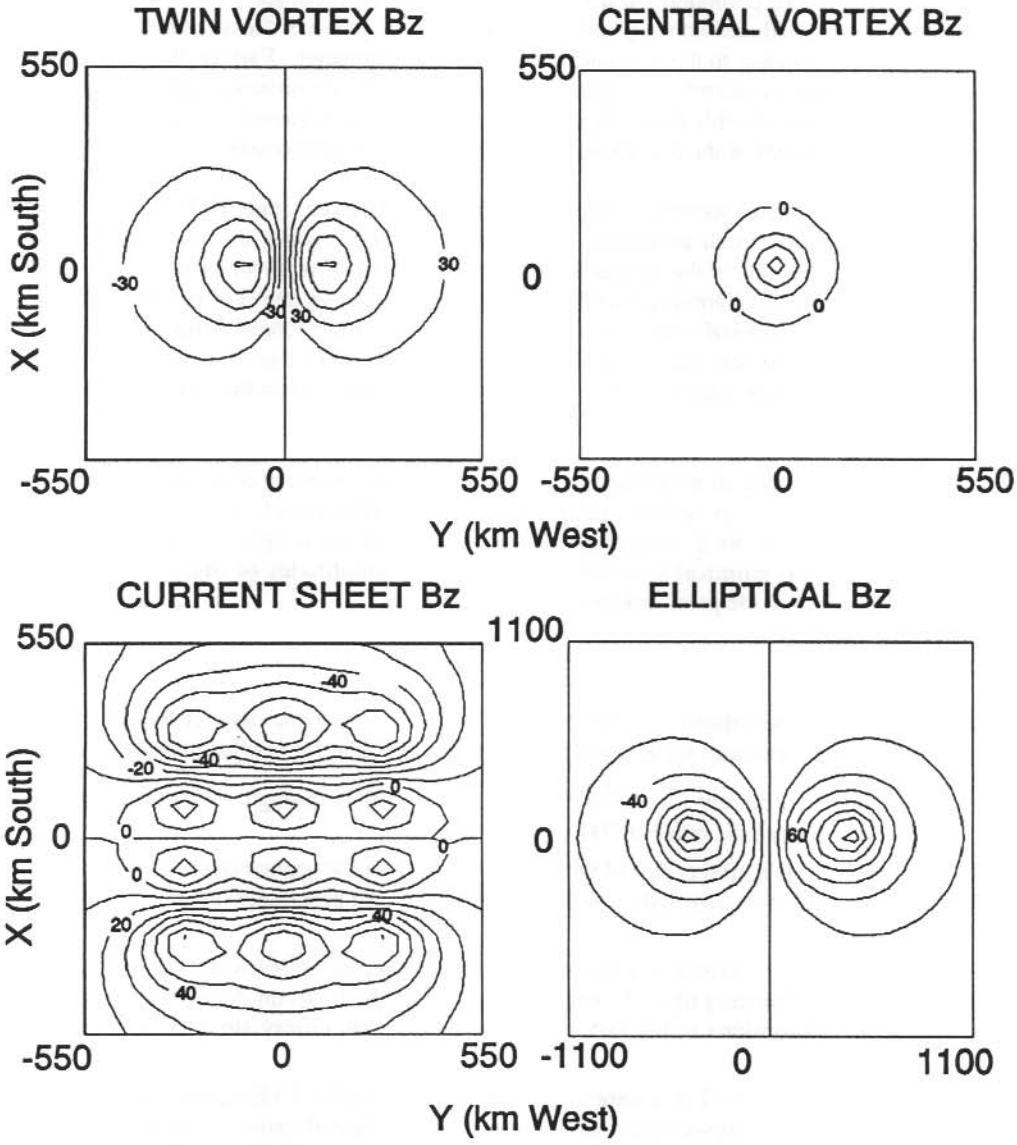

Figure 5c. Z-component ground field distribution established by field-aligned current models in the southern hemisphere. Contours represent lines of equal field strength in nanoteslas.

Figures 6a, b, c and d show the magnetic signatures to be expected from a Southwood (1987) twin vortex and a Saunders et al. (1984) / Lee (1986) central vortex. The distinctive differences between the signatures predicted from each model are in the recorded phase and amplitude. However, if the field induced on the ground is asymmetric the phase of the measured signature is reversed for FTE's passing to the east and west of the magnetometer. Further, the amplitude of the measured signal is dependent upon the distance of the disturbance from the station. Consequently, it is not possible to distinguish between the signatures associated with each model without knowing the path of the disturbance with respect to the magnetometer.

Figure 6e illustrates the expected magnetic signature for the current sheet FTE model. The X-component consists of small amplitude oscillations of a few cycles, the phase of which is dependent upon which side of the magnetometer the FTE passes. The Y-component has a saddle-like structure with positive amplitudes of 65 nT and small negative peaks of the order of 10 nT occurring at the beginning and end of each disturbance. The X and Y-components vary negligibly with distance provided that some portion of the current system passes overhead. The Z-component however may vary by 2/3 in magnitude depending on whether the filaments pass directly overhead.

Figure 6f shows the expected magnetic signature for a poleward moving elliptical FTE footprint. The form of this signature is similar to that obtained for Southwood's twin vortex although the amplitudes, especially in the Z-component, are reduced. Equivalent signatures are expected for the east-west moving elliptical footprint. However, the amplitudes of these signatures are significantly less than in the poleward case.

4.4 CONCLUSION

Clearly, each of the postulated ionospheric current systems generate distinct large amplitude impulsive magnetic signatures on the ground. From this work several conclusions can be made.

1. For the same total current (2×10^5A, Saunders et al. 1984) through each of the proposed current systems, fields of the order of 100 nT are established.

2. The magnitude and spatial extent of the fields measured on the ground depends upon the size of the current system in the ionosphere and the spacing between oppositely oriented field-aligned current filaments.

3. All of the postulated current systems give rise to field perturbations with frequencies of the order of $1-2$ mHz depending upon the velocity of the flux tube footprint through the ionosphere. This places these pulsations in the Pc5 range, consistent with observations (Lanzerotti et al. 1987).

4. If a detection limit of 10 nT is assumed for the identification of an FTE signature the maximum separation between the magnetometer and the centre of the field distribution on the ground for each system based on the scale sizes and current magnitudes assumed here, are of the order of:

(a)	Southwood's twin vortex model	~ 600 km
(b)	Saunders et al. / Lee's central vortex model	~ 200 km
(c)	Current sheet model	~ 800 km
(d)	Elliptical model	~ 1100 km

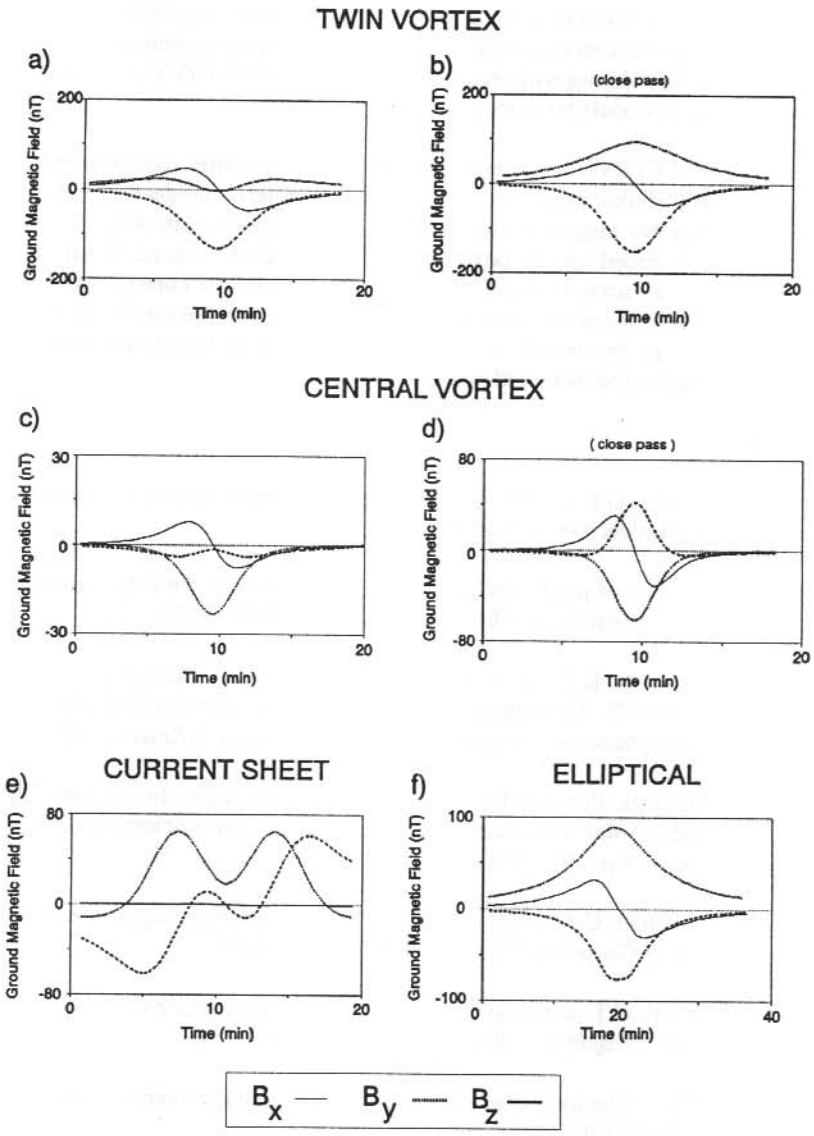

Figure 6. Ground magnetic signatures for postulated ionospheric field-aligned current models.

(a) Twin vortex passing 180 km to the west.

(b) Twin vortex passing 90 km to the west.

(c) Central vortex passing 180 km to the west.

(d) Central vortex passing 90 km to the west.

(e) Current sheet passing 180 km to the west.

(f) Elliptical twin vortex passing 180 km to the west.

It is important to note however that at these distances it would be very difficult to distinguish the impulsive signatures of these models from background variations associated with other effects. For positive identification during magnetically active times (when FTE's are typically observed) we believe these distances could be as much as halved.

To conclude, studies of FTE's from ground based magnetic signatures require an array of closely spaced magnetometers so that at any one time, a current pattern's magnetic field is identifiable from at least three different magnetometer stations. In this way the path of the flux tube through the ionosphere can be traced and its position relative to a given ground-based magnetometer determined. With such an array it would be possible to ascertain the current system in operation at the flux tube footprint, the scale size of the current system and the total field-aligned current carried by the flux tube to the ionosphere. For this to be viable we believe the maximum spacing of these stations should be less than 500 km.

REFERENCES

Crooker, N.A. *and* Siscoe, G.L. (1990). On mapping flux transfer events to the ionosphere. *Journal of Geophysical Research 95*:3795 – 3799.

Kan, J.R. (1988). A theory of patchy and intermittent reconnections for magnetospheric flux transfer events. *Journal of Geophysical Research 93*:5613 – 5623.

Lanzerotti, L.J., Hunsucker, R.D., Rice, D., Lee, L.C., Wolfe, A., MacLennan, C.G. *and* Medford, L.L. (1987). Ionosphere and ground based response to field-aligned currents near the magnetospheric cusp regions. *Journal of Geophysical Research 92*:7739 – 7743.

Lee, L.C. (1986). Magnetic flux transfer at the earth's magnetopause. In: Kamide, Y. *and* Salvin, J.A. (Eds). *Solar wind-magnetosphere coupling*. Terra Scientifica Publishing Company, Tokyo. Pp. 297 – 314.

McHenry, M.A. *and* Clauer, C.A. (1987). Modelled ground magnetic signatures of flux transfer events. *Journal of Geophysical Research 92*:11231 – 11240.

Saunders, M.A., Russell, C.T. *and* Sckopke, N. (1984). Flux transfer events: scale size and interior structure. *Geophysical Research Letters 11*:131 – 134.

Southwood, D.J. (1987). The ionospheric signature of flux transfer events. *Journal of Geophysical Research 92*:3207 – 3213.

Southwood, D.J. *and* Hughes, W.J. (1983). Theory of hydromagnetic waves in the magnetosphere. *Space Science Reviews 35*:301 – 366.

5. A MULTISTATION STUDY OF LONG PERIOD GEOMAGNETIC PULSATIONS IN THE POLAR CLEFT AND CUSP

I.S. Dunlop[1], F.W. Menk[1], H.J. Hansen[1], B.J. Fraser[1] and R.J. Morris[2]

[1] Department of Physics
University of Newcastle
Newcastle NSW 2308
Australia

[2] Auroral and Space Physics
Antarctic Division
Kingston Tasmania 7050
Australia

ABSTRACT

Long period ($1 < f < 15$ mHz) geomagnetic pulsations recorded at the Australian Antarctic stations Macquarie Island (-64.5° gm lat), Mawson (-70.3°), Davis (-74.5°) and Casey (-80.8°), and the New Zealand station Scott Base (-79.8°) have been examined in order to identify wave characteristics associated with different generation mechanisms and magnetospheric source regions. Three distinct wave types were found. First, sustained quasi-sinusoidal oscillations recorded for several hours around local noon at boundary layer latitudes are most likely explained by the excitation of field lines resonances by the Kelvin-Helmholtz instability. Second, irregular pulsations (IPCL) are found near local noon at cusp latitudes, but are not necessarily a cusp indicator. Finally, short bursts from one to a few cycles duration are observed both poleward and equatorward of the cusp during local daytime. Where these emissions are observed at only one station they may be signatures of magnetospheric flux transfer events (FTE). Their occasional observation simultaneously at several stations is suggestive of global impulsive compressions of the geomagnetic cavity.

5.1 INTRODUCTION

The study of high latitude magnetic pulsations at low frequencies (1 – 15 mHz) is important in understanding the generation of plasma waves and instabilities due to the interaction between the solar wind and the geomagnetic field. These low frequency waves are responsible for significant energy deposition within the magnetospheric and ionospheric environment, with a single Pc5 event capable of depositing around 7×10^9 W into the ionosphere through Joule heating (Walker and Greenwald 1980).

Although several generation mechanisms have been proposed for these low frequency emissions, the relative importance of each mechanism is uncertain. The most important mechanisms, and the corresponding expected wave characteristics, are outlined below.

Kelvin-Helmholtz instability. This well-known instability arises when there is a shear component in the relative motion of two interacting fluids. In the geospace environment this is due to the

flow of the solar wind past the geomagnetic boundary layer resulting in a spectrum of hydromagnetic waves at the boundary layer. As a result four basic wave features should be observable:

1. As a ground recording station passes through local midday, plasma motion associated with the instability changes from dawnward to duskward, resulting in a polarisation reversal (Chen and Hasegawa 1974). This was observed at middle latitudes by Samson et al. (1971).

2. Due to the shear flow nature of the instability the amplitude of the pulsations should peak near dawn and dusk and minimise at midday (Chen and Hasewaga 1974).

3. The instability is assumed to drive standing oscillations of magnetic field lines, resulting in resonances when the wave and field line eigenfrequencies match. The observed pulsations should therefore increase in frequency with decreasing latitude (Chen and Hasegawa 1974, Poulter et al. 1988).

4. Observed wave propagation velocities correspond to propagation of the instability at ground speeds around $5-15$ km s^{-1} (Rostoker et al. 1980).

Flux Transfer Events (reconnection). These occur when the interplanetary magnetic field connects with the outermost magnetospheric field lines, and as a result a tube of plasma is injected along the connected field line into the magnetosphere (Russell and Elphic 1978). Lee and Fu (1986) extended this concept to include reconnection over an entire shell of field lines such that the flux transfer event (FTE) should be observed simultaneously over the dayside at the latitude of the flux tube's footprint. The flux tube travels in an antisunward direction at velocities of $3-5$ km s^{-1} (Friis-Christensen et al. 1988) producing pulsations from 200 nT to $\leq$ 40 nT P-P at ground level (Friis-Christensen et al. 1988, Hönisch and Glassmeier 1986). Theoretical work shows that the maximum azimuthal extent of a single large FTE on the ground is of the order of 200 km (Chaston et al. 1992).

Global Cavity Compressions. These arise from sudden fluctuations in the pressure of the solar wind on the magnetosphere and result in an isolated 'breathing' motion of the whole geomagnetic cavity. The pulsation is produced at the nose of the magnetosphere due to compressional discontinuities in the solar wind and travels antisunward at velocities of $10-30$ km s^{-1} (Sibeck 1990). The ground signature of an isolated cavity compression is similar to that of an FTE (Lockwood et al. 1990, Sibeck 1990) and a number of stations are required to distinguish between the two types of events, since the former should be observed at widely spaced locations.

Irregular, Continuous Pulsations. The IPCL (Bol'shakova et al. 1977, Friis-Christensen et al. 1988) is a long continuous irregular signal with occasional discrete bursts and periods from $3-15$ minutes. Amplitudes vary from a few to tens of nanotesla, and appear to be directly related to the solar wind velocity and the B_z component of the IMF (Kleimenova et al. 1985). Troitskaya (1985) suggested that IPCLs are generated by patchy reconnection at the dayside polar cusp, and presented an empirical equation relating the location of the cusp to the maximum IPCL signature,

$$\Delta\phi^\circ = 1.8\Delta t - 0.2 \qquad (1)$$

where Δt is in hours and $\Delta\phi$ is the distance, in degrees, from the cusp.

This paper presents results from a multistation Antarctic study of 1 – 15 mHz geomagnetic pulsations with the aim of determining the source location and the likely generation mechanisms based on the observed signal characteristics.

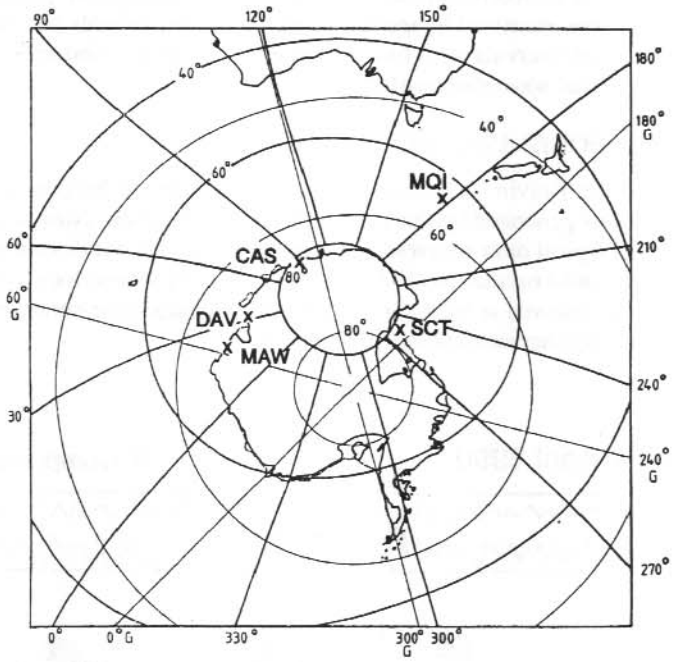

Figure 1. The location of the Antarctic and subantarctic stations from which data was analysed. The five stations used were Mawson (MAW), Davis (DAV), Casey (CAS), Scott (SCT) and Macquarie Island (MQI). The two coordinate systems shown are geographic (G) and invariant.

5.2 DATA RECORDING AND ANALYSIS

Long period (1 – 20 mHz) geomagnetic pulsation data used in this study were recorded with the five station Antarctic array of digital magnetometers shown in Figure 1. Stations span sub-auroral, boundary layer and cusp latitudes. These stations have been operated jointly by the University of Newcastle and the Australian Antarctic Division (MQI, MAW, DAV, CAS) and New Zealand DSIR Antarctic (SCT) since 1990. Each station uses identical instrumentation. For this study pulsations over the Pc1-5 (2 Hz – 1 mHz) range were detected in the geomagnetic north-south (X) and east-west (Y) components with induction sensors, and digitally recorded on hard disks using dedicated LSI-11 computers. Sensitivity of each system was typically 0.2 nT at 10 mHz, with a full scale range of 40 nT. Timing of the data logging was controlled by chronometers referenced to radio time standards, and the resultant interstation time error was typically ≤30 ms. Data were recorded at sample rates of 0.333 Hz. All Antarctic stations are linked by electronic mail to Newcastle University, where all data analysis was performed. More recent campaigns utilise sample rates of 2 Hz or 0.25 Hz and data are recorded on IBM compatible computers (Fraser et al. 1991).

Data analysed comes from a campaign conducted during 3 – 17 April 1990. Low altitude particle data from the DMSP-F7 polar orbiting satellite were also used to indicate the topology of the geomagnetic field (Newell and Meng 1988, Menk et al. 1992). Thirty MHz riometer records from Davis were used to monitor relative variations in ionospheric particle fluxes. The magnetometer data were examined by means of amplitude time records and dynamic and static power spectra. Selected intervals were further studied using polarisation and phase analysis and interstation comparison of wave characteristics.

5.3 KELVIN-HELMHOLTZ ASSOCIATED WAVES

The importance of the Kelvin-Helmholtz mechanism was tested by comparing the features expected for pulsations generated by this instability, outlined earlier. Nine days were examined and results from two typical days are presented here. Activity on these days was characterised by sustained, quasi-sinusoidal oscillations lasting for several hours around local noon, usually in the 2 – 8 mHz range and observed at least at two stations. A typical time-series record is shown in Figure 2. The following characteristics were observed.

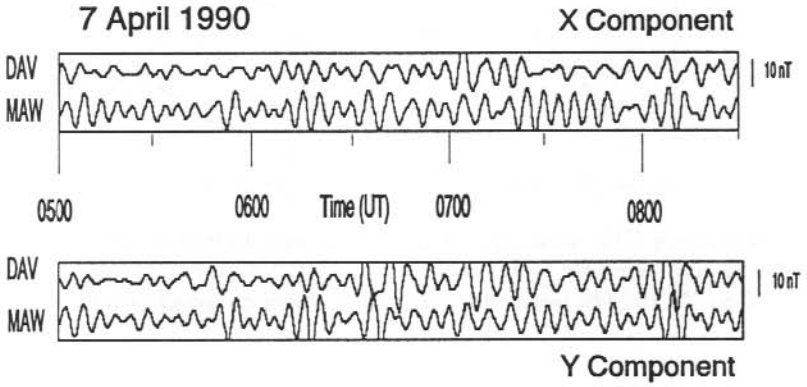

Figure 2. Amplitude time series for Mawson and Davis showing the Kelvin-Helmholtz type signals on 7 April 1990. The top trace is from Davis in each case with the geomagnetic X-component being the top box and the Y-component being the bottom box.

1. Figure 3 shows dynamic power spectra for 7 April 1990, when the DMSP spacecraft showed the cusp to be poleward of Davis. At Scott (same latitude as Casey) and Casey there was no evidence of the sustained low frequency signal seen at both Davis and Mawson. The signal frequency at Davis was around 3 mHz and at Mawson around 4 mHz. Occasionally signals near 8 – 9 mHz, which may be harmonics, were present at Davis. The signals were thus recorded at stations equatorward of the cusp.

2. Figure 4a summarises wave amplitude characteristics on two typical days. For 7 April 1990 the pulsations clearly had maximum amplitudes near 1000 and 1800 LT. Although this was not so clear on 6 April, the overall trend still agrees with the expected Kelvin-Helmholtz characteristic.

3. The sense of polarisation of these signals reversed near local noon; this is illustrated in Figure 4b.

4. Interstation comparison shows that these waves are associated with propagation speeds in the morning sector of 7 ± 2 km s^{-1}, from Davis to Mawson, i.e. to lower latitudes away from the poleward edge of the boundary layer, located by DMSP satellite particle data. These results are summarised in Table 1.

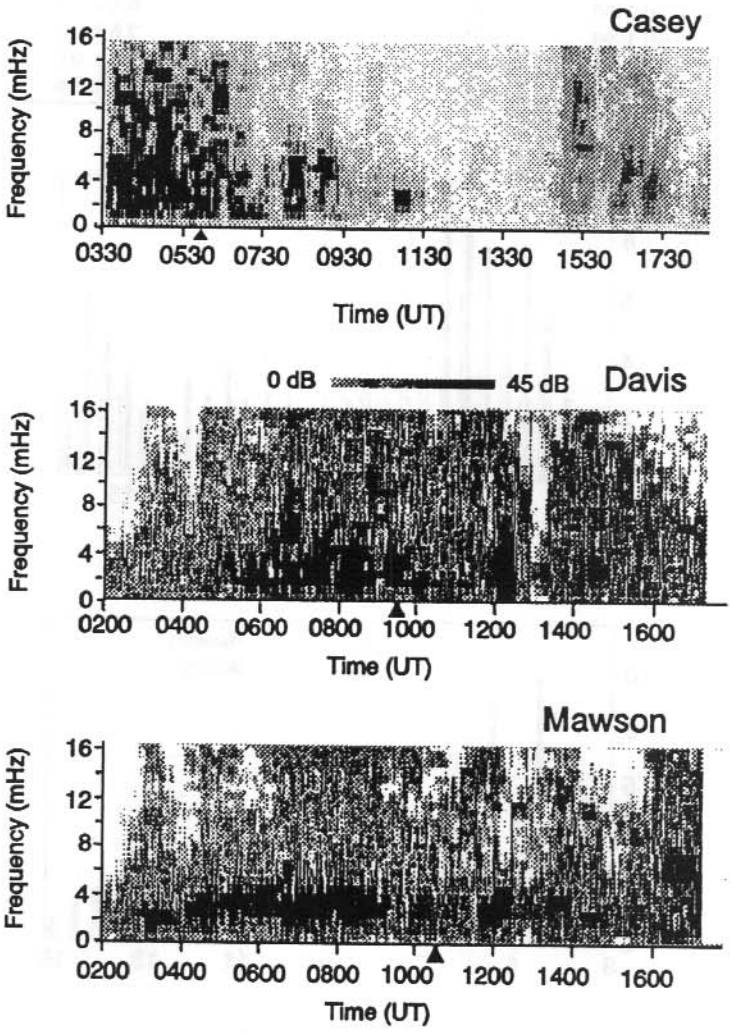

Figure 3. Dynamic power spectra for Casey (top), Davis (middle) and Mawson (bottom) for 7 April 1990. Local midday is indicated by the arrow on the time scale.

Table 1. Summary of propagation speeds calculated between Davis and Mawson for 6 and 7 April 1990.

Date	Time (UT)	Dt (s) Davis – Mawson	Speed (km/s)
6 April 1990	0520	102	6.3 ± 0.6
6 April 1990	0625	75	8.5 ± 0.6
6 April 1990	0650	84	7.6 ± 0.6
7 April 1990	0645	87	7.4 ± 0.6
7 April 1990	0745	93	6.8 ± 0.6
7 April 1990	1015	84	7.6 ± 0.6
7 April 1990	1040	78	8.2 ± 0.6
7 April 1990	1120	99	6.5 ± 0.6

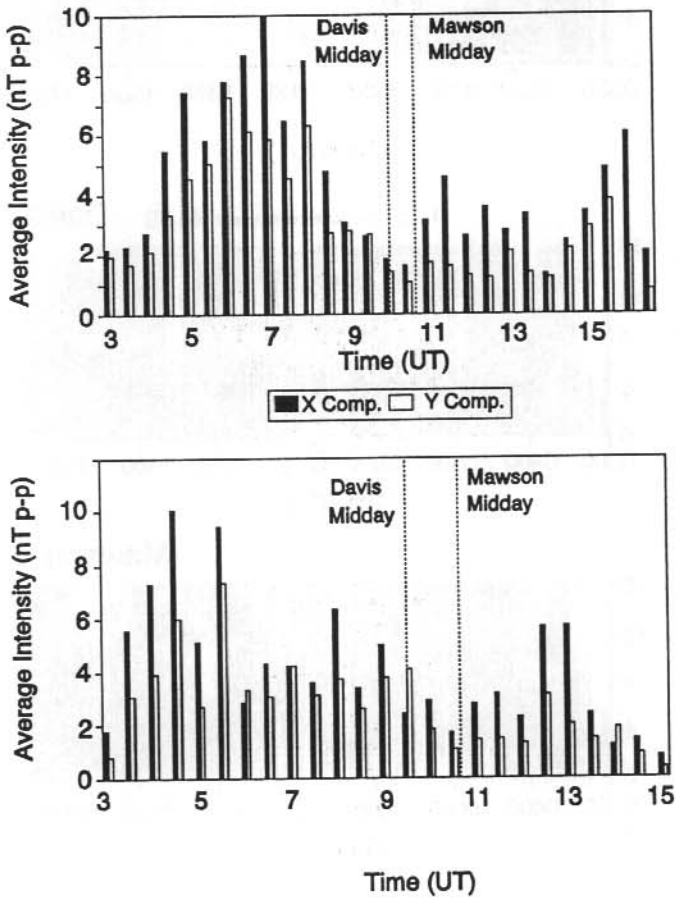

Figure 4a. Plot of the average pulsation amplitude at Mawson for 7 April 1990 (top), and 6 April 1990 (bottom); Kp ≈ 2.

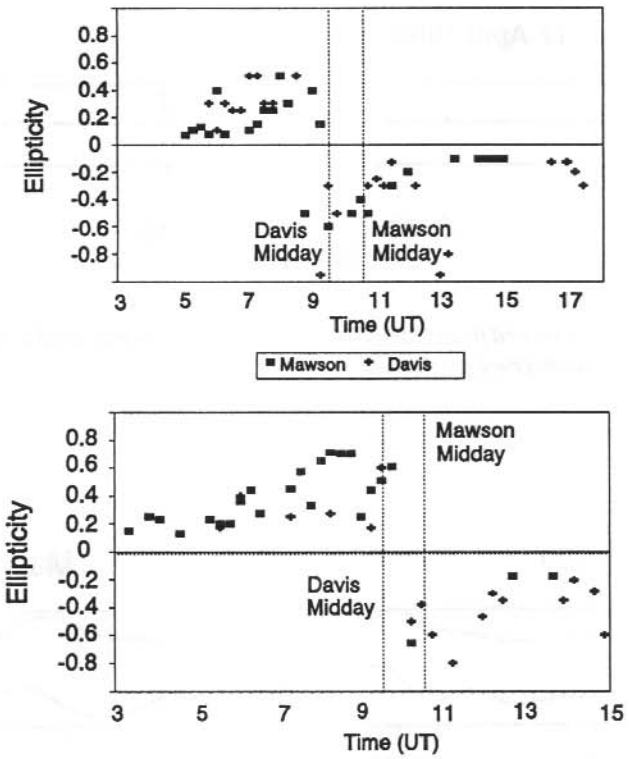

Figure 4b. Plot of the ellipticities of the Kelvin-Helmholtz type signal for both Davis and Mawson for 7 April 1990 (top) and 6 April 1990 (bottom); Kp ≈ 2. Negative values denote counter-clockwise sense of rotation.

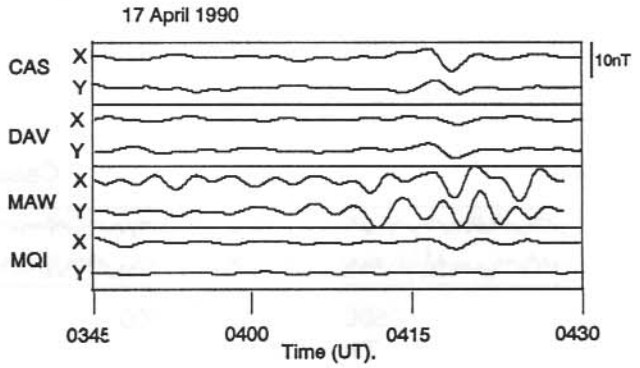

Figure 5. Pulsation magnetograms from Casey, Davis, Mawson and Macquarie Island showing the impulsive nature of events seen at all stations. In each magnetogram the top trace is the north–south component and the bottom trace is the east–west component on 17 April 1990; Kp ≈ 5 – 6.

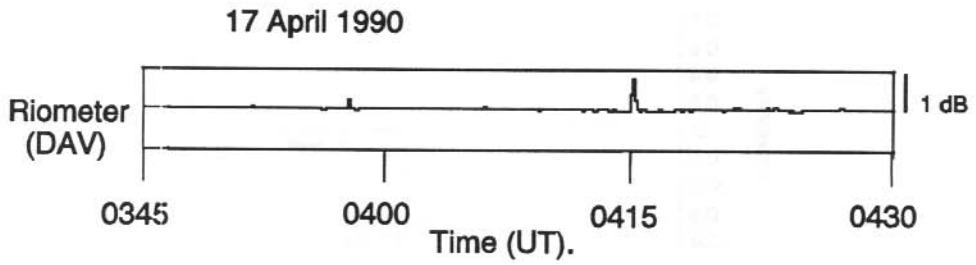

Figure 6. The riometer record from Davis for 17 April 1990 showing an absorption spike related to two FTE-like events observed at all stations.

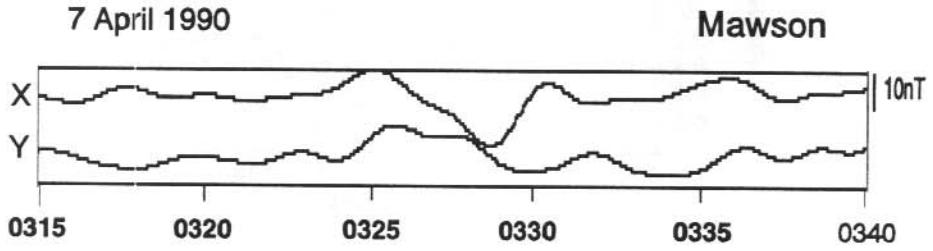

Figure 7. Impulsive event seen at Mawson only within the boundary layer, 3° equatorward of the cusp. 17 April 1990; Kp ≈ 5.

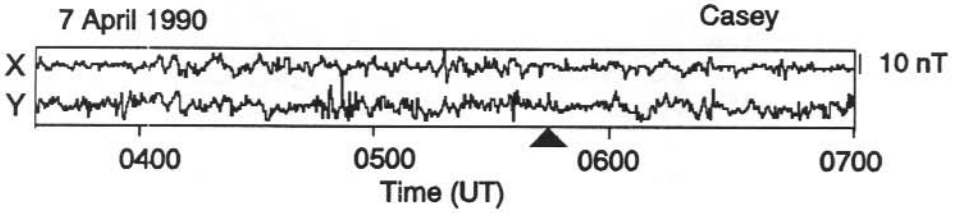

Figure 8. The gradual onset and decline of typical IPCL-like activity at Casey from 0330 UT to 0700 UT, on 7 April 1990.

5.4 IMPULSIVE EVENTS

Transient, impulsive events, illustrated in Figure 5, occur both as an isolated pulsation seen only at one station, and as a widely distributed pulsation seen at all stations including Macquarie Island. The latter events were found to coincide with transient enhancements in particle precipitation on the 30 mHz riometer record, e.g. Figure 6. This type of event is not very common, with only two cases being identified on the magnetically disturbed day, 17 April 1990, and none on the magnetically quiet days 6–7 April 1990.

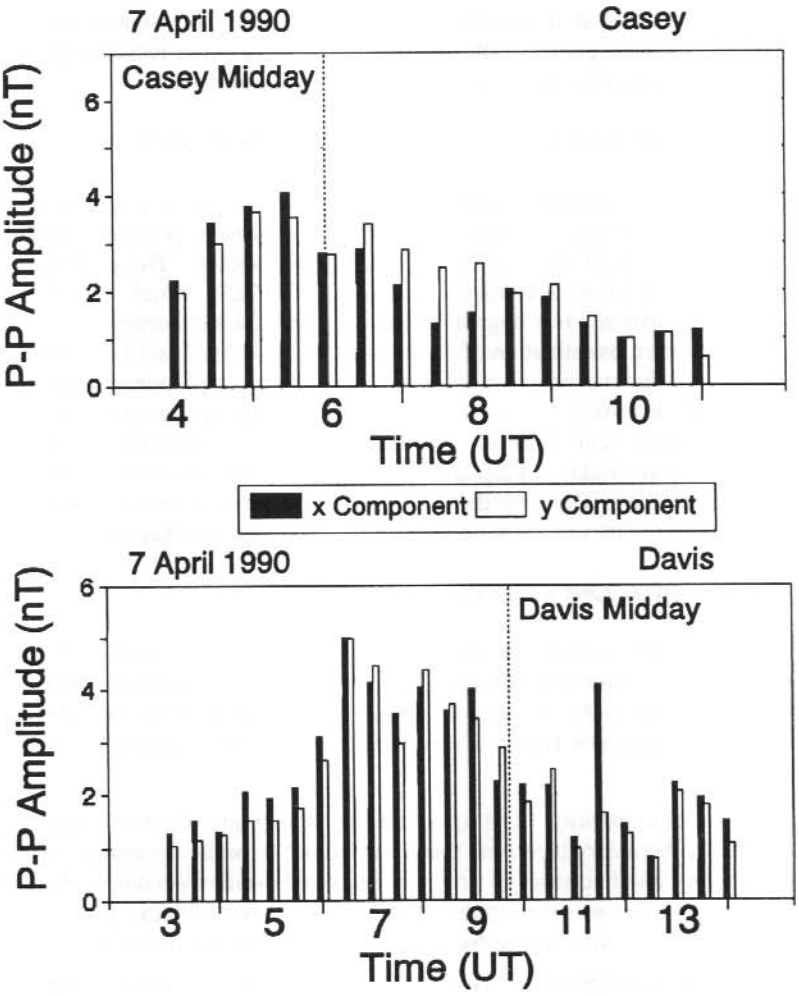

Figure 9. Plot of the average IPCL intensity against UT for Casey (top) and Davis (bottom) on 21 July 1990. The data are organised in 30 minute bins (Kp ≈ 2).

Single, isolated transient events, such as the example illustrated in Figure 7, were only seen at one or two stations at a given time and have no associated particle precipitation. These events are clearly more localised and exhibit FTE-like appearance (e.g. Lanzerotti et al. 1986, Friis-Christensen et al. 1988). The ground recording stations are however too far apart to permit definite identification of these as FTE signatures. The Casey-Davis distance is 1420 km and Davis-Mawson distance 640 km, indicating an upper scale size limit for these pulsations. The events seen at only one station are the most common, with up to 10 such events being seen on more active, $K_P \cong 6$, days and only one or two on quiet, $K_P \cong 2$, days at any one station. The events are seen both on open and closed field lines but are limited to locations near the boundary layer.

At least two different generation mechanisms are required to explain the observed features. Those transient pulsations recorded at all stations and which have a corresponding riometer signature are most likely connected with global cavity compressions, while those recorded at only one, or at most two, stations are probably associated with an FTE-like mechanism.

5.5 SUSTAINED IRREGULAR LONG PERIOD PULSATIONS (IPCL)

Figure 8 shows a typical example of long period signals with a highly irregular structure which were found daily, commencing in the morning sector. Amplitudes generally peaked during the middle of the day at ~30 nT and waned in the afternoon sector. These irregular pulsations resemble the IPCL signature described by Troitskaya (1985), which she found reached a maximum at stations within a few degrees of the cusp and quickly decreased in intensity away from the cusp. However, examination of the data collected in April and July 1990 suggests that there is no simple and direct connection between the maximum amplitude of these signals and the location of the cusp, determined using DMSP particle data, as suggested by equation (1). The results are summarised in Table 2. It was also found that the maximum IPCL amplitude does not necessarily peak at local midday at cusp latitudes. Figure 9 shows an example where amplitudes peaked in the late morning. On other days there may be no clear time of maximum amplitude, suggesting that the waves are not always generated by a spatially confined source.

5.6 DISCUSSION AND CONCLUSION

At least four generation mechanisms are required to explain the properties of low frequency pulsations observed at Antarctic latitudes. These mechanisms seem to operate in specific geomagnetic regions and so the resulting pulsations are limited to certain latitudes depending on the topography of the magnetic field at a particular time. The mechanisms suggested to explain these pulsations are:

1. Kelvin-Helmholtz instability. The associated pulsations are observed equatorward of the poleward edge of the boundary layer, and may be responsible for the resonance excitation of field lines resulting in very low frequency (3 – 6 mHz) sustained oscillations during the local morning and afternoon sector. The waves propagate antisunward in the morning sector at velocities of approximately 7 ± 2 km s^{-1} and their sense of polarisation changes at or around local midday.

2. Global geomagnetic compression. Transient pulsations driven by sudden compressions of the geomagnetic cavity are most likely generated at the boundary layer and propagate antisunward through the cavity, resulting in their observation at all stations. The pulsation signal is associated

with a transient particle precipitation event in the dayside auroral oval and a resulting global pulsation.

3. Flux transfer events. The transient pulsations associated with these are a localised phenomenon and although they appear identical to pulsations associated with cavity compressions, they are recorded at only one or two stations. Such transient signatures are seen on both open and the first closed field lines, occurring more frequently on more active days.

4. Continuous, irregular pulsations. These are a dominant feature within a few degrees of the cusp in the noon sector. The local time of maximum amplitude was not found to correlate with the location of the cusp as defined by low altitude particle measurements. It appears likely that these long period, long wavelength fluctuations are more likely associated with boundary layer/cusp current systems rather than localised particle features.

Table 2. Summary of the IPCL cusp latitude location results using equation (1) for three days of ground and corresponding DMSP satellite data.

Date	Calculated Cusp Latitude, °S			Measured Cusp Lat. with Satellite, °S
	Casey	Davis	Mawson	
7 April 1990	81.5 ± 0.5°	78 ± 1°		79 ± 2°
17 April 1990	76.5 ± 0.9°	78.5 ± 0.9°	75.4 ± 0.6°	70 ± 4°
21 July 1990	82.4 ± 0.9°	–	–	77 ± 1°

To study the IPCL and FTE processes in more detail a more closely spaced station array is required, to record the motion of flux tubes antisunward and delineate between isolated flux tubes and multiple flux tubes as suggested by Lee and Fu (1986). Spatial characteristics of IPCL signals also require further investigation on a small scale size. Another problem is lack of information on cusp dynamics. This may be resolved using photometric observations of the cusp in conjunction with ground magnetometer and in situ particle measurements.

5.7 ACKNOWLEDGMENTS

Dr A. Klekociuk and the Auroral Space Physics group, Antarctic Division, collected the Australian National Antarctic Research Expedition (ANARE) station magnetometer and riometer data. The Scott base data were recorded by the New Zealand Antarctic Research Program members, under the direction of Dr M. McFarlane and Mr H. Logan. The DMSP satellite data were kindly provided by Dr P.T. Newell. This work was supported by the Australian Research Council (ARC), the Antarctic Science Advisory Committee (ASAC) and the University of Newcastle.

REFERENCES

Bol'shakova, O.V., Troitskaya, V.A. *and* Hessler, V.P. (1977). Dynamics of the dayside cusp, according to observations of long-period geomagnetic pulsations. *Geomagnetism and Aeronomy 17*:722–725.

Chaston, C.C., Hansen, H.J., Menk, F.W. *and* Fraser, B.J. (1992). Modelled ground and ionospheric signatures of magnetospheric flux transfer events. In: Burns, G.B. *and* Duldig, M.L. (Eds). *ANARE Research Notes Number 88*. Australian Antarctic Division.

Chen, L. *and* Hasegawa, A. (1974). A theory of long-period magnetic pulsations 1. steady state excitations of field line resonance. *Journal of Geophysical Research 79*:1024–1032.

Fraser, B.J., McNabb, P.W., Menk, F.W. *and* Waters, C.L. (1991). A personal computer induction magnetometer system for recording geomagnetic pulsations. In: Burns, G.B. (Ed.). *ANARE Research Notes Number 80*. Australian Antarctic Division. Pp. 83–92.

Friis-Christensen, E., McHenry, M.A., Clauer, C.R. *and* Vennerstrom, S. (1988). Ionospheric travelling convection vortices observed near the polar cleft: a triggered response to sudden changes in the solar wind. *Geophysical Research Letters 15*:253–256.

Hönisch, M. *and* Glassmeier, K.H. (1986). Isolated transient magnetic variations in the auroral zone. *EOS Transactions of the American Geophysical Union 67*. P. 1163.

Kleimenova, N.G., Bol'shakova, O.V., Troitskaya, V.A. *and* Friis-Christensen, E. (1985). Two forms of long-period geomagnetic pulsations near the equatorial border of the dayside polar cusp. *Geomagnetism and Aeronomy 25*:139–140.

Lanzerotti, L.J., Lee, L.C., MacLennan, C.G., Wolfe, A. *and* Medford, L.V. (1986). Possible evidence of flux transfer events in the polar ionosphere. *Geophysical Research Letters 13*:1089–1092.

Lee, L.C. *and* Fu, Z.F. (1986). Multiple X line reconnection, 1, a criterion for the transition from a single X line to a multiple X line reconnection. *Journal of Geophysical Research 91*:6807–6815.

Lockwood, M., Cowley, S.W.H., Sandholt, P.E. *and* Lepping, R.P. (1990). The ionospheric signatures of flux transfer events and solar wind dynamic pressure changes. *Journal of Geophysical Research 95*:17113–17135.

Menk, F.W., Fraser, B.J., Hansen, H.J., Newell, P.T., Meng, C.-I. *and* Morris, R.J. (1992). Identification of the magnetic cusp and cleft using Pc1-2 ULF pulsations. *Journal of Atmospheric and Terrestrial Physics*. (in press).

Newell, P.T. *and* Meng, C.-I. (1988). The cusp and cleft/boundary layer: low altitude identification and statistical local time variation. *Journal of Geophysical Research 93*:14549–14556.

Poulter, E.M., Allan, W. *and* Bailey, G.J. (1988). ULF pulsation eigenperiods within the plasmasphere. *Planetary and Space Science 36*:185 – 196.

Rostoker, G., Samson, J.C. *and* Olson, J.V. (1980). Latitudinal and longitudinal variation of Pc4, 5 pulsations and implications regarding source mechanisms. *Journal of Geomagnetism and Geoelectricity 21, Supplement II*. Pp. 1 – 15.

Russell, C.T. *and* Elphic, R.C. (1978). Initial ISEE magnetometer results: magnetopause observations. *Space Science Reviews 22*:681 – 715.

Samson, J.C., Jacobs, J.A. *and* Rostoker, G. (1971). Latitude-dependent characteristics of long-period geomagnetic pulsations. *Journal of Geophysical Research 76*:3675 – 3683.

Sibeck, D.G. (1990). A model for the transient magnetospheric response to sudden solar wind dynamic pressure variations. *Journal of Geophysical Research 95*:3755 – 3771.

Troitskaya, V.A. (1985). ULF wave investigations in the dayside cusp. *Advances in Space Research 5*:219 – 228.

Walker, A.D.M. *and* Greenwald, R.A. (1980). Pulsation structure in the ionosphere derived from auroral radar data. *Journal of Geomagnetism and Geoelectricity 32, Supplement II*. Pp. 111 – 127.

6. SOURCES OF SOLAR WIND ASSOCIATED Pc3-5 MAGNETIC PULSATIONS IN THE MAGNETOSPHERE

H.J. Hansen[1], B.J. Fraser[1], F.W. Menk[1], P.T. Newell[2], C.-I. Meng[2] and R.J. Morris[3]

[1] Department of Physics
University of Newcastle
Newcastle NSW 2308
Australia

[2] Applied Physics Laboratory
The Johns Hopkins University
Laurel MD 20707 USA

[3] Auroral and Space Physics
Antarctic Division
Kingston Tasmania 7050
Australia

ABSTRACT

Dayside Pc3-5 (30 – 70 mHz) magnetic pulsations have been recorded during a 14-day campaign in April 1990 with a three station array of induction magnetometers in Antarctica spanning 70 – 80°S MLAT and almost five hours in local time. During two intervals when it was possible to associate these pulsation signals with the solar wind upstream of the bowshock, interstation cross-spectral and polarisation analysis shows the waves enter via two regions simultaneously. One is situated in the pre-noon local time sector in the sun-earth reference frame where bow shock turbulence near the nose of the magnetosphere maximises. The other is most likely along the magnetospheric boundary plasmasheet region which maps down to the dayside auroral region.

6.1 INTRODUCTION

Solar wind turbulence generated upstream of the bow shock is a major source of Pc3-4 (15 – 100 mHz) pulsation activity in the dayside magnetosphere. These pulsations exhibit frequencies directly in accordance with IMF magnitude (Gul'elmi et al. 1973, Vero and Hollo 1978) and have been correlated with IMF cone angle – the angle between the IMF and the sun-earth line (Greenstadt et al. 1980, Odera 1986).

Despite the connection between solar wind and magnetospheric Pc3-4 pulsations, little is known about the roles different processes play in transmitting solar wind energy into the magnetosphere. The region upstream of the bow shock provides energy which is able to enter directly from magnetosheath in the subsolar region as compressional magnetosonic (fast or slow) waves (Wolfe and Kaufmann 1975). Alternatively, velocity shear at the dayside boundary between streaming solar wind plasma and the magnetosphere allows the development of the Kelvin-Helmholtz wind-over-water instability and energy can spread into the magnetic cavity from the magnetopause surface. Recently, it has been shown that precipitating electrons associated with the dayside cusp

(the region located at local noon where magnetosheath particles have direct access to the ionosphere from the nose of the magnetopause) are modulated simultaneously with the occurrence of harmonically structured Pc3 pulsations in the magnetosphere (Engebretson et al. 1990). This suggests that the cusp region provides an additional entry point of solar wind energy.

This paper identifies both the bow shock and the boundary layer auroral region as participants in jointly providing solar wind energy to the magnetosphere.

6.2 OBSERVATIONS

The signals were recorded with an array of induction magnetometers spanning the Australian Antarctic Territory. Figure 1 shows the magnetometer sites. Casey (gm 80.6°S; 85.3°E) is situated beneath the polar cap region, Davis (gm 74.5°S; 29.6°E) rotates beneath those field lines which map through the polar cusp, and Mawson (gm 70.1°S; 19.6°E) is normally beneath the auroral oval region.

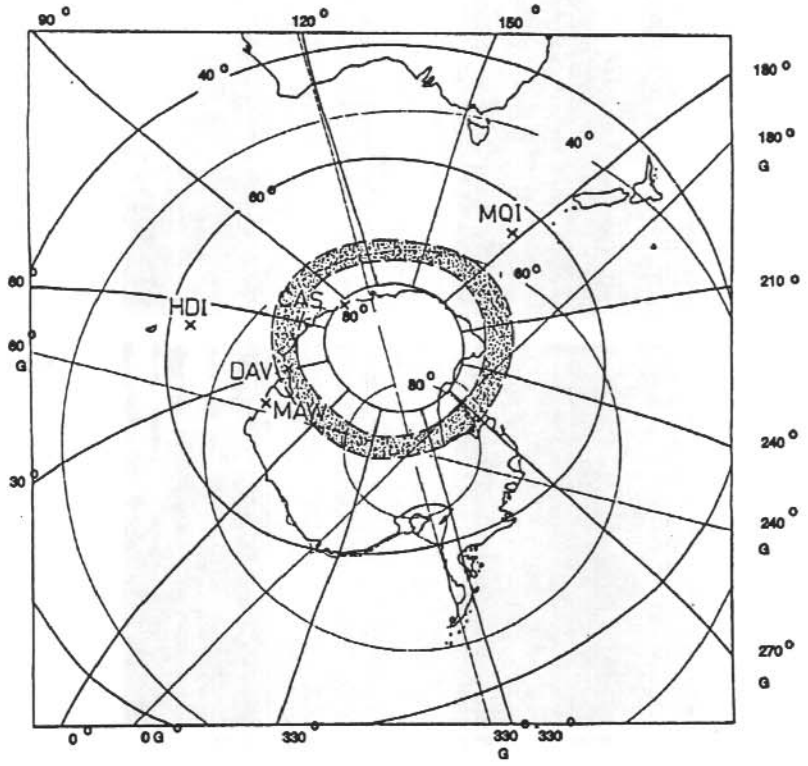

Figure 1. The locations of Casey (CAS), Davis (DAV) and Mawson (MAW). The bold/fine curves indicate geomagnetic/geographic coordinates. The speckled region indicates those locations on Earth that rotate beneath the average location of the dayside cusp. Heard Island (HDI) and Macquarie Island (MQI) were not used in this study.

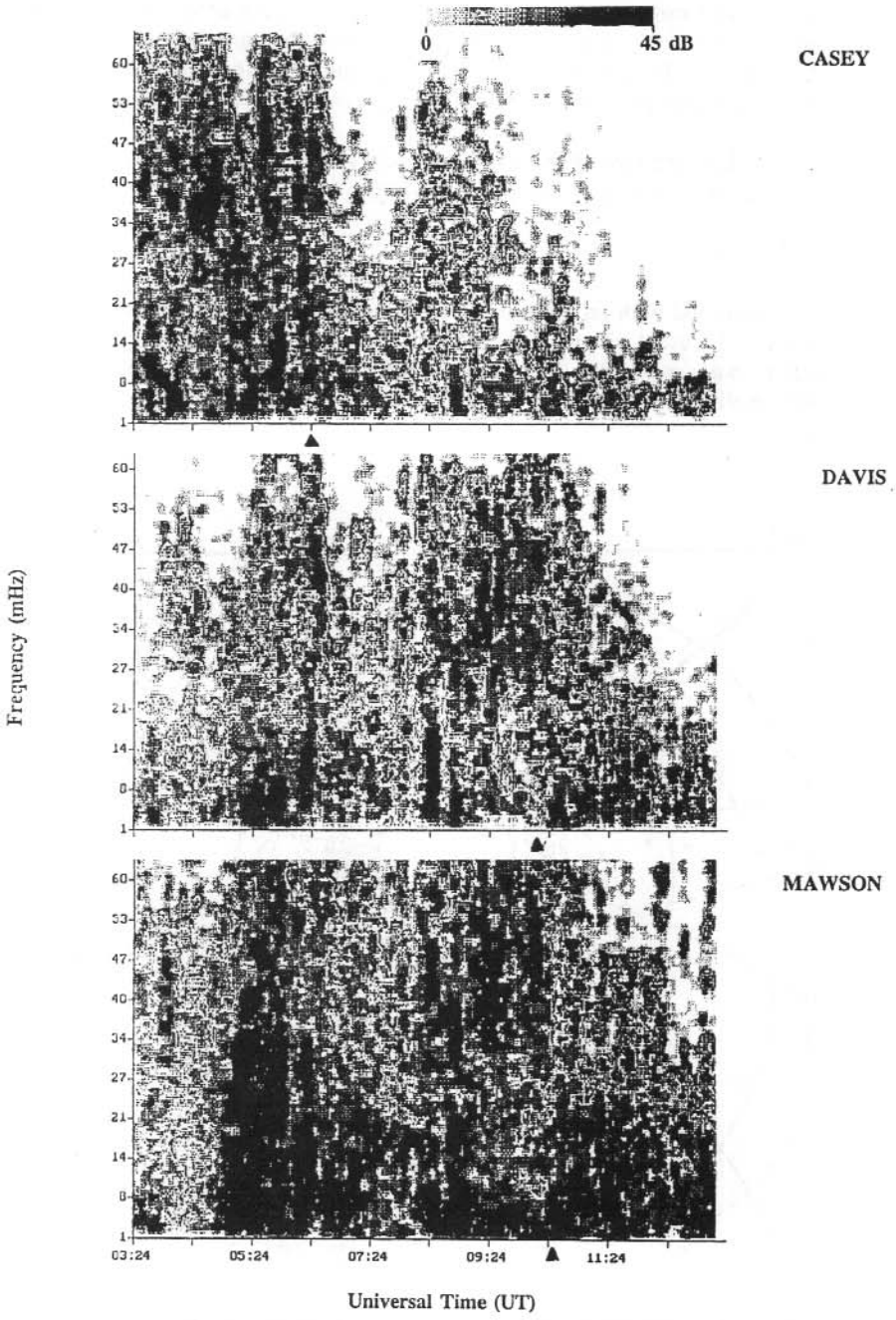

Figure 2. Frequency-time spectra of concurrent magnetic pulsation activity (0 – 70 mHz) at Casey, Davis and Mawson on 14 April 1990. Local noon at each station is shown by the triangles.

At each recording site, induction sensors in the magnetic north-south (H) and east-west (D) directions record magnetic variations due to ionospheric current perturbations, which are related through electrodynamic coupling to magnetospheric/solar wind processes. The sensors consist of 250 000 turns wound over a high permeability μ metal core giving a response of approximately 350 V (nT) $(Hz)^{-1}$ at frequencies less than 1 Hz. The data were recorded digitally at 0.33 Hz using a PDP-11 computer. The PDP-11 was networked via an ANARESAT link to the Antarctic Division and the University of Newcastle. At Newcastle, the data were converted to a common format using a customised Data Base Management System and accessed through a dedicated LAN with six PC286/386 microcomputers. The selected data were analysed using multi-channel state vector time series and cross spectral analysis techniques (Samson et al. 1971).

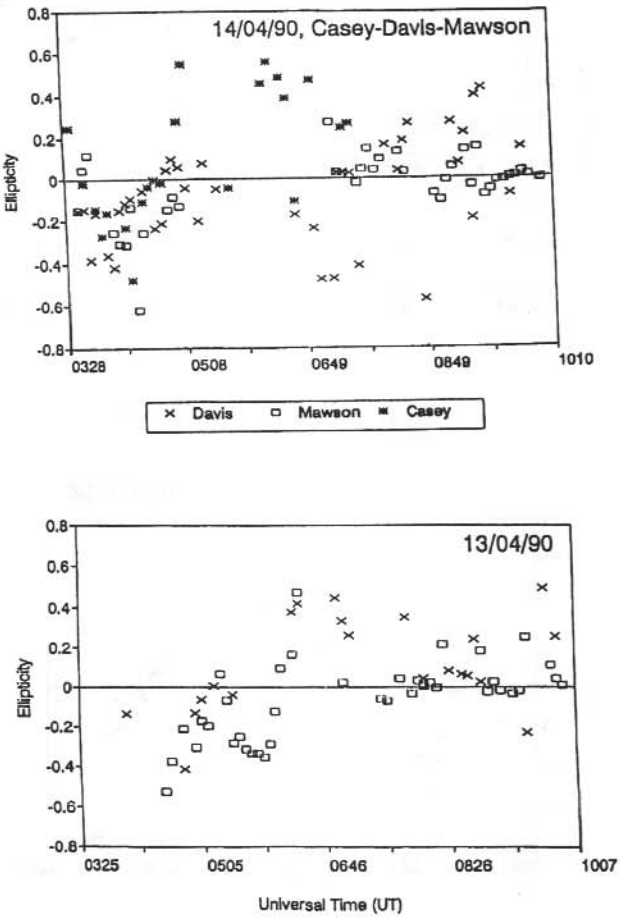

Figure 3. Ellipticity parameter vs UT corresponding to solar wind associated activity received on 14 April (top) and 13 April (bottom).

Details of two successive days of pulsation activity are presented here. Figure 2 displays the frequency-time spectra of concurrent H component signals at Casey (top), Davis (middle) and Mawson (bottom) between 0325 and 1349 UT on 14 April 1990. Local noon is indicated at each site by the triangle. Signals between 35 and 45 mHz occurred in the pre-noon sector and are believed to be associated with the upstream solar wind, because the amplitudes peak in the local time sector where the bow shock turbulence maximises. Frequencies for this type of activity vary with IMF magnitude according to f ~B/160 (Gul'elmi et al. 1973). The activity is centred on 49

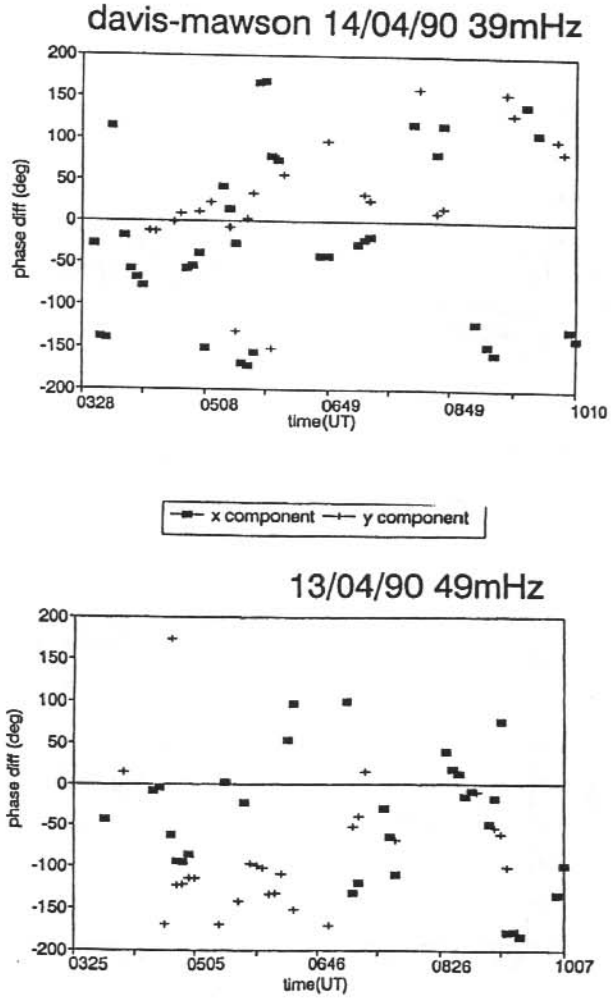

Figure 4. Phase differences vs UT of solar wind associated activity propagating between Davis and Mawson for 14 April (top) and 13 April (bottom) intervals. The x(y) component refers to phase differences between H and D signals.

mHz during the 14 April period. On 13 April, the activity was centred on 49 mHz and the IMF was correspondingly higher (7.4 < IMF < 8.5 nT compared to 6.7 < IMF < 7.1 nT).

Polarisation analysis of the signals yields information about the wave properties. The sense of polarisation and the orientation of the major axis of the polarisation ellipse was determined from the H and D signals at each site. Positive ellipticities imply right hand circular polarised waves, negative imply left hand waves, when viewed in the direction of the ambient field. Figure 3 (top) displays the ellipticity variation in the 35 – 45 mHz frequency band at Casey, Davis and Mawson during the 14 April interval. The ellipticities changed from negative to positive (left-hand to right-hand sense of rotation of the polarisation ellipse) around 0700 UT, ~3 hrs before local noon at Davis and Mawson. Similar behaviour, associated with the 45 – 55 mHz activity recorded on 13 April, is shown in Figure 3 (bottom).

Phase differences between concomitant pulsations at Davis and Mawson were evaluated. For the 14 April interval, 39 mHz signals were compared whilst for the 13 April period, 49 mHz signals were of interest. Figure 4 shows the phase differences between both H and D components at Davis and Mawson for both intervals. The Mawson signals mostly led those at Davis (indicated by the negative phase values). The only period during which positive phase differences predominated was between 0700 and 1000 UT whilst Davis was in the immediate vicinity of the cusp. Since Mawson is an auroral oval station, most of the common signals thus seem to propagate from auroral oval locations towards Davis, the polar cap site.

6.3 DISCUSSION

It is believed that the association of solar wind and IMF parameters with pulsation amplitudes and frequencies points to ion cyclotron waves in the region upstream of the bowshock as being responsible for this class of (30 – 70 mHz) Pc3 activity within the magnetosphere (Greenstadt et al. 1980).

The polarisation reversal from negative to positive values suggests a magnetospheric source for this activity which is seen first at Casey, then Davis and finally Mawson as the stations rotate in the sun-earth reference frame. The enhanced amplitudes occurring around the same time (~3 hrs before local noon at each site) endorses this view. This activity can be connected to the upstream solar wind region via the bowshock since during both intervals, the IMF cone angle is ~50° which will provide the region of maximum bowshock turbulence in the pre-noon local time sector.

Alternatively, the observation of concurrent wave activity mostly propagating from Mawson to Davis (i.e., lower to higher latitudes) suggests that the boundary layer plasmasheet which maps to the auroral oval ionosphere is also a source of solar wind associated magnetic variations within the magnetosphere. This region appears to be the dominant source of propagating activity on the dayside. The phase delays shown in Figure 3 correspond to time delays between 3 and 7 s and these relate to apparent ionospheric phase speeds of ~10's of km s^{-1}. Since many of the associated bursts between Davis and Mawson occur within $1/(2\pi f)$ s or ~5 s (for f ~45 mHz) of each other, the group and phase velocities can be regarded as equivalent (Althouse and Davis 1978). These speeds are consistent with the fast compressional Alfven mode (waves propagating through boundary layer field lines in the equatorial magnetosphere).

This study demonstrates that solar wind associated Pc3 pulsations are delivered into the magnetosphere through joint wave generation processes in the bowshock and in the auroral boundary layer regions.

6.4 ACKNOWLEDGMENTS

Thanks to Dr A. Klekociuk and the Auroral Space Physics group, Antarctic Division, for collection of the Australian National Antarctic Research Expedition (ANARE) station data. We acknowledge financial support from the Australian Research Council (ARC), the Antarctic Science Advisory Committee (ASAC) and the University of Newcastle.

REFERENCES

Althouse, E.L. *and* Davis, J.R. (1978). Five-station observations of Pc1 micropulsation propagation. *Journal of Geophysical Research 83*:132 – 144.

Engebretson, M.J., Anderson, B.J., Cahill, L.J., Arnoldy, R.L., Rosenberg, T.J., Carpenter, D.L., Gail, W.B. *and* Eather, R.H. (1990). Ionospheric signatures of cusp latitude Pc3 pulsations. *Journal of Geophysical Research 95*:2447 – 2456.

Greenstadt E., McPherron, R.L. *and* Takahashi, K. (1980). Solar wind control of daytime, mid-period geomagnetic pulsations. *Journal of Geomagnetism and Electricity 32*:89 – 108.

Gul'elmi, A.V., Plyasova-Bakunina, T.A. *and* Shchepetnov, R.V. (1973). Relation between the period of geomagnetic pulsations Pc3, 4 and the parameters of the interplanetary medium at the earth's orbit. *Geomagnetism and Aeronomy 13*:331 – 333.

Odera, T.A. (1986). Solar wind controlled pulsations, a review. *Reviews of Geophysics 24*:54 – 65.

Samson, J., Jacobs, J.A. *and* Rostoker, G. (1971). Latitude dependent characteristics of long period geomagnetic pulsations. *Journal of Geophysical Research 76*:3675 – 3683.

Vero, J. *and* Hollo, L. (1978). Connections between interplanetary magnetic field and geomagnetic pulsations. *Journal of Atmospheric and Terrestrial Physics 40*:857 – 865.

Wolfe, A. *and* Kaufmann, R.L. (1975). MHD wave transmission and production near the magnetopause. *Journal of Geophysical Research 80*:1764 – 1775.

7. RADIAL EXTENT OF SOURCE REGIONS OF ION CYCLOTRON WAVES IN THE MAGNETOSPHERE

Y.D. Hu and B.J. Fraser

Physics Department
University of Newcastle
Newcastle NSW 2308
Australia

ABSTRACT

The amplification of electromagnetic waves in the magnetosphere with frequencies near the ion cyclotron frequency is studied by integrating local convective growth rates along the wave path. This integrated wave amplification is used to investigate the radial extent of wave source regions. It is found that the source region of the lowest frequency wave branch is restricted to near the plasmapause and inside the plasmasphere, whereas the other wave branches can be amplified over the whole magnetosphere. It is suggested that the structured Pc 1-2 waves observed mainly on the ground are due to the lowest frequency wave branch, and the unstructured Pc 1-2 waves observed both on the ground and in space are caused by the other wave branches.

7.1 INTRODUCTION

One of the most important considerations in the generation/amplification and propagation of electromagnetic waves with frequencies near the ion cyclotron frequencies in the magnetosphere is the location of the wave source regions, where the left-hand polarised ion cyclotron waves experience significant amplification. This involves the following: (1) the latitudinal extent of wave source regions on a fixed L-shell or along a fixed field line; (2) the radial or L extent of wave source regions; and (3) the local time distribution of wave source regions. Hu et al. (1990) studied (1), considering the effect of multiple ion species on wave generation/amplification. In this paper, we consider (2) for the dayside magnetosphere using integrated growth rates of the ion cyclotron instability in a multi-ion plasma. The waves considered here are observed on the ground as Pc 1-2 magnetic pulsations.

Most of the previous theoretical work on the radial extent of wave source regions was based on an $e^- - H^+$ plasma model (Perraut et al. 1976, Kaye et al. 1979 and references therein). For a multi-component magnetosphere, theoretical attention has been only given to the region at or near geostationary orbit. Experimental investigations on wave source regions have been made both on the ground and on satellites. In order to identify the wave source region from ground observations, characteristics of wave frequency, dispersion and wave packet bounce period, amplitude, and polarisation parameters of structured and unstructured waves have been used (Fraser 1985, Webster and Fraser 1985 and references therein). Satellites record mainly unstructured waves, and may directly detect source regions by, for example, wave polarisation and the Poynting vector properties.

Ground observations showed that structured Pc 1-2 waves were traced to the region in the vicinity of the plasmapause (L ~3 – 6). For the unstructured pulsations, ground and satellite records showed that the source region may extend from the inside of the plasmasphere to the outer plasmatrough (L ~3 – 10).

Previous theoretical work on the ion cyclotron instability across L supported the idea that the wave amplification is restricted to the region near the plasmapause (Perraut et al 1976; Kaye et al. 1979 and references therein). A brief physical interpretation for this follows. In a single-ion plasma, the Alfvén velocity V_a has a minimum just inside the plasmapause because of the low $|\mathbf{B}_E|$ and the high cold plasma density, and consequently the parallel resonant energy of the interacting protons E ($E = 0.5V_R^2 m_{H^+} = 0.5(1 - F_c/F)^2 V_a^2 (1 - F/F_c) m_{H^+}$, see Hu et al. (1990)) is low and more energetic protons may resonate with waves. For calculation of E, the Alfvén velocity is $V_a = B_E/(4\pi N_c m_{H^+})^{1/2}$, where V_R is the parallel resonant velocity of the proton, F_c the proton cyclotron frequency, F the wave frequency, m the mass of the proton, and N_c the electron density. A large flux of energetic and anisotropic ring current ions are known to exist over the L range 3 – 9. Accordingly, it is expected that the ion cyclotron instability would be likely to occur in the region of overlap between the ring current ions and the dense cold plasma with a low background magnetic field, i.e. in the vicinity of the plasmapause.

However, when multiple ion species in the magnetosphere are included, the above interpretation becomes questionable. In this paper, we will show that the minimum E may occur on more than one L shell for the same wave frequency. Furthermore, an analysis of integrated growth rates of the ion cyclotron instability will also show the growth rate peaking over a wide range of L values, both inside and outside the plasmapause, and amplification of structured waves differs from that of unstructured waves.

In section 2, we will consider the particle resonant energy in the magnetosphere. In section 3 we present the integrated growth rate across L. This will show the L values of the wave sources. Applications of these results to wave observations are discussed in section 4, and conclusions are also given in section 4.

7.2 ION RESONANT ENERGY

Let us consider the parallel resonant energy of the interacting ring-current protons in the presence of He^+ and O^+ ions. For electromagnetic left-hand ion cyclotron waves propagating along the background magnetic field, the local dispersion relation is (Hu et al. 1990):

$$V_p^2 \equiv (2\pi F/k)^2 = c^2 \left(1 + \sum_i \frac{\eta_i c^2}{V_a^2 \left(\frac{1}{M_i} - \frac{F}{F_c(H^+)} \right)} \right)^{-1}$$

where $\eta_i = N_i/N_e$, $M_i = m_i/m_{H^+}$, $i = H^+$, He^+ and O^+ ion species and c is the velocity of light. It is well known that the presence of He^+ and O^+ ions leads to two stop bands in F – k space:

$0<F<F_c$ (O^+): pass band, the O^+ wave branch,

$F_c(O^+) \leq F \leq F_{cf}(O^+)$: stop band,

$F_{cf}(O^+)<F<F_c(He^+)$: pass band, the He^+ wave branch,

$F_c(He^+) \leq F \leq F_{cf}(He^+)$: stop band,

$F_{cf}(He^+)<F<F_c(H^+)$: pass band, the H^+ wave branch,

$F \geq F_c(H^+)$: stop band

Two cutoff frequencies, $F_{cf}(O^+)$ and $F_{cf}(He^+)$, are the real solutions of the equation

$$\sum_i c^2 \eta_i^2 \left[V_a^2 \left(1/M_i - F/F_c\left(H^+\right) \right) \right]^{-1} = -1$$

Dipole magnetic field lines are used. The variation of cold ion density with latitude λ is assumed to be $N_c(\lambda)/N_c(0) \sim B_o(\lambda)/B_o(0)$. The equatorial plasma density profile across L is shown in Figure 1. In this figure, model 1 represents the normal plasma density profile for moderate geomagnetic activity with the plasmapause at L ~4.5 – 5.0; and model 2 corresponds to the typical plasma density profile for the afternoon bulge region or quiet geomagnetic activity with an extended plasmapause at L ~6.0 – 6.5. To simplify the problem, we assume the relative concentrations of ion species in the magnetosphere are fixed at typical values (η_{H^+} 0.7, η_{He^+} = 0.2 and η_{O^+} = 0.1). The variation of E across L for various wave branches are displayed in Figure 2. In this figure, the wave-particle interaction region is assumed to be the equator.

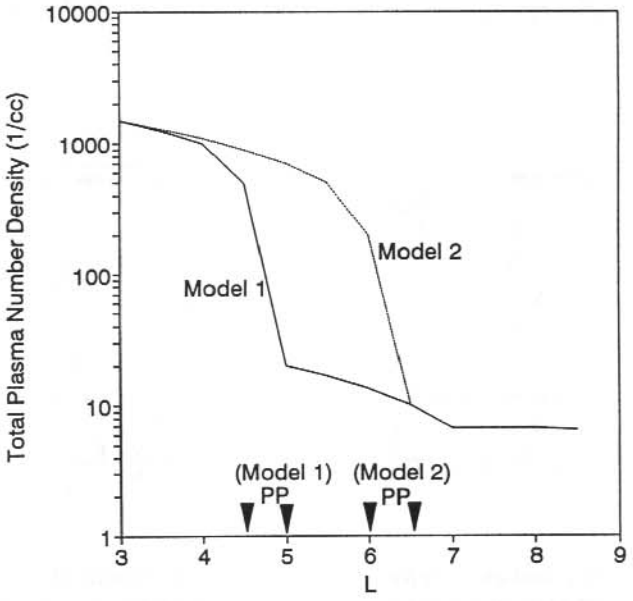

Figure 1. Plasma density profiles. For model 1, the plasmapause (PP) is at L ~4.5 and for model 2 at L ~6, indicated by triangles on the L axis.

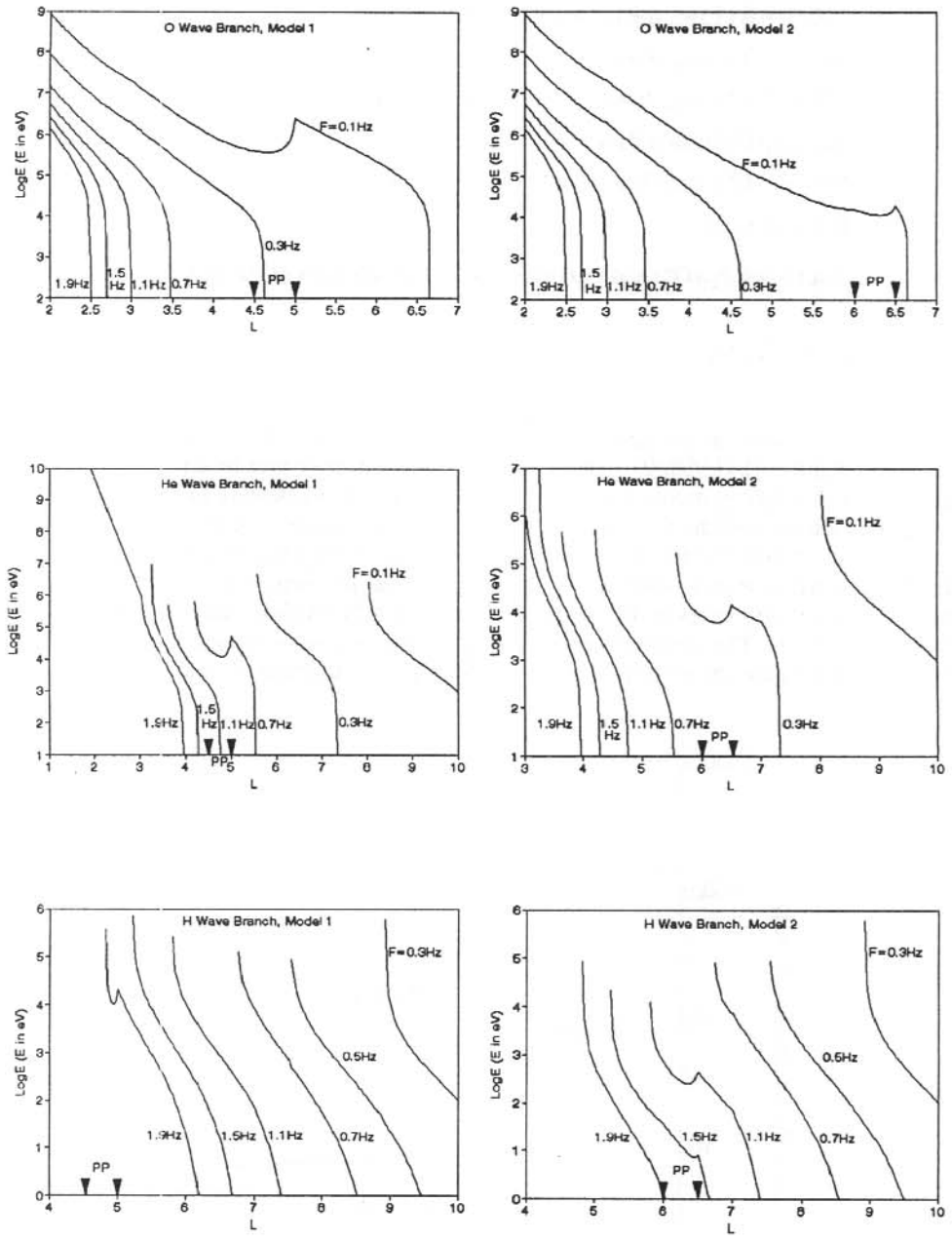

Figure 2. Equatorial resonant energies for those protons interacting with O^+ (top panels), He^+ (middle panels), and H^+ (bottom panels) wave branches. The left three panels are for model 1 (Figure 1) and right three for model 2. The position of plasmapause (PP) is indicated by triangles on the L axis.

Because of the existence of various wave branches due to the presence of heavy ion species, it is not unexpected that a fixed wave frequency may resonate on more than one L shell (two or three L shells for the $e^- - H^+ - He^+ - O^+$ plasma). For example, when F = 0.5 Hz the O^+ wave branch interacts with E = 10 keV protons at L ~3.8 for model 1 (the left top panel of Figure 2), the He^+ wave branch at L ~5.8 (the left middle panel), and the H^+ wave branch at L ~7.6 (the left bottom panel). It should be remembered that proton interaction with a certain wave branch does not necessarily imply wave growth. Wave growth or damping depend upon the result of a calculation of instability growth rate. Anyhow, the result that the ring-current ions, which are widely spread over L ~2 – 9, may resonate with waves with fixed frequencies on several different L shells indicates, at least, that we cannot use only E to estimate the wave source region. Therefore, the previous conclusion that waves are amplified only near the plasmapause must be reassessed.

When F is not very low, for example F > 0.3 Hz, the variation of plasma density profile does not influence E of the O^+ wave branch (top two panels of Figure 2). For the He^+ and H^+ wave branches, E – L curves exhibit the same shape: when E is higher than a certain value (E_1) or lower than a certain value (E_2), L remains almost a constant for various E. When $E_1 > E > E_2$, a spatial energy (L – E) dispersion for a fixed F occurs. In our model, E_1 ~100 keV for the He^+ wave branch and ~1 – 10 keV for the H^+ wave branch; E_2 ~100 eV for the He^+ wave branch, and ~0.1 – 1.0 eV for the H^+ wave branch. The effect of the plasmapause on the E – L curves is to distort the curves in the energy range $E_1 > E > E_2$. This modification provides a local U type energy minimum inside the plasmapause. The local minimum implies that the plasmapause is an important region of cyclotron resonance for those frequencies which have E – L curves passing through the plasmapause. Normally, if there is a local minimum in E caused by the plasmapause, then there is another interaction region outside the plasmapause. For instance, the left middle panel of Figure 2 shows that if F = 0.5 Hz the E minimum caused by the plasmapause is above 100 keV, and an interaction of this wave with ~10 keV protons occurs outside of the plasmapause. Thus, when the wave frequency is high (e.g. $\gtrsim$ 1.5 Hz), the ion cyclotron interaction takes place near the plasmapause, mainly within the plasmasphere. For middle and low frequencies, the interaction region may spread across a wide range of L.

7.3 INTEGRATED GROWTH RATES ACROSS L

The local dispersion relation, including the energetic ions, for parallel wave propagation is written as (Hu et al. 1990)

$$D(F, k_\parallel) = D_c(F, k_\parallel) + D_w(F, k_\parallel) = 0$$

where

$$D_c(F, k_\parallel) = c^2 k_\parallel^2 - 4\pi^2 F^2 + \sum_{j=e,i} \omega_{pj}^2 F / [F - F_c(j)] ,$$

and

$$D_w(F, k_\parallel) = -\sum_w \left\{ \omega_{pw}^2 A_w + \omega_{pw}^2 [2\pi A_w F_c(w) + 2\pi F(A_w + 1)] Z(\xi_w) / k_\parallel V_{T\parallel w} \right\}$$

Here, ω_{pw} are the angular plasma frequencies for energetic ion species (with $w = H^+$), A_w is the thermal anisotropy and $Z(\xi_w)$ is the plasma dispersion function with $\xi_w = 2\pi[F - F_c(w)]/k_{\parallel}V_{T\parallel w}$, where $V_{T\parallel w}$ is the parallel thermal velocity for the energetic ions. The method used to calculate local growth rates is described in Hu et al. (1990).

Hu et al. (1990) showed that the local growth rate is not sufficient to describe the total wave amplification, because of the contribution of off-equator sources which appear when multi-ion components are included. Therefore, it is necessary to consider an integration of the convective growth rate (γ/V_g) along the wave path.

In the case of parallel wave propagation, we can take the wave path along geomagnetic field lines. If oblique propagation is considered, the wave amplification must be integrated along the wave path obtained from ray tracing. Because the waves are generated with left-hand polarisation, the spectral characteristics remain almost unchanged for $\theta \lesssim 30°$, where θ is the wave normal angle (Ludlow 1989). Therefore, parallel propagation can represent the basic spectral structure of the ion cyclotron instability. Furthermore, the left-hand polarised branches of the wave modes are propagating mainly along field lines, so the field line is a good approximation for an integration path of the instability. Consequently, in this paper, wave growth will be integrated along field lines.

In calculations of the integrated growth rate G along the field lines, from the equator to the bottom of the magnetosphere, we assume that the interaction which provides the ion cyclotron wave growth is linear. When saturation of the instability is quasi-linear, the energetic proton distribution will still be self-consistent with those used in our linear calculation if we choose suitable parameters such as A_w and $T_{\parallel w}$, so that our treatment is still valid. But, when non-linear processes such as wave trapping occur, the wave is at least partially saturated by these processes rather than a quasi-linear process. In this case, the linear treatment becomes invalid. When considering non-linear processes, normally only the wave trapping was taken into account (e.g. Vomvoridis and Denavit 1980 and references therein). Mauk and McPherron (1980) used observed wave events to examine nonlinear wave trapping, and found that the linear theory is most likely appropriate at least for wave events observed at geostationary orbit. Furthermore, the following points may support the linear assumption in our calculations of the integrated wave amplification: (a) gradients in B_E which detrap energetic protons; (b) a single pass of waves through source regions (it was argued by Mauk and McPherron (1980) that non-linear phenomena may not be significant in a single pass case); (c) source regions may be narrow. Even if nonlinear processes are present in the interaction, the linear situation provides a basic understanding for wave amplification.

The total wave amplification or absorption in an interaction region for a single wave branch is defined as

$$G = 20\log_{10}\left[\exp\int_{\lambda_1}^{\lambda_2}\left(\gamma / V_g\right) ds\right] \text{ (in dB)},$$

where λ_2 and λ_1 are the upper and lower latitude limits of the source region. The integration in G is along the field line. The total amplification or absorption at a certain frequency is equal to the sum of G for the three wave branches.

Before we calculate G for various L values, a magnetospheric model, describing the variation of plasma parameters with L and λ, must be chosen. It is assumed that

$$N_c(\lambda)/N_c(\lambda=0) = B_E(\lambda)/B_E(\lambda=0),$$

$$A_w(\lambda) = A_w(\lambda=0),$$

$$T_{\|w}(\lambda) = T_{\|w}(\lambda=0) \text{ and}$$

$$N_w(\lambda)/N_w(\lambda=0) = \left[B_E(\lambda=0)/B_E(\lambda)\right]^{Aw}$$

along all dipole field lines considered (L ~3 – 8). A dipole magnetic field model is assumed with

$$B_E(\lambda=0, L)/B_E(\lambda=0, L=1) = L^{-3}.$$

The model for energetic ion parameter variations as a function of L is more difficult to predict, and various models have been suggested before. In this paper, we assume

$$T_{\|w}(L)/T_{\|w}(L=Lo) = (Lo/L)^{2.5} \quad \text{and} \quad A_w(L) = [A_w(L=Lo)+1]\,(Lo/L)^{1/2} - 1$$

(Ashour-Abdalla and Cowley 1974), where Lo is an L value at which parameters for energetic ions are known. We consider only energetic protons in our calculation and take

$$Lo = 6.6, \quad A_w(L=Lo) = 1.0 \quad \text{and} \quad T_{\|w}(L=Lo) \sim 18.5 \text{ keV}.$$

It has been shown that

$$N_w(L)/N_w(L=Lo) \sim (Lo/L)^{\kappa}$$

with $\kappa = 4$ for strong pitch angle diffusion and $\kappa = 4.3$ for no pitch angle diffusion. However, the energetic proton density obtained from this relation is much higher than it should be, because of the presence of Alfvén layers (e.g. Cowley and Ashour-Abdalla 1975). In fact, we have used the $\kappa = 4.3$ model to calculate G over various L but found that G at small L values are too great to be physically acceptable. In many previous studies, $N_w(L)$ was often assumed to be a constant (e.g. Gendrin 1975). Therefore we can assume that $N_w(L)$ decreases slightly with increasing L value as listed in Table 1. This assumption is not inconsistent with observed particle data.

Table 1. N_w variation as a function of L.

L	3.0	3.5	4.0	4.5	5.0	5.5	6.0	6.5	7.0	7.5	8.0
N_w (cm^{-3})	1.0	0.95	0.9	0.85	0.8	0.75	0.7	0.65	0.6	0.6	0.6

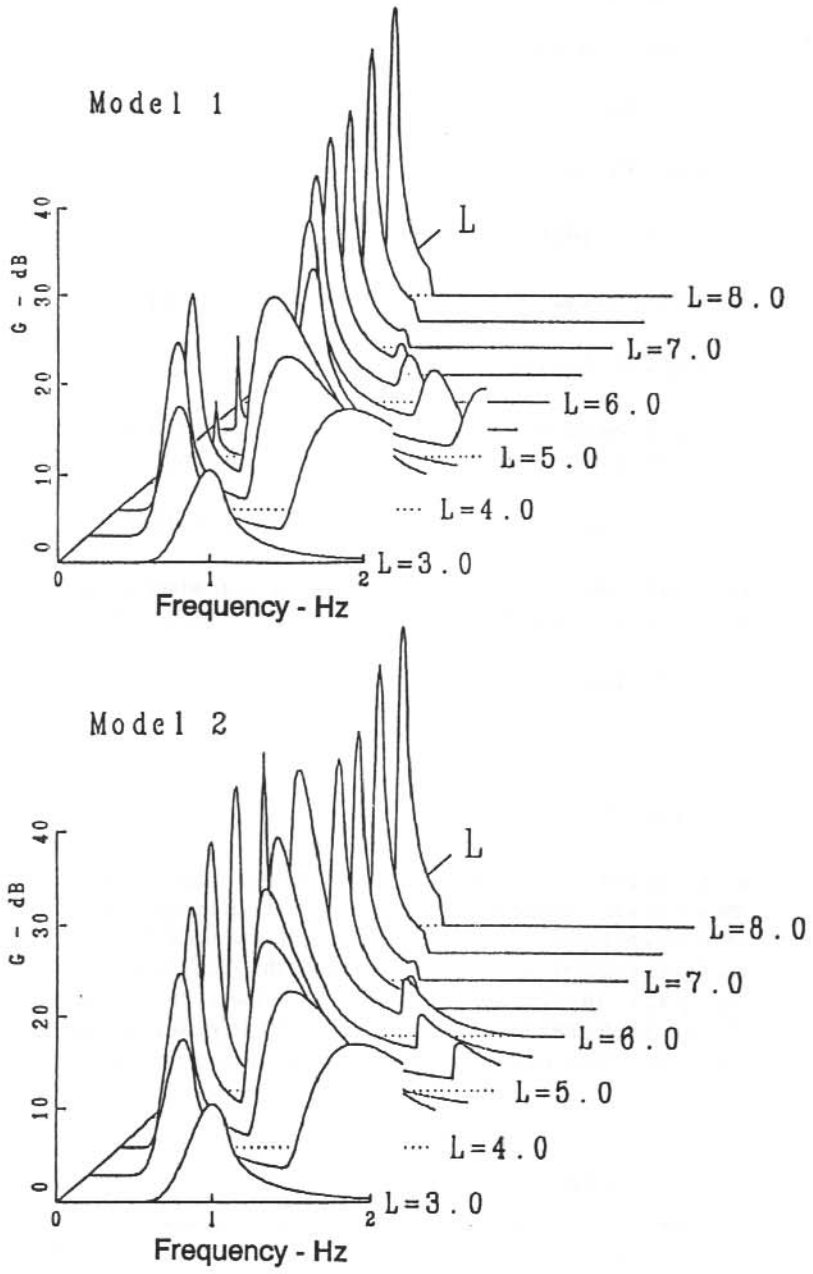

Figure 3. Variation of G with L for wave frequencies ≤ 2 Hz.

Figure 3 displays how the G – F curves vary with L value. The top and bottom panels relate to model 1 and 2 of the cold plasma respectively. When L is small, e.g. L = 3, there is only one peak in G over the frequency range F ≤2 Hz and this peak can be traced to the instability in the O^+ wave branch. When L ~3.5 – 4.5, there are two peaks in G corresponding to the O^+ (lower frequency peak) and He^+ (higher frequency peak) wave branches. At L ~5 – 7, the peak in G from the instability in the H^+ wave branch appears, although this peak is smaller than those for the He^+ and O^+ branches. When L is high e.g. L >7.0, the peak in G for the H^+ branch disappears because of thermal damping, since A_w in this region is low and correspondingly the maximum unstable frequency is low too.

It can be seen from our modeling that significant wave amplification occurs only in the O^+ and He^+ wave branches, the instability in the H^+ branch is not effective, and the maximum of G in this branch is less than 10 dB.

The plasmapause has varying effects on the instability in the He^+ and O^+ wave branches (see Figure 3). For the O^+ branch, G increases with increasing L and maximises just at the inner edge of the plasmapause. Inside the plasmasphere, G of the O^+ branch may be more important than that of the He^+ wave branch. In the plasmapause region, G decreases rapidly, and then becomes low (<5 dB) in the plasmatrough. Although G of the O^+ wave branch will increase slightly with L in the outer magnetosphere, it will not be important again. For the He^+ wave branch, the effect of the plasmapause is not as obvious as that for the O^+ wave branch. G of the He^+ wave branch continuously increases with increasing L over the whole extent of the magnetosphere, and therefore maximises at large L.

Comparing the values of G for the $He^+$and O^+ wave branches, instabilities in both the O^+ and He^+ branches are important inside the plasmasphere. However, in the region outside the plasmapause, the instability in the He^+ wave branch provides the primary contribution to G. We note that this conclusion may be important for explaining the structured and unstructured Pc 1-2 waves occurring in different L regions and will be discussed later.

7.4 DISCUSSION AND CONCLUSION

In an e – H^+ plasma, studies of γ, γ/V_g, G, E, E_{RC} and E_{EM}, where E_{RC} is a critical parallel resonant energy depending on the thermal anisotropy of the energetic ions and E_{EM} is a parallel resonant energy of ions resonating with the most amplified wave (Gendrin 1975), concluded that the total wave amplification is a maximum only near the plasmapause. However, the situation becomes much more complicated when multiple ion species are included.

Observations have shown that ground recorded structured Pc 1-2 waves occur over a wide range of L (from inside the plasmasphere to the outer plasmatrough) with the restricted magnetospheric sources near the plasmapause (Webster and Fraser 1985, Fraser 1985 and references therein). However, it has been found the source regions of the unstructured waves observed on the ground can be at any L in the range of L ~3 – 10 (Fukunishi 1969, Arnoldy et al. 1979, Hayashi et al. 1989). Satellites observe mainly unstructured events near geostationary orbit and at higher L values. Recently, observations from EXOS-D, AMPTE and CRRES satellites, covering a wider L range, found that the unstructured waves can occur over the entire magnetosphere (see references in Hu 1991). For the satellite observations the wave source region should be located almost on the same field line as the satellite if the waves are guided. This result may imply that

the unstructured waves observed by satellites should be amplified over a wide range of L. Structured wave packet propagation has rarely been seen by satellites. Only recently, Erlandson et al. (1991) reported one event of structured Pc 1 waves on VIKING at L ~4, i.e. near the plasmapause (to be discussed later). These ground and satellite observations indicate a disparity between structured and unstructured waves on the ground compared with unstructured waves in space. This disparity is unresolved at present, and may relate to theoretical wave generation theories and the location of the wave source region. It is considered here that ion cyclotron instability theory for a single ion plasma cannot be used to explain the L distribution of wave source regions. In this study we suggest that a combination of the ion cyclotron instability and wave propagation is necessary to explain the observations both on satellites and on the ground. Considerations are based on the following three key arguments.

1. Sources of the waves which belong to the wave branch with the lowest frequency (in this paper the O^+ branch) are restricted to low L regions in the plasmasphere and near the plasmapause. Calculations of the integrated wave amplification show that G of the lowest frequency wave mode is large inside the plasmasphere, reaches a maximum near the plasmapause, and decreases rapidly outside of the plasmapause (see the O^+ wave branch in Figure 3).

2. The waves of other wave branches (in this paper the He^+ and H^+ wave branches) can be generated over the entire magnetosphere. In section 3, we have seen the integrated wave amplification for the He^+ wave branch remains large over a wide range of L values. This amplification may peak at the plasmapause, however the variation may not be large. This implies that the plasmapause may not be a preferred region for these waves. In fact, in the plasmatrough, G will increase to values greater than the peak at the plasmapause (see Figure 3).

3. Structured waves generated inside the magnetosphere may belong to the wave mode with the lowest frequency (i.e. the O^+ wave branch in the model in this paper). Propagation of this mode is not affected by other ion species, and the waves can reach the ionosphere (Rauch and Roux 1982). Structured wave packets may be formed by reflection from the ionosphere. It is expected that these waves should be restricted to the regions in the plasmasphere or near the plasmapause. However, structured waves with high frequencies (up to ~2 Hz) are seen on the ground sometimes. This may be due to the following reasons:

a. The waves are generated at a low L (~2 – 4) region so that wave frequency is high. Although these waves are generated at low L, they may be seen over a wide range of L on the ground (e.g. at L >4) due to propagation in the ionospheric waveguide. Observations have confirmed that the source region of high-frequency pulsations (e.g. F >1 Hz) is in the plasmasphere (Fukunishi 1984).

b. The waves are generated near the plasmapause but the thermal O^+ ion concentration is so low that the O^+ ions become unimportant. In this case, the lowest frequency wave mode is the He^+ wave branch which can be present at higher frequencies.

It is necessary to point out that not all structured waves observed on the ground are restricted to the low L region (e.g. $L \lesssim 4-6$). For example, some structured emissions observed at high latitudes may be generated in the high latitude boundary regions. Unstructured waves generated inside the magnetosphere may be those of the wave branches for ion species with masses lighter than O^+ (or He^+ if the O^+ ion concentration is too low to significantly influence wave amplification/propagation). For these waves, the reflection should most likely take place before

the waves reach the ionosphere. The location of the reflection region may depend on wave frequency (Hu 1991), and this region may behave as a lowpass filter for the waves (Perraut et al. 1984). These properties could destroy the formation of a well-structured wave packet, causing the waves to appear as unstructured events.

Thus, it can be explained why ground observed structured Pc 1-2 waves always show their source regions near the plasmapause or inside the plasmasphere, if these waves are generated inside the magnetosphere. Generally, it remains unclear why structured waves are rarely observed on satellites. One reason could be due to the cross-field motion of the satellite, unless at the apogee when it is moving tangent to the field line, or at geostationary orbit. Another possibility is that since many of the satellite observations were at geostationary orbit or high L and these regions are usually located outside the plasmapause, the structured waves generated only in the plasmapause or near the plasmapause would not be observed. For the unstructured waves, direct measurement from satellites confirmed that they exist over the whole magnetosphere, and ground records also showed that the source regions of unstructured Pc 1-2 may range from L ~3 to L ~10. This supports our explanation for generation of the unstructured waves.

Sometimes, structured waves are observed in the geomagnetic latitude range of $\sim 60^\circ - 70^\circ$ (Hayashi et al. 1981, Fukunishi 1984). However, the high latitude location of these wave regions always corresponds to the duskside bulge in the thermal plasma. This confirms that the structured waves follow the region corresponding to the averaged plasmapause locations (Fukunishi 1984).

The sources of structured waves observed on the ground are considered to be located in the plasmasphere and near the plasmapause, while ionospheric wave guide propagation (e.g. Manchester 1966) distributes the wave energy over wide latitude ranges. Ionospheric propagation is more likely to occur at night when wave guide attenuation is minimum, and less likely during the day when the attenuation is the greatest. However, Campbell and Stiltner (1965) and Fraser (1968) found that wave occurrence is more prevalent at night when the wave frequencies are high and L value of wave path in the magnetosphere is low, whereas the occurrence peaks during the day when wave frequencies are low and the wave path L is high (see Figure 6 of Fraser 1968). This is in conflict with observations in the magnetosphere (Anderson et al. 1991) which show the highest frequency around local noon. This may imply that the ionospheric wave guide is attenuating the high frequency waves propagating during the day.

Recent observations by the AMPTE/CCE satellite covering an L range $3.5 < L < 9$ showed a predominance of wave event occurrence at $L > 7$ (Anderson et al. 1991). This seems to agree with calculations of G in this paper. In our calculation, we assumed N_w remains almost a constant at the high L region (see Table 1). This does not disagree with the argument that the plasmasheet ions may play an important role in generating the waves at high L (Anderson et al. 1991). Normally, N_w should decrease with increasing L, but the plasmasheet may provide additional energetic ions in the high L region so that N_w remains higher than that calculated from trapped ions which come from the ring current.

Furthermore, in recent work Erlandson et al. (1991) found a unique Pc 1 structured wave packet recorded on VIKING satellite with frequency at 1.4 Hz. The amplitude distribution showed that the strongest waves were recorded from L = 3.8 to L = 4.1, near the expected position of the

plasmapause, and lower amplitude waves occurred from L = 3.6 to L = 3.8, in the plasmasphere. These results agree well with our wave generation model.

In conclusion, the total amplification for waves in the lowest frequency branch is sensitive to the cold plasma density profile. These waves are mainly restricted to the regions in the plasmasphere and near the plasmapause. For the waves of other branches, the amplification is not sensitive to the cold plasma profiles, and can occur over the whole magnetosphere. Structured waves may result from amplification in the wave mode which has the lowest frequencies. Therefore, source regions of the structured waves may be restricted inside the plasmasphere and near the plasmapause. Unstructured waves may belong to the other wave branches. These waves are controlled by the heavy ion parameters, but the presence of the cold plasma density gradient will not restrict the spatial distribution of the wave source regions. The waves can be generated over a wide range of L, from the plasmasphere to the outer magnetosphere.

REFERENCES

Anderson, B.J., Erlandson, R.E. *and* Zannetti, L.J. (1991). A statistical survey of Pc 1-2 properties AMPTE/CCE results. *EOS Transactions AGU 72*. P. 255.

Arnoldy, R.L., Lewis, P.B. Jr. *and* Cahill, L.J. Jr. (1979). Polarization of Pc 1 and IPDP pulsations correlated with particle precipitation. *Journal of Geophysical Research 84*:7091 – 7098.

Ashour-Abdalla, M. *and* Cowley, S.W.H. (1974). Wave-particle interactions near the geostationary orbit. In: McCormac, B.M. (Ed.). *Magnetospheric Physics*. D. Reidel, Dordrecht, Holland. P. 241.

Campbell, W.H. *and* Stiltner, E.C. (1965). Some characteristics of geomagnetic pulsations at frequencies near 1 c/s. *Radio Science 69D*:1117 – 1132.

Cowley, S.W.H. *and* Ashour-Abdalla, M. (1975). Adiabatic plasma convection in a dipole field: variation of plasma bulk parameters with L. *Planetary and Space Science 23*:1527 – 1549.

Erlandson, R.E., Anderson, B.J., Zanetti, L.J. *and* Block, L.P. (1991). VIKING satellite observations of Pc 1 pearl pulsations near the plasmapause. *EOS Transactions AGU 72*. P. 255.

Fraser, B.J. (1968). Temporal variations in Pc 1 geomagnetic micropulsations. *Planetary and Space Science 16*:111 – 124.

Fraser, B.J. (1985). Observations of ion cyclotron waves near synchronous orbit and on the ground. *Space Science Reviews 42*:357 – 374.

Fukunishi, H. (1969). Occurrence of sweepers in the evening sector following the onset of magnetospheric substorm. *Report of Ionosphere and Space Research in Japan 23:21*–34.

Fukunishi, H. (1984). Pc 1-2 pulsations and related phenomena: review. In: *Proceedings of Conference on Achievements of the IMS, ESA SP–217*. P. 437. European Space Agency Special Publication.

Gendrin, R. (1975). Is the plasmapause a preferential region for proton precipitation? *Annales de Geophysique 31*:127 – 135.

Hayashi, K., Kokubun, S., Oguti, T., Tsuruda, K., Machida, S., Kitamura, T., Saka, O. *and* Watanabe, T. (1981). The extent of Pc 1 source region in high latitudes. *Canadian Journal of Physics 59*:1097 – 1105.

Hayashi, K., Yamamoto, T., Kokubun, S., Oguti, T., Ogawa, T., Iwagami, N., Araki, T., Kitamura, T.I., Saka, O., Makita, K., Sato, N., Watanabe, T., Horita, R., McEwen, D., Kim, J.S. *and* Egeland, A. (1989). Multi-station observation of IPDP micropulsations – two-dimensional distribution and evolution of the source regions. *Journal of Geomagnetism and Geoelectricity 40*:583 – 619.

Hu, Y.D. (1991). *Electromagnetic waves in the magnetosphere with frequencies near the ion cyclotron frequency: propagation, amplification and wave-particle interaction.* Ph.D. thesis. University of Newcastle, Australia.

Hu, Y.D., Fraser, B.J. *and* Olson, J.V. (1990). Amplification of electromagnetic ion cyclotron waves along wave path in the Earth's multicomponent magnetosphere. *Geophysical Research Letters 17*:1053 – 1057.

Kaye, S.M., Kivelson, M.G. *and* Southwood, D. (1979). Evolution of ion cyclotron instability in the plasma convection system of the magnetosphere. *Journal of Geophysical Research 84*:6397 – 6406.

Ludlow, G.R. (1989). Growth of obliquely propagating ion cyclotron waves in the magnetosphere. *Journal of Geophysical Research 94*:15385 – 15392.

Manchester, R.N. (1966). Propagation of Pc 1 micropulsations from high to low latitudes. *Journal of Geophysical Research 71*:3749 – 3754.

Mauk, B.H. *and* McPherron, R.L. (1980). An experimental test of the electromagnetic ion cyclotron instability within the Earth's magnetosphere. *Physics of Fluids 23*:2111 – 2127.

Perraut, S., Gendrin, R. *and* Roux, A. (1976). Amplification of ion cyclotron waves for various typical radial profiles of magnetospheric parameters. *Journal of Atmospheric and Terrestrial Physics 38*:1191 – 1199.

Perraut, S., Gendrin, R., Roux, A. *and* de Villedary, C. (1984). Ion cyclotron waves: direct comparison between ground-based measurements and observations in the source region. *Journal of Geophysical Research 89*:195 – 202.

Rauch, J.L. *and* Roux, A. (1982). Ray tracing of ULF waves in a multicomponent magnetospheric plasma: consequences for the generation mechanism of ion cyclotron waves. *Journal of Geophysical Research 87*:8191 – 8198.

Vomvoridis, J.L. *and* Denavit, J. (1980). Nonlinear evolution of monochromatic whistler wave in a nonuniform magnetic field. *Physics of Fluids 23*:174 – 183.

Webster, D.J. *and* Fraser, B.J. (1985). Source regions of low latitude Pc 1 pulsations and their relationship to the plasmapause. *Planetary and Space Science 33*:777 – 793.

8. DISPERSION RELATION OF ELECTROMAGNETIC ION CYCLOTRON WAVES IN A MULTICOMPONENT PLASMA WITH STATIC ELECTRIC AND MAGNETIC FIELDS

Y.D. Hu and B.J. Fraser

Department of Physics
University of Newcastle
Newcastle NSW 2308
Australia

ABSTRACT

An analytical expression of the dispersion relation for linear electromagnetic ion cyclotron waves propagating along a background magnetic field is provided. The plasma system considered here contains a static magnetic field and a weak static electric field. Because wave frequencies are lower than the proton cyclotron frequency, multiple ion species existing in the magnetosphere and ionosphere are important in controlling the wave propagation and generation processes, and this effect is included in the dispersion relation. Some new features and applications of the dispersion relation are discussed. A static parallel electric field exists in high latitude regions of the ionosphere, and therefore the dispersion relation presented here may be helpful in understanding the observation of ion cyclotron waves recorded as Pc 1-2 pulsations by ground stations at high latitudes.

8.1 INTRODUCTION

A magnetised plasma model is usually invoked for the study of electromagnetic ion cyclotron waves in the Pc 1-2 frequency range generated in the magnetosphere and recorded on the ground and by satellites (Fraser 1985 and references therein). This plasma model includes only a static magnetic field. However, there exist static electric fields in the magnetosphere and ionosphere, which may also play an important role in controlling wave generation and propagation processes. For example, the ionospheric electric field may affect ion cyclotron wave propagation in the ionospheric waveguide, and thus modify the waves seen on the ground. In the magnetosphere the static electric field may also influence the wave propagation characteristics. Under some special conditions, the static electric field may destabilise ion cyclotron waves, and this process may affect the wave amplification/generation mechanism. In order to investigate these problems in detail, it is important to consider the dispersion relation for electromagnetic ion cyclotron waves in a plasma with a static magnetic field and a weak static electric field. This has rarely been studied. In this paper, we present a dispersion relation in an analytical form for parallel propagating ion cyclotron waves.

In the magnetosphere and ionosphere, multiple ion species, such as H^+, He^+ and O^+, in both cold and energetic components are important (e.g. Geiss et al. 1978, Balsinger et al. 1983 and references therein). The multiple ion species significantly modify the ion cyclotron wave properties (Fraser 1985 and references therein), therefore the plasma model used here must include these ion species.

8.2 BASIC EQUATIONS

The distribution function $f_i(\mathbf{r},\mathbf{v},t)$ of particle species i is governed by the Boltzmann-Vlasov equation:

$$\frac{\partial f_i}{\partial t} + \mathbf{v}\cdot\nabla f_i + \frac{e_i}{m_i}\left(\mathbf{E}+\frac{\mathbf{v}\times\mathbf{B}}{c}\right)\nabla_v f_i = 0 \tag{1}$$

Electric and magnetic fields in the plasma are governed by Maxwell's equations:

$$\nabla\times\mathbf{B} = \frac{4\pi}{c}\mathbf{J} + \frac{1}{c}\frac{\partial\mathbf{E}}{\partial t} \tag{2}$$

$$\nabla\times\mathbf{E} = -\frac{1}{c}\frac{\partial\mathbf{B}}{\partial t} \tag{3}$$

$$\nabla\cdot\mathbf{B} = 0 \tag{4}$$

$$\nabla\cdot\mathbf{E} = 4\pi\rho \tag{5}$$

where $\mathbf{J}$ and ρ are related to f_i by

$$\mathbf{J} = \sum_i e_i\int f_i\mathbf{v}d^3v \tag{6}$$

and

$$\rho = \sum_i e_i\int f_i d^3v \tag{7}$$

8.3 LINEAR EQUATIONS OF THE SYSTEM

Assume that the magnetic field $\mathbf{B}$ and electric field $\mathbf{E}$ in the considered plasma are given by

$$\mathbf{B} = \mathbf{B_0}\mathbf{e_z} + \mathbf{B_1}(z,t), \quad \mathbf{E} = E_{0z}\mathbf{e_z} + E_{0y}\mathbf{e_y} + E_{0x}\mathbf{e_x} + \mathbf{E_1}(z,t)$$

and other physical quantities represented by

$$P = P_0 + P_1(z,t)$$

where $|\mathbf{B_1}| \ll |\mathbf{B_0}|$, $|\mathbf{E_1}| \ll |\mathbf{E_0}|$, and $|P_1| \ll |P_0|$. Space-time varying quantities have the form of $\exp[j(\omega t - kz)]$. The first order equations (2) – (7) give

$$-k^2E_{1z}\mathbf{e_z} + k^2\mathbf{E_1} - \frac{\omega^2}{c^2}\mathbf{E_1} = -\frac{4\pi\omega j}{c^2}\mathbf{J_1}\,. \tag{8}$$

Assume

$$E_{1\pm} = \frac{1}{2}\left(E_{1x} \pm jE_{1y}\right), \quad B_{1\pm} = \frac{1}{2}\left(B_{1x} \pm jB_{1y}\right),$$

then equation (8) becomes

$$E_{1z} = \frac{4\pi j}{\omega}\sum_i e_i \int v_z f_{1i} d^3v \tag{9}$$

and

$$E_{1\pm} = \frac{2\pi\omega j}{\left(\omega^2 - c^2k^2\right)}\sum_i e_i \int f_{1i} v_r e^{\pm j\varphi} d^3v, \tag{10}$$

where a cylindrical coordinate system is used: $v_x = v_r\cos\varphi$, $v_y = v_r\sin\varphi$, and $v_z = v_z$. By using equations (2) and (3), the linearised equation (1) is written as

$$j(\omega - kv_z) f_{1i} + \frac{e_i}{m_i}\left(\mathbf{E_0} + \frac{\mathbf{v}\times\mathbf{B_0}}{c}\right)\cdot\left(\frac{\partial f_{1i}}{\partial v_r}\mathbf{e_r} + \frac{1}{v_r}\frac{\partial f_{1i}}{\partial\varphi}\mathbf{e_\varphi} + \frac{\partial f_{1i}}{\partial v_z}\mathbf{e_z}\right) +$$

$$\frac{e_i}{m_i}\left\{\mathbf{E_1} + \frac{k}{\omega}\left[(\mathbf{v}\cdot\mathbf{E_1})\mathbf{e_z} - v_z\mathbf{E_1}\right]\right\}\cdot\left(\frac{\partial f_{0i}}{\partial v_r}\mathbf{e_r} + \frac{1}{v_r}\frac{\partial f_{0i}}{\partial\varphi}\mathbf{e_\varphi} + \frac{\partial f_{0i}}{\partial v_z}\mathbf{e_z}\right) = 0. \tag{11}$$

If the following expressions are used

$$a_\pm = \frac{E_{0x} \pm jE_{0y}}{2}$$

$$a_z = \frac{e_i E_{0z}}{m_i}$$

$$D_\pm = \frac{\partial}{\partial v_r} \pm \frac{j}{v_r}\frac{\partial}{\partial\varphi}$$

$$M_{\pm i} = \left(1 - \frac{kv_z}{\omega}\right)\left(\frac{\partial f_{0i}}{\partial v_r} \mp \frac{j}{v_r}\frac{\partial f_{0i}}{\partial\varphi}\right) + \frac{kv_r}{\omega}\frac{\partial f_{0i}}{\partial v_z}$$

equation (11) can be written as

$$\left[j(\omega - kv_z) - \Omega_i\frac{\partial}{\partial\varphi}\right]f_{1i} + a_z\frac{\partial f_{1i}}{\partial v_z} + \frac{e_i}{m_i}\left(a_+ D_- f_{1i} e^{-j\varphi} + a_- D_+ f_{1i} e^{j\varphi}\right) +$$

$$\frac{e_i}{m_i}\left(E_{1z}\frac{\partial f_{0i}}{\partial v_z} + M_{+i}E_{1+}e^{-j\varphi} + M_{-i}E_{1-}e^{j\varphi}\right) = 0. \tag{12}$$

If f_{1i} is expressed as

$$f_{1i} = f_{1i+}(z, v, t)e^{-j\varphi} + f_{1i-}(z, v, t)e^{j\varphi} + g_i(z, v, t) ,$$

equation (12) leads to the following equations, in terms of e^0, $e^{-j\varphi}$, and $e^{j\varphi}$ respectively:

$$j(\omega - kv_z)g_i + a_z\frac{\partial g_i}{\partial v_z} + \frac{e_i}{m_i}E_{1z}\frac{\partial f_{0i}}{\partial v_z}$$

$$+ \frac{e_i}{m_i}\left(a_+\frac{\partial f_{1i-}}{\partial v_r} + \frac{a_+}{v_r}f_{1i-} + a_-\frac{\partial f_{1i+}}{\partial v_r} + \frac{a_-f_{1i+}}{v_r}\right) = 0$$

$$j(\omega - kv_z + \Omega_i)f_{1i+} + a_z\frac{\partial f_{1i+}}{\partial v_z} + \frac{e_i}{m_i}a_+\frac{\partial g_i}{\partial v_r} + \frac{e_i}{m_i}M_{i+}E_{1+} = 0$$

$$j(\omega - kv_z - \Omega_i)f_{1i-} + a_z\frac{\partial f_{1i-}}{\partial v_z} + \frac{e_i}{m_i}a_-\frac{\partial g_i}{\partial v_r} + \frac{e_i}{m_i}M_{i-}E_{1i-} = 0 . \qquad (13)$$

Because the terms $e^{-2j\varphi}$ and $e^{2j\varphi}$ in equation (12) give

$$\frac{\partial f_{1i\pm}}{\partial v_r} = \frac{f_{1i\pm}}{v_r} ,$$

the first equation of equation (13) becomes

$$j(\omega - kv_z)g_i + a_z\frac{\partial g_i}{\partial v_z} + \frac{e_i}{m_i}E_{1z}\frac{\partial f_{0i}}{\partial v_z} + \frac{e_i}{m_i}\left(\frac{2a_+}{v_r}f_{1i-} + \frac{2a_-}{v_r}f_{1i+}\right) = 0. \qquad (14)$$

8.4 GENERAL DISPERSION RELATION

Equations (13) and (14) can be expressed in the form

$$\begin{pmatrix} a^i_{11} & a^i_{12} & a^i_{13} \\ a^i_{21} & a^i_{22} & a^i_{23} \\ a^i_{31} & a^i_{32} & a^i_{33} \end{pmatrix}\begin{pmatrix} f_{1i+} \\ f_{1i-} \\ g_i \end{pmatrix} = \begin{pmatrix} E_{1+} \\ E_{1-} \\ E_{1z} \end{pmatrix} \qquad (15)$$

where

$$a^i_{11} = \left(-\frac{m_i}{e_i}\right)\frac{1}{M_{i+}}\left[j(\omega - kv_z + \Omega_i) + a_z\frac{\partial}{\partial v_z}\right]$$

$$a^i_{12} = 0$$

$$
\begin{aligned}
a_{13}^{i} &= \frac{-a_{+}}{M_{i+}}\frac{\partial}{\partial v_r} \\
a_{21}^{i} &= 0 \\
a_{22}^{i} &= \left(-\frac{m_i}{e_i}\right)\frac{1}{M_{i-}}\left[j(\omega - kv_z - \Omega_i) + a_z\frac{\partial}{\partial v_z}\right] \\
a_{23}^{i} &= \frac{-a_{-}}{M_{i-}}\frac{\partial}{\partial v_r} \\
a_{31}^{i} &= -\frac{2a_{-}}{v_r}\left(\frac{\partial f_{0i}}{\partial v_z}\right)^{-1} \\
a_{32}^{i} &= -\frac{2a_{+}}{v_r}\left(\frac{\partial f_{0i}}{\partial v_z}\right)^{-1} \\
a_{33}^{i} &= \left(-\frac{m_i}{e_i}\right)\left(\frac{\partial f_{0i}}{\partial v_z}\right)^{-1}\left[j(\omega - kv_z) + a_z\frac{\partial}{\partial v_z}\right]
\end{aligned}
\tag{16}
$$

In equation (16), a_{11}^{i},a_{22}^{i}, a_{33}^{i}, a_{13}^{i}, and a_{23}^{i} are taken as operators since $\partial/\partial v_r$ and $\partial/\partial v_z$ will act on either g_i or $f_{1i\pm}$. In calculations, the following equations may be used:

$$
\begin{aligned}
a_{11}^{i} &= \left(-\frac{m_i}{e_i}\right)\frac{1}{M_{i+}}\left[j(\omega - kv_z + \Omega_i) + \frac{a_z}{f_{1i+}}\frac{\partial f_{1i+}}{\partial v_z}\right] \\
a_{22}^{i} &= \left(-\frac{m_i}{e_i}\right)\frac{1}{M_{i-}}\left[j(\omega - kv_z - \Omega_i) + \frac{a_z}{f_{1i-}}\frac{\partial f_{1i-}}{\partial v_z}\right] \\
a_{33}^{i} &= \left(-\frac{m_i}{e_i}\right)\left(\frac{\partial f_{0i}}{\partial v_z}\right)^{-1}\left[j\left(\omega - kv_z\right) + \frac{a_z}{g_i}\frac{\partial g_i}{\partial v_z}\right] \\
a_{13}^{i} &= \frac{-a_{+}}{M_{i+}g_i}\frac{\partial g_i}{\partial v_r} \\
a_{23}^{i} &= \frac{-a_{-}}{M_{i-}g_i}\frac{\partial g_i}{\partial v_r}\,.
\end{aligned}
\tag{16'}
$$

The solution of f_{1i} is obtained from eq. (15):

$$
\begin{pmatrix} f_{1i+} \\ f_{1i-} \\ g_i \end{pmatrix} = \begin{pmatrix} b_{11}^{i} & b_{12}^{i} & b_{13}^{i} \\ b_{21}^{i} & b_{22}^{i} & b_{23}^{i} \\ b_{31}^{i} & b_{32}^{i} & b_{23}^{i} \end{pmatrix}\begin{pmatrix} E_{1+} \\ E_{1-} \\ E_{1z} \end{pmatrix}
\tag{17}
$$

where

$$b^i_{11} = \frac{1}{a^i_{11}} + \frac{\zeta_1}{\left(a^i_{11}\right)^2 \delta}$$

$$b^i_{12} = \frac{a^i_{13} a^i_{32}}{a^i_{11} a^i_{22} \delta}$$

$$b^i_{13} = \frac{-a^i_{13}}{a^i_{11} \delta}$$

$$b^i_{21} = \frac{a^i_{23} a^i_{31}}{a^i_{11} a^i_{22} \delta}$$

$$b^i_{22} = \frac{1}{a^i_{22}} + \frac{\zeta_2}{\left(a^i_{22}\right)^2 \delta}$$

$$b^i_{23} = \frac{-a^i_{23}}{a^i_{22} \delta}$$

$$b^i_{31} = \frac{-a^i_{31}}{a^i_{11} \delta}$$

$$b^i_{32} = \frac{-a^i_{32}}{a^i_{22} \delta}$$

$$b^i_{33} = \frac{1}{\delta} \qquad (18)$$

in which

$$\zeta_1 = \frac{2a_+a_-}{M_{i+}v_r}\left(\frac{\partial f_{0i}}{\partial v_z}\right)^{-1} \frac{1}{g_i}\frac{\partial g_i}{\partial v_r}$$

$$\zeta_2 = \frac{2a_+a_-}{M_{i-}v_r}\left(\frac{\partial f_{0i}}{\partial v_z}\right)^{-1} \frac{1}{g_i}\frac{\partial g_i}{\partial v_r}$$

$$\delta = a^i_{33} - \left(\frac{\zeta_1}{a^i_{33}} + \frac{\zeta_2}{a^i_{22}}\right). \qquad (19)$$

From equations (9), (10) and (17), the solution of the wave electric field can be written in the form

$$\begin{pmatrix} R_{11}-1 & R_{12} & R_{13} \\ R_{21} & R_{22}-1 & R_{23} \\ R_{31} & R_{32} & R_{33}-1 \end{pmatrix} \begin{pmatrix} E_{1+} \\ E_{1-} \\ E_z \end{pmatrix} = 0, \tag{20}$$

where

$$R_{1l} = \frac{2\pi j\omega}{\left(\omega^2 - c^2k^2\right)} \sum_i \int_{-\infty}^{\infty} \int_0^{\infty} v_r^2 \int_0^{2\pi} \left(b_{1l}^i + b_{2l}^i e^{2j\varphi} + b_{3l}^i e^{j\varphi} \right) d\varphi dv_r dv_z, \quad l = 1, 2, 3 \tag{21}$$

$$R_{2p} = \frac{2\pi j\omega}{\left(\omega^2 - c^2k^2\right)} \sum_i \int_{-\infty}^{\infty} \int_0^{\infty} v_r^2 \int_0^{2\pi} \left(b_{1p}^i e^{-2j\varphi} + b_{2p}^i + b_{3p}^i e^{-j\varphi} \right) d\varphi dv_r dv_z, \quad p = 1, 2, 3 \tag{22}$$

$$R_{3q} = \frac{4\pi j}{\omega} \sum_i \int_{-\infty}^{\infty} \int_0^{\infty} v_r^2 \int_0^{2\pi} \left(b_{1q}^i e^{-j\varphi} + b_{2q}^i e^{j\varphi} + b_{3q}^i \right) d\varphi dv_r dv_z, \quad q = 1, 2, 3 . \tag{23}$$

Thus, the general dispersion relation is

$$\begin{vmatrix} R_{11}-1 & R_{12} & R_{13} \\ R_{21} & R_{22}-1 & R_{23} \\ R_{31} & R_{32} & R_{33}-1 \end{vmatrix} = 0. \tag{24}$$

8.5 SOME SPECIAL CASES

From equation (20), it can be seen that the three modes (i.e. the left-hand and right-hand circularly polarised modes and the longitudinal mode) are coupled. However, there are several special cases in which the dispersion relation may be simplified.

8.5.1 *Left-Hand Polarised Waves Coupling with the Longitudinal Mode*

When there exists only the left-hand polarised and longitudinal modes, the term that contains f_{1i+} in equation (14) can be neglected, and then g_i can be written as

$$g_i = \frac{je_i}{m_i\left(\omega - kv_z - \frac{ja_z}{g_i}\frac{\partial g_i}{\partial v_z}\right)} \left(\frac{2a_+}{v_r} f_{1i-} + E_{1z} \frac{\partial f_{0i}}{\partial v_z} \right). \tag{25}$$

Substituting equation (25) into the last equation of (13) and using $(\partial f_{1i-}/\partial v_r) = f_{1i-}/v_r$, we obtain

$$f_{1i-} = \frac{\dfrac{je_i}{m_i}\left\{M_{i-}E_{1-} + \dfrac{je_i a_-}{m_i\left[\omega - kv_z - ja_z g_i^{-1}(\partial g_i/\partial v_z)\right]}\dfrac{\partial(E_{1z}\partial f_{0i}/\partial v_z)}{\partial v_r}\right\}}{\omega - kv_z - \Omega_i - ja_z f_{1i-}^{-1}\left(\partial f_{1i-}/\partial v_z\right)} . \tag{26}$$

Equations (26) and (10) yield the dispersion relation for the left-hand polarised mode

$$\omega^2 = c^2k^2 - 2\pi\omega\sum_i \frac{e_i^2}{m_i}\int \frac{\left\{M_i + \dfrac{je_i a_-}{E_{1-}m_i\left[\omega - kv_z - \Omega_i - ja_z g_i^{-1}(\partial g_i/\partial v_z)\right]}\dfrac{\partial(E_{1z}\partial f_{0i}/\partial v_z)}{\partial v_r}\right\}_{v_r}}{\omega - kv_z - \Omega_i - ja_z f_{1i-}^{-1}\partial f_{1i-}/\partial v_z} d^3v . \tag{27}$$

Similarly, the dispersion relation for the longitudinal mode can be obtained. However, because the interest of this paper focuses on transverse waves, the longitudinal wave dispersion relation is not shown here.

8.5.2 *Right-Hand Polarised Waves Coupling with the Longitudinal Mode*

If there are only right-hand polarised and longitudinal waves, the dispersion relation for the right-hand polarised waves is in the form of equation (27), except that $-\Omega_i$ is replaced by $+\Omega_i$, a_- by a_+, E_{1-} by E_{1+}, M_{i-} by M_{i+} and f_{1i-} by f_{1i+}.

8.5.3 $E_{0x} = E_{0y} = 0$

In this case $a_\pm = 0$, if the $\partial f_{0i}/\partial\varphi = 0$ three modes are decoupled. The dispersion relations for left-hand polarised (bottom sign) and right-hand (top sign) polarised modes are:

$$1 = \frac{2\pi j\omega}{c^2k^2 - \omega^2}\sum_i \frac{e_i^2}{m_i}\int_{-\infty}^{\infty}\int_0^{\infty}\int_0^{2\pi} \frac{M_i v_r^2 d\varphi dv_r dv_z}{j(\omega - kv_z \pm \Omega_i) + a_z f_{1i\pm}^{-1}\partial f_{1i\pm}/\partial v_z} . \tag{28}$$

But, in general $\partial f_{0i}/\partial\varphi = 0$ therefore the three modes remain coupled.

8.5.4 $E_{0z} = 0$

In this case $a_z = 0$. The three modes may still remain coupled, and equation (24) should be solved to obtain the wave dispersion characteristics. However, when only two modes (the left- or right-hand polarised mode and the longitudinal mode) exist, the dispersion relation for the right-hand (top sign) or left-hand (bottom sign) polarised wave is:

$$\omega^2 = c^2k^2 - 2\pi\omega\sum_i \frac{e_i^2}{m_i}\int \frac{\left[M_{i\pm} + \dfrac{je_ia_\pm}{E_{1i\pm}m_i(\omega - kv_z \pm \Omega_i)}\dfrac{\partial(E_{1z}\partial f_{0i}/\partial v_r)}{\partial v_r}\right]v_r}{\omega - kv_z \pm \Omega_i} d^3v . \tag{29}$$

8.6 DISCUSSION

8.6.1 *f_{1i}, f_{0i}, and $E_{1z}/E_{1\pm}$*

In eqs. (16), (19), (25), (26), (27) and (28), it is necessary to determine how to calculate

$$\frac{1}{g_i}\frac{\partial g_i}{\partial v_z}, \quad \frac{1}{f_{1i\pm}}\frac{\partial f_{1i\pm}}{\partial v_z} .$$

There are two ways:

1. Assume g_i and $f_{1i\pm}$ have v_z dependence of the form $\exp(-v_z^2/2V_{Ti}^2)$, where V_{Ti} is the thermal velocity of the particle species i. In this case, the above two factors are equal to $-v_z/V_{Ti}^2$.

2. When $E_{0x} = E_{0y} = 0$ and the bi-Maxwellian distribution function is used to describe f_{0i}, we may modify the parallel temperature $T_{\|i}$ in f_{oi} to a complex temperature $T_{\|i}'$, and then the factor $a_z f_{1i\pm}^{-1}\partial f_{1i\pm}/\partial v_z$ will be neglected from equation (28):

$$T_{\|i}' = T_{\|i}\left(1 - \frac{je_iE_{0z}}{kk_BT_{\|i}}\right)$$

where k_B is the Boltzmann constant. This method was used by Pines and Schrieffer (1961) in solid-state plasmas.

Another consideration is the choice of f_{0i}. For the magnetospheric plasma, there are cold and energetic components. For the energetic ions, observations have shown that the distribution function is mainly an anisotropic loss-cone distribution (e.g. Joselyn and Lyons 1976); and for the cold plasma, the ion distribution is mainly isotropic (e.g. Horwitz et al. 1983), when the effect of dc electric field is not considered. When a weak static electric field is included, in different regions of the magnetosphere and ionosphere, some or all of the following effects should be considered: (1) the plasma drift velocity caused by the transverse electric field (Hu 1991), (2) parallel beams (Hu 1991) and (3) the electric scalar potential when E_{0z} appears. These will be discussed in other papers associated with numerical analysis.

When considering the two mode coupling cases (see section 4), we have to estimate E_{1z}/E_{1-} (or E_{1z}/E_{1+}). This can be done from

$$E_{1z} = \frac{4\pi j}{\omega}\sum_i e_i^2\int \frac{jv_z}{m_i(\omega - kv_z)}\left(\frac{2a_+}{v_r}f_{1i-} + E_{1z}\frac{\partial f_{0i}}{\partial v_z}\right)d^3v \tag{30}$$

and equation (26).

8.6.2 *Some Important Results*

In order to study the wave propagation and generation process in plasmas with static electric and magnetic fields, various models for different plasma environments in the magnetosphere and the ionosphere are considered in calculations of the frequency-wave number relationship and of growth rates for electromagnetic waves with $\omega \sim \Omega_s$ ($s = H^+$, He^+ and O^+). The detailed discussion on wave propagation and amplification/attenuation will be reported in other papers. Here we just list some important features of the system.

1. The presence of a weak static electric field leads to coupling between left- and right-hand polarised modes, and between the longitudinal mode and a transverse circularly polarised mode. This can be seen from the fact that $R_{ij} \neq 0$ ($i \neq j$).

2. There may be an instability induced by E_{0z} (i.e. the parallel electric field).

3. Ion cyclotron anisotropic instability stimulated by the thermal anisotropy of the energetic ions and thermal damping will be modified by E_{0z}.

8.6.3 *Applications*

The dispersion relation obtained in this paper may be used to solve the following problems:

1. Electromagnetic ion cyclotron waves may be important for ion heating in high latitude regions (e.g. Johnson et al. 1989 and references therein). These waves may be generated in the equatorial region and propagate to the high latitudes (Johnson et al. 1989, Rönmark and André 1991). When considering the characteristics of these waves in the high latitude region, the parallel electric field should be included. At least, the parallel static electric field will modify the attenuation of the waves.

2. The ionospheric electric field may lead to a modification of wave attenuation in the ionospheric wave guide. This ionospheric wave guide is parallel to the earth's surface and centred in the F2 region (e.g. Manchester 1966). Due to the modification by the electric field, the temporal and spatial occurrence of ground observed Pc 1-2 waves may be affected.

3. Mode coupling caused by a static electric field may be helpful for understanding the satellite observations of ion cyclotron waves with low ellipticities over a wide spatial region in the magnetosphere (e.g. Anderson et al. 1991). There are two possible mechanisms to explain these low ellipticities. One considers the mode coupling at a crossover frequency caused by heavy ions (Fraser 1985 and references therein). However, the spatial region where mode coupling occurs is much more narrow than the region where the low ellipticity has been observed. The other mechanism uses the instability induced by an energetic loss-cone-like distribution (Denton et al. 1992). But, it has not been confirmed that this loss-cone-like distribution driven instability does occur in the magnetosphere. If a weak static electric field is included in the magnetospheric plasma, the left-hand and right-hand polarised modes are coupled and the ellipticity for the total wave field may be low. This may provide another explanation.

8.7 CONCLUSION

1. A general dispersion relation for ion cyclotron waves propagating in a plasma with static magnetic and weak electric fields has been given. Some special cases have been discussed. Also, some important features of wave dispersion in this plasma have been discussed.

2. Possible applications of this dispersion relation in the magnetosphere and ionosphere have been forwarded.

REFERENCES

Anderson, B.J., Erlandson, R.E. *and* Zanetti, L.J. (1991). A statistical survey of Pc 1-2 properties AMPTE/CCE results. *EOS, Transactions AGU 72*. P. 255.

Balsinger, H., Geiss, J. *and* Young, D.T. (1983). The composition of thermal and hot ions observed by GEOS – 1 and –2 spacecraft. In: Johnson, R.G. (Ed.). *Energetic Ion Compositions in the Earth's Magnetosphere*. Terra Scientific Publishing, Tokyo.

Denton, R.E., Hudson, M.K. *and* Roth, I. (1992). Loss–cone-driven ion cyclotron waves in the magnetosphere. *Journal of Geophysical Research*. In press.

Fraser, B.J. (1985). Observations of ion cyclotron waves near synchronous orbit and on the ground. *Space Science Reviews 42*:357 – 374.

Geiss, J., Balsiger, H., Eberhardt, P., Walker, H.P., Weber, L., Young, D.T. *and* Rosenbauer, H. (1978). Dynamics of magnetospheric ion composition as observed by the GEOS mass spectrometer. *Space Science Reviews 22*:537 – 566.

Horwitz, J.L., Chappell, C.R., Reasoner, D.L., Craven, P.D., Green, J.L. *and* Baugher, C.R. (1983). Observations of low–energy plasma composition from ISEE-1 and -2 spacecraft. In: Johnson, R.G. (Ed.). *Energetic Ion Composition in the Earth's Magnetosphere*. Terra Scientific Publishing, Tokyo.

Hu, Y.D. (1991). *Electromagnetic waves in the magnetosphere with frequencies near the ion cyclotron frequency: propagation, amplification and wave-particle interaction*. Ph.D. thesis, University of Newcastle, Australia.

Johnson, J.R., Chang, T., Crew, G.B. *and* André, M. (1989). Equatorial generated ULF waves as a source for the turbulence associated with ion conics. *Geophysical Research Letters 16*:1469 – 1472.

Joselyn, J.A. *and* Lyons, L.R. (1976). Ion cyclotron wave growth calculated from observations of the proton ring current during storm recovery. *Journal of Geophysical Research 81*:2275 – 2282.

Manchester, R.N. (1966). Propagation of Pc 1 micropulsations from high to low latitudes. *Journal of Geophysical Research 71*:3749 – 3754.

Pines, D. *and* Schrieffer, J.R. (1961). Collective behaviour in solid-state plasmas. *Physical Review 124*:1387 – 1400.

Rönmark, K. *and* André, M. (1991). Convection of ion cyclotron waves to ion heating regions. *Journal of Geophysical Research 96*:17573 – 17579.

9. GROUND-SATELLITE OBSERVATIONS OF HIGH LATITUDE Pc1-2 PULSATIONS

H.J. Hansen[1], B.J. Fraser[1], F.W.Menk[1] and R.E. Erlandson[2]

[1] Department of Physics
University of Newcastle
Newcastle NSW 2308
Australia

[2] Applied Physics Laboratory
The Johns Hopkins University
Laurel MD 20707
USA

ABSTRACT

During 1986, the Viking polar orbiting satellite (apogee = 13.5 x 10^3 km) identified 21 intervals of high latitude Pc1 (0.2–5 Hz) activity from 59–77° MLAT above the northern hemisphere. This paper presents an analysis of concurrent Pc1 activity recorded at Mawson Antarctica (gm 70°S; 19°E) where similar activity was found on 7 occasions when Viking was located essentially conjugate. As ion cyclotron waves are considered to be responsible for the Viking observations, the analysis of this associated Mawson activity contributes towards understanding how ion cyclotron wave energy is transmitted from the high latitude equatorial magnetosphere to the ground. Consequently, this study elucidates the relationship between the frequency changes of Pc1 waves observed at Mawson and the morphology and dynamics of magnetospheric ion cyclotron wave generation regions responsible for this activity.

9.1 INTRODUCTION

Magnetic pulsations in the Pc1 (0.2–5 Hz) frequency range are believed to result from the electromagnetic ion cyclotron (EMIC) resonance instability in the equatorial magnetosphere (Dowden 1965, Gendrin et al. 1971). Ion cyclotron waves are generated in the vicinity of the equatorial plasmasphere where ring current anisotropies exceed a critical value necessary for wavegrowth (Kennel and Petschek 1966). The waves are guided along geomagnetic field lines to the ionosphere where they give rise to Pc1 magnetic pulsations which may be recorded by ground-based magnetometers. The F2 region plays a role in ducting wave energy away from the point where the ion cyclotron waves enter the ionosphere to higher and lower latitudes.

It has become increasingly apparent that to correctly interpret satellite observations of Pc1 activity requires a full understanding of the propagation of EMIC waves in multicomponent plasmas. In situ observations using GEOS-1, GEOS-2 and ATS-6 in geostationary orbit yield frequency spectra which display a slot in the spectral density around the equatorial He^+ gyrofrequency (Young et al. 1981, Mauk 1982). It has been shown that relative growth at frequencies above and below this slot is controlled by the pitch angle anisotropies and energies of the resonant ions, and the densities of the ion species constituting the cold background plasma (Mauk 1982,

Gomberoff and Neira 1983, Kozyra et al. 1984). Recent observations (Erlandson et al. 1990, Anderson et al. 1992a, b) indicate that activity on field lines below L = 8 is dominated by wave growth below the helium slot whilst activity above L = 8 occurs mostly above it. The different anisotropy and fluxes of the resonant ion population at mid-latitudes compared to that in the magnetospheric boundary layer region can account for this (Anderson et al. 1992a, b). However, it is difficult to understand how activity above the helium slot can be responsible for the rich spectrum of ground based Pc1 activity recorded by magnetometers in the vicinity of the auroral oval and the low altitude cusp (Menk et al. 1992). This is because ray tracing studies have shown that a wave above the equatorial He^+ gyrofrequency propagating from the equator is reflected at around 30° latitude when its wave frequency equals the local bi-ion frequency (Rauch and Roux 1982).

In addition, once the wave energy reaches the ionosphere, the manner in which it is dissipated towards both high and low latitudes is not well understood. At mid-latitudes, the F2 ionosphere layer acts as a duct distributing the energy in the isotropic compressional mode (Manchester 1968, Fraser 1975). At high latitudes, it is not known whether the F2 layer is able to trap the waves of lower frequencies compared to those at mid-latitudes, nor the extent to which propagation of the waves is affected by the continual particle precipitation found in the polar regions.

This paper describes concurrent Pc1 activity recorded aboard the polar orbiting Viking spacecraft (apogee ~13 x 10^3 km above the Arctic) and at Mawson (gm 70.1°S; 19.6°E) in Antarctica. The ionosphere's role in dissipating Pc1 energy to high and low latitudes from the auroral region appears limited as concurrent activity was only received when the satellite and ground station were essentially conjugate. It is shown that EMIC waves responsible for the observations can propagate from the magnetospheric equator to the ground if the helium and oxygen concentrations are negligible compared to the proton concentration.

9.2 INSTRUMENTATION AND ANALYSIS

The Viking magnetic field experiment includes a fluxgate magnetometer system with sensors mounted on a 2 m boom (Potemra et al. 1987, Erlandson et al. 1990). All the events discussed were obtained near apogee where the instrument's range was ~4000 nT ± 1 nT, commensurate with a 13 bit A/D converter. The analysis procedures and output are as described in Erlandson et al. (1990).

At Mawson, the induction magnetometer comprises two coils, one aligned in the geomagnetic north-south and the other in the east-west direction. The magnetic variations were modulated on a 25 Hz carrier and recorded on slow speed tape. Dynamic spectral analysis from 0.1 to 0.79 Hz was performed on the Mawson signals after demodulation and digitisation. Polarisation analysis (Samson et al. 1971) of the Mawson signals yielded the ellipticity and azimuth parameters from which wave mode and propagation characteristics in the ionosphere were deduced.

9.3 OBSERVATIONS

Details of the concurrent ground satellite activity are summarised in Table 1. This was mostly in the Pc1 (0.2 – 5 Hz) frequency range. Viking recorded such signals on 21 occasions during 1986 (Erlandson et al. 1990) and during the 7 intervals listed, similar variations were received at Mawson. For these intervals, Viking was threaded by lines of force which passed through the

geocentric equator to the ionosphere near Mawson, i.e. Viking's conjugate point was between gm 65° – 74° and gm 3°E – 29°W).

Table 1. Concurrent Pc1 activity on Viking and at Mawson, 1986.

Orbit	Time (UT)	Kp	Inv Lat	Inv Long	Freq. (Hz)
950	1318 – 1323	3-	69	-22.1	0.30 – 0.45
977	1119 – 1125	1-	70	3.1	0.20 – 0.45
1005	1322 – 1325	4	71	-32.2	0.30 – 0.45
1038	1325 – 1326	4	71	-38.0	0.40 – 0.60
1043	1127 – 1128	3-	71	-11.4	0.50 – 0.70
1076	1131 – 1132	2-	73	-19.6	0.60 – 0.70
1219	1059 – 1125	3-	64	-29.5	0.30 – 0.70

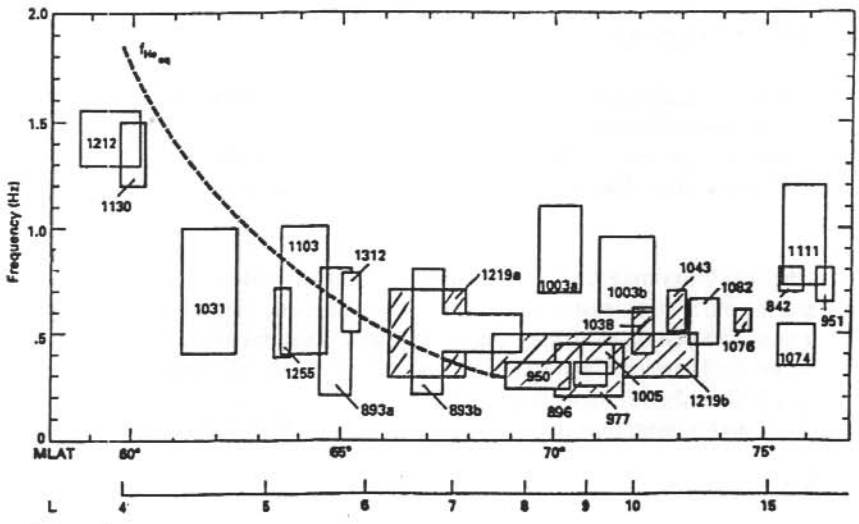

Figure 1. Pc1 events as a function of magnetic latitude (MLAT) (after Erlandson et al. 1990). The frequencies exhibited by the concurrent activity recorded at Mawson are shown by the shaded areas.

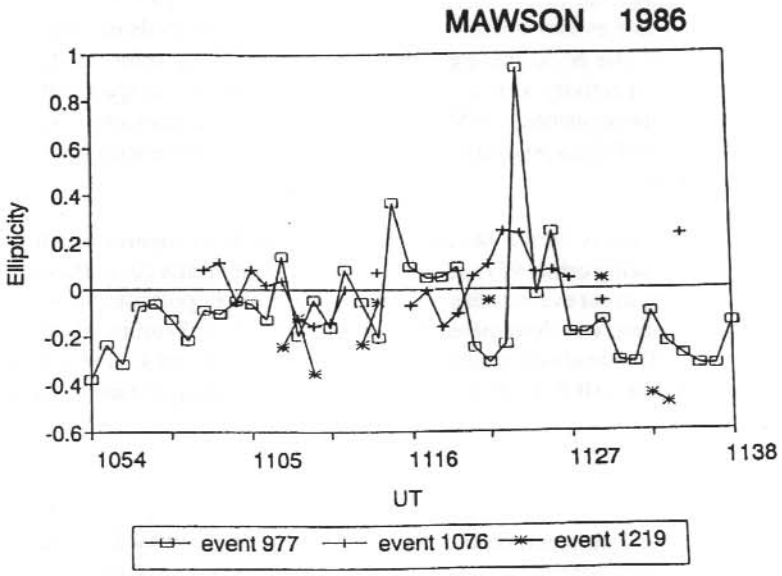

Figure 2. Frequency (at which power peaks in successive 256 point spectral estimates, time-lag = 100 pts) changes at Mawson as a function of UT between 1054 and 1138 UT for three intervals. Sampling period = 0.64 s.

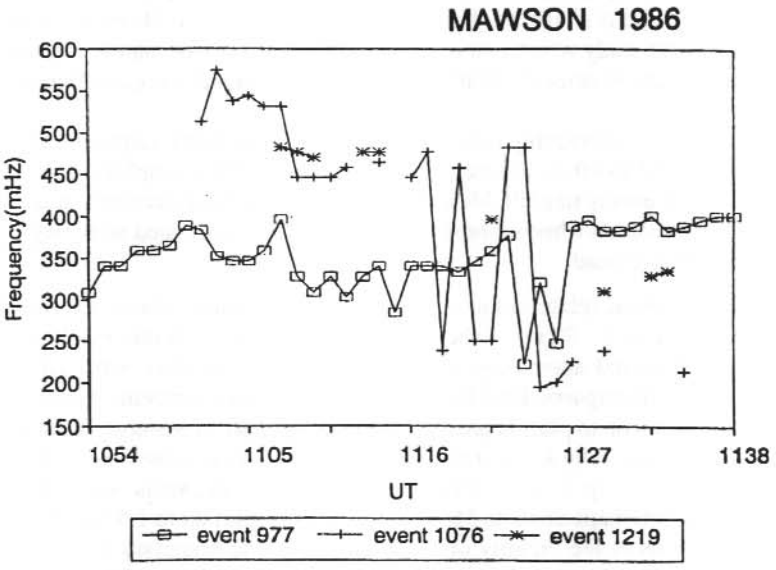

Figure 3. Ellipticities associated with the spectral peaks plotted in Figure 2. Positive values indicate counter-clockwise sense of rotation.

Figure 1 displays the frequencies of the Viking Pc1 activity as a function of magnetic latitude. The dashed curve shows the calculated equatorial helium gyrofrequency and its variation with magnetic latitude. Those events which are shaded indicate the intervals of concurrent activity at Mawson. On at least one occasion, e.g. the event during Viking orbit 1219, the frequencies exhibited by the ground activity were a subset of those recorded at the spacecraft. It should also be noted that on certain occasions, the Mawson pulsations were coincident with the presence of magnetic waves on field lines poleward of Mawson and with frequencies above the equatorial helium gyrofrequency.

The polarisation properties of the Mawson activity have been determined for the intervals recorded during the Viking orbits 977, 1076 and 1219. These events cover the complete latitude range over which concurrent events were observed. The sense of polarisation and the orientation of the polarisation ellipse was determined from the magnetic north-south (H) and east-west (D) signals at Mawson. This analysis is summarised in Figures 2, 3 and 4. The ground ellipticities were essentially linear (+0.2 to -0.2), consistent with the ellipticities associated with the spacecraft signals.

9.4 DISCUSSION

In accordance with the interpretation of Viking observations given by Erlandson et al. (1990), these Pc1 observations arise from ion cyclotron waves generated in the equatorial outer magnetosphere. The waves propagate along magnetic flux tubes northward to the Viking spacecraft and southward to the Mawson ionosphere. Common frequencies were exhibited by the Viking and Mawson signals when the two recording sites were conjugate. During those Viking orbits when there were no corresponding activities at Mawson, the two recording sites were either in completely different time sectors, or the magnetospheric Pc1 activities map to ionospheric source regions situated at latitudes further than 7° from Mawson's location (~70°S). This confirms a recent study which demonstrated that a high latitude station must be within 7° of the auroral oval in order to detect Pc1 pulsations associated with this region (Hansen et al. 1991).

The polarisation properties relating to the Mawson observations are surprising. The ellipticities are linear (range = -0.2 to +0.2), irrespective of the fact that the ionospheric sources of the orbit 977 and 1219 Viking events straddle Mawson's latitude. Left hand circularly polarised activity is expected at a ground station when ionospheric sources of Pc1 associated with magnetospheric ion cyclotron waves are overhead.

The frequencies observed relate to ion cyclotron wave generation above the equatorial helium gyrofrequency near L = 8. Figure 4 shows the convective growth rate resulting from 10 keV resonant protons (thermal anisotropy $A = (T_{\parallel}/T_{\perp}-1) = 1.5$, density = 0.1 cm^{-3}) at different frequencies in an 80 nT magnetic field for two sets of cold ion constituents (Gomberoff and Neira 1983). The ratio of kinetic to plasma pressure (β) in the vicinity of the nose of the magnetosphere is ~1 and it has been shown by Roux et al. (1982) that convective growth theory is valid in such a plasma for anisotropies up to 1.5. Typically 80 nT field strengths would be found in the equatorial region which maps down to Mawson and anisotropies up to 1.5 have been attributed to hot particle pulsations in the vicinity of the magnetospheric boundary layer (Anderson et al. 1992a, b). Most of the Mawson signals exhibited frequencies from 0.3-0.5 Hz, where the slot between the helium and hydrogen branches is found. Figure 5 depicts this slot for two sets of cold ion constituents, (N_H; N_{He}; N_O) = (10; 0.8; 0.2) cm^{-3} (the solid curve) and (10; 0.2; 0.05)

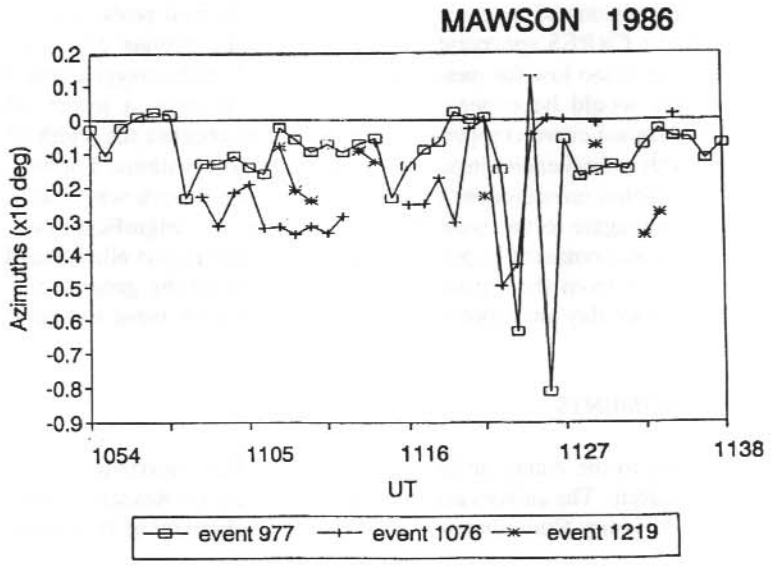

Figure 4. Azimuth, corresponding to the ellipticities displayed in Figure 3, plotted as a function of UT. Positive values indicate the major axis of the polarisation ellipse orientated in the NE-SW quadrants.

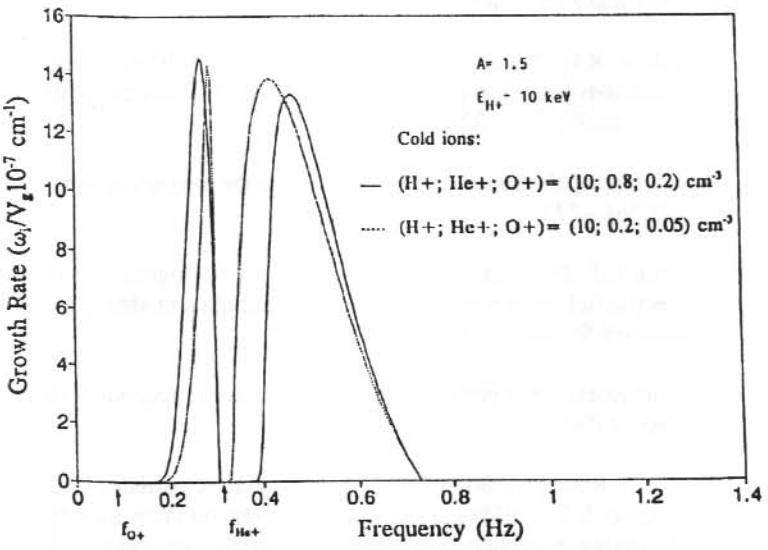

Figure 5. Linear convective wavegrowth calculations for two possible plasma environments situated just inside the dayside magnetosphere.

cm^{-3} (the dashed curve) respectively. These plasma environments would be typical in the high latitude plasmatrough region and are consistent with Viking langmuir probe observations and with measurements on the CRRES spacecraft at L = 7 – 9 (Fraser, private communication). The oxygen concentration is too low for measurable wavegrowth in the oxygen branch of the cases shown (these peaks would be expected at ~0.07 Hz). Clearly, a lower relative helium concentration (the dashed curve compared to the solid one) reduces the width of the slot, and results in wavegrowth at frequencies in accordance with the observations. Furthermore, it is well known that a pure proton environment enables the hydrogen branch waves above the helium gyrofrequency to propagate to the ground. Consequently, as insignificant concentrations of helium and oxygen ions compared to protons in the interaction region allow the observed wave activities to propagate from the equatorial magnetosphere to the ground, the cold plasma environment appears to play an important role in accounting for these spacecraft and ground observations.

9.5 ACKNOWLEDGMENTS

Thanks are extended to the Antarctic Division and to Dr R.J. Morris for providing the field logistics for this research. The authors acknowledge the Australian Research Council (ARC), the Antarctic Science Advisory Committee (ASAC) and the University of Newcastle for financial support.

REFERENCES

Anderson, B.J., Erlandson, R.E. *and* Zanetti, L.J. (1992a). A statistical study of Pc1-2 pulsations in the equatorial magnetosphere: 1. Equatorial occurrence current distributions. *Journal of Geophysical Research 97*:3075 – 3088.

Anderson, B.J., Erlandson, R.E., Takahashi, K. *and* Zanetti, L.J. (1992b). A statistical study of Pc1 magnetic pulsations in the equatorial magnetosphere: 2. Wave properties. *Journal of Geophysical Research 97*:3089 – 3102.

Dowden, R.L. (1965). "Micropulsation mode" propagation in the magnetosphere. *Planetary and Space Science 13*:761 – 772.

Erlandson, R.E., Zanetti, L.J., Potemra, T.A., Block, L.P. *and* Holmgren, G. (1990). Viking magnetic and electric field observations of Pc1 waves at high latitudes. *Journal of Geophysical Research 95*:5941 – 5955.

Fraser, B.J. (1975). Ionospheric duct propagation and Pc1 sources. *Journal of Geophysical Research 80*:2790 – 2796.

Gendrin, R., Lacourly, S., Roux, A., Solomon, J., Feigen, F.Z., Gokhberg, M.V., Toitskaya, V.A. *and* Yakimenko, V.L. (1971). Wave packet propagation in an amplifying medium and its application to the dispersion characteristics and to the generation of Pc1 events. *Planetary and Space Science 19*:165 – 194.

Gomberoff, L. *and* Neira, R. (1983). Convective growth rate of ion cyclotron waves in a H^+ – He^+ and H^+ – He^+ – O^+ plasma. *Journal of Geophysical Research 88*:2170 – 2174.

Hansen, H.J., Fraser, B.J., Menk, F.W., Hu, Y.D., Newell, P.T. *and* Meng, C-I. (1991). High latitude unstructured Pc1 emissions generated in the vicinity of the dayside auroral oval. *Planetary and Space Science 39*:709 – 719.

Kennel, C.F. *and* Petschek, H.C. (1966). Limit on stably trapped particle fluxes. *Journal of Geophysical Research 71*:1 – 28.

Kozyra, J.U., Cravens, T.E., Nagy, A.F. *and* Fontheim, E.G. (1984). Effects of energetic heavy ions on electromagnetic ion cyclotron wave generation in the plasmapause region. *Journal of Geophysical Research 89*:2217 – 2233.

Manchester, R.N. (1968). Correlation of Pc1 micropulsations at spaced stations. *Journal of Geophysical Research 73*:3549 – 3556.

Mauk, B.H. (1982). Helium resonance and dispersion effect on geostationary Alfven/ion cyclotron waves. *Journal of Geophysical Research 87*:9107 – 9119.

Menk, F.W., Fraser, B.J., Hansen, H.J., Newell, P.T. *and* Meng, C-I. (1992). Multistation observations of Pc1-2 ULF pulsations between the plasmapause and polar cap. *Journal of Geophysical Research*. In press.

Potemra, T.A., Zanetti, L.J., Erlandson, R.E., Bythrow, P.F., Gustafsson, G., Acuna, M.H. *and* Lundin, R. (1987). Observations of large Birkeland currents with Viking. *Geophysical Research Letters 14*:419 – 423.

Rauch, J.L. *and* Roux, A. (1982). Ray tracing of ULF waves in a multicomponent magnetospheric plasma: consequences for the generation mechanism for ion cyclotron waves. *Journal of Geophysical Research 87*:8191 – 8198.

Roux, A., Perrault, S., Rauch, J.L., de Villedary, C., Kremser, G., Korth, A. *and* Young, D.T. (1982). Wave-particle interactions near Ω_{He+} on GEOS 1 and 2, 2, Generation of ion cyclotron waves and heating of He+ ions. *Journal of Geophysical Research 87*:8174 – 8190.

Samson, J., Jacobs, J.A. *and* Rostoker, G. (1971). Latitude-dependent characteristics of long period geomagnetic pulsations. *Journal of Geophysical Research 76*:3675 – 3683.

Young, D.T., Perrault, S., Roux, A., de Villedary, C., Gendrin, R., Korth, A., Kremser, G. *and* Jones, D. (1981). Wave-particle interactions near Ω_{He+} observed on GEOS 1 and 2, 1, Propagation of ion cyclotron waves in He+ -rich plasma. *Journal of Geophysical Research 86*:6755 – 6772.

10. THE PROPAGATION OF Pc1 MAGNETIC BURSTS ACROSS THE POLAR CAP REGION

M.H. Francke[1], H.J. Hansen[1], F.W. Menk[1], B.J. Fraser[1] and R.J. Morris[2]

[1] Department of Physics
University of Newcastle
Newcastle NSW 2308
Australia

[2] Auroral and Space Physics
Antarctic Division
Kingston Tasmania 7050
Australia

ABSTRACT

Pc1 (0.2 – 5 Hz) magnetic pulsations were recorded during a 14-day campaign in July 1990 using a ground array of induction magnetometers in the Australian Antarctic Territory. This paper is concerned with the analysis of the spatial characteristics of discrete Pc1 bursts or packets, often recorded in association with solitary magnetic impulses (period = 1 to 10 min). Interstation cross-spectral analysis of these Pc1 events allows their phase velocities to be determined and their ionospheric attenuation to be studied. The ionospheric source of high latitude Pc1 signals has previously been interpreted in terms of the arrival at the ionosphere of magnetospheric ion cyclotron waves. These results thus relate to the dissipation and propagation of magnetospheric ion cyclotron wave energy in the ionosphere.

10.1 INTRODUCTION

Pc1 (0.2 – 5 Hz) geomagnetic pulsations recorded by ground-based magnetometers have been associated with the ion cyclotron resonance process in the equatorial magnetosphere (Dowden 1965, Kennel and Petschek 1966, Gendrin et al. 1971). The process occurs as ions move through the equatorial plane, with left hand circularly polarised Alfven waves growing at the expense of energy manifest in the gyrating motions of the ions. The waves propagate from the wave growth region along magnetic field lines and down to the ionosphere. There they perturb the ionospheric current patterns and are detected by ground-based magnetometers as Pc1 signals.

The manner in which the wave energy is distributed to both high and low latitudes from the ionospheric source is not well understood, particularly at high latitudes. At plasmapause or mid-latitudes, the F2 ionosphere layer acts as a duct distributing the wave energy in the isotropic fast mode (Manchester 1968, Fraser 1975). However at high latitudes, it is not clear whether the F2 layer is able to trap the signals, nor the extent to which propagation of the waves is affected by the particle precipitation prevalent in the polar regions.

This paper describes a preliminary case study of dayside high latitude magnetic Pc1 (frequency ~0.3 Hz) burst activity recorded at Mawson (MLAT ~70°S; MLONG ~90°E) and Davis

(MLAT ~75°; MLONG ~103°E) in the Australian Antarctic Territory. From the days examined, six Pcl bursts recorded at two or more stations were chosen for detailed analysis using cross-spectral and polarisation techniques. These events are found to be most likely associated with magnetospheric electromagnetic ion cyclotron waves generated above the equatorial helium gyrofrequency (Young et al. 1981, Roux et al. 1982, Mauk 1982, Anderson et al. 1991a, b, Erlandson et al. 1990). Propagation velocities between Mawson and Davis, and polarisation characteristics of the signals at each site, suggest that the energy is being propagated toward lower latitudes in the fast right hand mode. This mode of energy dissipation is consistent with that found for Pc1 activity at middle latitudes.

10.2 INSTRUMENTATION AND ANALYSIS TECHNIQUES

The magnetic pulsations were recorded with two component induction magnetometers at the stations shown in Figure 1. During daytime, Mawson is located at the foot of field lines equatorward of the cleft in the plasmatrough. Davis near local noon is beneath the average position of the dayside cleft/cusp. This is the region through which high fluxes of magnetosheath particles have direct access to ionospheric altitudes. Those locations on earth that rotate beneath the cusp are shown by the shaded annular region.

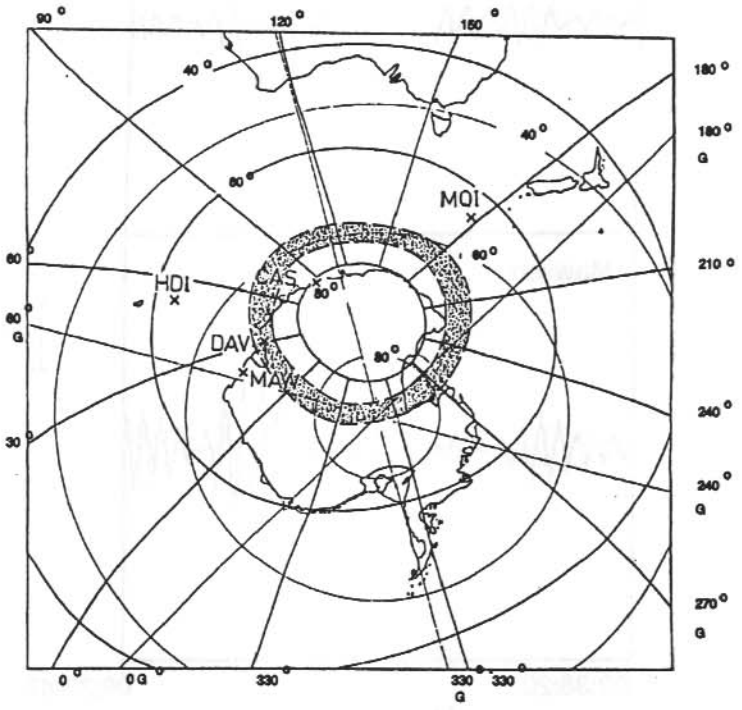

Figure 1. The locations of Davis (DAV) and Mawson (MAW). The bold/fine curves indicate geomagnetic/geographic coordinates. The shaded region indicates those locations on earth that rotate beneath the average position of the dayside cusp.

The magnetometer systems record Pc1-5 signals over the 3 mHz – 3 Hz range with a sensitivity of 5 pT Hz^{-1}. The data were recorded digitally using a PDP-11 computer. Data were sampled at 1.25 Hz with a time accuracy of 5 ms. The PDP-11 was networked via an ANARESAT link to the Antarctic Division and the University of Newcastle. At Newcastle, the data were converted to a common format using a customised Data Base Management System and accessed through a dedicated LAN with six PC 286/386 microcomputers. The selected data were analysed using multi-channel state vector time series and cross spectral analysis techniques (Samson et al. 1971). In this way, wave spectra and the polarisation properties of the signals at each site were obtained and the phase difference, time lags and phase velocities of correlated activity determined.

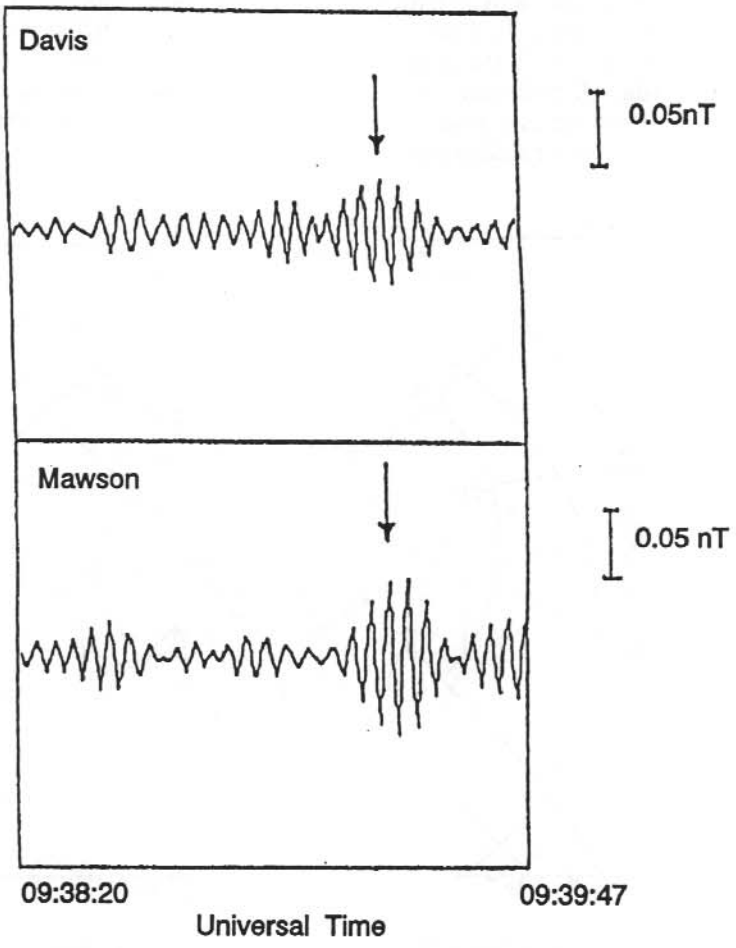

Figure 2. Amplitude time variations of the event commencing at 09:39:16 UT for Davis (upper panel) and Mawson (lower panel).

10.3 OBSERVATIONS

Concurrent Pc1 bursts may be observed at Mawson and Davis as the ground magnetometer sites pass through noon. Local noon at Davis is 0945 UT and at Mawson is 1030 UT. Six Pc1 bursts were analysed in detail for the 21 July 1990 interval.

Figure 2 depicts the amplitude-time variations of a typical event at Davis (upper panel) and Mawson (lower panel). The peak amplitude is 0.08 ± 0.01 nT at Davis and 0.12 ± 0.02 nT at Mawson. The power spectra of these signals, shown in Figure 3, depict common spectral peaks between 0.27 and 0.35 Hz.

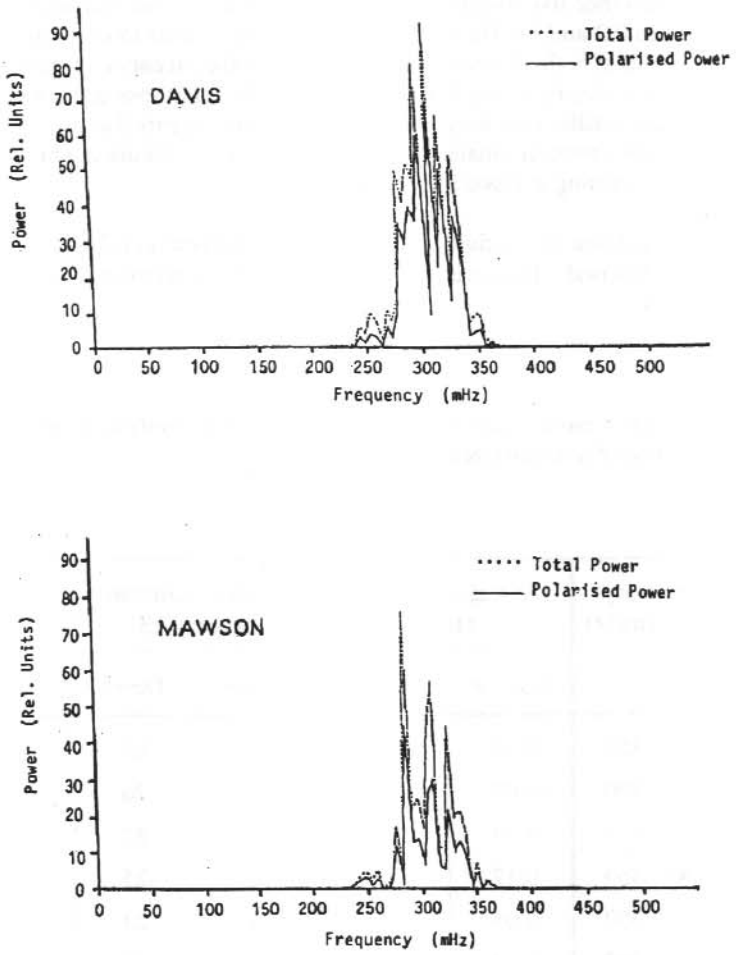

Figure 3. Power spectra for ~2 minutes of activity commencing at 09:39:16 UT for Davis (upper panel) and Mawson (lower panel). The raw signal was band-pass filtered between 0.25 and 0.35 mHz.

Polarisation parameters determined between the north-south and east-west sensors at each site show similar ellipticities (+0.24 ±0.05 for the typical event), when averaged over the 0.27 – 0.35 mHz range. This relates the activity to a wave with right-handed/linear polarisation. Positive ellipticity implies a right hand circularly polarised wave, negative implies left handed activity when viewed in the direction of the ambient field.

Finally, phase differences between Mawson and Davis have been estimated. The activity at Davis leads that at Mawson by ~100°, for the interval shown. This relates to a phase velocity component of 740 ±50 km s^{-1} between the stations and is an estimate of the group velocity as the associated bursts at Davis and Mawson occur within $1/(2\pi f)$ s or ~0.5 s (for f = 0.3 Hz) of each other (Althouse and Davis 1978).

Similar details for the other five events are outlined in Table 1. The frequencies of common activity range between 0.2 and 0.4 Hz with spectra generally similar to those in Figure 3. The ellipticities of the signals at both Mawson and Davis are, with the exception of one event, linear or right handed. It should also be noted that the Davis signals lead those at Mawson, exhibiting phase angle differences smaller than those for the typical event described above. The amplitudes of all these signals were generally smaller than those displayed in Figure 2 with the larger peak amplitude sometimes occurring at Davis rather than Mawson.

It should be emphasised that Pc1 activity was continually received at both Mawson and Davis during the complete interval. However, concurrent pulsations relating to propagating wave activity occurred rarely.

Table 1. Details of six Pc1 bursts examined. Ellipticities, azimuths and phase angles were averaged over the range of common frequencies.

Time (UT)	Frequency Range (mHz)	Average Ellipticity ±0.05		Average Azimuth (degree) ±3		Average Phase (degree) ±5	
		Mawson	Davis	Mawson	Davis	XX	YY
09:39:17	270 – 350	0.24	0.24	4	-65	95	129
10:16:56	280 – 320	-0.07	0.03	14	-26	-15	43
10:18:40	300 – 330	0.29	0.51	18	-32	31	89
10:32:09	300 – 350	0.12	0.07	26	-25	25	1
10:32:30	300 – 350	0.03	-0.22	6	23	9	119
10:43:02	250 – 300	0.14	-0.52	10	46	55	13

10.4 DISCUSSION

In accordance with the interpretation of Pc1 activity at mid-latitudes, the speeds of propagation and wave polarisation properties suggest the right-hand fast mode is responsible. Group speeds of at least 740 km s^{-1} are suggested. These are consistent with the 500 to 2500 km s^{-1} duct velocities in the F2 ionospheric waveguide (Fraser 1975).

Particle energy and flux data from the DMSP spacecraft in an 840 km altitude polar orbit show boundary layer plasmasheet (BPS) plasma above or slightly poleward of Davis (74 – 78° MLAT) when these events were recorded. Together with the Davis signal leading Mawson, this suggests that boundary layer plasma provides the free energy for ion cyclotron wave growth in the equatorial magnetosphere.

The BPS environment favours wavegrowth above the equatorial helium gyrofrequency (Anderson et al. 1992a) – under the conditions of high anisotropy, high fluxes of resonant ions, low cold plasma densities – at frequencies between 0.2 – 0.4 Hz on ~L = 8 field lines. An important consideration now is to understand how such wave energy propagates to the ground as theoretical studies suggest helium branch waves are reflected at the altitude where the propagating wave frequency equals the local bi-ion frequency.

The infrequent occurrence of concurrent activity at Mawson and Davis suggests most of the activity is localised. This implies that the dissipation of Pc1 wave energy in the F2 waveguide at high latitudes is inefficient and shows that most of these signals are attenuated within the 400 km separation distance between Davis and Mawson.

10.5 ACKNOWLEDGMENTS

Thanks to Dr A. Klekociuk and the Auroral and Space Physics group, Antarctic Division, for collection of the Australian National Antarctic Research Expedition (ANARE) station data. The authors acknowledge the Australian Research Council (ARC) and the Antarctic Science Advisory Committee (ASAC) for financial support.

REFERENCES

Althouse, E.L. *and* Davis, J.R. (1978). Five-station observations of Pc1 micropulsation propagation. *Journal of Geophysical Research 83*:132 – 144.

Anderson, B.J., Erlandson, R.E. *and* Zanetti, L.J. (1992a). A statistical study of Pc1-2 pulsations in the equatorial magnetosphere: 1. Equatorial current distributions. *Journal of Geophysical Research 97*:3075 – 3088.

Anderson, B.J., Erlandson, R.E. *and* Zanetti, L.J. (1992b). A statistical study of Pc1 magnetic pulsations in the equatorial magnetosphere: 2. Wave properties. *Journal of Geophysical Research 97*:3089 – 3102.

Dowden, R.L. (1965). 'Micropulsation mode' propagation in the magnetosphere. *Planetary and Space Science 13*:761 – 772.

Erlandson, R.E., Zanetti, L.J., Potemra, T.A., Block, L.P. *and* Holmgren, G. (1990). Viking magnetic and electric field observations of Pc1 Waves at high latitudes. *Journal of Geophysical Research 95*:5941 – 5955.

Fraser, B.J. (1975). Ionospheric duct propagation and Pc1 sources. *Journal of Geophysical Research 80*:2790 – 2796.

Gendrin, R., Lacourly, S., Roux, A., Solomon, J., Feigen, F.Z., Gokhberg, M.V., Troitskaya, V.A. *and* Yakimenko, V.L. (1971). Wave packet propagation in an amplifying medium and its application to the dispersion characteristics and to the generation of Pc1 events. *Planetary and Space Science 19*:165 – 194.

Kennel, C.F. *and* Petschek, H.C. (1966). Limit on stably trapped particle fluxes. *Journal of Geophysical Research 71*:1 – 28.

Manchester, R.N. (1968). Correlation of Pc1 micropulsations at spaced stations. *Journal of Geophysical Research 73*:3549 – 3556.

Mauk, B.H. (1982). Helium resonance and dispersion effect on geostationary Alfven/ion cyclotron waves. *Journal of Geophysical Research 87*:9107 – 9119.

Roux, A., Perrault, S., Rauch, J.L., de Villedary, C., Kremser, G., Korth, A. *and* Young, D.T. (1982). Wave-particle interactions near Ω_{He^+} on GEOS 1 and 2, 2, Generation of ion cyclotron waves and heating of He^+ ions. *Journal of Geophysical Research 87*:8174 – 8190.

Samson, J., Jacobs, J.A. *and* Rostoker, G. (1971). Latitude-dependent characteristics of long period geomagnetic pulsations. *Journal of Geophysical Research 76*:3675 – 3683.

Young, D.T., Perrault, S., Roux, A., de Villedary, C., Gendrin, R., Korth, A., Kremser, G. *and* Jones, D. (1981). Wave-particle interactions near Ω_{He^+} observed on GEOS 1 and 2, 1, Propagation of ion cyclotron waves in He^+-rich plasma. *Journal of Geophysical Research 86*:6755 – 6772.

11. GENERATION AND PROPAGATION MECHANISMS OF Pi2 GEOMAGNETIC PULSATIONS

Y.Li, D.J. Webster, F.W Menk and B.J. Fraser

Department of Physics
University of Newcastle
Newcastle NSW 2308
Australia

ABSTRACT

Impulsive transient geomagnetic pulsations in the 5 – 25 mHz range (Pi2) at auroral latitudes accompany the onset of geomagnetic substorms. They can also be recorded at low latitudes although how the signals propagate to these regions is unknown. In this study Pi2 events recorded across an induction and fluxgate magnetometer array from L = 5.3 (Macquarie Island) to L = 1.44 (Gladstone, Qld), and Auckland, New Zealand, are examined. Wave spectra, latitudinal amplitude distribution, phase and polarisation characteristics are obtained using pure state analysis techniques. These results imply that low latitude Pi2 are associated with distinctly different generation and propagation mechanisms to those at high latitudes.

11.1 INTRODUCTION

Geomagnetic Pi2 pulsations are generally interpreted as a transient hydromagnetic signal associated with a sudden change in the physical state of the magnetosphere at substorm onset. The Pi2 begins at the time of substorm onset, and lasts for not more than 10 – 15 minutes after the onset. Observed Pi2 signals are impulsive damped trains of waves in the 40 – 150 sec period range, with maximum occurrence frequency near the local midnight meridian. The amplitudes of Pi2's exhibit a maximum in the auroral zone and decrease sharply at both higher and lower latitudes. At mid-latitudes however, the amplitude does not continue to decrease monotonically, but shows a secondary maximum. This was found at 50° N by Jacobs and Sinno (1960), and a mid-latitude maximum between L ≈ 3.3 and 3.8 by Stuart (1974).

The source region of Pi2s is at auroral zone latitudes (L = 6 – 7), and their generation is associated with the substorm current system (Rostoker and Samson 1981, Pashin et al. 1982). Different models for Pi2 generation and propagation have been proposed. Each can explain some but not all of the observed Pi2 characteristics. Samson (1982) proposed a model for high latitude Pi2 after reviewing high latitude experimental results. The Pi2 perturbation begins with an initial upward field aligned current pulse which is responsible for precipitation and arc brightening. Within the first cycle of the Pi2, the field lines on which the original current pulse started collapse to dipolar. The electrojet and precipitation then move to higher latitudes as an auroral surge forms. The original current pulse is reflected on the dipolar field lines and propagates along field lines as a shear Alfven wave. Multiple reflections from the north and south auroral ionospheres lead to the typical Pi2 wavetrain. There is still uncertainty about the propagation of these pulsations from high to low latitudes. Lester et al. (1989) used a current wedge model to interpret the observed mid-latitude polarisation pattern of the Pi2s. The simple three-dimensional substorm

current wedge model orders the Pi2 polarization signature quite well, but not the amplitude distribution at middle to low latitudes. For the mid-latitude maximum of Pi2s, Stuart (1974) suggested an explanation involving a secondary resonance of field lines within the plasmasphere. Recently, a cavity resonance explanation has been considered for middle and low latitude Pi2s by several authors (e.g. Yeoman and Orr 1989, Sutcliffe and Yumoto 1991). The cavity resonance model has been described by Kivelson and Southwood (1985) and Allan et al. (1985, 1986). An impulsive compression sets up multiple compressional resonances in the magnetospheric cavity, and these resonances drive multiple field-line resonances where the field-line eigenfrequencies match the cavity resonance eigenfrequencies.

This paper aims to present new observational data of Pi2s, and discuss generation and propagation mechanisms.

11.2 DATA RECORDING AND ANALYSIS

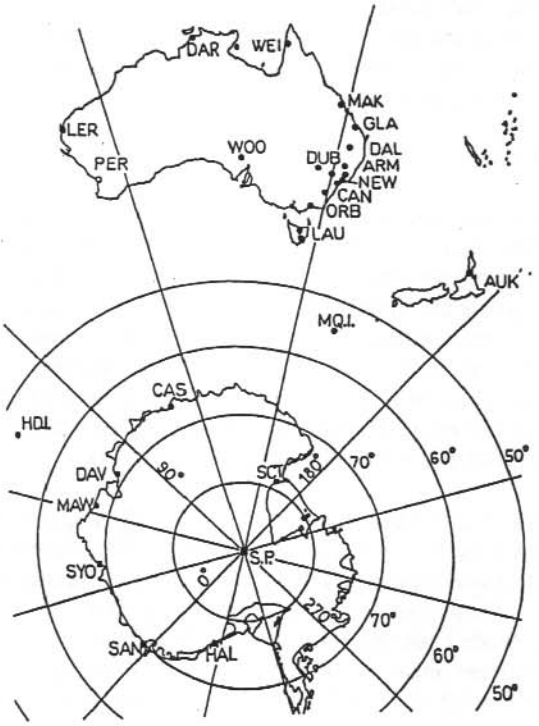

Figure 1. University of Newcastle ground stations array in eastern Australia, New Zealand and Macquarie Island.

The data used in this paper were recorded in 1989 by the University of Newcastle magnetometer array including stations in eastern Australia, New Zealand and Macquarie Island (Figure 1). Table 1 shows the coordinates of stations included in this study. Auckland used a fluxgate magnetometer while the other stations used induction magnetometers. Each magnetometer recorded time variations in the magnetic field in two channels, geomagnetic north-south (X), and east-west (Y). For the induction magnetometer, the sensitivity was 1.00 nT V^{-1} at 15 mHz, and 0.80 nT V^{-1} at 10 mHz. For the fluxgate magnetometer, the sensitivity was 1.00 nT V^{-1} from 5 – 100 mHz. Timing at each station was obtained from a chronometer referenced to a time standard radio station.

Table 1. Geographic and geomagnetic coordinates, L values of the stations and time of local noon.

Station		Geographic °S	Geographic °E	Geomagnetic °S	Geomagnetic °E	L value	Local noon
Gladstone	GLA	24.2	151.2	33.6	225.6	1.44	0136 UT
Armidale	ARM	30.5	151.6	40.2	227.2	1.71	0130 UT
Newcastle	NEW	32.6	151.7	42.3	228.1	1.83	0126 UT
Canberra	CAN	35.3	149.5	45.6	226.2	2.04	0135 UT
Auckland	AUK	37.0	175.0	43.0	255.4	1.87	2333 UT
Macquarie Is	MQI	54.5	159.0	64.5	246.8	5.4	2324 UT

During analysis, we first selected common Pi2-like signals from each station, and then used the higher latitude MQI data to confirm that these events were indeed substorm associated. Events were then analysed in detail following the method outlined in Figure 2. To date 14 events have been examined in this way. Figures 3 to 6 illustrate the processing of a representative event, which occurred on 20 August 1989 at 19:23:23 LT (= UT + 10 hr) and was observed at 4 stations. Figures 3 a, b, c show the raw data, the polarised wave, and the narrow band polarised wave. Timing at GLA was inaccurate and could not be used for obtaining phase velocity estimates. Figure 4 shows polarised wave power spectra for 3 stations at different latitudes and one station at a different local time. The frequency for the main peak is around 15 mHz for every station, and the maximum amplitude for this event is at ARM (L = 1.71). Figure 5 is the narrow band polarised wave power spectrum for the NEW station for this event. Figure 6 shows polarisation hodograms for the main spectral peak at 4 stations. The azimuth changes with latitude. The orientation of the main axis is north-east at GLA, and north-west at ARM, NEW and AUK.

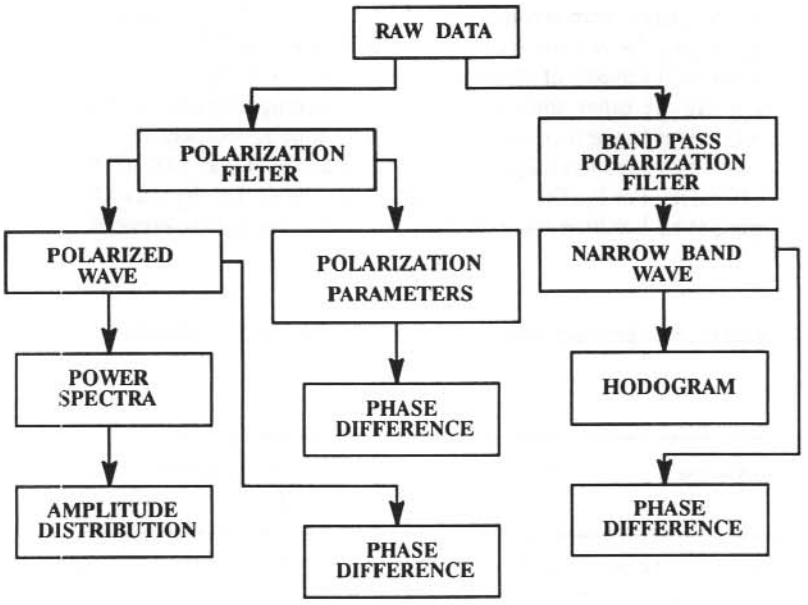

Figure 2. Flowchart of analysis procedure.

The cross station phase difference was obtained by averaging the results of three different techniques: (a) directly comparing the wave peak and trough to obtain the time delay and then phase difference, (b) computing the wave's cross phase using the FFT, and (c) deducing the phase difference from measurement of the polarisation characteristics (i.e. azimuth angle). Phase velocity was in each case calculated from

$$v = \Delta s \frac{\omega}{\Delta \phi} = 2\pi f \frac{\Delta s}{\Delta \phi}$$

where f is the frequency of the Pi2 wave, $\Delta\phi$ is the phase difference between two stations, and Δs is the distance between the stations. Phase velocity for the representative example shown in Figure 3 was 66 $\pm$19 km s^{-1} equatorward. The phase velocities are listed in Table 2 and have an error of 30%. The frequency range, amplitude distribution, phase velocity and polarisation characteristics of these events are discussed in the next section.

11.3 SUMMARY AND DISCUSSION

Table 2 lists the date and time of the 14 events examined, and results of the data analysis. All 14 events occurred between 19:23 and 03:13 LT. Their frequencies ranged from 7.8 mHz to 17.6 mHz. In seven of the events, maximum power (or amplitude) occurred at L = 1.71 (ARM). For the other events, maximum amplitudes would have occurred outside the range of our station array.

Phase analysis showed that the waves propagated equatorward, with speed <100 km s^{-1}. For the east-west phase velocity, we only have one station pair, and the results are less conclusive.

We also examined spatial and temporal polarisation characteristics of the waves. Results of five typical events are shown in Figure 7. It is obvious that the polarisation characteristics change between L = 1.44 and L = 1.71. The sense of rotation and the orientation of the main axis reverse with increasing latitude from L = 1.44 to L = 1.71. On the other hand, there is also a temporal effect. At L = 1.44, the orientation of the main axis changes from north-east pre-midnight to north-west post-midnight. At L $\geq$ 1.71, it changes from north-west pre-midnight to north-east post-midnight, and the rotation sense from right hand to left hand. This agrees with previous work at higher latitudes (e.g. Lester et al. 1989).

In our study, the frequency does not change with latitude for individual events, although for different events, the maximum amplitude could be at different latitudes. Figure 8 shows the latitudinal variation of the peak amplitude against Pi2 frequency. The tendency is for maximum amplitudes of lower frequency events to be located at higher latitudes.

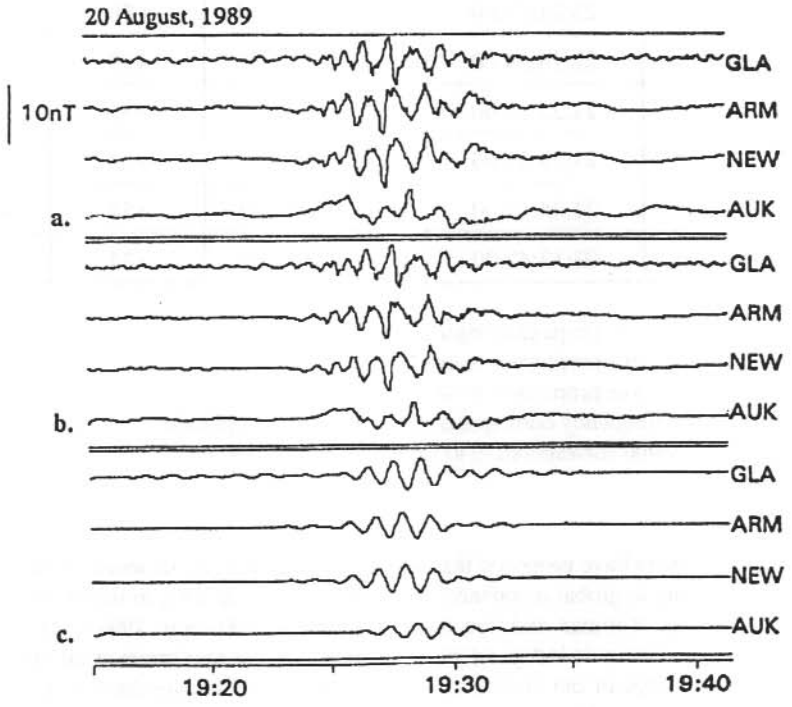

Figure 3. a. Raw data time series
b. Polarised wave time series
c. Narrow band polarised wave time series

Table 2. Summary of results for 14 events.

Event No.	Date day/mth	Local Time (at Newcastle)	f_{max}^{Δ} mHz	$L^{\Delta\Delta}$	Phase Velocity (km s^{-1})	
					NS	EW
1	09/08	23:30:55.00	12	>1.83	+46*	**
2	10/08	00:11:55.00	10	>1.83	+25	
3	10/08	02:37:51.00	12	1.71	+30	
4	10/08	20:49:27.10	9	>1.83	+34	
5	10/08	20:49:27.10	16	1.71	+57	
6	20/08	19:23:23.01	17	1.71	+66	
7	20/08	19:49:19.01	8	>1.83	+56	+140
8	02/09	22:56:51.00	14	1.71	+65	+98
9	02/09	23:21:23.00	18	<1.44	+70	+70
10	11/09	22:18:54.00	8	1.71	+39	-140
11	21/09	21:22:53.00	14	1.71	+55	+123
12	21/09	21:29:21.00	18	1.71	+63	+127
13	28/09	21:24:11.00	10	>2.04	+34	+1764
14	29/09	03:13:47.00	10	>2.04	+34	-1764

* "+" means the wave propagates equatorward
** "+" means the wave propagates to east
"-" means the wave propagates to west
Δ means the frequency corresponding to maximum amplitude
$\Delta\Delta$ means L value corresponding to maximum amplitude

Some previous workers have proposed that low latitude Pi2 pulsations result from the coupling of fast mode waves, due to global resonance of magnetosphere cavities, to transverse standing field line oscillations (e.g. Yeoman and Orr 1989, Sutcliffe and Yumoto 1991). In our results, the observation that frequency is independent of latitude and that maximum amplitude often occurs within the latitude range of our station array supports this. However there is as yet insufficient data to draw a definite conclusion.

For further investigation of the generation and propagation mechanisms of low latitude Pi2 pulsations, we need to obtain further data from an array of stations with a larger spread in latitude and longitude.

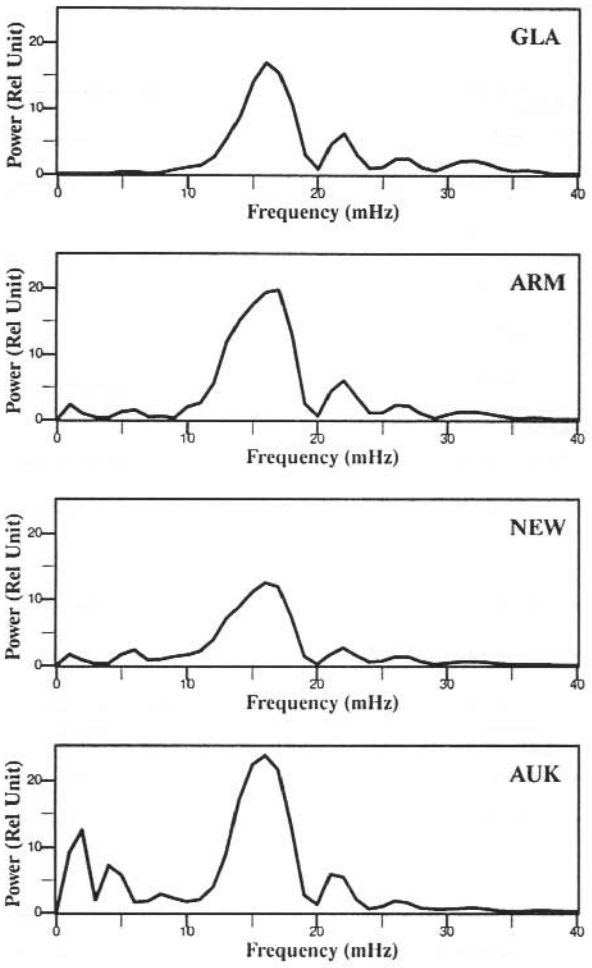

Figure 4. Polarised wave power spectra for GLA, ARM, NEW and AUK.

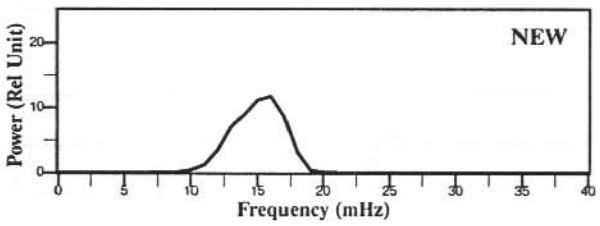

Figure 5. Narrow band polarized wave power spectra for NEW.

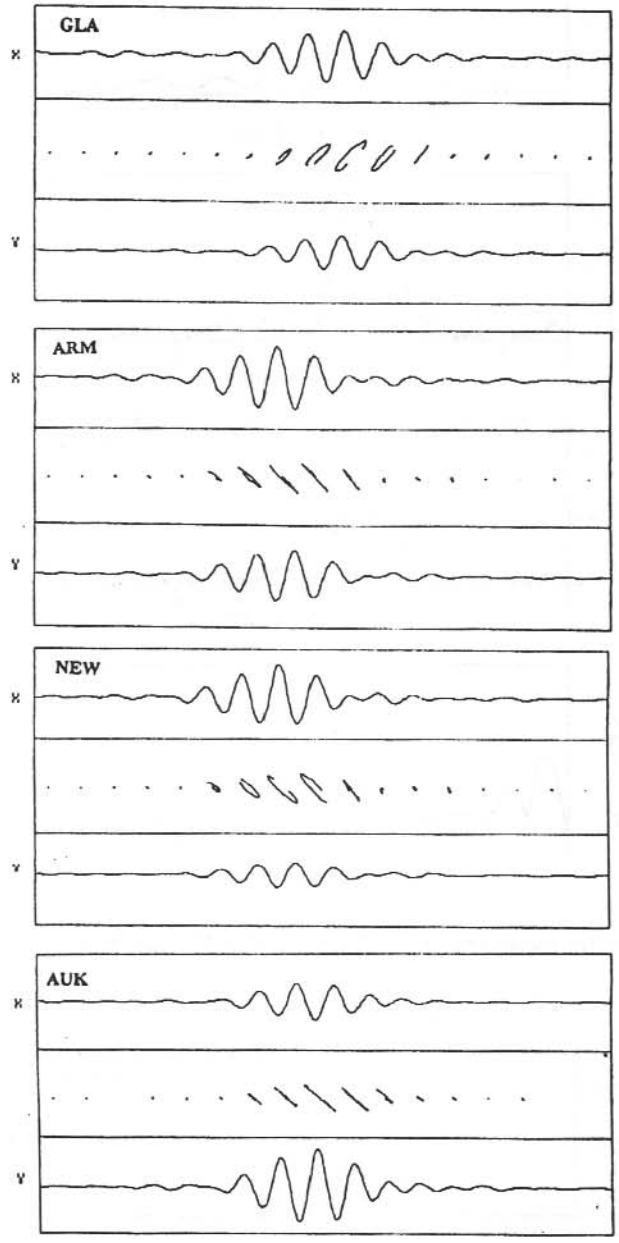

Figure 6. Narrow band polarised wave hodograms for GLA, ARM, NEW and AUK.

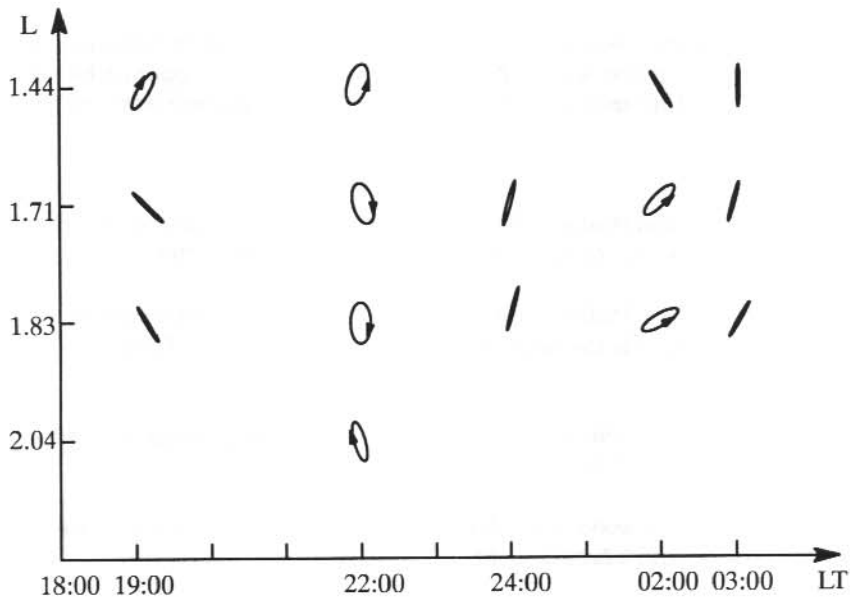

Figure 7. Distribution of polarisation characteristics against local time and latitude.

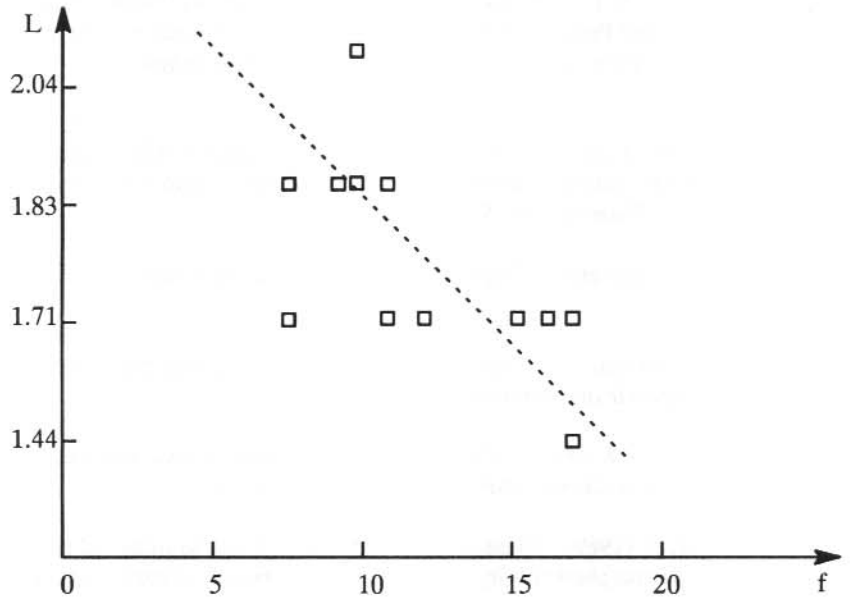

Figure 8. Distribution of L value (corresponding to maximum amplitude) against the Pi2's wave frequency.

11.4 ACKNOWLEDGMENTS

The Macquarie Island data were recorded by members of the Australian Antarctic Division under the direction of Dr G. Burns and Dr R. Morris. This work was supported by the Australian Research Council, the University of Newcastle and the Antarctic Science Advisory Committee.

REFERENCES

Allan, W., White, S.P. *and* Poulter, E.M. (1985). Magnetospheric coupling of hydromagnetic waves – initial results. *Geophysical Research Letters 12*:287 – 290.

Allan, W., White, S.P. *and* Poulter, E.M. (1986). Impulse-excited hydromagnetic cavity and field-line resonances in the magnetosphere. *Planetary and Space Science 34*:371 – 385.

Jacobs, J.A. *and* Sinno, K. (1960). Worldwide characteristics of geomagnetic micropulsations. *Geophysical Journal 3*:333 – 353.

Kivelson, M.G. *and* Southwood, D.J. (1985). Resonant ULF waves: a new interpretation. *Geophysical Research Letters 12*:49 – 52.

Lester, M., Singer, H.J., Smits, D.P. *and* Hughes, W.J. (1989). Pi2 pulsation and the substorm current wedge: low-latitude polarization. *Journal of Geophysical Research 94*:17133 – 17141.

Pashin, A.B., Glassmeier, K.H., Baumjohann, W., Raspopov, O.M., Yahnin, A.G., Opgenoorth, H.J. *and* Pellinen, R.J. (1982). Pi2 magnetic pulsations, auroral break-ups, and the substorm current wedge: A case study. *Journal of Geophysics 51*:223 – 233.

Rostoker, G. *and* Samson, J.C. (1981). Polarization characteristics of Pi2 pulsations and implications for their source mechanisms: Location of source regions with respect to auroral electroject. *Planetary and Space Science 29*:225 – 255.

Samson, J.C. (1982). Pi2 pulsations: High latitude results. *Planetary and Space Science 30*:1239 – 1247.

Stuart, W.F. (1974). A mechanism of selective enhancement of Pi2's by the plasmasphere. *Journal of Atmospheric and Terrestrial Physics 36*:851 – 859.

Sutcliffe, P.R. *and* Yumoto, K. (1991). On the cavity mode nature of low-latitude Pi2 pulsations. *Journal of Geophysical Research 96*:1543 – 1551.

Yeoman, T.K. *and* Orr, D. (1989). Phase and spectral power of mid-latitude Pi2 pulsations: Evidence for a plasmaspheric cavity resonance. *Planetary and Space Science 37*:1367 – 1383.

12. MAGNETIC TIME FOR AUSTRALIA'S ANTARCTIC STATIONS

G.B. Burns and H.M. Beggs

Auroral and Space Physics
Antarctic Division
Kingston Tasmania 7050
Australia

ABSTRACT

Magnetic models and the concept of magnetic time are briefly reviewed.

The Polar Anglo-American Conjugate Experiment (PACE) geomagnetic coordinate system (PGM, epoch 1988, Baker and Wing 1989) is used to investigate the seasonal and diurnal variations in magnetic time at the Australian National Antarctic Research Expeditions (ANARE) stations. The PGM coordinate system is derived from a field-line trace of a full Internal Geomagnetic Reference Field (IGRF) model. The results from the PGM coordinate system are compared to an eccentric dipole (ED) magnetic time model of epoch 1977.25 (Boyd 1983). The comparisons are made between models of different epochs because they are presently used, published models. Magnetic time occurs at a later Universal Time (UT) for the PGM than for the eccentric dipole model, for all the ANARE stations. The average differences are: Casey – 50 minutes, Davis – 26 minutes, Mawson – 14 minutes and Macquarie Island – 2 minutes. If a timing accuracy of greater than these amounts were required for relating events to, for example, magnetic noon or magnetic midnight, then a timing system derived from a full field-line traced model (such as the PGM) must be used. Timing differences between the models for Casey and Davis are possibly significant for studies associated with the location of the magnetospheric cusp. The timing differences between the models result principally from the location of the stations with respect to the south magnetic pole of the different models, not from the approximately ten year difference in model epochs.

An eccentric dipole magnetic time formulation, with the magnetic poles set at the location of the invariant poles (epoch 1977.25, Boyd 1977) and the dipole fixed mid-way between the two poles, gives good agreement with the PGM system. Despite the success of this eccentric dipole formulation, field-line traced, full internal field models (such as the PGM) remain the desirable reference system at all latitudes.

The average annual UT time of magnetic noon and magnetic midnight are given for the four ANARE stations, for the PGM system. Minimum and maximum annual values are also listed. Diurnal variations in the difference between UT and Magnetic Local Time (MLT) for selected days are plotted.

12.1 MAGNETIC MODELS FOR MAGNETIC TIME

A system of magnetic time may be derived from any magnetic model that defines magnetic longitude. MLT for any site is derived from the difference between the magnetic longitude of the site and the magnetic longitude of the sub-solar point, measured westward from the magnetic

longitude of the site. The angular difference is converted to 'hours' by dividing by 15, added to 12 and then expressed in 'modulo 24' to give MLT. Magnetic noon is defined as the time when the sun is above the same magnetic longitude as the site. Magnetic midnight is defined as the time when the sub-solar point is above the magnetic longitude differing by 180° from that of the site.

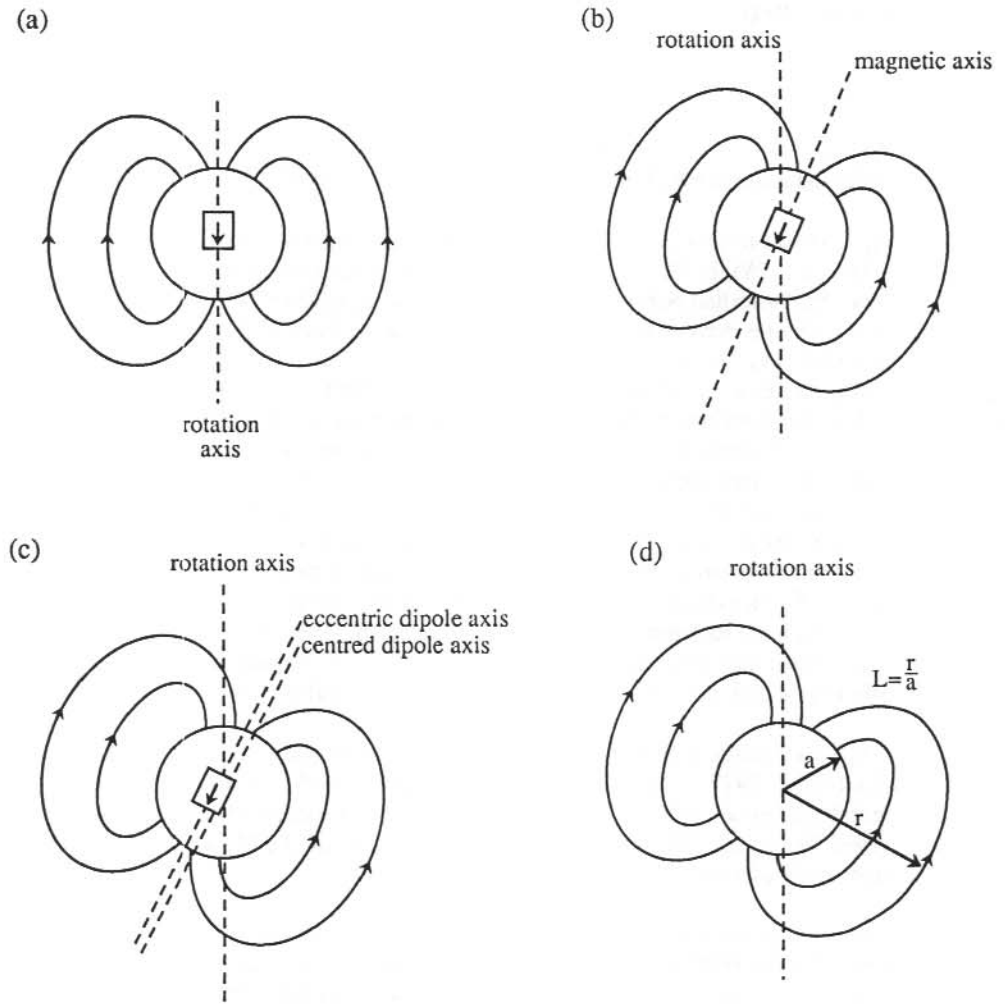

Figure 1. Diagrammatic representations of various magnetic field models.
(a) A dipole model, with the dipole axis aligned with the earth's rotation axis
(b) A centred dipole model
(c) An eccentric dipole model, with the dipole axis parallel to the centred dipole axis
(d) An internal field model, showing the definition of the L parameter

A multitude of magnetic models have been used to represent the earth's magnetic field. The simplest representation of the geomagnetic field is as a magnetic dipole at the earth's centre, aligned along the earth's rotation axis. Figure 1(a) shows a diagrammatical representation of this model. In such a model a magnetic coordinate system equivalent to the geographic system can be defined. The simplicity of this model would not justify a magnetic time system. It is, however, worthy of note that while UT progresses at a uniform rate, the sub-solar longitude at each UT time varies slightly throughout the year. This is principally due to factors associated with the elipticity of the earth's orbit around the sun. The variation is described in the so-called 'equation of time'.

A more accurate representation of the geomagnetic field is given by a dipole, located at the earth's centre, but not constrained to lie along the earth's rotation axis. This is the centred dipole approximation. Figure 1(b) represents this model. A magnetic coordinate system for a centred dipole model can be readily derived from the geographic coordinate system by a trigonometric rotation (Fraser-Smith 1987). Magnetic time derived from such a magnetic model contains a diurnal variation with respect to UT because of the different rate at which magnetic longitudes are cut by the sub-solar point and a seasonal variation due to variations in the declination of the sub-solar point.

The next level of sophistication in geomagnetic models is to not constrain the dipole to the earth's centre. This is an eccentric dipole approximation. This model is represented in Figure 1(c). Various eccentric dipole models have been defined. In its most common formulation, the dipole axis of the eccentric dipole is constrained to lie parallel to the axis of the 'best-fit' centred dipole. Although more mathematically complex, a magnetic coordinate system can be analytically derived for an eccentric dipole representation. Fraser-Smith (1987) gives an excellent review of centred dipole and eccentric dipole formulations.

All the models so far discussed can be derived from the lower order terms of a full spherical harmonic representation of the internal magnetic field such as the IGRF (Fraser-Smith 1987). The IGRF and associated Definitive Geomagnetic Reference Field (DGRF) series represent the geomagnetic field as the gradient of a scalar potential, with the scalar potential being defined in terms of a spherical harmonic expansion. The IGRF/DGRF models are defined at five year intervals so as to map the 'secular variations' in the internal magnetic field. There is no simple method of deriving a magnetic coordinate system from a full IGRF/DGRF representation, however models have been derived for particular epochs. One particular technique involves tracing the magnetic field lines to their most distant point from the earth's centre, and defining the dimensionless parameter L as the ratio of this distance to the radius of the earth. The magnetic latitude (Λ) of all points along the field line are then defined by the equation

$$\cos^2\Lambda = 1/L$$

This equation would map to geographic coordinates for a magnetic dipole. Magnetic longitude is generally defined as equally spaced around the magnetic equator, with the zero longitude meridian open to choice but irrelevant to a system of magnetic time. Figure 1(d) attempts to represent an internal field model, and shows the parameters related to the derivation of magnetic latitude.

Although magnetic coordinate and timing systems derived from field-line traces of full internal field models, such as the IGRF/DGRF series, contain no representation of the variable currents of

the magnetosphere and ionosphere, they provide the best reference systems for investigating the variations due to those currents. However, eccentric dipole magnetic field models are often used for the determination of magnetic time because of their relative analytic simplicity. Timing discrepancies between eccentric dipole models and full internal field models can be attributed to the approximations of the eccentric dipole model.

12.2 MAGNETIC TIME AT THE ANARE STATIONS

The Australian Antarctic Division has until recently been using the magnetic invariant coordinate system of Boyd (1977, 1983) derived for epoch 1977.25 as its magnetic coordinate system. It is now more appropriate to adopt the magnetic coordinate system introduced by Baker and Wing (1989) for epoch 1988, the PGM system. The geographic coordinates of the ANARE stations are followed by their magnetic coordinates under the PGM system in the list below. Also given, in brackets at the end of each station list, are the invariant latitudes of the stations for the 1977.25 epoch. A minor difference between the systems is that the 1977.25 epoch coordinates were calculated for a height of 105 km, while we have chosen a height of 120 km for our calculations with the PGM system. A comparison of magnetic longitudes between the systems is irrelevant, as each system has a different method of choosing the prime magnetic meridian. The most significant variation, in the approximately ten years between the model epochs, is for Mawson which is some 0.4 degrees higher in latitude for the PGM system.

Station	Geog. Coords	PGM Mag. Coords.	Boyd (1977)
Casey	66.28°S, 110.5°E	80.39°S, 156.1°E	(80.64°S)
Davis	68.58°S, 78.0°E	74.61°S, 102.3°E	(74.48°S)
Mawson	67.60°S, 62.9°E	70.52°S, 92.1°E	(70.11°S)
Macquarie Island	54.50°S, 159.0°E	64.34°S, 246.9°E	(64.46°S)

Despite having available the full internal field invariant model of Boyd (1977), the Australian Antarctic Division has generally used an eccentric dipole system for determining magnetic time. The eccentric dipole model (epoch 1977.25) was derived from the invariant coordinate system by producing a least-squares fit to the invariant coordinates between latitudes 40° and 75° by the method of successive approximations (Boyd 1983). The eccentric dipole co-ordinates were calculated as described by Cole (1963).

Figure 2 shows the seasonal variation of magnetic noon for the four ANARE stations using the PGM model. Figure 3 shows the seasonal variation of magnetic midnight for the four ANARE stations. Figure 4 shows the variation in magnetic noon and magnetic midnight for the 1988 epoch PGM coordinate system and for the 1977.25 epoch eccentric dipole model, for Casey.

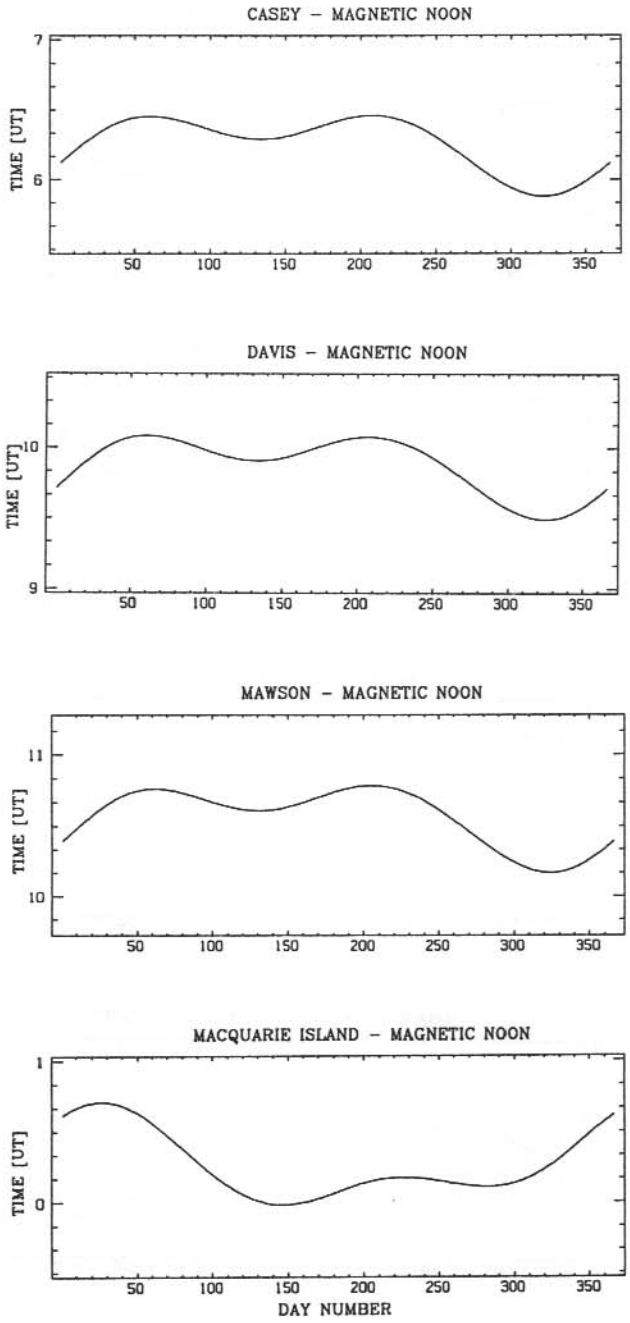

Figure 2. The seasonal variation of magnetic noon for the four ANARE stations, as per the PGM coordinate system.

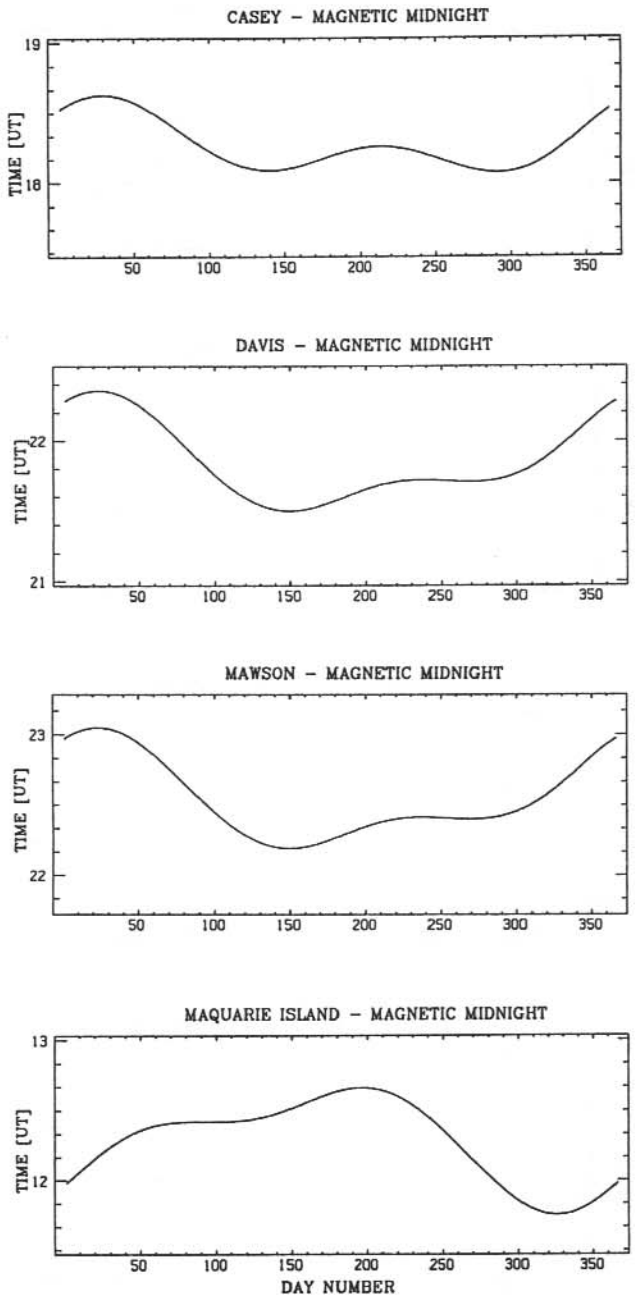

Figure 3. The seasonal variation of magnetic midnight for the four ANARE stations, as per the PGM coordinate system.

The tables below list the annual average UT times for magnetic noon and magnetic midnight for the four ANARE stations, the minimum and maximum values, and the annual range in minutes, for the PGM system. Also shown in the tables are the average annual values of magnetic noon and magnetic midnight for the 1977.25 epoch eccentric dipole (ED) model.

Magnetic noon

STATION	PGM ann. ave.	PGM minimum	PGM maximum	PGM range	ED ann. ave.
Casey	0615 UT	0553 UT	0627 UT	34 mins	(0526 UT)
Davis	0952 UT	0929 UT	1005 UT	35 mins	(0926 UT)
Mawson	1034 UT	1010 UT	1047 UT	37 mins	(1019 UT)
Macquarie Island	0016 UT	2359 UT	0042 UT	43 mins	(0014 UT)

Magnetic midnight

STATION	PGM ann. ave.	PGM minimum	PGM maximum	PGM range	ED ann. ave.
Casey	1816 UT	1804 UT	1837 UT	33 mins	(1726 UT)
Davis	2151 UT	2129 UT	2221 UT	52 mins	(2125 UT)
Mawson	2232 UT	2211 UT	2302 UT	51 mins	(2218 UT)
Macquarie Island	1217 UT	1145 UT	1240 UT	55 mins	(1215 UT)

In all cases the magnetic times occur at a later time for the PGM system than for the eccentric dipole model. The average temporal displacements between the models for the ANARE stations (calculated as the average of the difference between the annual magnetic noon and magnetic midnight values) are Casey – 50 minutes, Davis – 26 minutes, Mawson – 14 minutes and Macquarie Island – 2 minutes. If a timing accuracy of greater than these amounts were required for relating event occurrences to, for example, magnetic noon or magnetic midnight, then a timing system derived from a full field-line traced model (such as the PGM) must be used. The

differences at Casey and Davis are possibly significant for studies associated with the location of the cusp region.

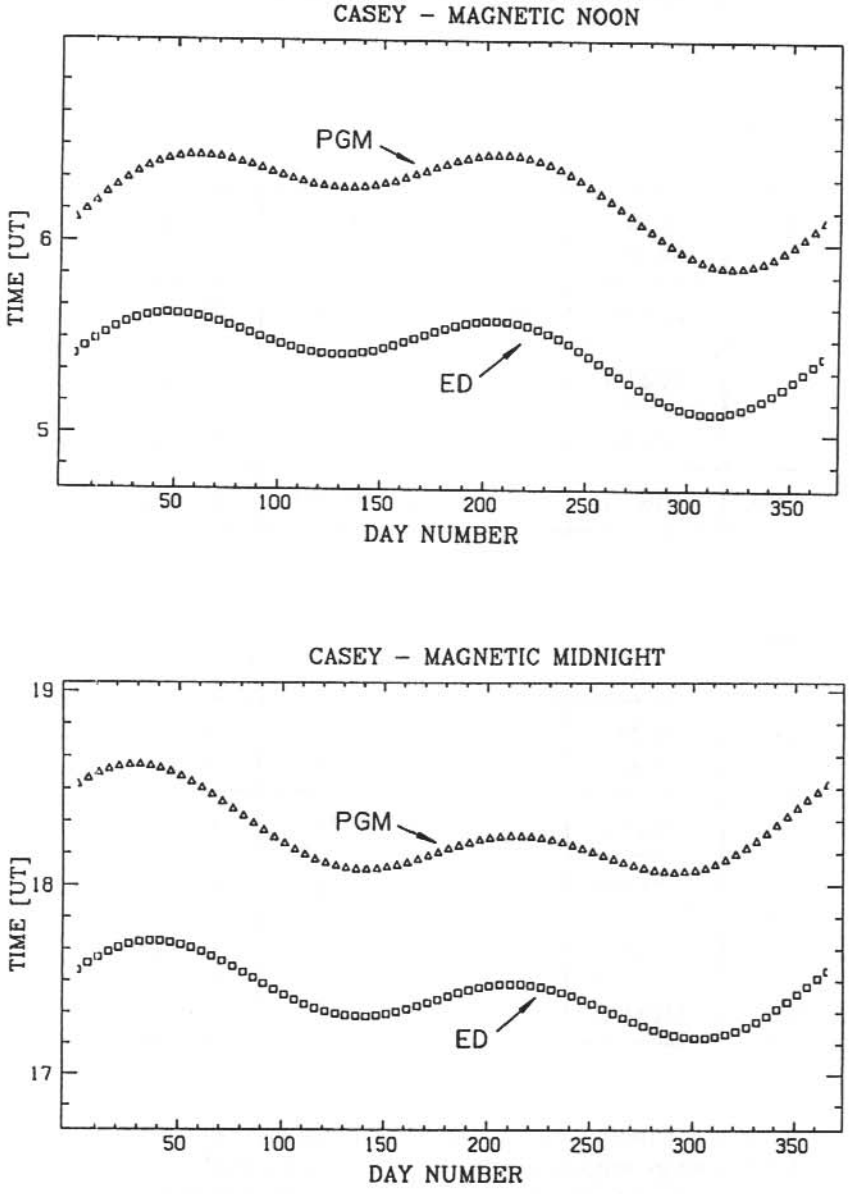

Figure 4. A comparison of the PGM (epoch 1988, field-line traced, triangles) and eccentric dipole (epoch 1977.25, squares) determinations of magnetic noon and magnetic midnight for Casey.

Figure 5 shows the locations of the south magnetic pole of the PGM system (74.19°S, 128.3°E), the southern ED pole in 1977.25 (74.7°S, 119°E) and some Antarctic stations. The reason for the large discrepancy between the two magnetic models for Casey is due to its location, which is close to the great circle which passes through the mid-point of the line joining the respective magnetic poles and which is perpendicular to the line joining the magnetic poles (Figure 5). For a site with Casey's magnetic latitude, such alignment is near optimal for maximising the discrepancy between the models. It should be noted that this does not mean that Casey has been poorly located. Casey is in fact a very valuable site for the study of cusp and polar cap phenomena. It is simply necessary to ensure that a field-line traced, full internal field model is used for ordering events recorded at Casey if a magnetic timing accuracy of better than 50 minutes is required. The sense and the relative magnitudes of the differences between the models for the other Antarctic ANARE stations are also determined principally by their location with respect to the magnetic poles of the models.

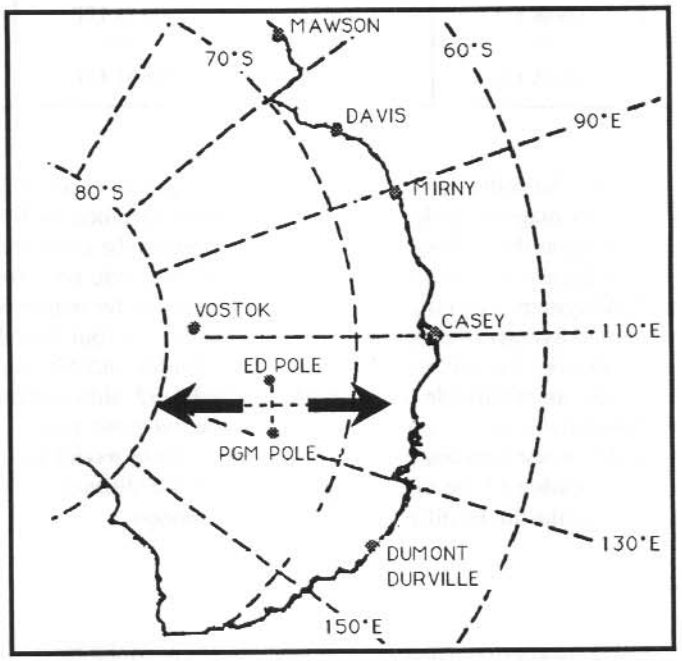

Figure 5. The locations of the south magnetic pole of the PGM system (74.19°S, 128.3°E), the southern eccentric dipole pole in 1977.25 (74.7°S, 119°E) and Casey.

Figure 6 shows the diurnal range in the difference between Magnetic Local Time (MLT) and Universal Time (UT) for the equinoxes and solstices, for the PGM (epoch 1988) and the ED (epoch 1977.25) models, for Casey. The diurnal range in the 'MLT-UT' value is the same for all sites, for each model. Similarly, the difference in its average value from day to day is the same for all sites, for each model. This is because the variation in the difference 'MLT – UT' depends only

on the magnetic longitude of the sub-solar point. The average value and the range of the 'MLT–UT' values for each of the days plotted in Figure 6, for the PGM model, are listed in the table below.

Casey – diurnal variation in magnetic time (MLT – UT)

Date	Average	Minimum	Maximum	Range
21/3/88	0534 UT	0526 UT	0540 UT	14 mins
21/6/88	0539 UT	0507 UT	0603 UT	56 mins
21/9/88	0548 UT	0540 UT	0555 UT	15 mins
21/12/88	0545 UT	0522 UT	0607 UT	45 mins

Although rarely used, the Australian Antarctic Division developed an eccentric dipole magnetic time model that has as its magnetic poles the invariant poles determined by Boyd (1977). The location of the dipole is set as the mid-point between the line joining the north and south magnetic poles. Figure 7 shows the annual variation of the UT time of magnetic noon for Casey, for this model and for the PGM system. Also shown is a similar comparison for magnetic midnight. The differences in the annual averages between the two models for the four ANARE stations are: Casey – 3.3 minutes, Davis – 2.0 minutes, Mawson – 0.5 minutes and Macquarie Island – 2.8 minutes. The differences are negligible, even for Macquarie Island, although the approximation will in general be less reliable away from the vicinity of the magnetic poles. That this model removes most of the difference between the original eccentric dipole model and the PGM model, indicates that it is the location of the magnetic poles and not the differences in epoch that are principally responsible for the timing differences between the models.

12.3 DISCUSSION

Eccentric dipole models are approximations to full representations of the earth's internal magnetic field, such as the IGRF/DGRF models. By reference to the ANARE stations, significant discrepancies between eccentric dipole magnetic time and magnetic time derived from a field-line traced model are shown for high magnetic latitudes. The difficulty with adopting appropriate magnetic models for high latitude studies has in the past been due to the amount of computation required to derive a model. Further difficulties arise because new models are needed as the secular variation in the geomagnetic field renders earlier models obsolete, and because a range of methods have been used for determining the models. Although the eccentric dipole model derived from the location of the 'invariant' magnetic poles gave good correspondence to a full internal field model, the computing power now generally available means that such approximations should not be necessary. It is highly desirable that magnetic coordinate systems be derived for each of

the epochs of the IGRF/DGRF series, and that these reach the levels of acceptance and usage of the magnetic models themselves.

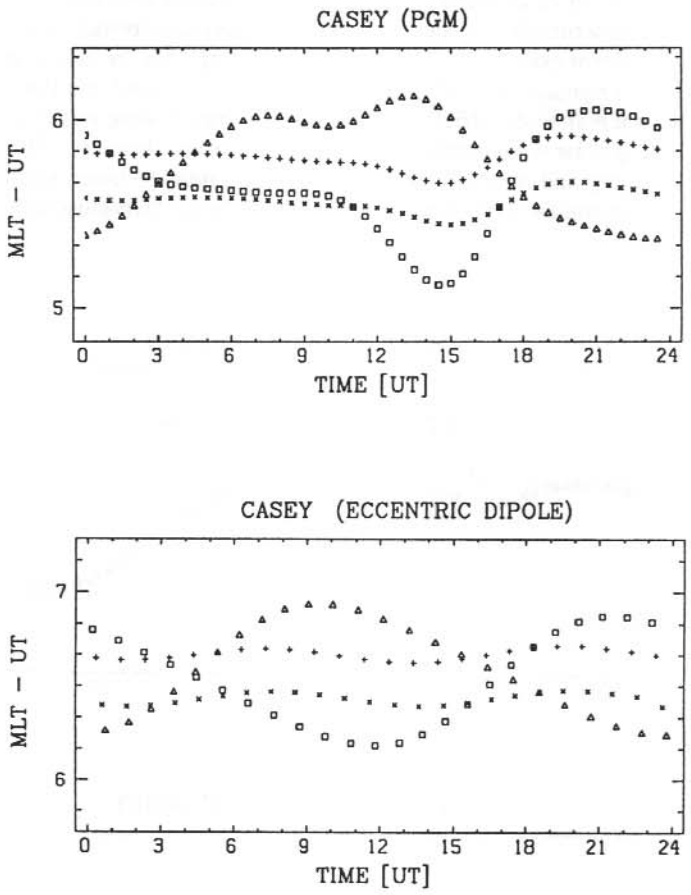

Figure 6. The diurnal range in the difference between Magnetic Local Time (MLT) and Universal Time (UT) for the equinoxes and solstices, for the PGM (epoch 1988) and eccentric dipole (epoch 1977.25) models, for Casey.
crosses – 21/3/88 *squares – 21/6/88*
pluses – 21/9/88 *triangles – 21/12/88*

The diurnal and annual variations in magnetic time for the ANARE stations have been calculated using the PGM (epoch 1988) coordinate system. As was indicated by Baker and Wing (1989), these variations do not include any effects due to the ionospheric and magnetospheric current systems. The full internal field model coordinate systems do, however, remain the best coordinate system presently available for ordering magnetospheric events. External magnetic field

models, which attempt to model the external current systems, can effectively account for the general variations due to the diurnal and seasonal variations in the angle of the earth's magnetic field with respect to the solar wind. They may also model, but only in a broad manner, the variations due to the level of disturbance in the magnetosphere (see Burns et al. 1991, for a general discussion of external field models and for some specific information with respect to the ANARE stations). Present external field models do not incorporate the effects of interplanetary magnetic field (IMF) orientations on the interaction of the solar wind and the earth's magnetic field. They also cannot map with sufficient time resolution the response of the magnetosphere to changes due to varying solar wind parameters or substorm onsets. Because of this, external field models are still evolving and magnetic coordinate systems derived from field-line traced, full internal field models remain the best reference system for ordering magnetospheric events.

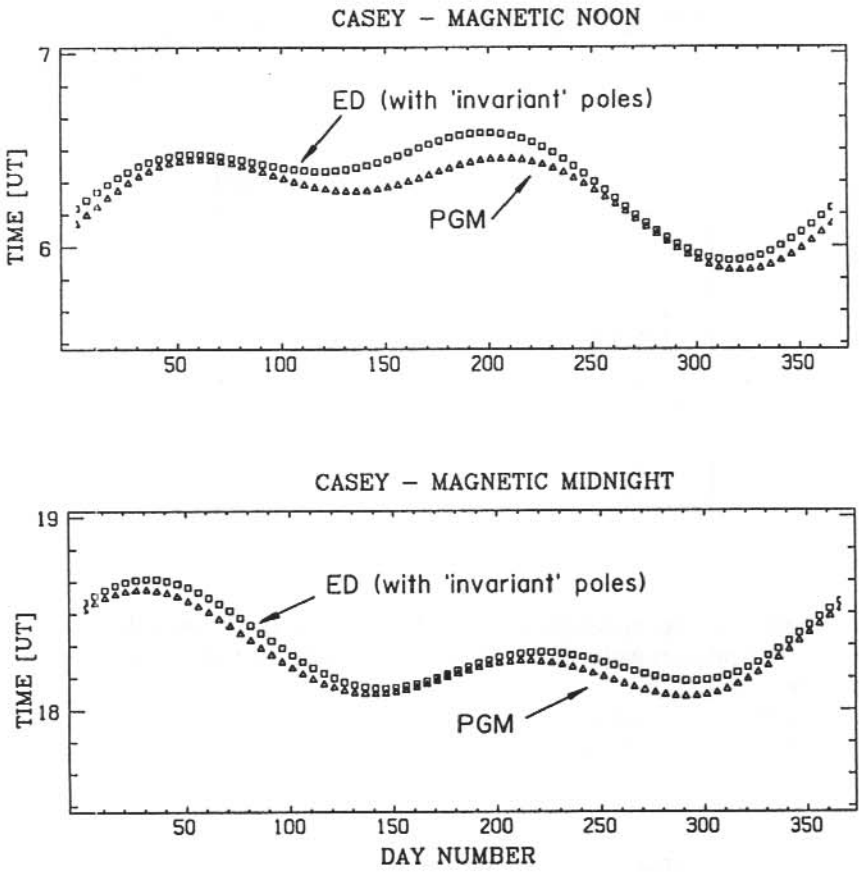

Figure 7. The annual variation of the UT of magnetic noon for Casey, for the ED model based on the 'invariant' poles and for the PGM system. Also shown is a similar comparison for magnetic midnight (triangles – PGM: squares – ED model based on 'invariant' poles).

12.4 ACKNOWLEDGMENTS

We are grateful to those involved in deriving the PGM coordinate system and in making it freely available. One of us (Burns) appreciates Mark Conde's AGRO (plotting routine), and thanks Mick Hesse for explaining it to him. Danny Ratcliffe helped prepare the diagrams for this paper.

REFERENCES

Baker, K.B. *and* Wing, S. (1989). A new magnetic coordinate system for conjugate studies at high latitudes. *Journal of Geophysical Research 94*:9139–9143.

Boyd, J.S. (1977). Invariant geomagnetic coordinates for epoch 1977.25. *Planetary Space Science 25*:411–414.

Boyd, J.S. (1983). Invariant geomagnetic coordinates for epoch 1977.25. *ANARE Research Notes Number 19*.

Burns, G.B., McEwen, D.J., Steele, D. *and* Hearn, D. (1991). Optical auroral conjugacy: history and potential. In: Burns, G.B. (Ed.). *ANARE Research Notes Number 80*. Pp. 283–300.

Cole, K.D. (1963). Eccentric dipole coordinates. *Australian Journal of Physics 16*:423–429.

Fraser-Smith, A.C. (1987). Centred and eccentric geomagnetic dipoles and their poles, 1600–1985. *Reviews of Geophysics 25*:1–16.

13. ANALYSIS OF HIGH-RESOLUTION MESOSPHERIC SODIUM TWILIGHT SPECTRAL EMISSION PROFILES

P.A. Greet[1,2] and F. Jacka[2]

[1] Auroral and Space Physics
Antarctic Division
Kingston Tasmania 7050
Australia

[2] Department of Physics and Mathematical Physics
University of Adelaide
Adelaide SA 5000
Australia

ABSTRACT

High-resolution Fabry-Perot spectrometers have been used for observations of mesospheric sodium spectral emissions excited by resonant scattering of sunlight. These observations are used to estimate winds and temperatures in the emission region. To extract wind estimates from the Doppler shift of sky emissions hollow-cathode lamps have been used to define the rest wavelength of the emission. Careful analysis of both lamp and sky spectra show the presence of self-absorption. The nature of the absorption is different for lamp and sky profiles, in the former case absorption occurs after emission, and in the later absorption occurs in the incident radiation prior to emission. There is a further complication in the latter case viz. the Doppler shift of the absorption is determined by the wind component in the direction of the sun while the Doppler shift of the emission is determined by the wind component in the direction of viewing.

The effects of these absorption processes on wind and temperature estimates is discussed.

13.1 INTRODUCTION

Neutral sodium atoms form a thin layer in the mesosphere; it peaks near 90 km and is approximately 12 km full-width at half-maximum. The spectral doublet emission from this layer at λ588.995/ 589.592 nm is frequently used for photometric studies of the atmosphere. Resonant scattering by sunlight excites ~1 – 5 kR during the day and at twilight. A photo-chemical source excites ~30 – 100 R at all times (Chamberlain 1961).

The D2, λ588.995 nm, line of the doublet is twice as intense at the D1, λ589.592 nm, line. Earth's magnetic field produces anomalous Zeeman splitting of the lines resulting in hyperfine structure. The D2 line has 2 groups (designated *a* and *b*) of 3 hyperfine components and the D1 line has 2 groups of 2 hyperfine components. In the D2 line the two groups of components are separated by 1.975 pm and in the D1 line, 2.127 pm. Each group is 0.2 pm wide (very small compared to the Doppler width).

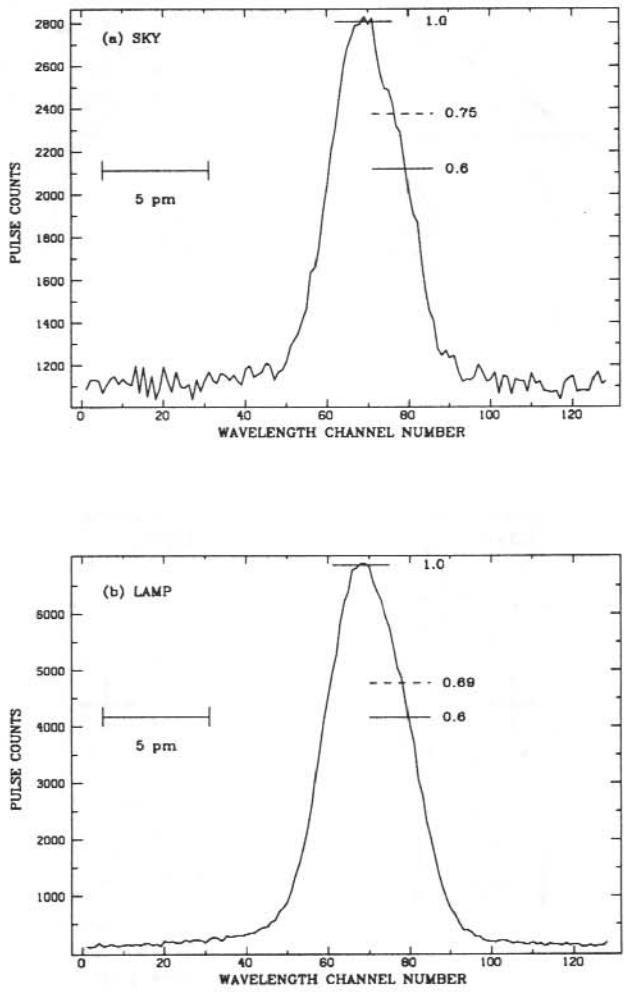

Figure 1. Sodium D2 spectral line profiles as recorded by the high-resolution, single-etalon FPS at Mawson, Antarctica. (a) is a typical sky profile obtained in 3.23 mins, observing at a zenith angle of 60°, azimuth 0°, with the sun at a zenith angle of 96°. (b) is a hollow-cathode lamp profile obtained in 1.07 mins. In both profiles the solid lines indicate the theoretical intensity of the a and b groups of hyperfine components and the dashed line indicates the intensity of the b group from a four parameter, two-Gaussian curve fit. In both the lamp and sky spectra the hyperfine intensity ratio [b]/[a] is larger than expected. The wavelength scale is indicated by the 5 pm bar.

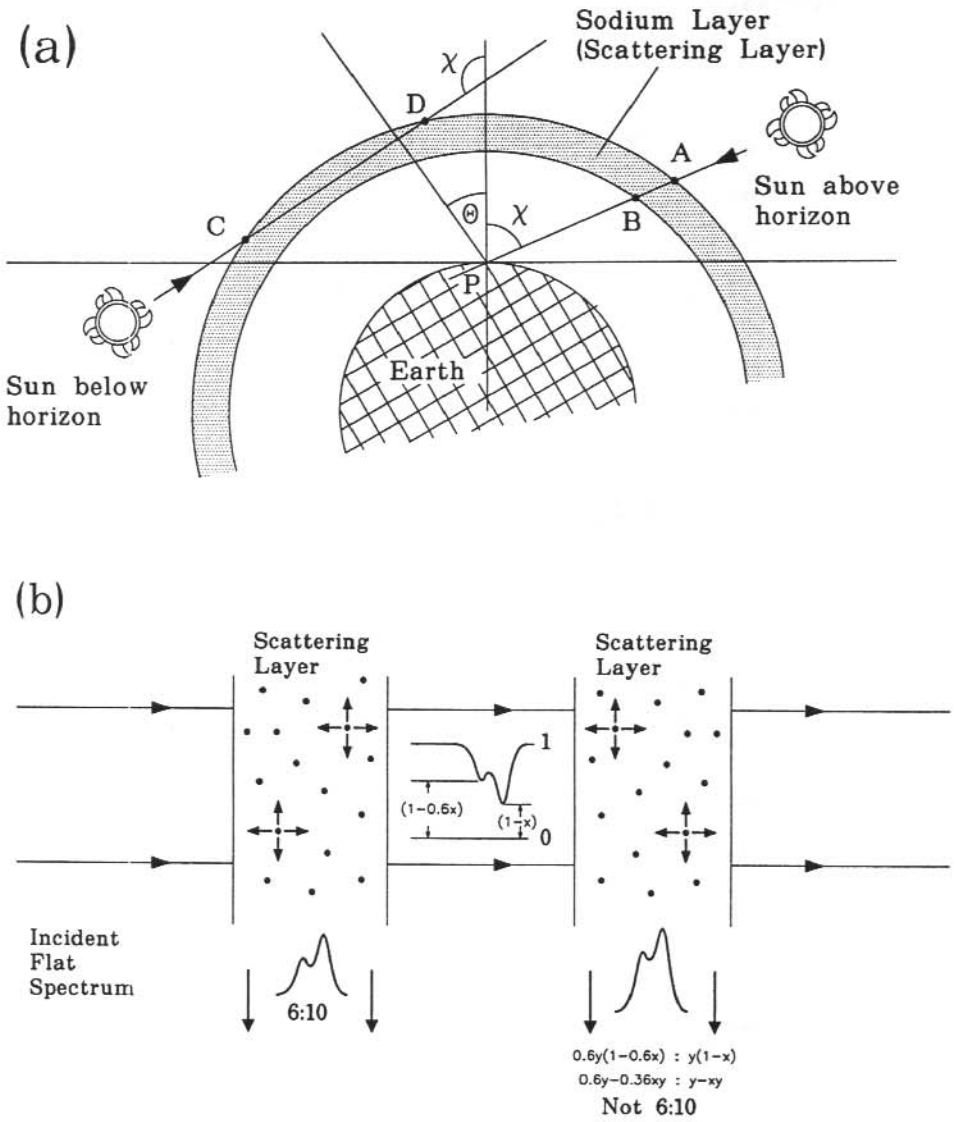

Figure 2. (a) Path length within the sodium layer is given by A-B for the sun above the horizon, and C-D for the sun below the horizon. For a layer 12 km thick and the sun on the horizon the path length is about 300 km (not to scale.) (b) Schematic representation of the twilight sodium emission. For long light paths through the sodium layer the path may be considered in two parts. Although the incident light has a flat spectrum, on its passage through the first part of the layer photons at sodium wavelengths are resonantly scattered and the transmitted light has spectral structure. The intensity of light incident on the second part of the scattering layer varies at wavelengths of the a and b components, hence an observer below sees a resonantly scattered emission which has [b]/[a] >0.6.

Figure 1(a) shows typical sky, and 1(b) hollow-cathode lamp, spectral profiles recorded with the single high-resolution etalon of the Fabry-Perot spectrometer (FPS) system at Mawson during 1990. The instrument is described by Jacka (1984). The sky profile was obtained at twilight by summing 30 scans of 128 channels, dwelling 50 ms per channel. The theoretical heights of the *a* and *b* groups of components are shown by solid lines. The dashed line indicates the height of the *b* group from a four parameter fit of two Gaussian curves. Two intensities, one peak position, and one temperature were fitted and the theoretical separation of the lines was assumed. The hyperfine intensity ratios obtained [*b*]/[*a*] were 0.75 for the sky and 0.69 for the lamp, well above the theoretical ratio of 0.60. The temperature of the lamp is about 500 K and atmospheric models predict mesospheric temperatures at 90 km of about 200 K in mid-winter.

The hyperfine intensity ratio is considerably higher than would be predicted by a simple emission mechanism. Self-absorption is the most likely cause of this and can explain both the lamp and the sky observations in the following way.

Considering the lamp first: Absorption and scattering by gas within the lamp, cooler than the gas in the emission region, occurs after emission. The resulting spectrum is non-Gaussian.

The situation at twilight is more complex: Figure 2(a) shows the oblique path through the sodium layer at twilight. To a first approximation this extended twilight path can be considered as a path through two layers as shown in Figure 2(b). Assuming the incident light has a flat spectrum in the region of interest, after the first scattering the [*b*]/[*a*] emission ratio from the layer would be 6:10. The light passing through the layer would show an absorption feature with the same hyperfine intensity ratio. The transmitted light is then incident on the part of the atmosphere under observation. This spectrum is not flat in the region of interest; there is more light at the shorter wavelengths to excite the *b* component hence the observed line profile does not have the 6:10 hyperfine intensity ratio. Although the amount of light exciting the *a* and *b* groups of hyperfine components is different each still has, to a first approximation, a Gaussian distribution reflecting the motion of the atoms involved in the scattering.

13.3 CONCLUSIONS

Self-absorption is present and measurable in twilight sky and hollow-cathode lamp spectral profiles. In lamp profiles absorption occurs after emission resulting in non-Gaussian profiles. In sky profiles absorption occurs prior to emission resulting in Gaussian profiles with hyperfine intensity ratios varying from the theoretical value of 0.6.

Preliminary simulations suggest that if the velocity of atoms where absorption occurs is significantly different from that where emission occurs then this may produce an apparent shift in the spectral profile. The magnitude of this effect will depend on the amount of absorption occurring in the first path through the layer and the variation in the wind velocities. Twilight sky profiles are obtained at times when solar zenith angles vary from 93 – 100° corresponding to path lengths within the sodium layer of ~120 – 70 km. Thus the amount of absorption will decrease through twilight. Analysis of dual etalon sun profiles obtained just prior to sunset suggests that the amount of absorption occuring on the first path through the layer would be less than ~10% of total sky brightness. However the first pass occurs at increasing distances, up to ~2000 km, from the region of observation thus the probability of wind variations would increase. Work is continuing on simulation of these absorption processes.

We are in the process of developing a computing routine which will fit a function describing self-absorption in the profiles, F(1 – F) where F is the sum of two Gaussian curves. This will account for the non-Gaussian nature of hollow-cathode lamp profiles. Combined with 4 parameter fitting to the sky profiles, this may enable wind and temperature estimates to be obtained from twilight FPS sodium spectra.

13.4 ACKNOWLEDGMENTS

The observations on which this work has been based were made at Mawson, Antarctica as part of the Australian National Antarctic Research Expeditions and was partly funded by the Antarctic Science Advisory Committee grants scheme. We would like to thank Damian Murphy and John French for helpful discussions; Damian also for more detailed lamp measurements at Mawson; and John Cox for preparation of schematic diagrams.

REFERENCES

Chamberlain, J.W. (1961). *Physics of the Aurora and Airglow*. Academic Press, London.

Jacka, F. (1984). Application of Fabry-Perot spectrometers for measurement of upper atmosphere temperature and winds. *Middle Atmosphere Handbook for MAP 13*:19 – 40.

14. $O(^1S)$ EXCITATION AND EFFECTIVE LIFETIMES

A.R. Klekociuk and G.B. Burns

Auroral and Space Physics
Antarctic Division
Kingston Tasmania 7050
Australia

ABSTRACT

Intensity time-series with a 0.05 s time resolution were obtained for the 428 nm N_2^+ (1NG) band and 558 nm $O(^1S)$ line emissions during intervals of rapidly fluctuating auroral intensities at Macquarie Island during 1988. Similar measurements have been used by previous workers to infer the effective lifetimes of the $O(^1S)$ state and the existence of, and percentage contribution from, an indirect excitation process. Using 'constructed data' and an impulse function analysis technique (Burns and Reid 1984), we introduce a method of analysis that shows that variations in the energy of the precipitating auroral electrons during the intensity fluctuations may be mis-interpreted as an indirect excitation process of low percentage contribution. Subsequent to our analysis of the data presented here, we became aware of 'pulse pile-up' contaminations of our raw data files. We have not corrected for this in the examples presented. However, our analysis shows that noise on the intensity time-series by itself, or in combination with the energy fluctuations, may result in a significant over-estimation of the contribution of an indirect excitation process. Measurement of the $O(^1S)$ effective lifetime is accurate to within 0.05 s.

The method we introduce allows determination of an upper limit for the mis-interpretation as an indirect process of non-linearities known to exist between the 428 nm N_2^+ (1NG) band and 558 nm $O(^1S)$ line emissions. These non-linearities have been ignored in previous investigations of $O(^1S)$ excitation processes.

14.1 INTRODUCTION

The processes by which the $O(^1S)$ state, the upper state of the dominant auroral emission, is excited remains a subject of debate. A comparison of the time-varying N_2^+ (1NG) band intensities, which are directly excited by electron impact on nitrogen molecules, with the $O(^1S - ^1D)$ 'auroral green line' intensity has been used in investigations of the excitation processes of the $O(^1S)$ state (Parkinson 1971, Henriksen 1973, Burns and Reid 1984, Paulson et al. 1990). A major assumption of these analyses is that the time-varying N_2^+ (1NG) band intensity and the $O(^1S - ^1D)$ intensity are linearly related.

The impulse analysis technique is one method that has been used to extract information from N_2^+ (1NG) band intensity and $O(^1S - ^1D)$ line intensity time-series. The impulse analysis technique estimates the 558 nm signal that would result from an impulse in the ionisation function, which is assumed to be measured by the 428 nm emissions (Burns and Reid 1984).

If the $O(^1S)$ state were excited solely by direct auroral particle impact processes, then the impulse function { g(t) } relating the nitrogen and oxygen emissions would be a single exponential with a time-constant equal to the effective lifetime of the $O(^1S)$ state.

$$g(t) = A\, e^{-t/\tau}, \quad \text{where } \tau \text{ is the effective lifetime of the } O(^1S) \text{ state}$$

If an indirect process were also involved in the excitation of the $O(^1S)$ state (Parkinson 1971, Henriksen 1973, 1974), and the intermediate species is excited directly by particle impact, then the impulse function relating the nitrogen and oxygen emissions is given by the difference of two exponentials (Burns and Reid 1984).

$$g(t) = A'\, e^{-t/\tau} - B'\, e^{-t/\tau'}, \quad \text{where } \tau' \text{ is the effective lifetime of the intermediate state}$$

The relative contributions of the direct and indirect processes to the excitation of the $O(^1S)$ state can be calculated from the terms A', B', τ and τ' (Burns and Reid 1984).

The A', B', τ and τ' parameters can be evaluated in either the time-domain (Henriksen 1973, 1974, Burns and Reid 1984, 1985), or equivalently in the frequency-domain via evaluation of the frequency dependence of the 'cross-spectral phase' of the two auroral emission time series (Brekke and Pettersen 1972, Brekke 1973, Paulson et al. 1990).

The radiative lifetime of the $O(^1S)$ state is of the order of 0.80 s (Nicolaides et al. 1971). Collisional deactivation of the excited $O(^1S)$ atoms at auroral heights yields 'effective lifetimes' slightly lower than the radiative lifetime. In order to measure time delays of this magnitude, very rapid variations in auroral intensities are required. Figures 1 and 2 show examples of rapidly fluctuating N_2^+ (1NG) (0,1) band emissions (with a band-head at 428 nm) and O ($^1S - {}^1D$) line emissions (at 558 nm).

Burns and Reid (1984, 1985) report $O(^1S)$ effective lifetimes of the order of 0.7 s (Paulson et al. 1990 average 0.77 s), effective lifetimes for the species involved in the indirect process of approximately 0.1 s (Paulson et al. 1990 average 0.09 s) and that the indirect process accounts for between 50% and 100% of the excitation of the $O(^1S)$ state (Paulson et al. 1990 report varying contributions from the indirect process; from less than 10% to in excess of 90% in less than 3 minutes in one published example).

Two variations known to be associated with pulsating aurora will result in non-linearity between the O($^1S - {}^1D$) and N_2^+ (1NG) intensities which could be mis-attributed to an indirect process. One is the increase in average energy of the incident electrons from the 'off' state to the 'on' state of pulsating aurora (Johnstone 1978). The other is associated with the equatorial modulation of the source electrons responsible for pulsating aurora (Johnstone 1983). The equatorial modulation of the auroral fluxes means that the higher energy electrons reach the auroral ionosphere first. Both these variations will result in a non-linear relationship between the O($^1S - {}^1D$) and N_2^+ (1NG) intensities as the intensity ratio of these emissions in aurora is weakly energy dependent. The ratio of the O ($^1S - {}^1D$) intensity to the N_2^+ (1NG) intensity decreases as the energy of the incident electrons increases (Steele 1988).

14.2 DATA COLLECTION AND REDUCTION

The optical data were collected at Macquarie Island (54.5°S 159.0°E, geographic coordinates; 64.3°S magnetic latitude) during 1988 with a twin-channel, beam-splitting photometer with interference filters isolating the N_2^+ (1NG) (0,1) band at 428 nm and the O ($^1S - ^1D$) line at 558 nm. The photometer was pointed toward the magnetic zenith and has a one degree field-of-view. Data were collected simultaneously from both channels at a rate of 20 Hz. The data are stored, and generally analysed, in five minute blocks. Five minute data sequences are chosen as a compromise between a long data sequence, desirable to reduce the influence of noise, and a short data sequence, desirable so that the parameters being measured remain constant.

The impulse function relating the O ($^1S - ^1D$) line emission to the N_2^+ (1NG) (0,1) band emission for each five minute data sequence is evaluated by a maximum entropy technique described by Burns and Reid (1984). A twin exponential function is fitted by a non-linear least-squares technique to the first two seconds of the impulse function. The O(^1S) effective lifetime, the lifetime of the species associated with the indirect process, and the percentage of the O(^1S) state excited by the indirect process, are evaluated from the impulse function.

We have recently become aware that our data are effected by 'pulse pile-up' (McEwen, private communication). At higher auroral intensities, the pulse counting techniques we employ progressively underestimate the true intensity. This will affect mainly the O(^1S) intensity and will lead to an estimated 558 nm/428 nm ratio lower than is correct. It will also lead to a greater variation in this ratio between 'pulse on' and 'pulse off' measurements. This is because the higher the intensity, the greater is the under-estimation of the true intensity due to 'pulse pile-up'. As a result of not correcting for this in the analyses that follow, the mis-attribution to a possible indirect excitation process will be over-estimated. The analyses in this paper still represent an upper limit for the influence of noise and variations in the incident energy of the auroral electrons on the determinations of an indirect excitation process for the O(^1S) state from the data presented.

14.3 CONSTRUCTED DATA ANALYSIS

Five minute data sequences from 1520 – 1525 UT, 16 July 1988, and 1510 – 1515 UT, 22 July 1988, are utilised in a 'constructed data' analysis. Figures 1 and 2 show the measured data and the impulse functions derived directly from these data.

It must be emphasised that we do not claim that the τ' or the estimated contribution of the indirect process to the excitation of the O(^1S) state are valid for these events. Our aim is to determine if it is possible to generate results of this nature without resorting to the assumption of an indirect process. In particular, the 16 July data would not be accepted for investigating the indirect process under our present selection criteria. The magnitude of the impulse function point immediately prior to $t = 0$ is an indication that noise on the intensity time-series would affect the evaluation (Burns and Reid 1984). The 16 July data are chosen for this evaluation as they are not untypical of data that we would use for an evaluation of the O(^1S) lifetime, but would reject for investigating any indirect process. The 22 July data would be acceptable for looking for an indirect excitation process despite the fact that light cloud may have affected the measurement of the absolute intensities of the emissions. They are chosen for this analysis because the relatively short O(^1S) effective lifetime may be related to higher incident energies. These data have not

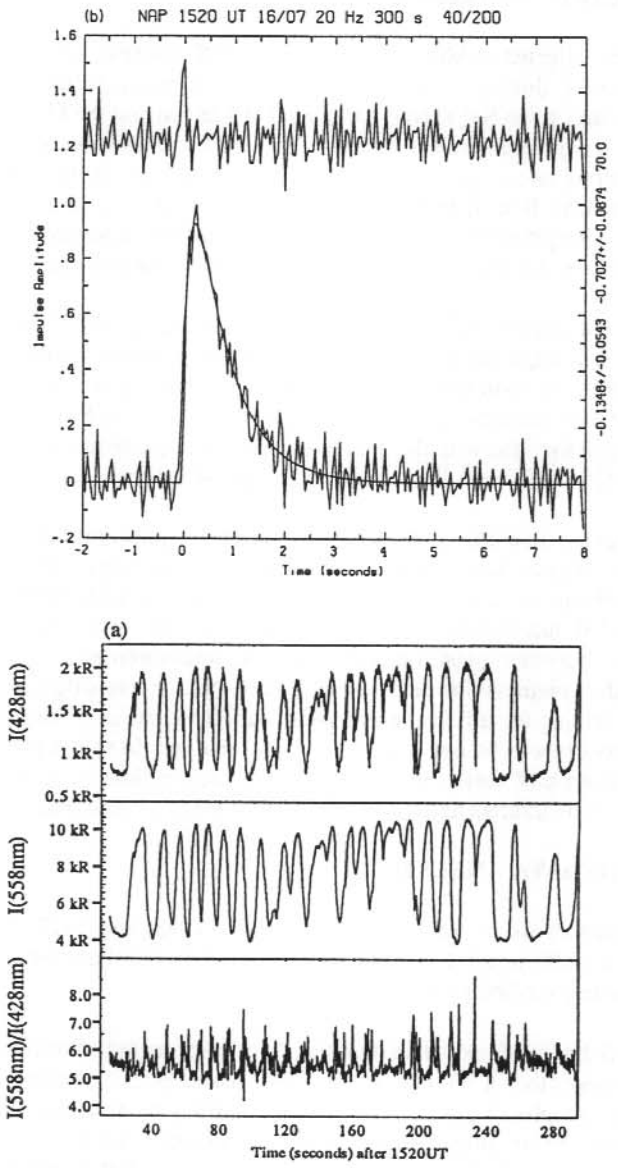

Figure 1. Data from 1520 – 1525 UT, 16 July 1988

(a) Plots of the 428 nm intensity { $I_N(t)$ }, the 558 nm intensity { $I_O(t)$ }, and the ratio $I_O(t+dt)/I_N(t)$.

(b) The impulse function from the data in (a) with the twin-exponential fit plotted over it. Above the impulse function, the residuals to the twin exponential fit are plotted. Along the right-hand edge are τ',τ and the estimated percentage contribution of the indirect excitation process.

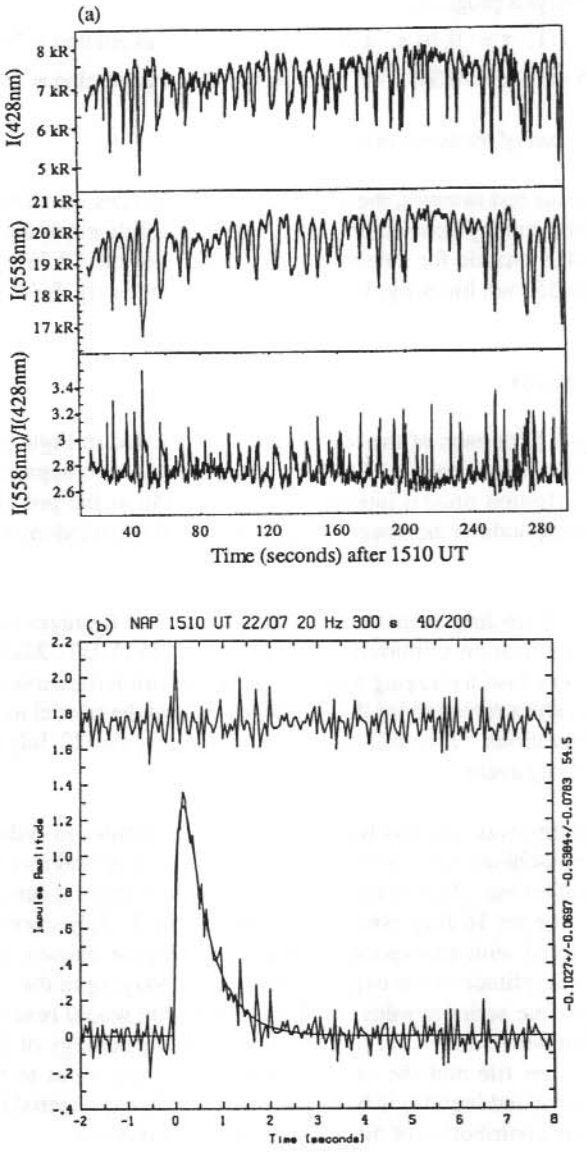

Figure 2. Data from 1510–1515 UT, 22 July 1988

(a) Plots of the 428 nm intensity { $I_N(t)$ }, the 558 nm intensity { $I_O(t)$ }, and the ratio $I_O(t+dt)/I_N(t)$

(b) The impulse function from the data in (a) with the twin-exponential fit plotted over it. Above the impulse function, the residuals to the twin exponential fit are plotted. Along the right-hand edge are τ', τ and the estimated percentage contribution of the indirect excitation process.

been corrected for 'pulse pile-up'. With these caveats, the real data yield the following values when fitted by our analysis program

16/7/88 1520–1525 UT: $\tau = -0.70$ s, $\tau' = -0.13$ s, indirect excitation = 70%

22/7/88 1510–1515 UT: $\tau = -0.54$ s, $\tau' = -0.10$ s, indirect excitation = 55%

14.3.1 *Energy variations of the incident particles*

For each of the 5-minute test samples, the 428 nm and 558 nm files were cross-correlated in order to determine the average delay between the files. For the 16 July event the 558 nm file was best correlated with the 428 nm file for a delay, dt, of 0.65 s. For the 22 July event, dt was 0.45 s. The ratio, R(t), of the 558 nm intensity, $I_O(t)$, to the 428 nm intensity, $I_N(t)$, was calculated across each of the test files as

$$R(t) = I_O(t+dt)/I_N(t)$$

The ratio series { R(t) } for each of the test samples is included in Figures 1 and 2. There is a significant amount of noise on each { R(t) } series. It is, however, apparent that R(t) reaches a higher level at the pulsation optical intensity minimum than at the pulsation optical intensity maximum. This corresponds to the lower average energy of the incident auroral particles at the pulsation minima.

For the 1520–1525 UT, 16 July event the 558 nm/428 nm ratio averages around 5.3 at pulsation maximum and 5.8 at pulsation minimum. For the 1510–1515 UT, 22nd July event the 558 nm/428 nm ratio is very low, averaging around 2.75 at pulsation maximum and 3.0 at pulsation minimum. The low values recorded for the 22 July event may be related to light cloud present at the time of the observations. It is still likely, however, that the 22 July event is much more energetic than the 16 July event.

The following procedure was adopted for each of the test samples in order to determine if the variation in the 558 nm/428 nm ratio could be mis-interpreted as an indirect excitation process. A fixed $O(^1S)$ effective lifetime, close to that measured from the original data, was chosen for each of the events; 0.70 s for the 16 July event and 0.55 s for the 22 July event. The measured 428 nm files were convolved with an exponential function with the chosen, fixed $O(^1S)$ effective lifetime, but with the amplitude of the exponential function varying in the manner of the { R(t) } series. The resultant time series mimics a 558 nm signal that would result from a solely direct excitation process, but which allows for the variation in average energy of the incident electrons. The constructed 558 nm file and the original 428 nm file are input to the impulse analysis program, and the determined impulse is best-fitted with a twin exponential function to determine τ, τ' and the percentage contribution of the indirect excitation process.

Figure 3 shows the results for the two test data sets.

16/7/88 1520–1525 UT: $\tau = -0.65$ s, $\tau' = -0.14$ s, indirect excitation = 7%

22/7/88 1510–1515 UT: $\tau = -0.51$ s, $\tau' = -0.09$ s, indirect excitation = 13%

The results show that the variation in the energy of the incident auroral electrons can be mis-interpreted as a low percentage contribution from an indirect process. Effects of this magnitude would not invalidate the general conclusions made for the real data. In the case of the 16 of

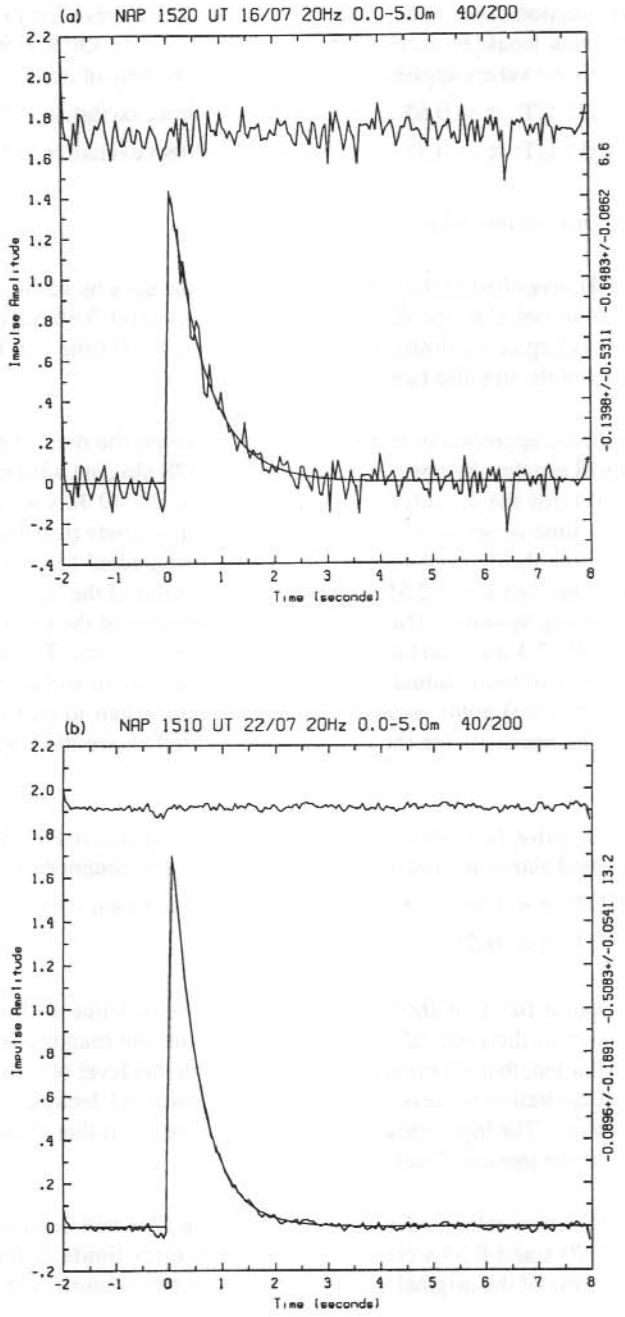

Figure 3. Impulse functions of constructed data investigating the effect of variations in the average energy of the incident electrons.

16 of July event, the non-linearity that has been applied has affected the magnitude of the initial point of the impulse function (Burns and Reid 1984). This would have led to us rejecting these data. The 22 of July event would be acceptable. The reduction in the $O(^1S)$ effective lifetimes by the order of 0.05 s from the values applied for both events, is worthy of note.

(a) 16/7/88 1520 – 1525 UT: $\tau = -0.65$ s, $\tau' = -0.14$ s, indirect excitation = 7%

(b) 22/7/88 1510 – 1515 UT: $\tau = -0.51$ s, $\tau' = -0.09$ s, indirect excitation = 13%

14.3.2 *The effect of noise on the data*

Burns and Reid (1984) investigated the effects of noise on the data by adding various levels of 'amplitude limited white noise' to the 428 nm file. The important features of the 'noisy data' response were the rounding of the impulse function near the t = 0 time and the existence of a significant acausal part of the impulse function.

We adopt a more realistic approach to test the effect of noise on the data. For each of the test events we construct 558 nm data by convolving the original 428 nm data with exponential decays with lifetimes of 0.70 s for the 16 July event and 0.55 s for the 22 July event. We then add noise, in the form of a time series with a zero mean and an amplitude distribution described by Gaussian statistics, to both the original 428 nm file and the constructed 558 nm file. The relative level of noise added to the 428 nm and 558 nm files is in the ratio of the noise expected for each of the two photon counting systems. This means that the variance of the noise added to the 428 nm time series is typically 2.4 times that added to the 558 nm time series. The absolute amount of noise added was set so that the residuals of the twin-exponential fit to the measured impulse function, away from the t = 0 point, were approximately equivalent to that obtained from the observational data. The residuals for the real data are plotted above the impulse functions in Figures 1 and 2.

Figure 4 shows the impulse functions and exponential fits obtained for the test data. The residuals are again plotted above the determined impulses. The fits obtained are

16/7/88 1520 – 1525 UT: $\tau = -0.69$ s, $\tau' = -0.08$ s, indirect excitation = 66%

22/7/88 1510 – 1515 UT: $\tau = -0.57$ s

The 16 July event impulse function shows a significant non-zero value at the t = -0.05 s point. This is most easily seen in the residuals. It is apparent, from the magnitude of the estimated indirect process contribution, that we must exclude events with this level of noise from any search for a possible indirect excitation process. Only a single exponential decay could be fitted to the constructed 22 July event. The high signal levels for this event mean that noise has not caused a measurable rounding of the impulse function.

The $O(^1S)$ effective lifetimes estimated from the 'noisy' data files still accurately represent the applied impulses of 0.70 s and 0.55 s respectively. Within error limits of the order of 0.05 s, which is the sampling time of the original data, the $O(^1S)$ effective lifetimes can still be recovered from these files.

14.3.3 *The combined effect of the energy variation and noise*

The combined effects of the energy variation in the incident electrons and noise on the data files were investigated in the following manner for each of the test events. The ratio variations were included in the convolution of the exponential decay with the real 428 nm file in the manner described in Section 14.3.1. Noise was then added to the real 428 nm file and the constructed 558 nm file in the manner described in Section 14.3.2. The constructed files, containing both noise to the appropriate level of the real data and the influence of the energy variation in the incident electrons, were then input to the analysis routine.

The results for both test events are shown in Figure 5.

16/7/88 1520–1525 UT: τ = -0.66 s, τ' = -0.05 s, indirect excitation = 85%

22/7/88 1510–1515 UT: τ = -0.51 s, τ' = -0.08 s, indirect excitation = 15%

The results for the 16 July event confirm that the original data for this event should not be used for any investigation of the indirect process. The value of the t = -0.05 s point in the impulse calculated from the observational data (Figure 1) provides the means for selecting against this type of event. A similar acausal response is seen in the constructed data for this event (Figure 5).

The 22 July event does not have a significant acausal signal at t = -0.05 s in either the real (Figure 2) or constructed (Figure 5) impulse. The constructed data for this event does however have a significant non-zero value for the initial impulse point (t = -2.0 s). This is an indication that there is significant non-linearity between the constructed data files. This probably means that our method of constructing the ratio files generates more non-linearity between the files than exists in reality. The testing process provides a means of determining the maximum effect of the influences investigated.

The experimental data for the 22 July event (Figure 2) indicate 55% O(^{1}S) excitation via an indirect process. The constructed data (Figure 5) indicate that, at most, 15% of this can be accounted for by noise in the data and energy variations in the incident particles.

14.4 CONCLUSIONS

We have introduced a method of analysis of ground based photometric time series that can determine an upper limit for the mis-interpreting of noise and non-linearities between the 428 nm N_2^+ (1NG) band and 558 nm O(^{1}S) line emissions as the signal of an indirect excitation process for the O(^{1}S) state. The method we have outlined for determining the effect of noise and variations in the average energy of the incident electrons will be applied to all future evaluations of data from which we seek to identify the signal of an indirect excitation process, once corrections for 'pulse pile-up' have been made.

The examples given show that we can still recover reasonable estimates of the O(^{1}S) effective lifetime from these data. In both cases the combined result of the energy variations and the level of noise on the data reduces the effective lifetime by 0.04 s.

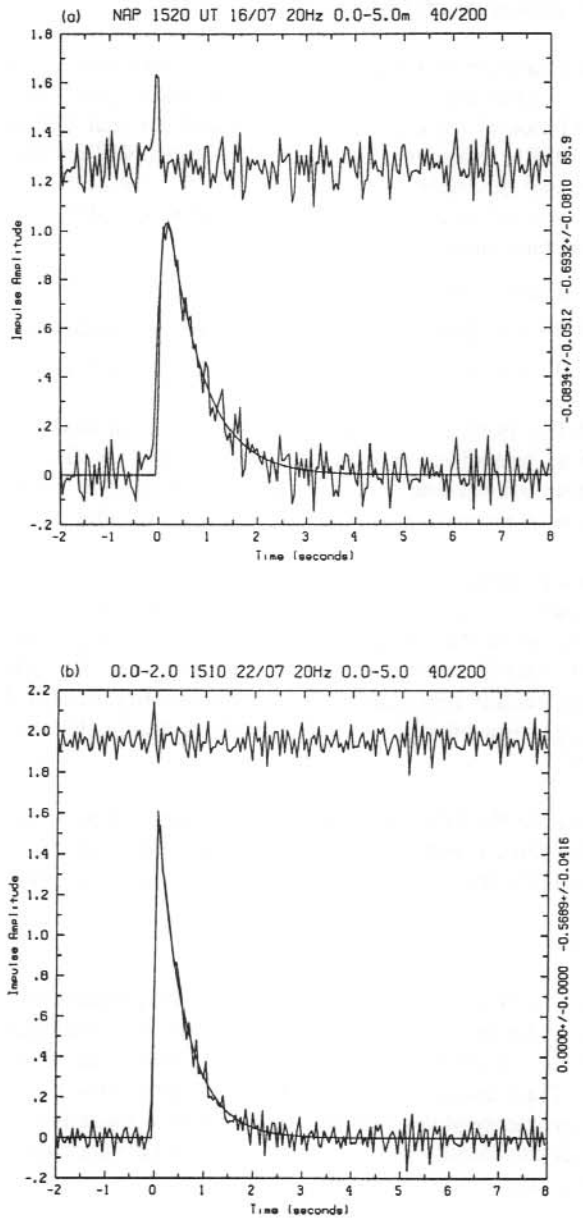

Figure 4. Impulse functions of constructed data investigating the effect of noise.
(a) 16/7/88 1520–1525 UT: τ = -0.69 s, τ' = -0.08, s indirect excitation = 66%
(b) 22/7/88 1510–1515 UT: τ = -0.57 s

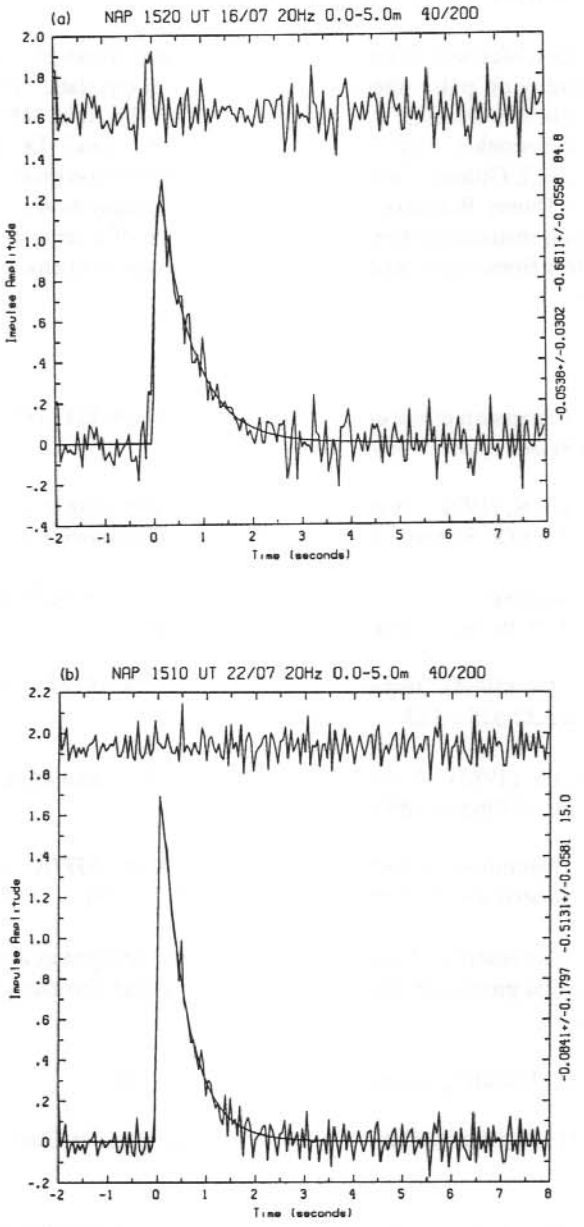

Figure 5. Impulse functions of constructed data investigating the combined effect of variations in the average energy of the incident electrons and of noise.

(a) 16/7/88 1520 – 1525 UT: τ = -0.66 s, τ' = -0.05 s, indirect excitation = 85%

(b) 22/7/88 1510 – 1515 UT: τ = -0.51 s, τ' = -0.08 s, indirect excitation = 15%

14.5 ACKNOWLEDGMENTS

We are grateful to Dr Don McEwen of the Institute of Space and Atmospheric Studies who made us aware of the possibility of 'pulse pile-up' contamination in our data. The impulse function analysis program used in this research was developed by Dr John Reid. Mr Jon Reeve assisted with the installation and operation of the equipment at Macquarie Island. Dr Dick Gattinger of the National Research Council, Ottawa, Canada assisted with information on the band profile of the 428 nm emission. Mr Danny Ratcliffe assisted in the final preparation of the diagrams. The manufacture of research instrumentation and the maintenance of a remote observatory facility requires concerted effort from many people. To those who assisted in ensuring the collection of these data, our thanks.

REFERENCES

Brekke, A. (1973). A discussion of the energy transfer from $N_2(A_3\Sigma_u^+)$ to $O(^1S)$ in pulsating aurora. *Planetary and Space Science 21*:698 – 702.

Brekke, A. *and* Pettersen, K. (1972). A possible method for estimating any indirect process in the production of the $O(^1S)$ atoms in aurora. *Planetary and Space Science 20*:1569 – 1576.

Burns, G.B. (1983). *Pulsating aurora: photometer, riometer and micropulsation coil observations*. Ph.D. thesis, LaTrobe University, Australia.

Burns, G.B. *and* Reid, J.S. (1984). Impulse response analysis of 5577Å emissions. *Planetary and Space Science 32*:515 – 523.

Burns, G.B. *and* Reid, J.S. (1985). A comparison of methods for calculating $O(^1S)$ lifetimes. *Australian Journal of Physics 38*:647 – 656.

Henriksen, K. (1973). Photometric investigation of the 4278Å and 5577Å emissions in aurora. *Journal of Atmospheric and Terrestrial Physics 35*:1341 – 1350.

Henriksen, K. (1974). The reaction of nitric oxide with atomic nitrogen as a possible excitation source of the auroral green line. *Journal of Atmospheric and Terrestrial Physics 36*:1437 – 1439.

Johnstone, A.D. (1978). Pulsating aurora. *Nature 274*:119 – 126.

Johnstone, A.D. (1983). The mechanism of pulsating aurora. *Annales Geophysicae 1*:397 – 410.

Nicolaides, C., Sinanoglu, O. *and* Westhaus, P. (1971). Theory of atomic structure in electron correlation. IV. Method of forbidden transmission probabilities, with results for [OI], [OII], [NI], [NII] and [CI]. *Physical Review A 14*:1400 – 1404.

Parkinson, T.D. (1971). A phase and amplitude study of auroral pulsations. *Planetary and Space Science 19*:251 – 262.

Paulson, K.V., Chang H. *and* Shepherd, G.G. (1990). The evaluation of time-varying parameters pertinent to the excitation of $O(^1S)$ in aurora. *Planetary and Space Science 38*:161 – 172.

Steele, D.P. (1988). *Coordinated ground-satellite auroral studies*. MSc. thesis, University of Saskatchewan, Canada.

15. INFERRING AURORAL ENERGIES

M. Craven[1], G.B. Burns[1], A.R. Klekociuk[1] and D.J. McEwen[2]

[1] Auroral and Space Physics
Antarctic Division
Kingston Tasmania 7050
Australia

[2] Institute of Space and Atmospheric Studies
University of Saskatchewan
Saskatoon Saskatchewan S7N0W0
Canada

ABSTRACT

A program has been undertaken at Mawson during the 1991 austral winter to infer auroral electron energies from ground-based optical and cosmic noise absorption (CNA) measurements. Energies inferred from these measurements will be compared with those recorded in situ by DMSP satellites crossing the observed region of interest. By comparing absorption levels with optical intensities it is hoped to extend to high energies the range for which this ground-based method can be used. Using the satellite particle data it is intended to establish some limits on the variability inherent in using instruments with wide fields-of-view for inferring auroral energies.

Zenith oriented, wide-angle (60° field-of-view) photometers were used to measure the absolute intensity of the O(^{1}D) 630.0 nm, O(^{1}S) 557.7 nm, and N_2^+(1NG) 427.8 nm auroral emissions at a rate of 10 Hz. Standard riometer data, with a frequency near 30 MHz, were simultaneously collected at a rate of 0.1 Hz. An Auroral Video System (AVS) was used to monitor the auroral forms to attempt first-order corrections for comparison of the absorption and optical measurements from the associated geometry of the particular events.

Limitations in the design of the photometers introduced a variety of difficulties in the determination of absolute intensities. These have been largely overcome for the three major auroral emissions listed. Unfortunately they precluded an attempt to measure the Hβ 486.1 nm emission, which was desired to estimate the degree of proton precipitation contribution to the auroral intensities. Some estimate of the proton contribution may be obtained from the satellite particle measurements.

15.1 INTRODUCTION

Precipitating electrons with a variety of energies are deposited at different altitudes in the upper atmosphere, where, with due account taken of the relative collision cross-sections, they excite atoms and molecules in proportion to the abundance of each species at that altitude. The spectroscopic emission features in the aurora will then be largely characterised by the altitude dependence of atmospheric chemistry. The quantitative nature of the relationship between auroral electron fluxes and the induced radiation response of the atmosphere has been examined both

from experimental (Brekke and Omholt 1968, Eather and Mende 1972, Eather et al. 1976, Duncan and McEwen 1979, Steele and McEwen 1990), and computational modelling (Rees and Luckey 1974) aspects. McEwen et al. (1981) have investigated the 557.7 nm to 427.8 nm ratio during pulsating auroral events (making due allowance for the 0.7 s time delay in the oxygen emission), with a view to examining the increase in energy from pulsation minimum to pulsation maximum.

Comparison between the results predicted from the models and direct experimental evidence, have shown that the ionised molecular nitrogen vibrational band emission at 427.8 nm is well understood (Rees et al. 1976), whilst the auroral atomic oxygen line emissions at 557.7 nm and 630.0 nm are not in total agreement with theory (Sharp et al. 1983). With the 557.7 nm emission, some of the discrepancy arises from the fact that indirect mechanisms are partly responsible for the excitation of the $O(^1S)$ state. It is useful therefore, to examine the intensity ratios I[630.0]/I[427.8], and I[557.7]/I[427.8], observed in auroral events, infer the characteristic electron energy of the flux using the Rees and Luckey (1974) model computations, and compare these with precipitating particle spectra as measured above the same aurora using satellite instrumentation. Empirical relationships can then possibly be established between the characteristic energy (E_0) of the precipitating auroral electrons, and its dependence on the calculated auroral intensity ratios. Steele and McEwen (1990), using ground-based observations from Rabbit Lake, Saskatchewan, and HILAT satellite passes, arrived at the following empirical relationships:

$$I[630.0]/I[427.8] \cong 3.3\,(E_0)^{-2.1}$$

$$I[557.7]/I[427.8] \cong 5.6\,(E_0)^{-0.3}$$

for auroral events with characteristic energies on the order of a few keV. Collisional quenching of the metastable species $O(^1S)$ before a radiative transition takes place (lifetime approximately 0.7 s), is believed to be responsible, at least in part, for the variation in the I[557.7]/I[427.8] ratio. An altitude dependence is thus introduced due to variation in the abundance of the quenching species with height. This is even more evident in the $O(^1D)$ 630.0 nm emission which, having a radiative lifetime on the order of 110 s, is thus heavily quenched at lower altitudes, with the emission intensity falling off rapidly as auroral electron energy increases.

That a correlation exists between auroral luminosity and the absorption of radio waves by the ionosphere, has been known for many years (Heppner et al. 1952). An altitude dependence of the radio wave absorption is immediately apparent, since any electrons created by the auroral precipitation will be more efficient as absorbers as the neutral density of the atmosphere increases. As the characteristic energy (E_0) of precipitating particles increases, the rate of ionisation escalates, and the altitude of peak production decreases, compounding the effect on the absorption of radio waves propagating through the atmosphere. The absorption (A) of cosmic radio waves of frequency ω is given by :

$$A \propto \int (\omega^2 + \nu^2)^{-1}\, N\nu\, dh$$

where N is the electron density, ν the electron collision frequency, and h the height (Eather and Jacka 1966). For an operating frequency around 30 MHz, $\omega \gg \nu$ for altitudes above about 80 km.

Studies have been made of the relationship between absorption measurements of cosmic radio noise and the intensity of auroral emissions for a variety of auroral forms (Holt and Omholt 1962, Eather and Jacka 1966, Berkey 1968). From considerations of the ionospheric rate equation, Omholt (1971) has shown that, to a first order, there exists a linear relationship between the square root of the auroral optical intensity (as measured by either the green atomic oxygen line at 557.7 nm, or the ionised molecular nitrogen vibrational band at 427.8 nm) and the cosmic radio noise absorption level:

$$\sqrt{(I(t))} = cA(t)$$

where the constant of proportionality c, decreases as the characteristic energy of the event increases.

15.2 INSTRUMENTATION

The photometric instrumentation applied to this project at Mawson in 1991 consisted of two twin-channel, 30° half-angle, zenith-oriented photometers. One system employed FACT-50 cooling systems to maintain the photomultiplier detectors at a temperature around -25°C, thus reducing dark noise to minimal counts (630.0 nm, and the incompletely calibrated 486.1 nm channel). Data were sampled at 10 Hz and stored digitally via locally generic software in consecutive files of 10 minutes duration for subsequent analysis.

Cosmic noise absorption levels were routinely sampled by a standard riometer with a central operating frequency of around 30.4 MHz. Digital files of 10 second interval readings were obtained via a separate software package.

An AVS obtained filtered (558.0 nm) images of the night sky on an intensive basis during a series of two-week auroral campaigns centred on each new moon period throughout the austral winter. Video sequences were retained for all nights where meteorological conditions did not preclude optical observation. Frame-grabbing circuitry obtained images integrated over 900 ms, with a 100 ms lag between frames during these intensive campaigns, whilst routine operation involved a 1 s integration period and a 9 s delay.

Auroral particle data are available on request (from the World Data Centre at Boulder, Colorado) for the DMSP satellite series, to be used in determining the integrity of the conclusions drawn from the ground-based analysis. Unfortunately the orbital parameters only became available after the event, and so it remained a matter of operator judgement on retention of possible events (out of a myriad of occurrences over a wide array of variability) for future analysis, rather than carefully planned preparation for intensive observation of predicted satellite passage times. This disadvantage was largely offset by the provision of ample data storage space for collection of a huge volume of files for later analysis.

15.3 DIFFICULTIES

A SIROSPEC monochromator was provided to allow the characteristics of each of the filters (central wavelength, full-width-half-maximum, transmission percentage at each wavelength) to be determined, and calibrated light sources (Hans Lauche 1987, private communication) were available to ascertain the absolute transmission within each optical channel. The results using the

calibrated light sources yielded highly ambiguous, and in fact, quite anomalous figures. Initial interpretations centred on this being due to low-level out-of-band filter leakage, and a series of long wavelength scans were carried out in order to ascertain the magnitude and wavelength dependencies. A second order passband was found to exist around 856.4 nm for the 427.8 nm filter, and a small out-of-band leakage seemed to be present as well. No second order passbands were detected for the 557.7 nm, or 630.0 nm channels (their wavelength doublings falling outside the spectral responses of the photomultiplier tubes), nor any leakage (above detector limits).

During this procedure it was alarmingly discovered that the real root of the problem lay in the fact that light was somehow managing to leak around the filters within their housings. This became apparent when the presence of two 427.8 nm filters in the one housing failed to remove, or even significantly diminish, the supposed out-of-band leakage problem. The series of stops and baffles along the optical path of the photometer systems did not totally preclude the possibility of minute leakage around the filters themselves. Whilst this problem would not manifest itself significantly in routine observational mode (due to the restriction of auroral emissions to a limited number of discrete lines and bands), it provided a healthy contribution to the count rates attained from the broadband emission of the calibration sources. Appropriate measures were taken to lightproof the filter housings, and subsequent calibrations yielded count ratios in much better agreement with those predicted for the three modes of operation of the calibrated light sources.

Despite the wide-angle nature of the optics it was easy to arrange the calibrated light source housing to fill the field-of-view of the photometers. However, intensity variations across the plane of the source result in minor systematic changes in the total count rates obtained, dependent on the separation between the source and the entrance aperture of the photometers. One of the sources was also highly voltage dependent, and as they had all been calibrated in Canada, a Variac was required to supply values around 110 V. These effects contribute relatively small errors to the final scale values.

Minor problems still appeared to exist with removal of the second-order passband contribution to the 427.8 nm scale value. This situation could be happily circumvented in future operations of this instrument by the adoption of a photomultiplier with a different spectral response in its photocathode material, one which reduced to a negligible quantum efficiency for 800.0 nm and greater wavelengths, whilst maintaining similar levels to the current system around the 427.8 nm regime. The 427.8 nm second-order passband has, however, since been attributed to a second-order effect of the grating within the monochromator itself, an artefact of the calibration system, and thus not a genuine transmission fault of the filter. No account need therefore be taken in determining the scale value for this channel, nor is any alternative photomultiplier tube required.

The photomultiplier tube characteristics do however contribute to one further refinement of the scale value figures. The transit time (the interval between the production of the light pulse and the peak of the output pulse), and its spread, are critical factors in the usage of photomultiplier tubes to detect the time occurrence of events. Pulse pile-up occurs when the output pulses from successive photons cannot be adequately resolved. For a nominal transit time spread of 40 ns, the maximum count rates allowed before pulse pile-up considerations are expected to become significant, are around 25 MHz. In practice this is an ideal upper limit due to the statistical nature of photon arrival, and some compensation is necessary for count rates as low as 200 kHz. The standard light sources used to calibrate the photometer channels were of sufficient intensity that

these considerations need to be taken into account. Relevant contributions for each channel will be determined and applied to the calculations for the production of the ultimate scale factors to be used in all subsequent analysis. The aurorae involved in this analysis were expected to sometimes reach intensities up to 100 kR. The count rates at these levels would also require some adjustment.

Mawson is subject to high levels of radio frequency interference (RFI). Standard riometers are particularly sensitive in this regard. Much effort has gone into reducing the interference levels suffered by the riometer. Nevertheless, RFI has intermittently crept into the records and rendered some of the data for 1991 unusable.

The AVS was a first generation system, operated for the first time on an ANARE station, at Mawson in 1991. It was subject to occasional failure of the mechanical shutter components, but this resulted in minimal loss of recording time. The AVS represents a most significant advance over the original black-and-white all-sky camera film recording systems, both operationally, and in the quality and versatility of the subsequent records.

Due to the nature of the offset between local magnetic midnight at Mawson, and geographic midnight, the passage times of the sun-aligned orbits of the DMSP satellite series are unfavourably distributed to capture energetic auroral events which have a morphology of maximum occurrence around and beyond local magnetic midnight.

It is not envisaged to make any attempt in this analysis to compensate for the effects of atmospheric scattering and absorption, which will quite obviously vary across the observing channels due to the wavelength dependent nature of these phenomena. Interestingly enough, there may be a significant contribution to be considered here, in the light of the extremely high levels of volcanicity apparent in 1991, the principal source being from Mount Pinatubo in the Phillipines. Dust in the high atmosphere certainly reached the high latitudes of Mawson station by August – September, as evidenced by significant differences in sunsets, post-sunset glows, and strong haze effects in the general direction of the sun throughout the duration of the day. Rayleigh scattering has its greatest effects at the shorter wavelengths (427.8 nm channel), whilst absorption dominates at longer wavelengths (630.0 nm channel). No account of such atmospheric extinction is attempted here, since the data presented are for events recorded prior to about mid-July, when it is believed very little of the volcanic ash had found its way into the local stratosphere.

15.4 OBSERVATIONS

Seven two-week intensive observational campaigns were conducted throughout the 1991 austral winter. There were 37 nights of cloud-free conditions, of which some 29 nights were classified as being aurorally active. Sixteen nights were lost due to blizzard conditions, and 2 further nights data were precluded due to instrumentation failure of one kind or another.

Initial analysis centred on identifying coincidences of events with satellite passage, auroral activity and riometer absorption. All clear sky campaign nights data were examined for such coincidences whenever the maximum elevation of the satellite orbit exceeded 30° above the local horizon. Some 21 events were chosen as promising candidates in the first instance, from which 5 events have been selected for detailed scrutiny (Table 1).

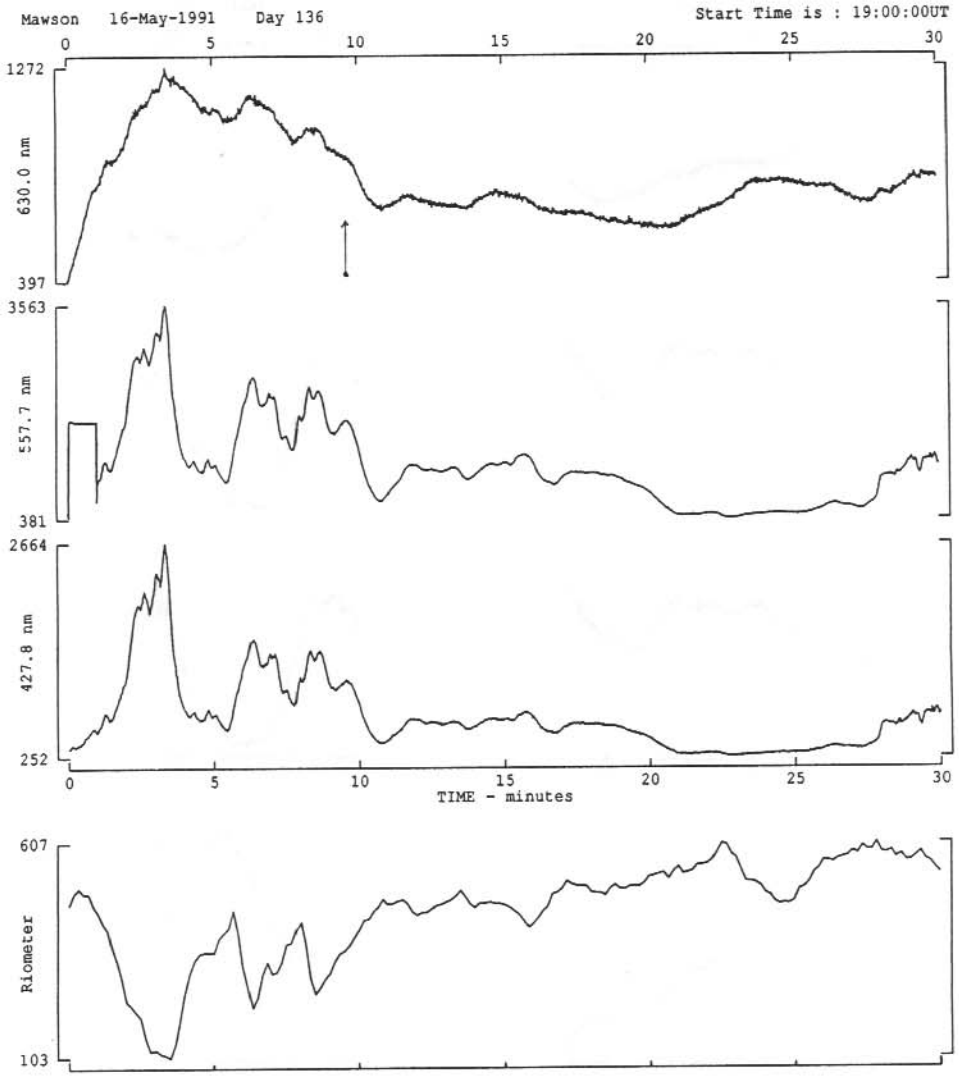

Figure 1 (a). Event on 16 May 1991. Plots of the optical emission, and the riometer absorption levels, for a half-hour period centred around the time of passage of a DMSP satellite across the Mawson skies. Preliminary scale values for the optical channels are : 630.0 nm at 4.1 ± 0.5 R(count)$^{-1}$, 557.7 nm at 11.0 ± 1.7 R(count)$^{-1}$, and 427.8 nm at 4.2 ± 0.7 R(count)$^{-1}$. The general trend of the cosmic noise absorption is given in the plot; no account of absorption level in dB is attempted here. The flat portion for the first minute of the 557.7 nm file represents the routine calibration lamp level (first minute every hour). The arrow indicates the time of maximum elevation of the satellite during its pass.

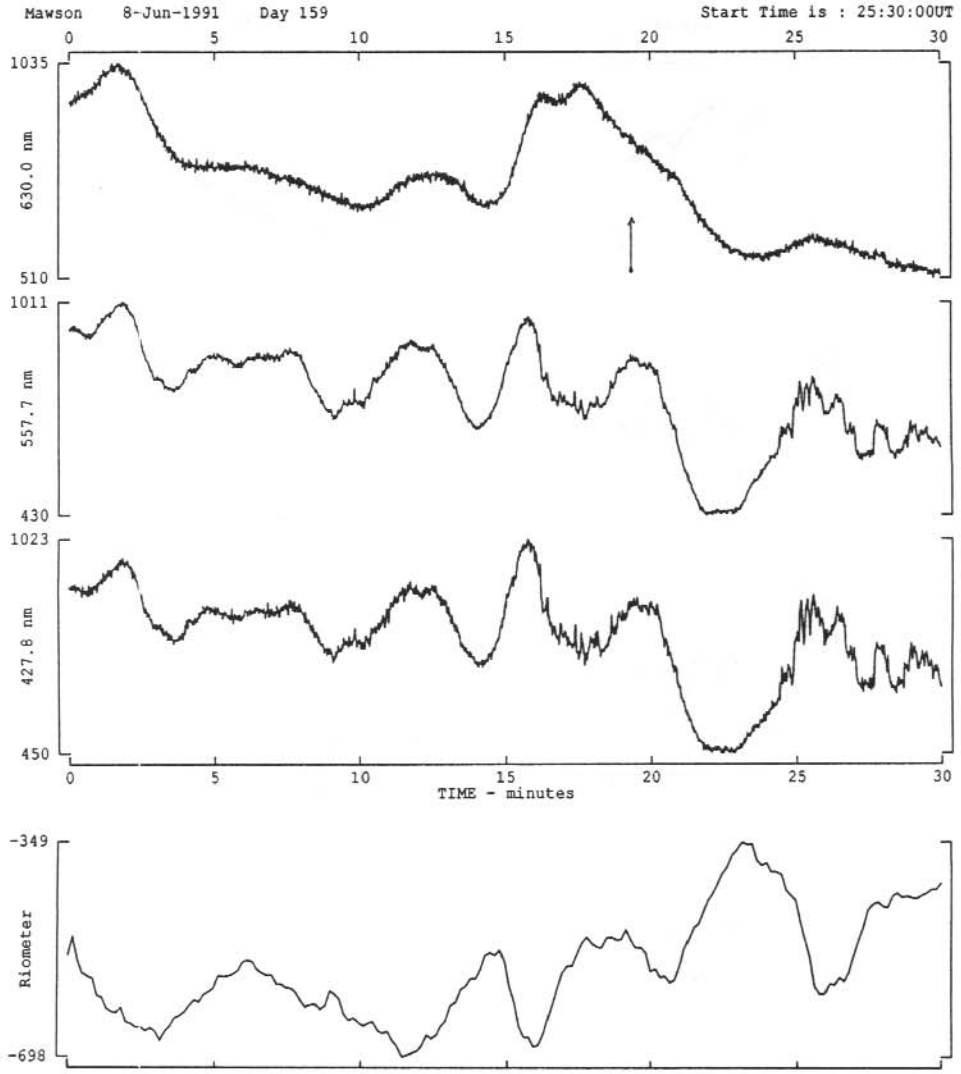

Figure 1 (b). Event on 8 June 1991. Plots of the optical emission, and the riometer absorption levels, for a half-hour period centred around the time of passage of a DMSP satellite across the Mawson skies. Preliminary scale values for the optical channels are : 630.0 nm at 4.1 ± 0.5 R(count)$^{-1}$, 557.7 nm at 11.0 ± 1.7 R(count)$^{-1}$, and 427.8 nm at 4.2 ± 0.7 R(count)$^{-1}$. The general trend of the cosmic noise absorption is given in the plot; no account of absorption level in dB is attempted here. The flat portion for the first minute of the 557.7 nm file represents the routine calibration lamp level (first minute every hour). The arrow ndicates the time of maximum elevation of the satellite during its pass. The start time of 25:30:00 UT is a manifestation of the current software routines, and the way in which continuous data are binned into consecutive files.

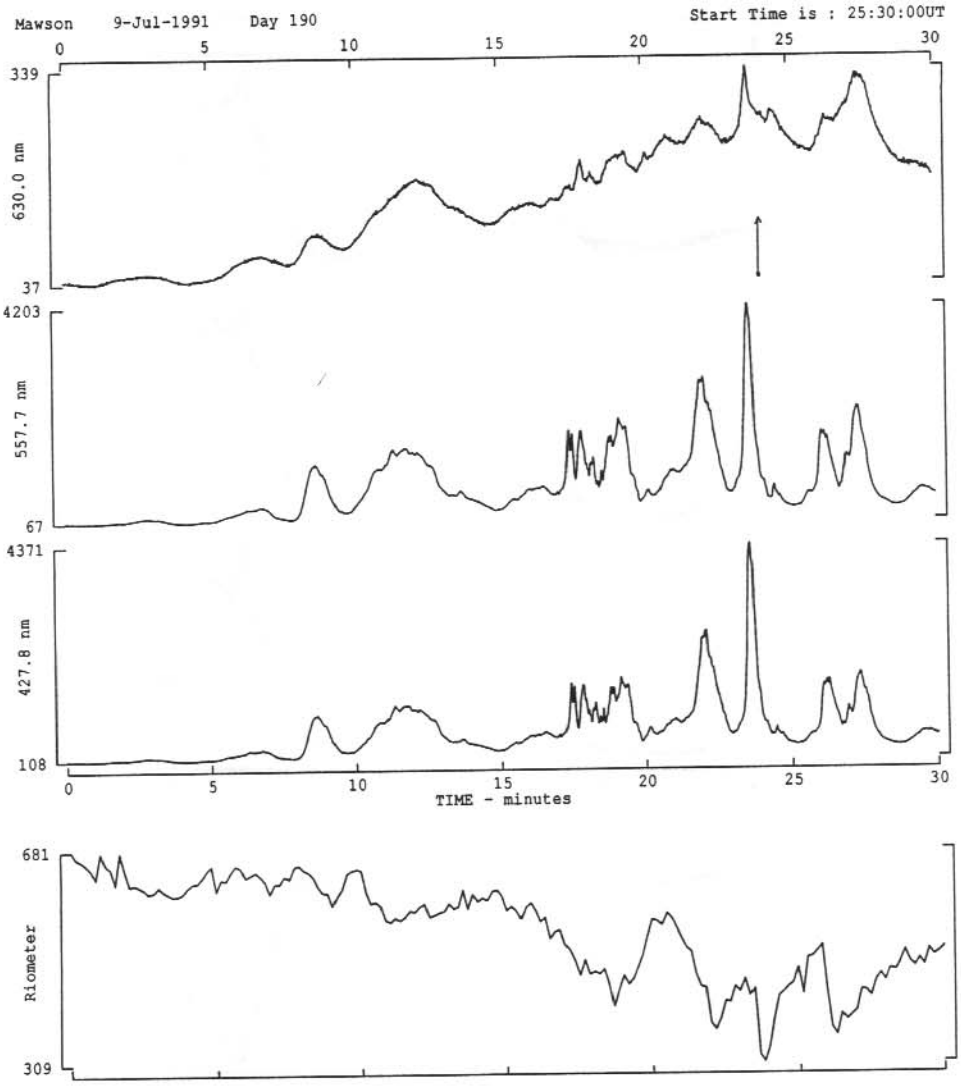

Figure 1 (c). Event on 9 July 1991. Plots of the optical emission, and the riometer absorption levels, for a half-hour period centred around the time of passage of a DMSP satellite across the Mawson skies. Preliminary scale values for the optical channels are : 630.0 nm at 4.1 ±0.5 R(count)$^{-1}$, 557.7 nm at 11.0 ± 1.7 R(count)$^{-1}$, and 427.8 nm at 4.2 ±0.7 R(count)$^{-1}$. The general trend of the cosmic noise absorption is given in the plot; no account of absorption level in dB is attempted here. The flat portion for the first minute of the 557.7 nm file represents the routine calibration lamp level (first minute every hour). The arrow indicates the time of maximum elevation of the satellite during its pass.

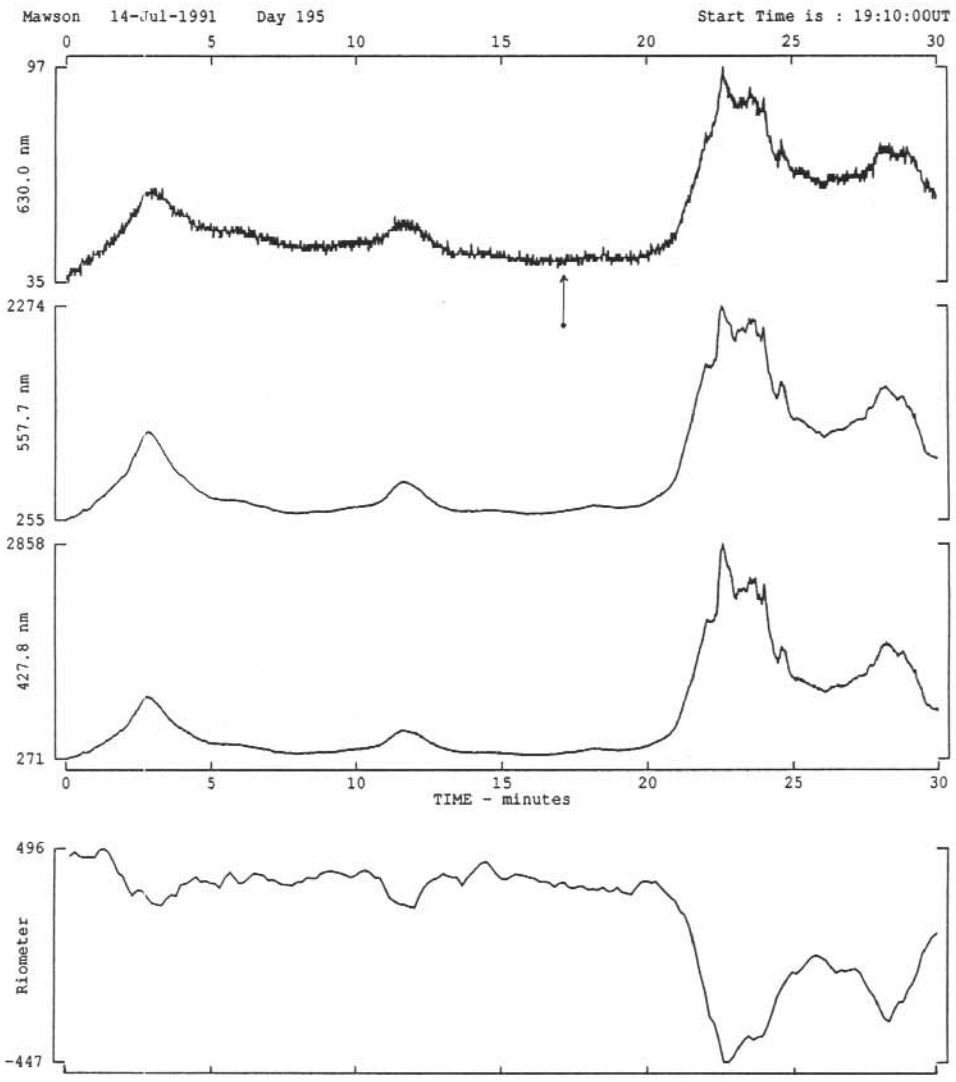

Figure 1 (d). Event on 14 July 1991. Plots of the optical emission, and the riometer absorption levels, for a half-hour period centred around the time of passage of a DMSP satellite across the Mawson skies. Preliminary scale values for the optical channels are : 630.0 nm at 4.1 ± 0.5 R(count)$^{-1}$, 557.7 nm at 11.0 ± 1.7 R(count)$^{-1}$, and 427.8 nm at 4.2 ± 0.7 R(count)$^{-1}$. The general trend of the cosmic noise absorption is given in the plot; no account of absorption level in dB is attempted here. The flat portion for the first minute of the 557.7 nm file represents the routine calibration lamp level (first minute every hour). The arrow indicates the time of maximum elevation of the satellite during its pass.

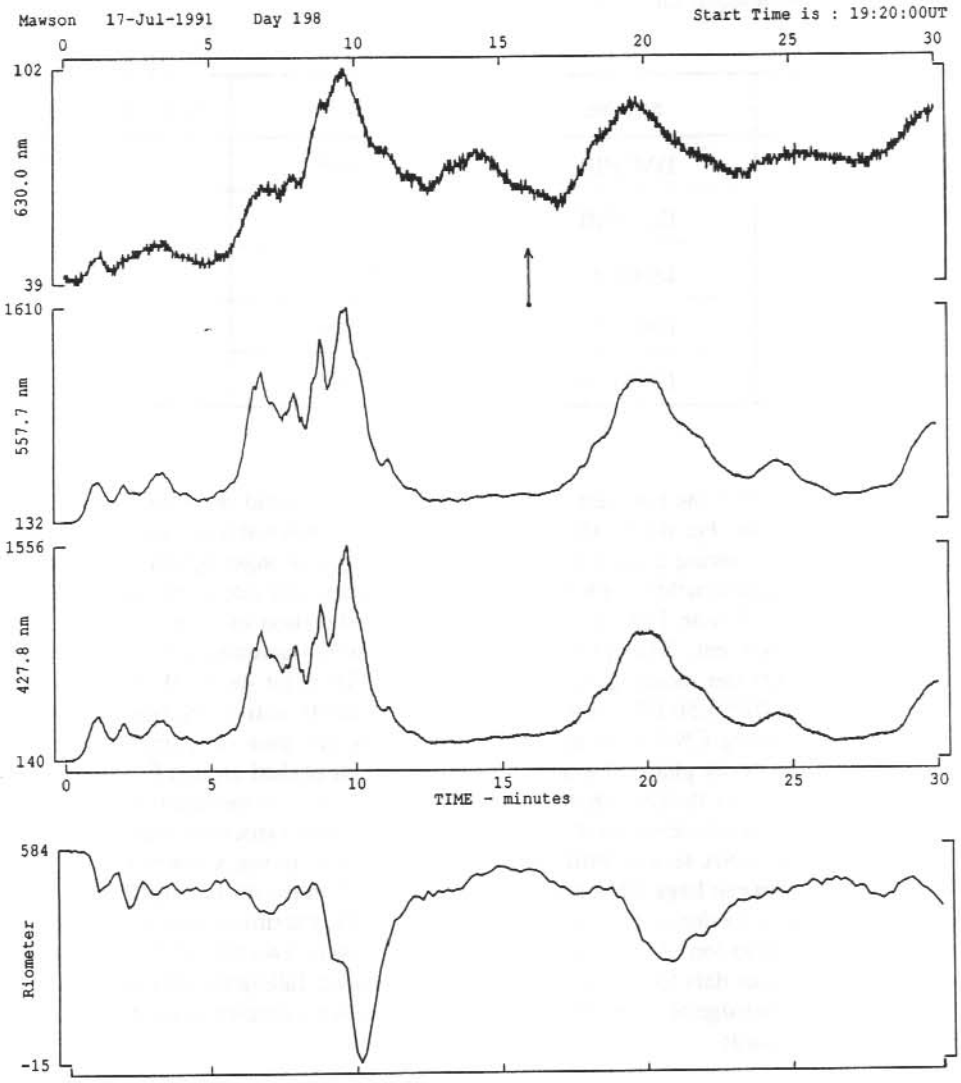

Figure 1 (e). Event on 17 July 1991. Plots of the optical emission, and the riometer absorption levels, for a half-hour period centred around the time of passage of a DMSP satellite across the Mawson skies. Preliminary scale values for the optical channels are : 630.0 nm at 4.1 ± 0.5 R(count)$^{-1}$, 557.7 nm at 11.0 ± 1.7 R(count)$^{-1}$, and 427.8 nm at 4.2 ± 0.7 R(count)$^{-1}$. The general trend of the cosmic noise absorption is given in the plot; no account of absorption level in dB is attempted here. The flat portion for the first minute of the 557.7 nm file represents the routine calibration lamp level (first minute every hour). The arrow indicates the time of maximum elevation of the satellite during its pass.

Table 1. The five satellite passes chosen for detailed study, showing the date, satellite, and the time and maximum elevation angle associated with the pass.

Date	Satellite	Time (UT)	Maximum Elevation
16 May 1991	DMSP10	19:09:45	32.5°
09 June 1991	DMSP10	01:49:17	67.6°
10 July 1991	DMSP8	01:53:56	34.0°
14 July 1991	DMSP10	19:27:03	32.8°
17 July 1991	DMSP10	19:36:03	31.0°

Figures 1 (a) to (e) depict the raw data for the five selected events and show the optical activity and cosmic noise levels. For the 16 May 1991 event, DMSP10 reached a maximum elevation of 32.5° at 19:09:45 UT, during a small enhancement following a stronger optical emission. The CNA levels fluctuate quite wildly for a period of over one hour either side of the satellite passage. In the early hours of 9 June 1991, DMSP10 achieved an elevation of 67.6° at 01:49:17 UT, during a strong CNA event. The optical emissions at this time fluctuated around continuously enhanced levels. On the morning of 10 July 1991, DMSP10 (at 49.1°, 01:12:23 UT) and DMSP8 (at 34.0°, 01:53:56 UT) both passed through locally active regions of the upper atmosphere with a strong CNA event accompanying the DMSP8 pass. The optical variation at this time was in the decay phase of a strong emission which peaked around 01:53:30 UT. A number of satellite passes flirted with intermittent auroral activity on the night of 14 July 1991. DMSP10 with a maximum elevation of 70.0° at 17:48:10 UT was associated with minor optical emission, and small CNA levels, whilst later at 19:27:03 UT during a lower elevation pass (32.8°) it crossed between large CNA and optical outbursts. Finally, on 17 July 1991, DMSP10 made a pass during a moderate optical event at 16:17:33 UT, maximum elevation 48.0°, then again achieved an elevation of 31.0° at 19:36:03 UT in between two moderate enhancements. Unfortunately the digital data for the earlier pass was not retained, falling victim to the situation of not having prior knowledge of satellite orbits, and therefore being deleted as a small event only, from the archived records.

15.5 DISCUSSION

This paper represents a preliminary report for the auroral energies project. At this stage of the research the intensity ratios have been determined only for the time of maximum elevation of the satellite for each event. These ratios are shown in Table 2. The values for the ratios exhibit quite a degree of variability across the five events, and again it is emphasised that they are only spot checks, and very preliminary in nature. The scale values need to be fully adjusted, the files used in calculating the ratios require a relative time displacement (to account for the radiative delay mechanisms in the oxygen emissions), and the ratios then need to be determined throughout the duration of these events.

Table 2. Preliminary figures for the intensity ratios spot calculated at the times of maximum satellite elevation for each pass. (No account taken for the time-delay present between the optical emissions, further refinements required for channel scale values, and dark count plus airglow background subtractions to be made.)

Date	Time (UT)	I[630.0]/I[427.8]	I[557.7]/I[427.8]
16 May 1991	19:09:45	0.72 ± 0.23	4.46 ± 1.72
09 June 1991	01:49:17	1.04 ± 0.36	2.72 ± 1.05
10 July 1991	01:53:56	0.25 ± 0.09	2.87 ± 1.10
14 July 1991	19:27:03	0.11 ± 0.04	2.66 ± 1.02
17 July 1991	19:36:03	0.18 ± 0.06	3.21 ± 1.24

Once the final scale values for each of the channels has been determined, software will be developed to plot out the values of the intensity ratios, and the intensity-CNA relationships throughout the duration of each of the selected events. AVS images of the events will be examined to determine if it is possible to use the recorded auroral geometries to see if adjustments are possible to the CNA levels calculated simply from the digital records. A knowledge of the riometer field-of-view, the geometry of the aurora within that field-of-view, and the orientation and location of the Milky Way radio source region across the area of interest, may lead to first-order corrections to the intensity-CNA results which improve its functional value as a measure of auroral electron energies.

Absolute intensity measurements are very difficult to make with a high degree of accuracy. Apart from the obvious fact that the measurements themselves are the result of a volume integration of the light emitted within the instruments field-of-view, there is the added complexity of achieving the necessary absolute calibration itself. This has proven to be exceedingly awkward with the 427.8 nm channel in particular. We have progressed however, a considerable distance along the learning curve in this instance, and have a much better understanding on which to base further research in this area.

15.6 ACKNOWLEDGMENTS

The observations were carried out at the Australian National Antarctic Research Expeditions (ANARE) station Mawson. The manufacture of research instrumentation and the collection of data at a remote observatory facility requires concerted effort from many people. To those who assisted in ensuring the collection of these data, our thanks. Special mention should be made of those fellow 1991 Mawson expeditioners who so cheerfully aided this cause, and we also extend our thanks to the Director, Antarctic Division, for logistical support for this program.

REFERENCES

Berkey, F.T. (1968). Coordinated measurements of auroral absorption and luminosity using the narrow beam technique. *Journal of Geophysical Research 73*:319 – 337.

Brekke, A. *and* Omholt, A. (1968). The intensity ratio I(4278)/I(5577) in aurora. *Planetary and Space Science 16*:1259 – 1264.

Duncan, C.N. *and* McEwen, D.J. (1979). Photometric studies of the post-noon dayside cleft region. *Journal of Geophysical Research 84*:6533 – 6539.

Eather, R.H. *and* Jacka, F. (1966). Auroral absorption of cosmic radio noise. *Australian Journal of Physics 19*:215 – 239.

Eather, R.H. *and* Mende, S.B. (1972). Systematics in auroral energy spectra. *Journal of Geophysical Research 77*:660 – 673.

Eather, R.H., Mende, S.B. *and* Judge, R.J.R. (1976). Plasma injection at synchronous orbit and spatial and temporal auroral morphology. *Journal of Geophysical Research 81*:2805 – 2822.

Heppner, J.P., Byrne, E.C. *and* Belon, A.E. (1952). The association of absorption and Es ionization with aurora at high latitudes. *Journal of Geophysical Research 57*:121 – 134.

Holt, O. *and* Omholt, A. (1962). Auroral luminosity and absorption of cosmic radio noise. *Journal of Atmospheric and Terrestrial Physics* 24:467 – 475.

McEwen, D.J., Duncan, C.N. *and* Montalbetti, R. (1981). Auroral electron energies : Comparison of in situ measurements with spectroscopically inferred energies. *Canadian Journal of Physics 59*:1116 – 1123.

Omholt, A. (1971). *The Optical Aurora.* Springer-Verlag, New York.

Rees, M.H., *and* Luckey, D. (1974). Auroral electron energy derived from ratio of spectroscopic emissions 1. Model computations. *Journal of Geophysical Research 79*:5181 – 5186.

Rees, M.H., Romick, G.J., Anderson, H.R. *and* Casserly, Jr., R.J. (1976). Calculation of auroral emissions from measured electron precipitation : Comparison with observations. *Journal of Geophysical Research 81*:5091 – 5096.

Sharp, W.E., Ortland, D. *and* Cageo, R. (1983). Concerning sources of $O(^1D)$ in aurora : Electron impact and dissociative recombination. *Journal of Geophysical Research 88*:3229 – 3232.

Steele, D.P. *and* McEwen, D.J. (1990). Electron auroral excitation efficiencies and intensity ratios. *Journal of Geophysical Research 95*:10321 – 10336.

16. ANTARCTIC POLAR CAP TOTAL ELECTRON CONTENT OBSERVATIONS USING A DIFFERENTIAL PHASE TECHNIQUE AT CASEY STATION

H.M. Beggs[1], E.A. Essex[2] and D. Rasch[1]

[1] Auroral and Space Physics
Antarctic Division
Kingston Tasmania 7050
Australia

[2] Department of Physics
La Trobe University
Bundoora Victoria 3083
Australia

ABSTRACT

In early 1990 a modified JMR-1 satellite receiver system was installed at Casey station, Antarctica (gg 66.28°S, 110.54°E, -80.4°Λ, magnetic midnight 1816 UT, L = 37.8), in order to monitor the differential phase between the 150 MHz and 400 MHz signals from polar orbiting NNSS satellites. Total electron content (TEC) was calculated using the differential phase and Casey ionosonde foF2 data, and is presented here for near sunspot maximum in August 1990 and exactly one year later. The data are used to investigate long-lived ionisation enhancements at invariant latitudes polewards of -80°Λ, and the 'polar hole', a region from -70° to -80°Λ on the nightside of the polar cap where reduced electron density exists because of the long transport time of plasma from the dayside across the polar cap. A comparison is made between the Casey TEC data and the Utah State University Time Dependent Ionospheric Model (TDIM) which uses as variables the solar index (F10.7), season (summer, winter or equinox), global magnetic index (Kp), IMF B_y direction, and universal time (UT) (Sojka et al. 1991).

16.1 INTRODUCTION

Rapid sunward convection from the post-noon ionosphere carries high-density solar-produced F region plasma through the dayside cleft and into the polar cap. This plasma is swept through the noontime cleft and enters the polar cap as a tongue of ionisation which delineates the convection trajectory and its dynamics, and provides the source for enhanced polar cap F region plasmas ('patches') which are observed at high polar latitudes away from noon. These 'patches' are localised regions of increased F region density (factor of 5 – 10 times above background with maximum values ~ 10^6 el cm^{-3} inside the patches) with horizontal dimensions ranging from a few hundred kilometres to 1000 km, which appear to originate from a region just equatorward of the dayside cusp region and drift antisunward through the polar cap with speeds from 250 to 750 ms^{-1}. Patches appear to be produced by solar radiation and not by soft particle precipitation and occur when the B_z component of the IMF is southward or when Kp > 4 (Tsunoda 1988).

It is possible to study the dynamics of the polar cap F region by monitoring the total columnar electron content (TEC) using dual frequency group delay measurements from high orbiting

satellites. Klobuchar et al. (1986), using this method in 1984 to monitor the northern polar F region near Thule (86°Λ), discovered that the variability of the TEC was extremely large (exceeding 2 x 10^{17} el m^{-2} at times), with increases above the background values of more than 100 per cent observed frequently. To our knowledge this method for measuring TEC has not previously been used in the southern polar cap. We shall present TEC data from -70°Λ to -90°Λ, collected during 1990 to 1991, and compare it with the Utah State University Time Dependent Ionospheric Model (TDIM).

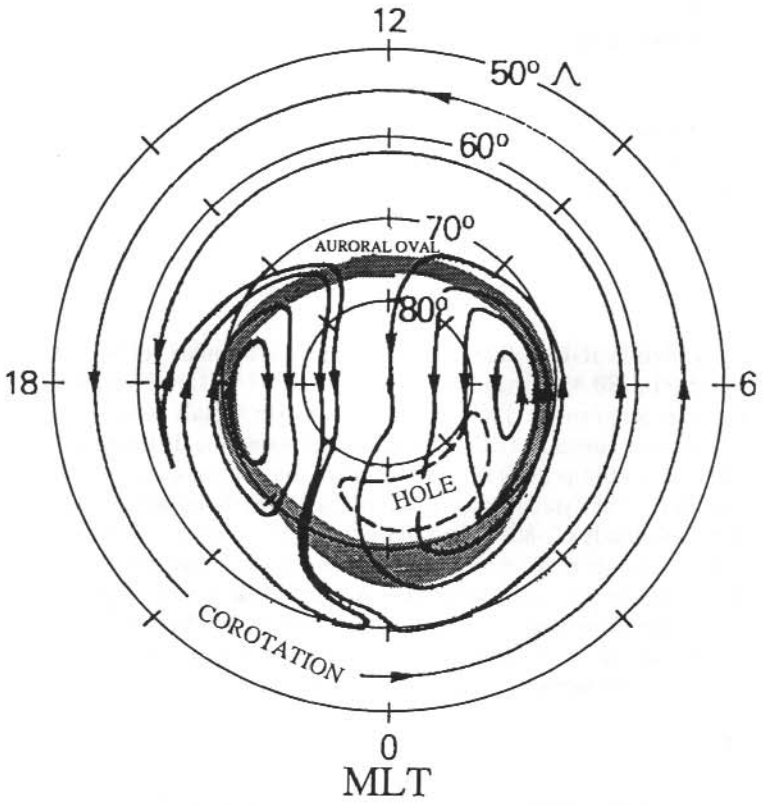

Figure 1. The plasma stagnation that may produce the polar ionisation hole in the northern hemisphere occurs when the magnetospheric convection pattern and the corotation velocity are combined as shown here. (After Brinton et al. 1978).

The TDIM is a global model, giving electron density contours in geomagnetic coordinates, at various altitudes, which has been compared extensively with observations and with the Hoegy and Grebowsky empirical plasma model (Sojka et al. 1991, Hoegy and Grebowsky 1991). It has proved an especially useful tool in the study of the polar ionisation hole, a region poleward of the nightside auroral zone between -70°Λ and -80°Λ where reduced ionisation exists because of the long transport time of ionisation from the dayside across the dark polar cap (Brinton et al. 1978). Figure 1 shows the plasma stagnation, producing the 'polar hole' in the Northern Hemisphere,

that occurs when the magnetospheric convection pattern and the corotation velocity are combined (Brinton et al. 1978). In the Southern Hemisphere the TDIM predicts that the convection pattern produced by a southward IMF with negative B_y (BC) has strong convection in the dawn sector with the polar hole located in the pre-midnight sector of the polar cap (21 to 24 MLT). It also predicts that the convection pattern produced by a southward IMF with positive B_y (DE) has strong convection in the dusk sector with the polar hole located in the post-midnight sector (0 to 3 MLT). This indicates that the polar hole is formed in regions of weak convection. In such regions the density is able to decay to the observed low values before the plasma flux tubes enter regions of strong ionisation, (i.e. auroral oval or sunlight) (Sojka et al. 1991).

Hoegy and Grebowsky (1991) found that the polar hole ionisation density was lowest during winter and there was a density minimum in the Southern Hemisphere at 20.3 UT for all seasons. The TDIM predicted that the polar hole is deepest in the Southern Hemisphere in the 1700 to 1900 UT period and least defined in the 0500 to 0700 UT period.

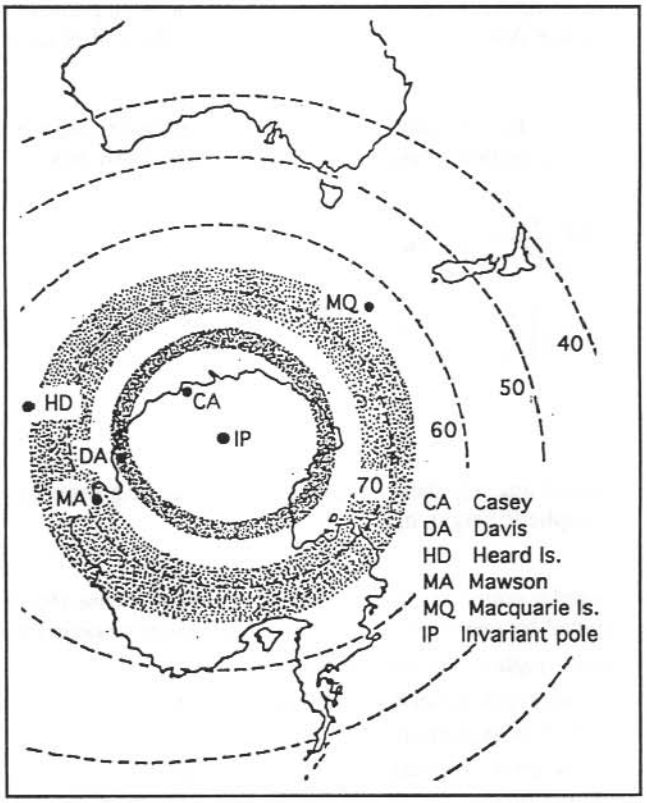

Figure 2. Australia's Antarctic station of Casey (CA) in relation to the 'cusp' (the inner dotted band) and the 'auroral zone' (the outer dotted band). Geomagnetic parallels are shown as dashed circles.

16.2 EXPERIMENT

Australia's Casey station (gg 66.28°S, 110.54°E, -80.4°Λ, magnetic midnight 1804 to 1837 UT, L = 37.8) is situated on the coast of Antarctica very close to both the invariant (74.19°S, 128.3°E) and eccentric dipole (74.7°S, 119°E) magnetic poles, and polewards of the cusp region (Figure 2). It is therefore in an ideal position for ground measurements to be made of the high magnetic latitude polar cap. In the summer of 1989–90 a modified JMR-1 satellite receiver system was installed in the old Casey station 'tunnel' in order to monitor the phase difference between two coherent radio signals at frequencies of 150 and 400 MHz (actually 149.988 MHz and 399.968 MHz) transmitted from polar orbiting satellites of the U.S. Navy Navigation Satellite System (NNSS). Calibrated values for the amplitude of the 150 MHz signals were also obtained using a prototype amplitude receiver. The NNSS ephemerides were directly decoded from the satellites' signals and automatically transmitted daily via the ANARESAT data link to the Antarctic Division's head office VAX computer where they were fed into a satellite orbital predictions program. This program determined times for the following day when only one satellite was expected in the field of view of the JMR's antennae and this satellite's elevation exceeded 10°. The Casey PDP-11/23 computer logged data at 44.373 Hz for these particular periods. The data files were transferred over ANARESAT to the Head Office VAX after each data campaign for analysis.

The absolute vertical total electron content (TEC) from the ground to the satellite was calculated using the differential phase method (Tyagi 1974, Leitinger et al. 1984, Mallis 1989), whereby

$$\int_o^{h_s} Ndh = \frac{2f_o c}{K_1}\left(\frac{m^2}{m^2-1}\right)\cos\chi_m\left(\int\frac{\Psi}{\lambda_o}dt + D\right)$$

$$= A\cos\chi_m\left(\int\frac{\Psi}{\lambda_o}dt + D\right) \qquad (1)$$

where

$\int_o^{h_s} Ndh$ = vertical total number of free electrons extending from the ground to the sub-ionospheric height, h_s,

$\int\frac{\Psi}{\lambda_o}dt$ = 'Doppler count' and is the number of radians phase change over some finite interval between two satellite signals due to ionospheric refraction,

χ_m = zenith angle at sub-ionospheric point,

f_o = satellite signal fundamental frequency (Hz),

λ_o = satellite signal carrier wavelength (meters),

m = f/f_o where f is a second satellite frequency,

Ψ = $\Delta P' - \Delta P$,

$\Delta P'$ = path length difference of a satellite signal with frequency mf_o ($m > 1$),

ΔP = path length difference of a satellite signal with frequency f_o,

D = Baseline TEC (radians),

K_1 = an integration constant.

The NNSS series of satellites are polar orbiting dual frequency beacon satellites which have f_o = 149.988 MHz and m = 8/3, and hence A = 6.48×10^{14} m^{-2}. The Doppler count term in equation (1) is output directly from the JMR-1 receiver and the geometric factor, $\cos\chi_m$, may be calculated from the satellite's known orbit, choosing a sub-ionospheric height of 350 km. The baseline, D, is more difficult to determine. An accurate means of determining the baseline TEC is to combine Faraday rotation data with phase path length variations (Garriott et al. 1970), but unfortunately there was no Faraday rotation experiment at Casey. An assumption then had to be made regarding the ionosphere above Casey. This was that the equivalent slab thickness, defined as the breadth (in kilometres) of an ionosphere of uniform electron density, was approximately 300 km.

From Fox and Mendillo (1991)

$$TEC = 1.24 \times 10^{13} (foF2)^2 \tau \qquad (2)$$

where

foF2 is measured by a vertical sounding ionosonde and is in MHz and
τ is the equivalent slab thickness (km).

Equating equations (1) and (2) gives:

$$D = \frac{1.24 \times 10^{13} \left(foF2(t_c)\right)^2 \tau}{6.48 \times 10^{14} \cos\chi_m(t_c)} - \int \frac{\Psi(t_c)}{\lambda_o} dt \qquad (3)$$

where

t_c = time of satellites closest approach to Casey.

16.3 RESULTS AND DISCUSSION

Total columnar electron content data (in units of 10^{15} el m^{-2}) for 20 August 1990 is presented in Figures 3(a)–(c) in terms of universal time, geographic latitude, magnetic local time (MLT) and invariant latitude (Λ). All these coordinates refer to the sub-ionospheric point which, in this case, is chosen to be the point on the line of sight from receiver to satellite which is 350 km in altitude. This is the approximate height of the F region peak in electron density. The magnetic local time and invariant latitude were calculated using the Baker and Wing (1989) PACE (Polar Anglo-American Conjugate Experiment) geomagnetic coordinate system which was specially formulated for use at high latitudes. 20 August 1990 was near the peak of the sunspot cycle with an F10.7 index of 277 and global three-hourly magnetic Kp indices of 3 to 3+ for the period 0700 to 0940 UT covered by Figures 3(a)–(c). The satellite trajectories for Figures 3(a)–(c) were nearly identical and situated just sunward of the invariant pole, in a region of the polar cap still in darkness at this time of year. The enhancement in TEC seen in Figures 3(a)–(c) is stationary in geomagnetic coordinates at around -85°Λ, 13 MLT, is 3 hours MLT in width, a factor of 2 peak-to-valley, and appears to maintain its strength over a span of at least 2.5 hours UT. A further pass by the same satellite at 1040 UT on 20 August 1990 showed this same enhancement at -85°Λ but having shifted to 12 MLT. It would appear, then, that this feature is one long-lived ionisation enhancement and not a series of patches. Whalen (1991) reports a peak in Northern Hemisphere F layer electron density near the cusp/cleft at 75°Λ, 12 MLT, which was 2 to 3 hours

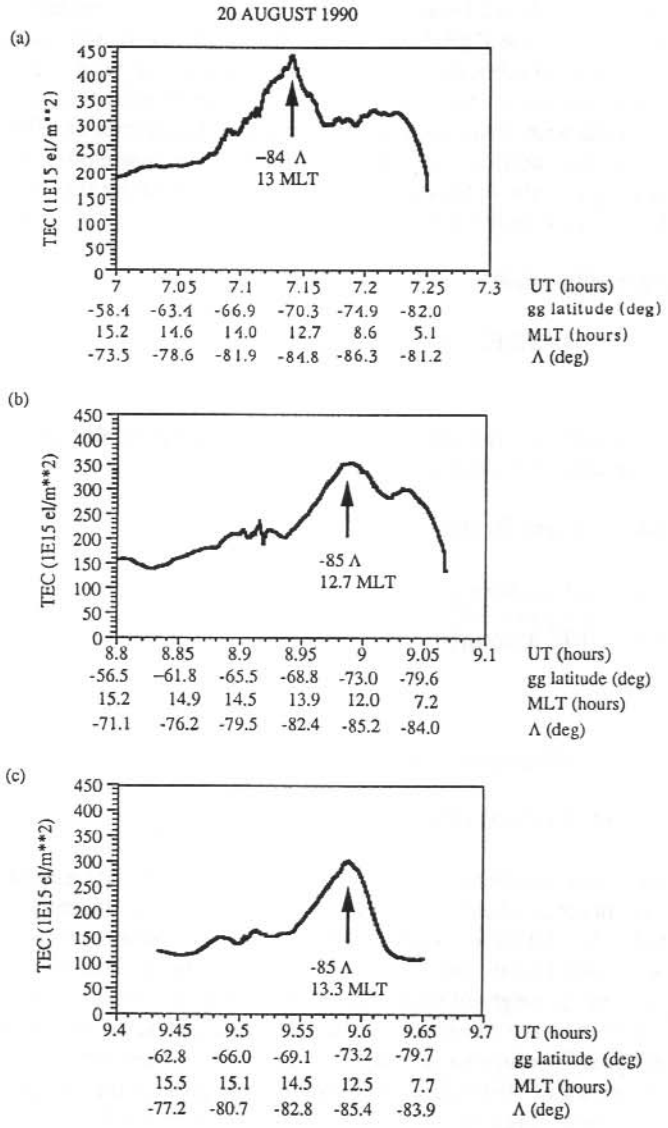

Figure 3. Columnar total electron content (in 10^{15} el m^{-2}) for 20 August 1990 (a) 0700 – 0715 UT, (b) 0848 – 0904 UT, and (c) 0926 – 0939 UT, derived from the differential phase between 150 MHz and 400 MHz signals from NNSS satellites with almost identical trajectories above Casey. The data shows an enhancement in TEC which is nearly stationary in Λ – MLT space, over 2.5 hours UT.

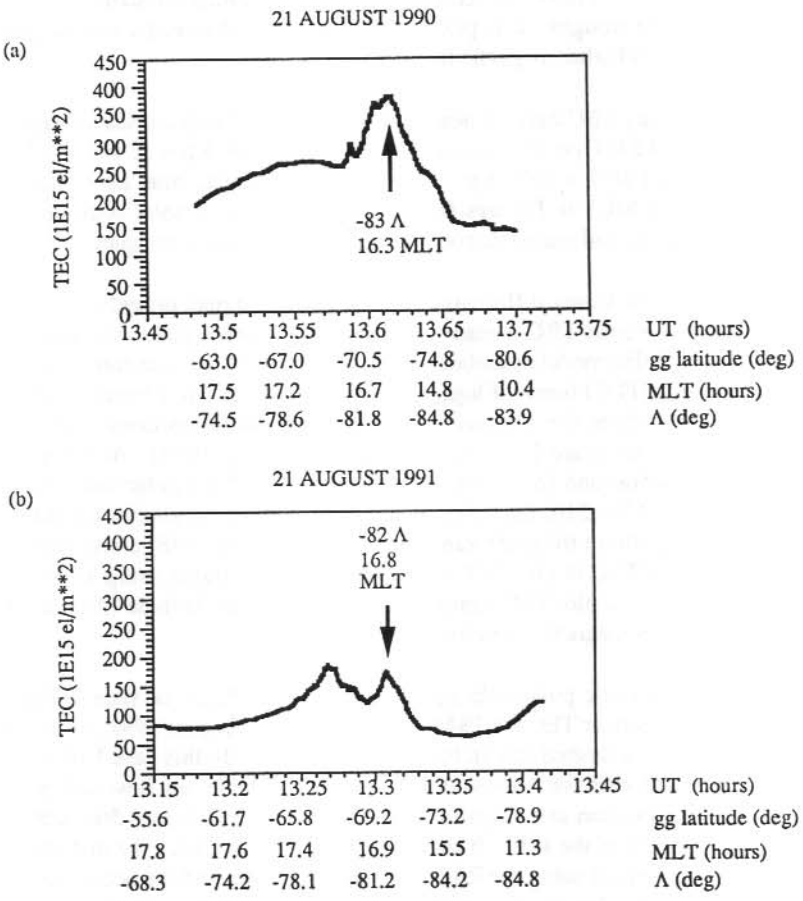

Figure 4. Columnar total electron content (in 10^{15} el m^{-2}) for almost identical satellite trajectories and magnetic and solar conditions for (a) 1329 – 1342 UT on 21 August 1990, and (b) 1307 – 1324 UT on 21 August 1991, showing an enhancement in TEC at nearly the same position in Λ – MLT space for both passes.

in width, a factor of 4 to 10 peak-to-valley and stable in MLT for many hours on individual days but highly variable from day-to-day. This peak was observed during nineteen consecutive months at solar maximum. The conclusion from Whalen's (1991) study was that the plasma in this peak is produced by solar radiation, not by particles precipitating through the cusp/cleft. The

peak corresponds to the passage of the sounder through the throat of the convection pattern and so consists of solar ionised plasma convected from lower latitudes on the dayside. The peak was further enhanced because it was flanked by regions of lower density plasma transported from the nightside by the dawn and dusk convection cells; regions which are extensions of the morning and afternoon daytime troughs. It is possible that we have observed a similar peak in F region electron density but at a higher magnetic latitude.

Figure 4 presents Casey TEC data for nearly identical satellite trajectories through the dark polar cap for (a) 1329 – 1342 UT on 21 August 1990, F10.7 = 293, Kp = 5; and (b) 1307 – 1324 UT on 21 August 1991, F10.7 = 285, Kp = 4-. It is interesting to note an enhancement in TEC around -82.5°Λ, 16.5 MLT in Figures 4(a) and (b) for identical solar position, universal time, and similar solar indices and magnetic conditions, but exactly one year apart.

It was supposed that the Casey differential phase experiment may provide some evidence of the polar hole in ground-based TEC measurements in the southern polar cap which could then be compared with the TDIM model described earlier. Sojka (1992, private communication) provided contour plots of $\log_{10}$(TEC) (units of $\log_{10}$(el m^{-2})) in the Λ vs MLT frame at 350 km altitude in the Southern Hemisphere for various solar and magnetic conditions and universal times, calculated from the Utah State University TDIM (Sojka et al. 1991). An example of these are presented in Figures 5(a) and (b) which show the location of the polar hole for the conditions: season = equinox, F10.7 = 210, Kp = 3+, time = 1900 UT and (a) southward IMF with negative B_y (BC) convection pattern; (b) southward IMF with positive B_y (DE) convection pattern. Sojka et al. (1991) maps the TEC in the MLT vs. magnetic latitude frame using an eccentric magnetic dipole model, whereas we plot TEC against MLT and invariant latitude (Λ) using the Baker and Wing (1989) PACE geomagnetic coordinate system.

Evidence of the ionospheric polar hole equatorwards of -83°Λ can be seen in Figure 6(a) which presents the Casey columnar TEC for 1844 – 1856 UT on 21 August 1991, for a sub-ionospheric satellite path shown as a dashed line in Figures 5(a) and (b). In this case F10.7 = 285 and Kp = 3-. Unfortunately IMF data for August 1991 is not yet available, but it would appear that Figure 6(a) agrees with the location and magnitude of the polar hole in Figure 5(a), corresponding to a negative B_y component of the IMF. It should be noted that at Casey the difference between the magnetic local time derived using the PACE coordinate system and the eccentric dipole system is on average 50 minutes, due to the station's location with respect to the south invariant and eccentric dipole magnetic poles (Burns and Beggs 1992).

An example of the very strong amplitude scintillation seen at Casey is shown in Figures 6(b) and (c) which give the amplitude of the 150 MHz satellite signal and the corresponding S_4 scintillation index, respectively, for 1844 – 1856 UT on 21 August 1991. The S_4 index, a measure of the scintillation strength, is defined as the square root of the variance of the received power for a chosen time interval (Briggs and Parkin 1963). The S_4 index presented here is evaluated over 20 second intervals. Amplitude scintillation was much greater when the satellite sub-ionospheric point passed through enhancements in the electron density, than when it passed through the polar hole.

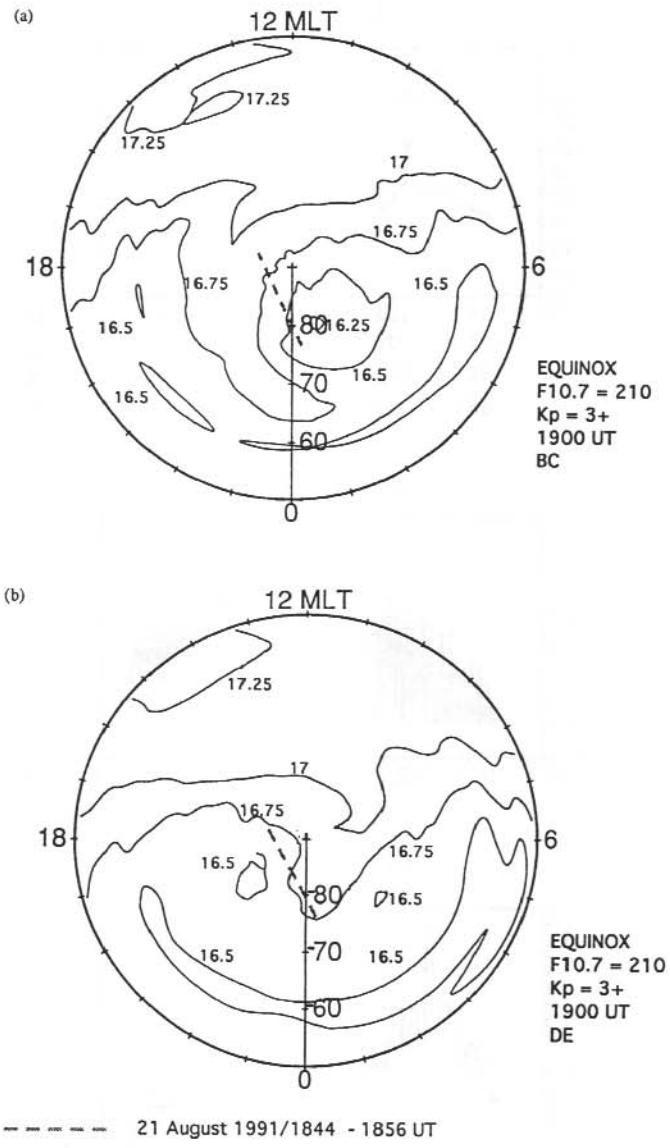

Figure 5. Plots of $\log_{10}$(TEC) (in $\log_{10}$ el m^{-2})) from the Utah State University TDIM (for Southern Hemisphere, equinox, F10.7 = 210, Kp = 3+ 1900 UT) in the magnetic local time vs. magnetic latitude frame. (a) IMF southward with B_y negative (BC) convection pattern; (b) IMF southward with B_y positive (DE) convection pattern (Sojka 1992, private communication).

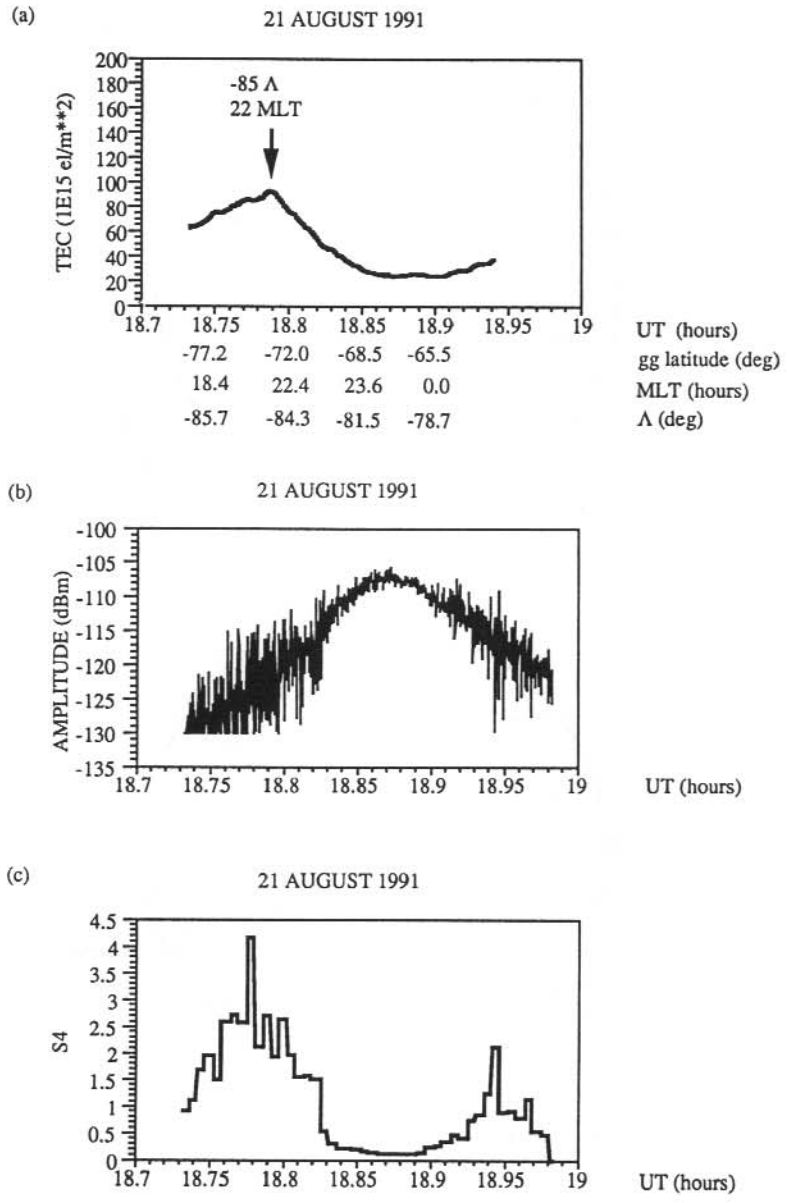

Figure 6. Plots of (a) columnar total electron content (in 10^{15} el m^{-2}), (b) amplitude of the 150 MHz satellite signal (in dB m), and (c) amplitude scintillation index (S_4) for 21 August 1991, 1844 – 1856 UT, F10.7 = 285, Kp = 3-. The satellite trajectory for the data presented here is shown in Figure 5(a) and (b) as a dashed line.

16.4 CONCLUSION

Using the NNSS series of polar orbiting satellites we were able to study the same region of the polar cap ionosphere over a number of similar satellite passes and show that on one occasion, 0700 – 0939 UT on 20 August 1990, an enhancement in ionisation at around -85°Λ, 13 MLT, of 3 hours MLT width and a factor of 2 peak-to-valley, rather than progressing rapidly anti sunward through the dark Antarctic polar cap, appeared to maintain its strength and position in geomagnetic coordinates for at least 2.5 hours and possibly up to 4 hours UT. It was also found that an ionisation enhancement in the F region at around -82.5°Λ, 16.5 MLT seen at 13.6 hours UT on 21 August 1990 was present exactly one year later for slightly less disturbed solar and magnetic conditions.

A comparison has been made between the Casey TEC data and the Utah State University TDIM and agreement was found for an ionospheric polar hole equatorwards of -83°Λ and greater than about 23.5 hours MLT at 1900 UT on 21 August 1991, assuming a southwards IMF with negative B_y.

The bulk of our amplitude data from satellite passes shows extremely strong scintillation from enhanced ionisation. This satellite scintillation is far stronger than any seen at lower invariant magnetic latitudes, such as Davis station (-74.34°Λ) (Essex and Rasch 1988).

This 1990 to 1991 study of the Antarctic polar cap F region has indicated areas for further investigation. It is planned to redeploy an upgraded version of the differential phase experiment using the JMR-1 receiver and a PC computer at Casey in the summer of 1992 – 93.

16.5 ACKNOWLEDGMENTS

The observations were carried out at the Australian National Antarctic Research Expedition's Casey station. The authors thank the Director, Antarctic Division for logistic support. We would also like to thank Perry Roberts (wintering Antarctic Division physicist/engineer at Casey in 1991) for his constant and enthusiastic technical support of the project, and the Glaciology Section of the Australian Antarctic Division for the loan of their JMR-1 receiver. We gratefully acknowledge Dr Jan Sojka who generously supplied the Utah State University TDIM convection model results for the Southern Hemisphere, Dr Kile Baker and Dr S. Wing for the PACE geomagnetic coordinate model software, and Australia's IPS Radio and Space Services for supplying the foF2 values. This work was supported by the Australian Antarctic Science Advisory Committee.

REFERENCES

Baker, K.B. *and* Wing S. (1989). A new magnetic coordinate system for conjugate studies at high latitudes. *Journal of Geophysical Research 94*:9139 – 9143.

Briggs, B.H. *and* Parkin I.A. (1963). On the variation of radio star and satellite scintillations with zenith angle. *Journal of Atmospheric and Terrestrial Physics 25*:339 – 365.

Brinton, H.C., Grebowsky, J.M. *and* Brace, L.H. (1978). The high-latitude winter F region at 300 km: thermal plasma observations from AEC. *Journal of Geophysical Research 83*:4767 – 4776.

Burns, G.B. *and* Beggs, H.M. (1992). Magnetic time for Australia's Antarctic stations. In: Burns, G.B. *and* Duldig, M.L. (Eds). *ANARE Research Notes Number 88*. Australian Antarctic Division.

Essex, E.A. *and* Rasch, D. (1988). Propagation studies at 244 MHz and 1.5 GHz at high southern latitudes. In: Conde, M. *and* Beggs, H. (Eds). *ANARE Research Notes 69*. Australian Antarctic Division. Pp. 102 – 114.

Fox, M.W. *and* Mendillo, M. (1991). Ionospheric equivalent slab thickness and its modeling applications. *Radio Science 26*:429 – 438.

Garriott, O.K., da Rosa, A.V. *and* Ross, W.J. (1970). Electron content obtained from Faraday rotation and phase path length variations. *Journal of Atmospheric and Terrestrial Physics 32*:705 – 727.

Hoegy, W.R. *and* Grebowsky, J.M. (1991). Dependence of polar hole density on magnetic and solar conditions. *Journal of Geophysical Research 96*:5737 – 5755.

Klobuchar, J.A., Anderson, D.N. *and* Bishop, G.J. (1986). Measurements of trans-ionospheric propagation parameters in the polar cap ionosphere. *Proceedings of the Beacon Satellite Symposium, Oulu, Finland 2*:59 – 67.

Leitinger, R., Hartmann, G.K., Lohmar, F.-J. *and* Putz, E. (1984). Electron content measurements with geodetic Doppler receivers. *Radio Science 19*:789 – 797.

Mallis, M. (1989). *An investigation of the southern-hemisphere ionospheric main trough using total electron content measurements*. Ph.D thesis, La Trobe University, Australia.

Sojka, J.J., Schunk, R.W., Hoegy, W.R. *and* Grebowsky, J.M. (1991). Model and observation comparison of the universal time and IMF By dependence of the ionospheric polar hole. *Advanced Space Research 11*:(10)39 – 42.

Sojka, J.J. (1992). Private communication.

Tsunoda, R.T. (1988). High-latitude F region irregularities: a review and synthesis. *Reviews of Geophysics 26*:719 – 760.

Tyagi, T.R. (1974). Determination of total electron content from differential Doppler records. *Journal of Atmospheric and Terrestrial Physics 36*:1157 – 1164.

Whalen, J.A. (1991). The origin of a peak in F layer electron density near the cusp/cleft. *AGU 1991 Fall Meeting Program and Abstracts, in supplement to EOS*. P. 355.

17. QUASI PERIODIC SCINTILLATION EVENTS AT SOUTHERN AURORAL LATITUDES

D.J. Rasch[1] and E. Essex[2]

[1] Auroral and Space Physics
Antarctic Division
Kingston Tasmania 7050
Australia

[2] Department of Physics
La Trobe University
Bundoora Victoria 3083
Australia

ABSTRACT

Quasi-periodic (QP) radio scintillations were observed during 1987 in the southern auroral zone, on 244 MHz and 1.5 GHz geostationary satellite transmissions, from Davis station (68.6°S, 78.0°E geographic, 74.6°S Λ) in Antarctica. The substantial loss of signal associated with these events may be an important factor in determining the reliability of satellite links in auroral regions. Three distinct types of QP events were identified, two of which could be adequately described by existing models involving the passage across the raypath of a narrow, highly ionised or highly depleted column irregularity. A third type of event observed on 244 MHz could be modelled by the passage of an opaque column irregularity which also supported a reflected ray at grazing incidence.

Previous studies at mid-latitudes have mainly observed QP events at zenith angles above 50° therefore a geometric effect may be enhancing the apparent plasma density of the irregularities. A model based on a tilted ionisation layer was found to produce similar diffraction effects to existing column models at significantly lower plasma densities, as well as demonstrating a more appropriate zenith angle dependence.

The dominant occurrence time for QP events on both frequencies was 18–00 hours MLT. At these times, the raypath may intersect the poleward edge of the trough where sporadic-E or low F-region tilted structures may be produced by the passage of medium-scale acoustic-gravity waves.

17.1 INTRODUCTION

A radio wave propagating through a region of the ionosphere which contains irregularities in electron density will be diffracted, causing fluctuations in signal power to be recorded at the ground. These fluctuations are termed scintillations. While most scintillations are random, one class exhibits periodic oscillations and has been named QP scintillations. Most previous observations of QP scintillations have been at mid-latitudes, but it appears that QP events are important at auroral latitudes also. QP scintillation is often associated with a substantial loss of

signal, and may prove to be important in determining the reliability of satellite data links at these latitudes.

17.2 DATA COLLECTION AND ANALYSIS

During 1987, beacon signals from geostationary satellites on 244 MHz and 1.5 GHz were continuously monitored from Davis station (68.6°S, 78.0°E geographic, 74.6°S Λ) in the Australian Antarctic Territory. The raypaths intersected the E-region ionosphere at ~72°S Λ, and the F-region (350 km) at ~67°S Λ. An observation period of 10 months on 244 MHz yielded 136 QP events while an 8 month observing period on 1.5 GHz produced 144 events. Depending on link margin, this latter result represents an average of one link failure every two days due to QP scintillations.

QP events were mainly confined to the period 21 ± 2 hours MLT on both 244 MHz and 1.5 GHz. No correlation with either the season or magnetic activity was observed. Several distinct types of QP events were seen during 1987, broadly classifiable into the following three categories:

1. QP with central minimum (244 MHz and 1.5 GHz)
2. QP with central maximum (244 MHz and 1.5 GHz)
3. QP with extended central minimum (244 MHz only)

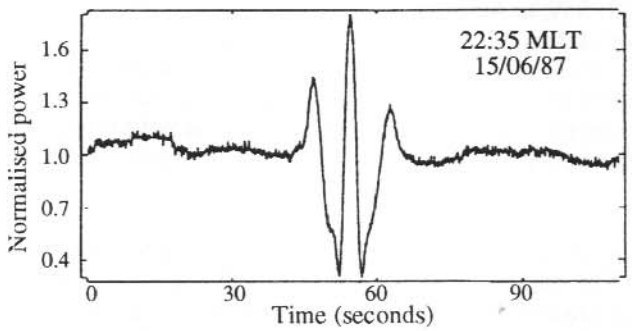

Figure 1. QP event with central minum – 244 MHz.

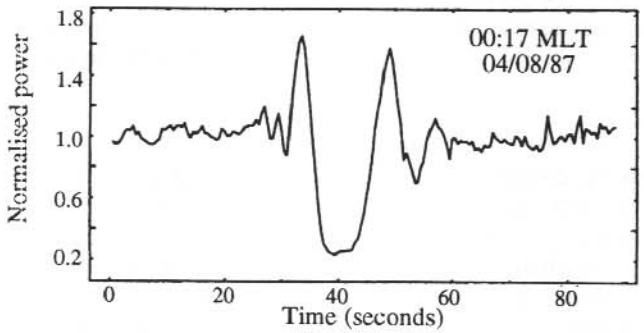

Figure 2. QP event with central maximum – 1.5 GHz.

The first category (Figure 1) is commonly observed to contain a negative 'spike' at the centre of a roughly symmetrical signature (Elkins and Slack 1969, Hajkowicz et al. 1981, Moriya and Sakurada 1983, Karasawa et al. 1985, Moriya et al. 1988, Maruyama 1991). By calculating the total intensity-time product over the duration of a QP event, Dagg (1957) demonstrated that most QP scintillations involve merely a redistribution of incident energy rather than any net absorption or enhancement of the incident radiation. Models involving diffraction of the radio wave around a densely ionised column or strip of several hundred metres width (Titheridge 1971, Heron 1976, Davies and Whitehead 1977, Fulford and Forsyth 1984, Karasawa 1987) appear to be most successful in duplicating the observed events.

The second category (Figure 2) has not previously been reported and only a small number of occurrences were noted during 1987 on both 244 MHz and 1.5 GHz. By replacing the region of ionisation enhancement with a depletion, category 1 models have been found to adequately simulate this type of event.

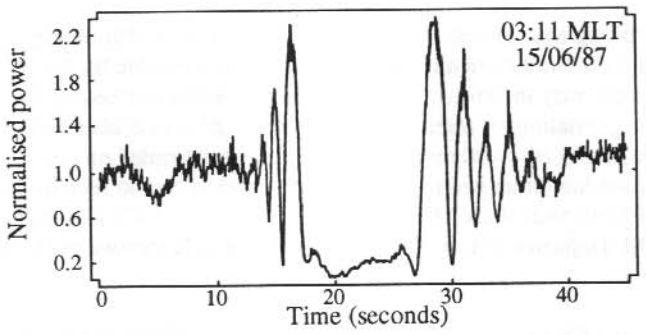

Figure 3. QP event with extended central minimum – 244 MHz.

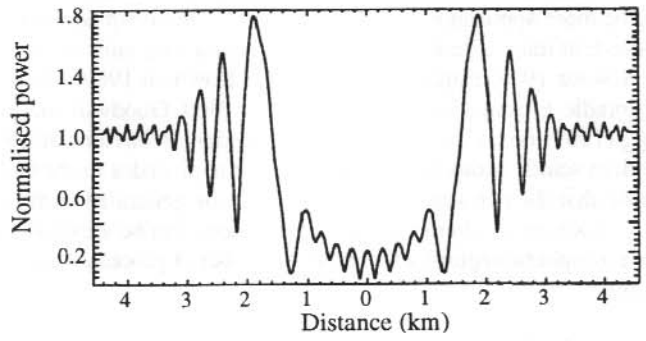

Figure 4. Model of extended central minimum event in Figure 3.

Examples at lower frequencies of the third category of QP event (Figure 3) have been published (Slack 1972 Figure 1, Elkins and Slack 1969 Figure 3b, Davies and Whitehead 1977 Figure 1 (40 MHz), Kelleher and Martin 1975 Figures 1b and 1c (40 MHz)), but not identified as a distinct type of event. While events in the first two categories involve merely a redistribution of incident energy rather than any net absorption or enhancement of the incident radiation (Dagg 1957), the third category appears to involve a net loss of signal power. During the extended central period, the signal is generally reduced at least 8 dB below normal signal levels and large oscillations are seen either side of the central region which approach in magnitude that of the central minimum itself. While models of diffraction at an opaque edge or strip (Jenkins and White 1965 Figures 18V, 18Q and 18R) result in an appropriate loss of signal at the event's centre, they fail to reproduce the magnitude of the oscillations either side of centre. A model based on an opaque strip but which includes an additional ray reflected from the irregularity at grazing incidence has been investigated and found to acceptably duplicate this category of event (Figure 4).

17.3 PHYSICAL INTERPRETATION AND MODELLING

Events recorded on orbiting and geostationary satellites show a marked similarity, suggesting that spatial gradients in ionisation rather than temporal effects are responsible for the appearance of the QP event. Such structures may therefore be stable over time periods exceeding the length of a QP event recorded from a geostationary satellite (> 1 minute). QP events also sometimes appear in groups, with time separations of 4 – 30 minutes between events recorded on geostationary satellite signals. This observation has either been specifically reported or can be seen in data presented in many publications (Elkins and Slack 1969 Figure 8, Titheridge 1971 Figure 9, Kelleher and Martin 1975 Figure 1d, Hajkowicz et al. 1981 Figures 4 and 7, Karasawa et al. 1985 Figure 4a, Bowman 1989 Figure 1).

The altitude at which the QP event is generated is not certain. While Elkins and Slack (1969) reported the QP event to be an F-region phenomenon, these measurements were based on an off-axis reflected ray model which may not be generally appropriate at their observing frequency (137 MHz), especially in view of the success of diffraction models which have proved less stringent on ionisation gradients. Height observations by Kelleher and Martin (1975) indicating altitudes of 100 - 260 km were also based on a reflection model, although at their observing frequency (40 MHz) this model may be more applicable. A morphological relationship between QP events and the presence of sporadic-E at mid-latitudes has been pointed out by a number of authors (Ireland and Preddy 1967, Hajkowicz 1977, Hajkowicz et al. 1981, Bowman 1989, Maruyama 1991) as has the existence of sporadic-E frontal behaviour (Bowman 1960, Goodwin and Summers 1970, Bowman 1989). Dagg (1957) noted the apparently independent behaviour of QP scintillations and superimposed random scintillations (normally attributed to altitudes in the vicinity of the F2 region peak), suggesting that the two scintillation types may be generated at different altitudes. What is not yet known, however, is whether all QP scintillations can be attributed to one process (and consequently one ionospheric region), or whether a number of processes can produce similar quasi-periodic signatures.

The ionisation density required by the 'column' models is often excessive, raising the question of why they are not detected by other techniques. Bowman (1989) argued this may be due to their extremely narrow radio cross-section. However, since previous studies of QP events using orbiting satellites have shown an increase in the number of events at zenith angles above 50°

(Kelleher and Martin 1975, Dagg 1957, Hajkowicz 1977), an alternative explanation may be that QP events do not result from an actual strip or column being present in the ionosphere but rather rely on a geometric effect such as the approximate alignment of a tilted layer with the raypath.

A diffraction model (Appendix A) based on a tilted layer has been investigated as an alternative to the column and strip models on 1.5 GHz. For modelling purposes, an arbitrary 'background' ionisation density of 10^{11} el m^{-3} was assumed throughout. The range to the irregularity from the observer was calculated using spherical Earth trigonometry. Results (Figures 5 and 6) indicate that a tilted layer can generate 'central minimum' QP events, with lower constraints on ionisation density and with a more appropriate zenith angle dependence than the column models.

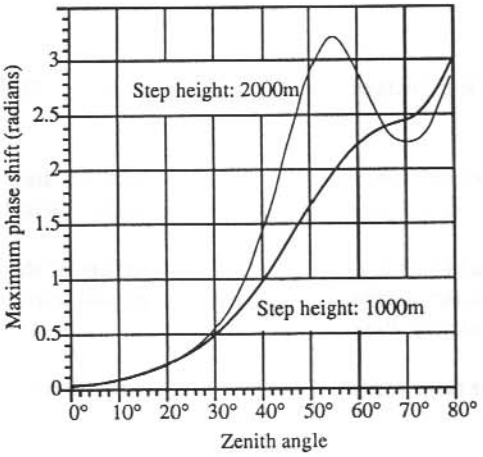

Figure 5. Modelled phase shift variation with zenith angle.

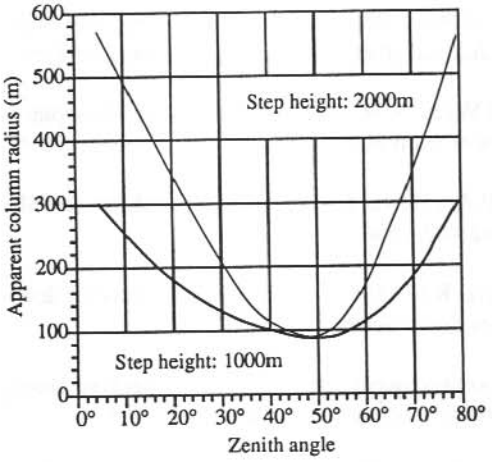

Figure 6. Modelled column radius variation with zenith angle.

In the pre-midnight sector, the raypaths may pass through a region where sporadic-E is a common feature, such as the poleward edge of the mid-latitude trough (Rodger et al. 1992). QP scintillation events might then be produced by the tilting of the layer (Bowman 1989, Woodman et al. 1991, Lanchester et al. 1991) towards alignment with the raypath, resulting from the passage of medium-scale acoustic-gravity waves (Hines 1960). Tilted structures in the F-region may also play a role in QP generation (Evans et al. 1983, Paul 1985). The few observations of QP disturbance propagation velocities (Elkins and Slack 1969, Hajkowicz et al. 1981) at mid-latitudes are in reasonable agreement with propagation velocities of medium-scale travelling ionospheric disturbances (TID) (Crowley et al. 1987) which have been associated with gravity wave propagation. At these latitudes, relocations of the auroral electrojet or heating associated with particle precipitation are candidates for gravity wave generation (Wilson 1962, Hunsucker 1982).

REFERENCES

Bowman, G.G. (1960). Some aspects of sporadic-E at mid-latitudes. *Planetary Space Science* 2:195–211.

Bowman, G.G. (1989). Quasi-periodic scintillations at mid-latitudes and their possible association with ionospheric sporadic-E structures. *Annales Geophysicae* 7:259–268.

Crowley, G., Jones, T.B. *and* Dudeney, J.R. (1987). Comparison of short period TID morphologies in Antarctica during geomagnetically quiet and active intervals. *Journal of Atmospheric and Terrestrial Physics* 49:1155–1162.

Dagg, M. (1957). Radio-star ridges. *Journal of Atmospheric and Terrestrial Physics* 11:118–127.

Davies, K. *and* Whitehead, J.D. (1977). A radio lens in the ionosphere. *Journal of Atmospheric and Terrestrial Physics* 39:383–387.

Elkins, T.J. *and* Slack, F.F. (1969). Observations of travelling ionospheric disturbances using stationary satellites. *Journal of Atmospheric and Terrestrial Physics* 31:421–439.

Evans, J.V., Holt, J.M. *and* Wand, R.H. (1983). A differential-Doppler study of travelling ionospheric disturbances from Millstone Hill. *Radio Science* 18:435–451.

Fulford, J.A. *and* Forsyth, P.A. (1984). High latitude ionospheric scintillations. *Canadian Journal of Physics* 62:487–504.

Goodwin, G.L. *and* Summers, R.N. (1970). E_s-layer characteristics determined from spaced ionosondes. *Planetary Space Science* 18:1417–1432.

Hajkowicz, L.A. (1977). Morphological and ionospheric aspects of quasiperiodic scintillations. *Journal of Atmospheric and Terrestrial Physics* 39:833–841.

Hajkowicz, L.A., Bramley, E.N. *and* Browning, R. (1981). Drift analysis of random and quasiperiodic scintillations in the ionosphere. *Journal of Atmospheric and Terrestrial Physics* 43:723–733.

Hines, C.O. (1960). Internal atmospheric gravity waves at ionospheric heights. *Canadian Journal of Physics 38*:1441 – 1481.

Heron, M.L. (1976). On the modelling of ionospheric irregularities from Fresnel diffraction patterns. *Journal of Atmospheric and Terrestrial Physics 38*:1027 – 1032.

Hunsucker, R.D. (1982). Atmospheric gravity waves generated in the high-latitude ionosphere. A review. *Reviews of Geophysical and Space Physics 20*:293 – 315.

Ireland, W. *and* Preddey, G.F. (1967). Regular fading of satellite transmissions. *Journal of Atmospheric and Terrestrial Physics 29*:137 – 148.

Jenkins, F.A. *and* White, H.E. (1965). *Fundamentals of optics*. 3rd Edition, International Student Edition. MacGraw-Hill.

Karasawa, Y.,Yasukawa, K. *and* Yamada, M. (1985). Ionospheric scintillation measurements at 1.5 GHz in mid-latitude region. *Radio Science 20*:643 – 651.

Karasawa, Y. (1987). Interpretation of quasi-periodic scintillation at frequencies above 1 GHz. *The Transactions of the IEICE E70*:768 – 774.

Kelleher, R.F. *and* Martin, P. (1975). Fresnel-type fading on satellite records at low latitudes. *Journal of Atmospheric and Terrestrial Physics 37*:1109 – 1116.

Lanchester, B.S., Nygren, T., Huuskonen, A., Turunen, T. *and* Jarvis, M.J. (1991). Sporadic-E as a tracer for atmospheric waves. *Planetary Space Science 39*:1421 – 1434.

Maruyama, T. (1991). Observations of quasi-periodic scintillations and their possible relation to the dynamics of E_s plasma blobs. *Radio Science 26*:691 – 700.

Moriya, Y. *and* Sakurada, H. (1983). Ionospheric scintillations shown in the MARISAT satellite. *Transactions of the IECE Japan J66-B(11)*:1430 – 1431.

Moriya, Y., Sakurada, H. *and* Wakai, N. (1988). The spike-type ionospheric scintillation observed in satellite signals at 1.5 GHz. *Proceedings of the International Symposium on Radio Propagation (Beijing)*. Pp. 181 – 184.

Paul, A.K. (1985). F region tilts and ionogram analysis. *Radio Science 20*:959 – 971.

Rodger, A.S., Moffett, R.J. *and* Quegan, S. (1992). The role of ion drift in the formation of ionisation troughs in the mid- and high-latitude ionosphere – a review. *Journal of Atmospheric and Terrestrial Physics 54*:1 – 30.

Slack, F.F. (1972). Quasiperiodic scintillation in the ionosphere. *Journal of Atmospheric and Terrestrial Physics 34*:927 – 939.

Titheridge, J.E. (1971). The diffraction of satellite signals by isolated ionospheric irregularities. *Journal of Atmospheric and Terrestrial Physics 33*:47 – 69.

Wilson, C.R. (1969). Infrasonic waves from moving auroral electrojets. *Planetary Space Science 17*:1107 – 1120.

Woodman, R.F., Yamamoto, M. *and* Fukao, S. (1991). Gravity wave modulation of gradient drift instabilities in mid-latitude sporadic E irregularities. *Geophysical Research Letters 18*:1197 -- 1200.

APPENDIX A

Modelling the phase path effects of a step ionisation profile in a sporadic-E layer at 1.5 GHz

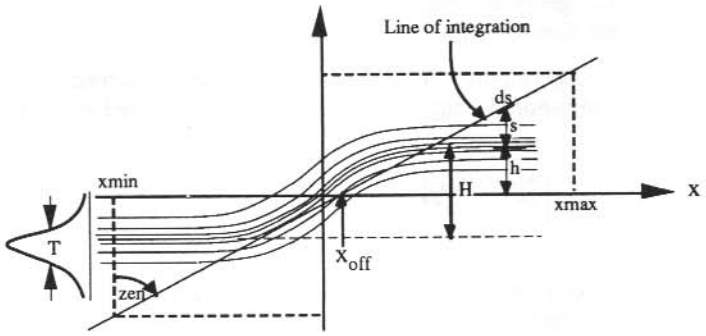

Figure A1

At GHz frequencies, a reasonable estimate of the phase effects introduced by a horizontally stratified layer containing a step profile (Figure A1) can be obtained by assuming that each ray from the satellite suffers no deviation in propagation direction through the region being investigated. Under these conditions, the phase path defect $\phi(s)$ relative to free space along a particular line of integration can be expressed in general as:

$$\phi(s) = \frac{2\pi}{\lambda} \int_{s\,min}^{s\,max} (1 - n(s))\, ds \qquad \text{(A1)}$$

where ϕ is measured in radians,
λ is the radio wavelength,
n(s) is the refractive index at each point along the line of integration, and
smin and smax represent lower and upper bounds on the region being investigated.

In this particular application, the radio wave frequency is much greater than the plasma frequency and the refractive index of the plasma at each point is approximately related to the electron density N by:

$$n(s) = \sqrt{1 - \frac{80.5\, N(s)}{f^2}} \qquad \text{(A2)}$$

where f is the radio wave frequency, and
N(s) is the electron density (el m^{-3}) at each point along the line of integration.

The height of the centre of a horizontally stratified layer containing a tilted section can conveniently be described by:

$$h(x) = \frac{H}{\pi} \arctan\left(\frac{\pi x}{H}\right) \qquad \text{(A3)}$$

where H is the vertical height of the step, and
x is the horizontal distance variable.

The vertical electron density variation through the layer has been assumed to vary in a Gaussian fashion, therefore the ionisation density N(x) at each point along the line of integration can be expressed as:

$$N(x) = N_B + N_0 e^{-\left(\frac{2[s(x)-h(x)]}{1.201\,T}\right)^2} \qquad \text{(A4)}$$

where N_B is the 'background' ionisation in the vicinity of the layer,
$N_0 + N_B$ is the maximum electron density at the layer centre,
T is the vertical half-width of the layer, and
s(x) is the particular line of integration given by:

$$s(x) = \cot(zen)(x - x_{off}) \qquad \text{(A5)}$$

where zen is the zenith angle of the line of integration, and
x_{off} defines the horizontal position of the integration line from the tilt centre.

In this particular case, the layer is assumed to be infinitely extended in the horizontal x-direction and so equation (A1) can be rewritten:

$$\phi(s) = \frac{2\pi}{\lambda \sin(zen)} \int_{x\,min}^{x\,max} \left(1 - n(s(x) - h(x))\right) dx - \phi_0 \qquad \text{(A6)}$$

Here ϕ_0 represents a baseline phase path defect introduced by the presence of the untilted layer, its value is calculated using equation (A6) with parameter x_{off} set to a large negative number to avoid integrating in the vicinity of the tilt.

For each line of integration defined by a particular value of x_{off}, integration is performed over the range:

$$xmin = \left(\frac{-h}{2} - 5T\right)\tan(zen) + x_{off} \text{ to } xmax = \left(\frac{h}{2} + 5T\right)\tan(zen) + x_{off}$$

The halfwidth of the resulting wave front normal to the line of integration is found iteratively via a step search in x_{off}, and interpolation.

18. GROUND BASED ELECTRIC FIELD MEASUREMENTS AT DAVIS STATION, ANTARCTICA

M.H. Hesse[1], G.B. Burns[1] and S. Malachowski[2]

[1] Auroral and Space Physics
Antarctic Division
Kingston Tasmania 7050
Australia

[2] Physics Department
La Trobe University
Bundoora Victoria 3083
Australia

ABSTRACT

An electric field mill has been used to measure the vertical component of the earth's electric field at Davis station, Antarctica (68.6°S, 78.0°E, geographic coordinates; 74.6°S, magnetic latitude) since March 1988. Comparisons of electric field values with a range of simultaneously recorded meteorological data are used to determine the magnitude and variability of local influences at the Davis site. Dependencies on wind speed, wind direction and airborne snow are demonstrated. The relationship between the electric field values and the wind speed is shown to be loosely dependent on the level of the relative humidity.

Approximately one year's data (8 July 1989 to 10 July 1990) is subjectively examined to determine periods when the 'fair weather' electric field is expected to be dominant. From this 'fair weather' data set, diurnal electric field curves are obtained for the four seasons. The data set is also examined for evidence of further contamination from local sources. On the basis of the results obtained, a program for investigating these effects, deriving more accurate diurnal 'fair weather' electric field curves, and determining the extent of any magnetospheric control of the electric field at Davis, is outlined.

18.1 INTRODUCTION

An electric field of the order of 300 kV is maintained, principally by world-wide thunderstorm activity, between the lowest reaches of the ionosphere and the ground. At ground level this electric field is of the order of 100 V m^{-1}. In regions of 'fair weather' a current density of the order of 3 pA m^{-2} (Burke and Few 1978) flows from the ionosphere to the earth.

In the polar regions, the interaction of the solar wind and the earth's magnetic field leads to the establishment of a variable electric potential of 20 to 150 kV between the dawn and dusk sectors of the polar cap. This electric potential drives the plasma flow in the polar ionosphere, and by collisional interaction also controls the motion of the neutral atmosphere in the polar thermosphere.

The interaction of these electric fields provides a mechanism by which a so-called 'sun-weather' process (i.e. a linkage between solar activity and tropospheric weather systems) may operate.

The possibility of distinguishing the various influences on the measurement of the vertical electric field at any site relies on expected differences due to the control mechanisms.

1. The thunderstorm generated electric potential should be globally synchronised and may be expected to vary diurnally and seasonally in a manner related to globally integrated thunderstorm activity.

2. Any magnetospheric influences should maximise where the diurnal variation of the ionospheric potential generated by the interaction of the solar wind and the earth's magnetic field maximises (i.e. at auroral latitudes). The magnitude of the modification to the diurnal variation should be dependent on the magnitude of the polar cap potential.

3. Local meteorological and anthropological influences will be related to local parameters.

The instrumentation for this experiment is located at Davis because, of the Australian Antarctic stations, it has the most consistently fine weather (no Australian Antarctic station is ideal in this respect). In addition, its magnetic invariant latitude is 74.6°S, an ideal latitude for seeking any magnetospheric influence.

18.2 INSTRUMENTATION AND DATA COLLECTION

A rotating dipole sensor of the 'field mill' type, similar to that used by Park (1976), is used to monitor the vertical electric field at the Davis site.

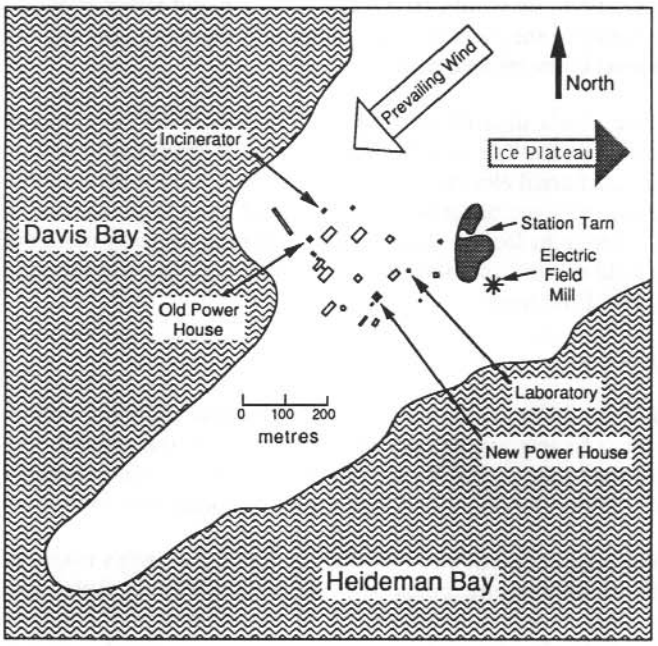

Figure 1. The location of the electric field mill site relative to Davis station buildings and the surrounding coastline.

The values for the electric field (in V m^{-1}, positive for a downward directed field) used in this paper refer to the potential applied across parallel plates of a calibration box used with the mill. They are not intended as an absolute representation of the electric field at the site. From the calibration measurements, the mill output is linear to the order of 0.1%. This amounts to less than 1 V m^{-1} for 'fair weather' values of the electric field. A variation in offset of up to 11 V m^{-1} between calibrations was recorded over the period of the measurements reported here.

The electric field mill is located approximately 200 m east (upwind) of the main physics laboratory (Figure 1). Measurements of the wind speed, wind direction, temperature, relative humidity and atmospheric pressure are also made at this remote site. Data from all sensors are recorded once every 10 seconds, and the data are transmitted back to the Antarctic Division (Hobart) via a satellite data link.

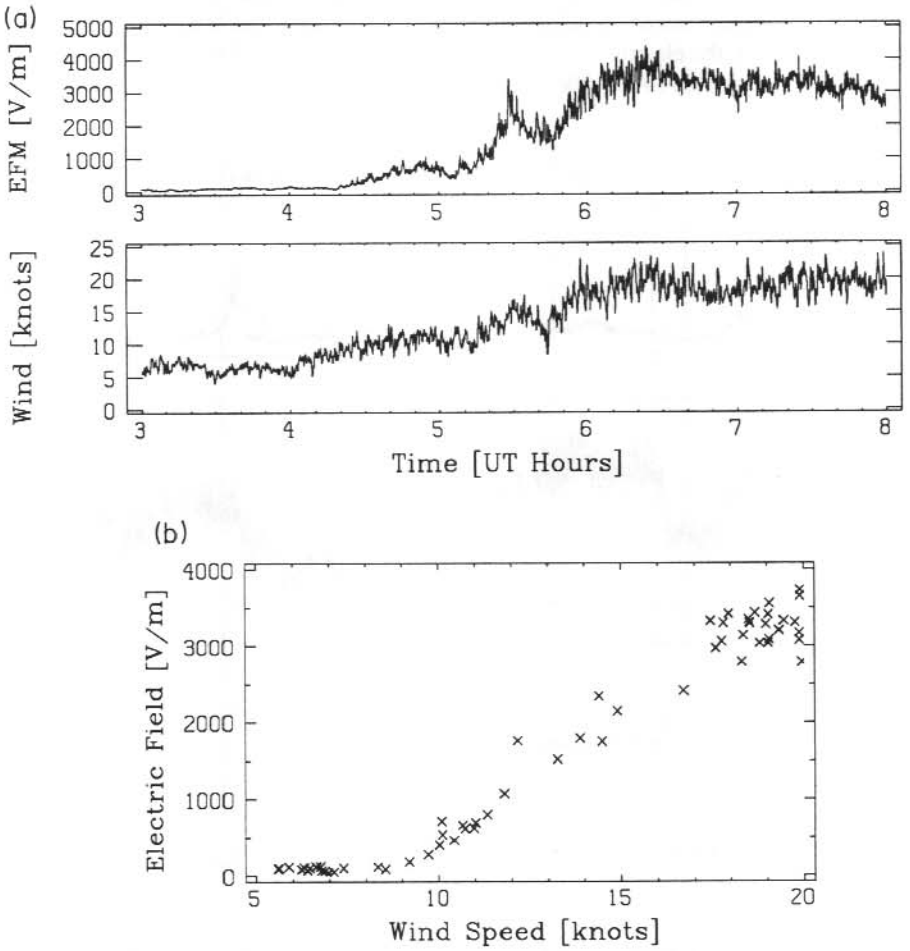

Figure 2. Data from 7 August 1990.
(a) The electric field response to a gradual rise in the wind speed
(b) A plot of five minute averages, for the event in (a).

18.3 LOCAL INFLUENCES ON THE VERTICAL ELECTRIC FIELD

A visual scan of the data from March 1988 to December 1990 was undertaken to identify cases where correlations with local phenomena were apparent. The bulk of the correlations found were with wind speed, but a limited number of wind direction and humidity effects were also detected. No correlations with temperature or pressure were visible in this initial examination of the data.

18.3.1 *Strong positive correlations of electric field with wind speed*

When the wind speed rises above a certain critical value, the electric field generally increases sharply with wind speed as shown in Figure 2. In this case a critical wind speed of around 9 knots is apparent. The critical wind speed values vary considerably from event to event however, and for 30 events specifically analysed, the values ranged from as low as 4 knots to as high as 28 knots. The 'fair weather' electric field at Davis lies between about 80 V m^{-1} and 250 V m^{-1}. In this example however, the electric field values reached in excess of 3500 V m^{-1}. Local effects of this magnitude are very easy to identify.

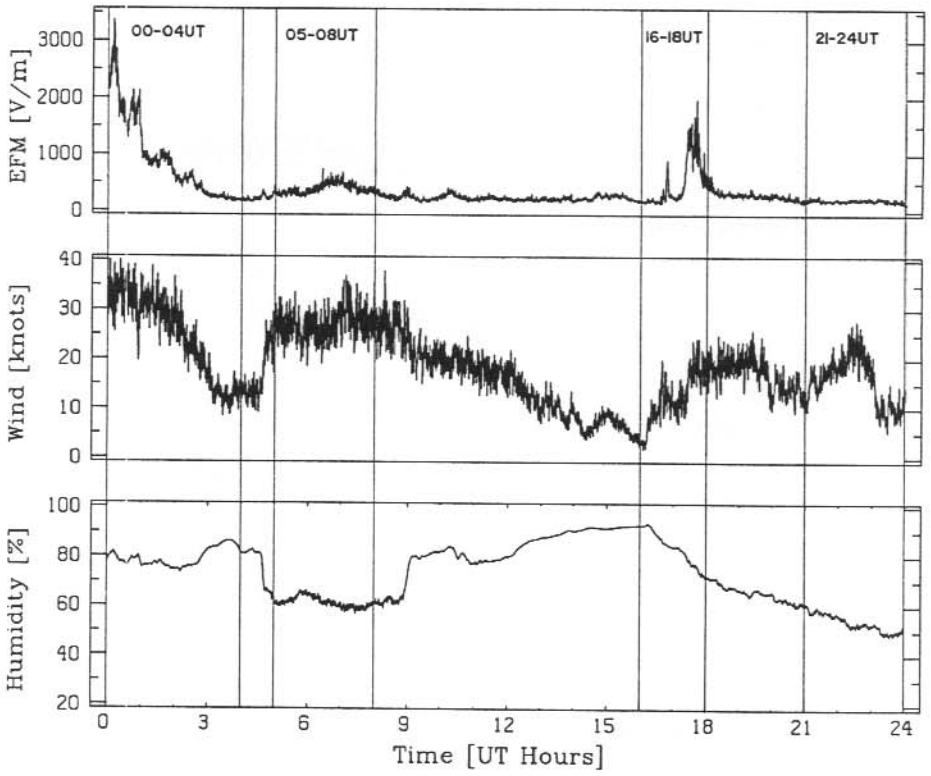

Figure 3. The electric field, wind speed and relative humidity recorded on 29 October 1989. Four intervals of varying average relative humidity are marked. When the relative humidity is high, the electric field responds more dramatically to the wind speed.

18.3.2 *The effect of humidity on strong positive correlations between the electric field and the wind speed*

There is evidence to suggest that the relative humidity plays a part in determining how strongly the electric field correlates with the wind speed. This dependence on relative humidity is best demonstrated by the data from 29 October 1989. Figure 3 shows the time-series of the electric field, wind speed and relative humidity for this day. Figure 4 shows plots of the electric field against wind speed for four intervals from this day. When the humidity is high, the correlations between wind speed and wind direction are strong, and when it is low, the correlations are weak.

Typically for electric field analysis, what appears dramatically correlated in one example is found to be highly variable when a larger number of events are investigated. In an attempt to gain some quantitative measure of the effect of humidity on the electric field, Figure 5 plots the 'electric field at 20 knots' against humidity for a number of events. The error bar indicates the range of electric field values recorded at a wind speed of 20 knots for each event. Figure 5 shows that below 45% humidity, there are no cases of the electric field having increased at wind speeds of 20 knots. The lower the humidity, the less likely the electric field will be dramatically influenced by the wind speed. There are however, exceptions at both high and low wind speeds.

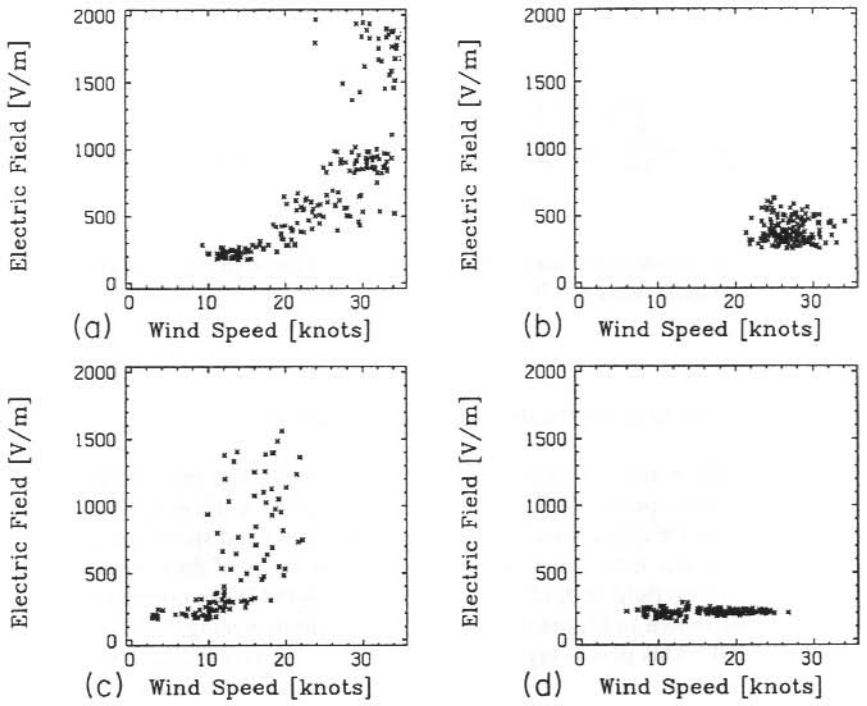

Figure 4. Plots of one minute averages of the electric field values against wind speed for the four intervals of varying humidity from 29 October 1989, marked in Figure 3.
(a) 00 UT to 04 UT, ave. humidity 79% *(b) 05 UT to 08 UT, ave. humidity 61%*
(c) 16 UT to 18 UT, ave. humidity 84% *(d) 21 UT to 24 UT, ave. humidity 45%*

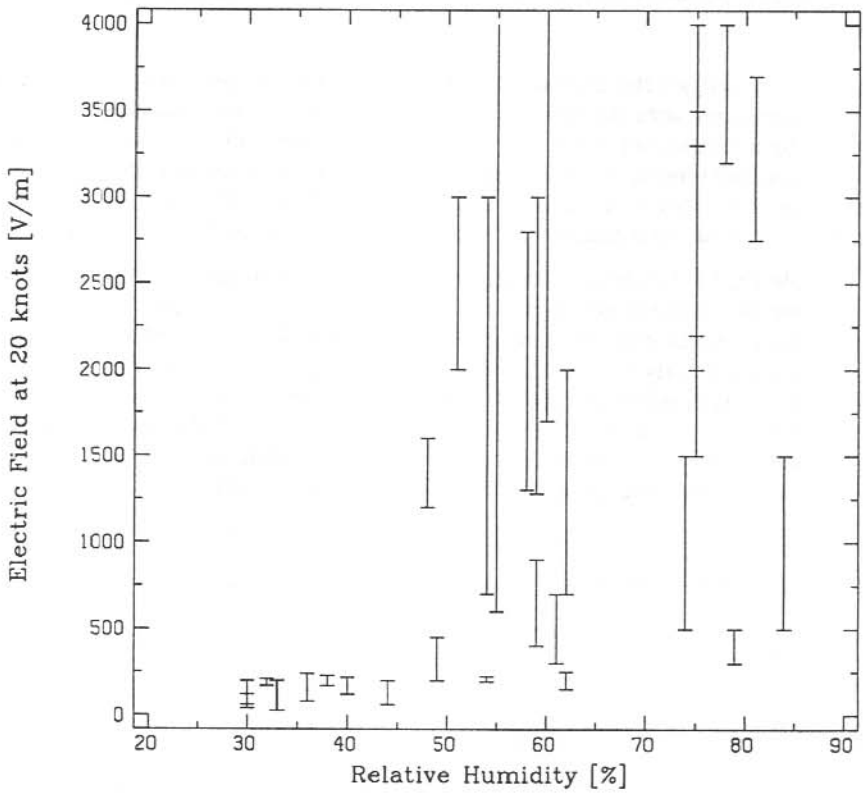

Figure 5. The range of electric field values observed at a wind speed of 20 knots, plotted against the average relative humidity value for 30 events.

18.3.3 *Negative correlations of electric field with low wind speeds*

At low wind speeds, there are examples of the average electric field increasing slightly with decreasing average wind speed. When viewed on an expanded time scale, this negative correlation generally has the appearance of a sudden decrease in wind speed corresponding to a positive spike in the electric field value. Figure 6 shows six hours of data from 28 July 1990. The major peaks in electric field at 0215 UT, 0415 UT and 0445 UT are correlated with dips in the wind speed. Also shown in Figure 6 is a plot of one-minute averages of the electric field against the wind speed. This plot is typical of negative correlations between wind speed and electric field.

Figure 7 shows an expanded time view of 24 minutes of data from 22 September 1990. The negative spike in wind speed, which correlates with the positive spike in electric field, lasts of the order of 6 minutes. This is more typical of the duration of these spikes than the event shown in Figure 6.

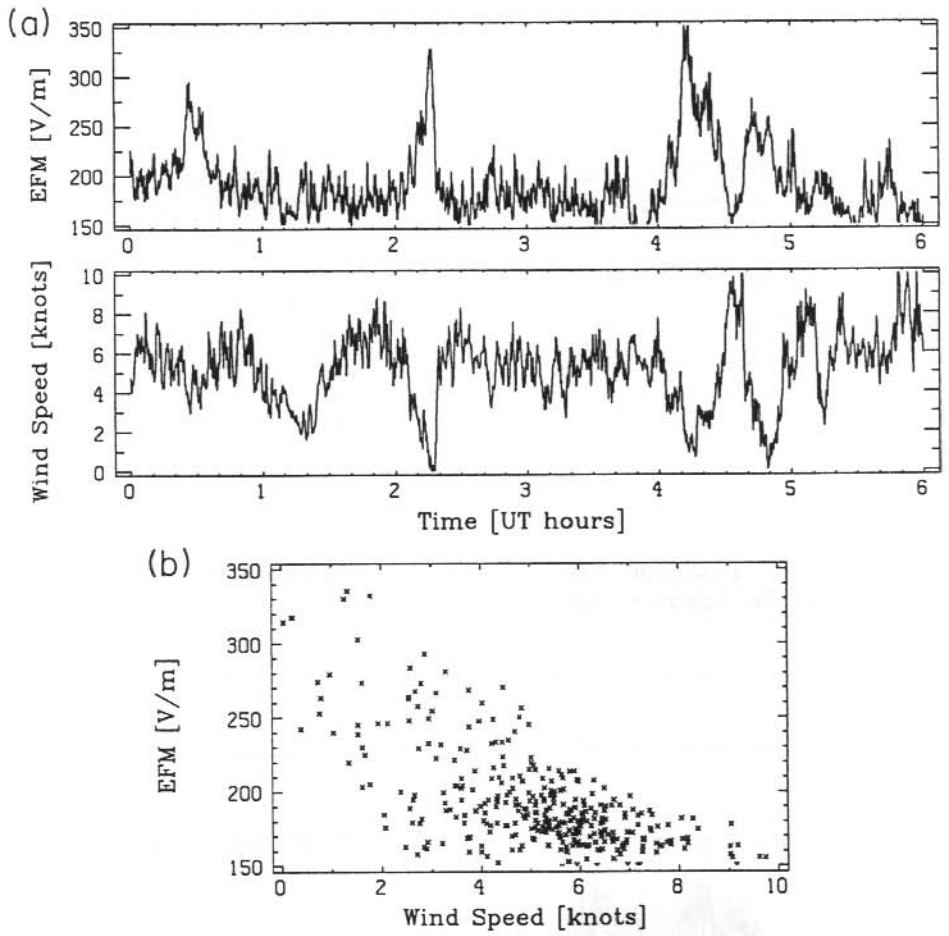

Figure 6. Six hours of data from 28 July, 1990.
(a) Showing a negative correlation between the electric field values and the wind speed.
(b) A plot of one-minute averages of the data shown in (a).

18.3.4 *Direct correlations of electric field with humidity and snow*

When the humidity rises to very high levels because of blowing or falling snow, dramatic positive and negative excursions appear on the the electric field signal. Blizzards are often accompanied or preceded by snow falls. In such cases the effect on the electric field is unpredictable, but often dramatic. It is likely that the effect is due to a direct interaction of the airborne snow with the electric field mill antenna, and that the high relative humidity is just an associated effect.

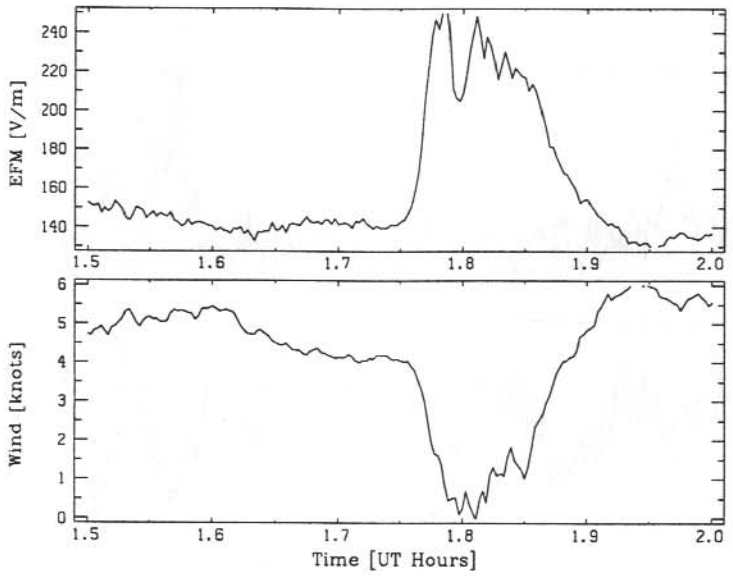

Figure 7. A high time resolution plot showing a decrease in wind speed associated with a spike in electric field values. The data are from 22 September 1990.

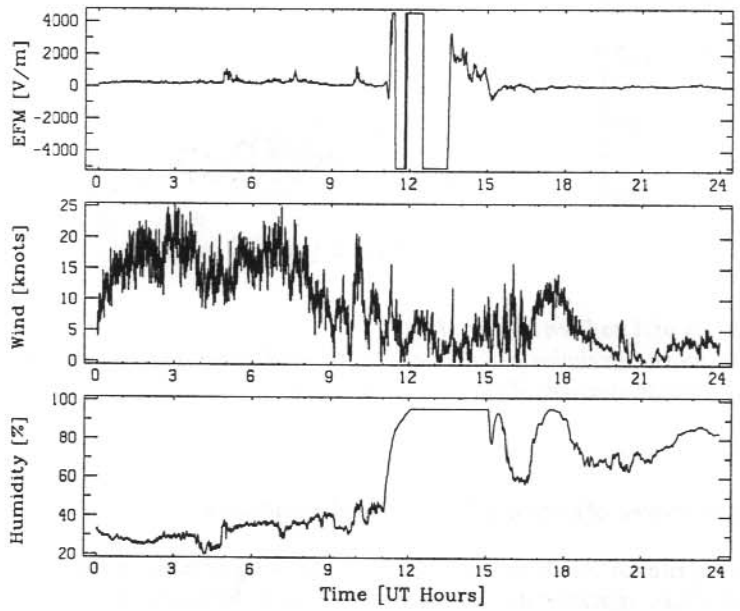

Figure 8. Data from 2 February 1990, showing the dramatic effect that snow showers (in the interval 11 UT to 15 UT) may have on the electric field values. Note the high humidity during this interval, and that the electric field excursions are both positive and negative.

Figure 8 shows electric field, wind speed and humidity data from 2 February 1990. Three-hourly meteorological observations record that from 00 UT to 09 UT the 'visibility' was around 30 to 40 km. By 12 UT the visibility dropped to 500 m, coinciding with a significant snowfall. The snow shower is clearly visible in the electric field signal, which undergoes several rapid sign reversals between 11 UT and 15 UT. The saturation of the electric field and humidity channels in this example occurs as a result of hardware limitations.

Figure 9 shows 4 hours of data from 5 June 1989. These data show a fall in the electric field preceding the rapid rise at 0830 UT. Note that while on the scale that the data is presented the electric field appears to be falling gradually, the magnitude of the variation is substantial and that the electric field actually reverses direction (becomes negative). Meteorology records indicate that the visibility was reducing from 10 km at 00 UT to 400 m at 09 UT, due to falling snow. This may account for the 'more negative' trend in the electric field measurements prior to the wind associated increase.

While the examples shown in Figures 8 and 9 are easy to pick and exclude from any fair-weather analysis, subtle gradual decreases in electric field which may be associated with local cloud cover, would be more difficult to notice. The difficulty with such possible variations is that they may not be correlated with any of the routinely recorded meteorological parameters.

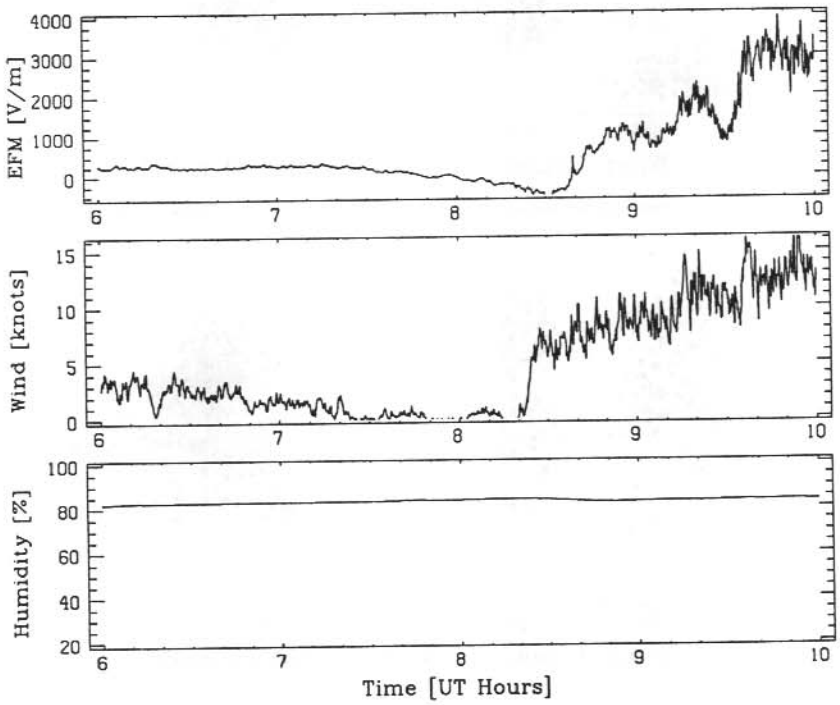

Figure 9. Data from 5 June 1989 showing a variation in the electric field associated with snow showers. Note that the electric field becomes substantially negative before the wind associated increase. The relative humidity maintains a high, fairly constant value throughout this event.

18.3.5 *Correlations of electric field with wind direction*

Station pollution may contaminate the electric field measurements when the wind comes from between 240°E and 320°E. The 14 hours of data plotted in Figure 10a illustrate a case where winds from the general direction of the station are associated with significantly higher electric field values. Figure 10b shows that this effect is not simply a by-product of the wind speed correlation covered in Section 18.3.1.

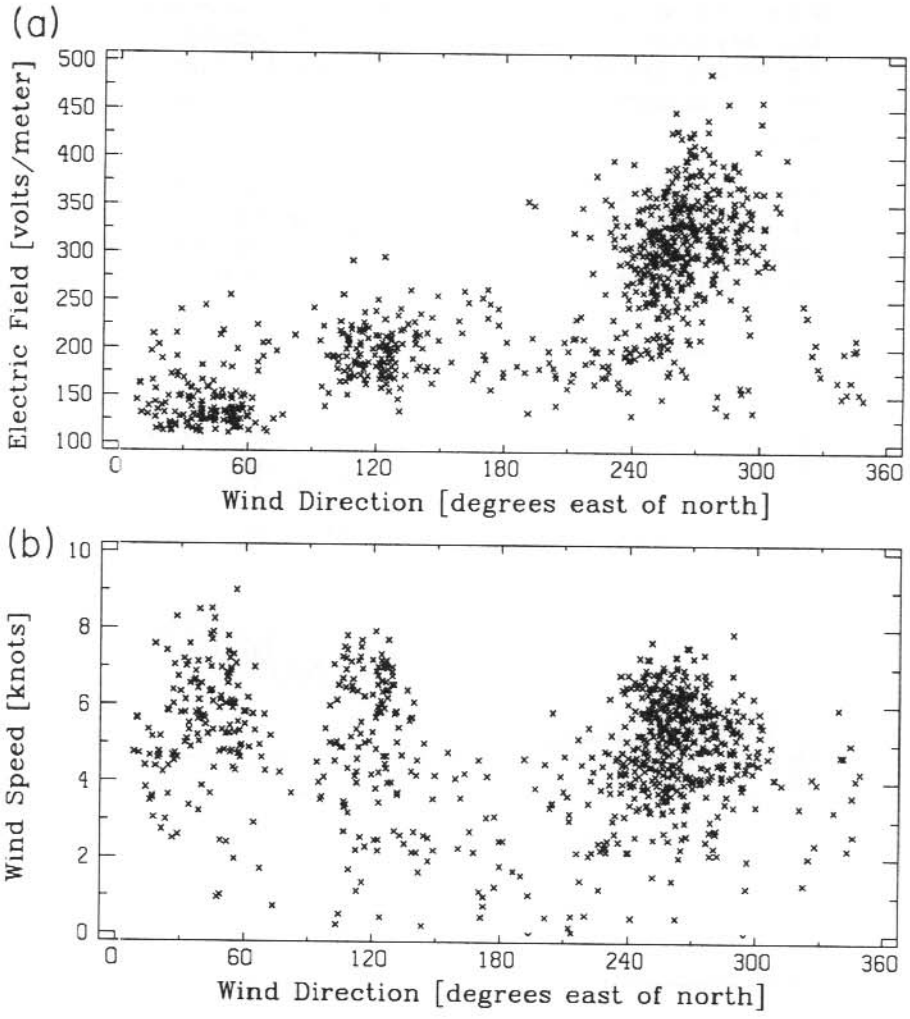

Figure 10. Data from 02 UT to 16 UT on 17 February 1990.
(a) electric field versus wind direction
(b) wind speed versus wind direction

18.3.6 *Selection of data to exclude local effects*

Recognising the more dramatic examples of local influences on the electric field measurements is relatively easy, but defining an objective method of data selection to exclude such events is very difficult. To ignore all electric field data with associated wind speeds above the lowest wind speed for which a strong positive association with electric field has been observed (Section 18.3.1), and to ignore all data with an associated wind speed less than the highest wind speed for which a negative correlation with wind speed has been observed (Section 18.3.3), is to exclude all data! Instead, we make the following subjective judgements.

Local effects are *very likely* to influence the measurement of the electric field at the Davis site if:

1. The wind speed is above 25 knots (Section 18.3.1). The probability of the electric field being affected at a particular wind speed is dependent on the relative humidity (Section 18.3.2), but for wind speeds above 25 knots the electric field measurement is *very likely* to be affected, independent of the relative humidity level.
2. The relative humidity is above 85% (snow a possibility, Section 18.3.4).
3. The wind is coming from the direction range between 240°E and 320°E (Section 18.3.5).

Local effects *might* influence the measurement of the electric field at the Davis site if:

1. The wind speed is above 20 knots (Section 18.3.1).
2. The wind speed is above 8 knots and the relative humidity is above 45% (Sections 18.3.1 and 18.3.2). The probability of the wind speed affecting the electric field is dependent on the relative humidity level at the time (Section 18.3.2).
3. The wind speed is below 10 knots (Section 3.3). Note the overlap with the item above, but remember that we are talking *might*.

Local effects are *unlikely* to influence the measurement of the electric field at the Davis site if:

The wind speed is above 10 knots *and* the wind speed is below 20 knots *and* the relative humidity is less than 45% *and* the wind is not coming from the direction range 240°E to 320°E.

There are four mechanisms which could account for each effect:

1. The local parameter is controlling the electric field.
2. The local parameter is affecting the measuring system directly.
3. The electric field is controlling the local parameter.
4. Both the electric field and the local parameter are related to a third parameter which has not been considered.

In the first two cases the measured electric field will not be representative of the global electric field, in the third case it will be, and in the fourth case it might be. As we do not have sufficient information to determine which of the four mechanisms is at work, it must be assumed that all data which shows a correlation with local parameters are not representative of the global field.

18.4 SEASONAL, DIURNAL VARIATIONS – AN INITIAL ANALYSIS

Approximately one year of Davis electric field and associated meteorological data was visually examined, and data periods when the fair-weather field was likely to be dominating were selected.

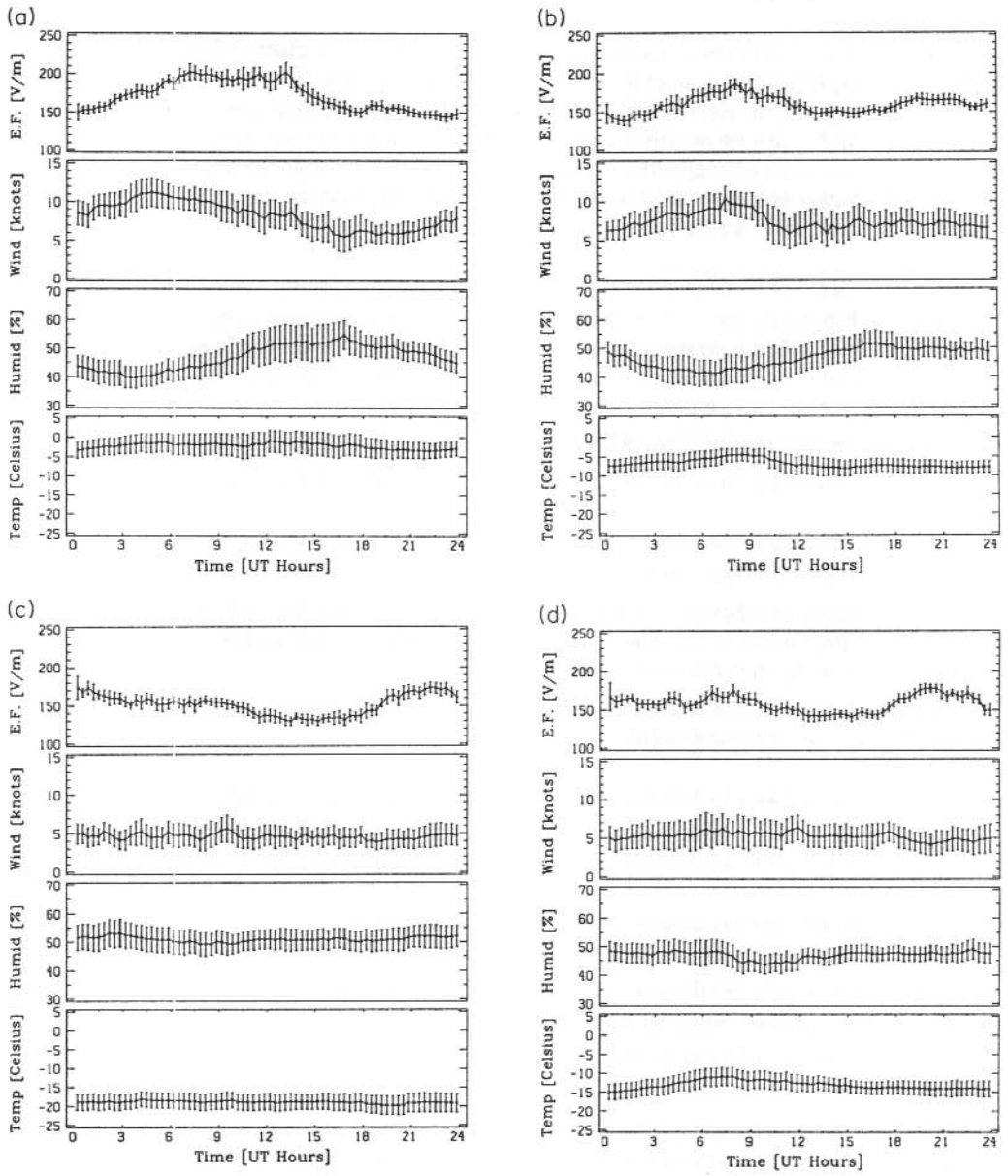

Figure 11. Seasonal diurnal curves of electric field, wind speed, humidity and temperature for the selected data.

(a) Summer (1 November – 31 January)
(b) Autumn (1 February – 30 April)
(c) Winter (1 May – 31 July)
(d) Spring (1 August – 31 October)

The data considered were from the period 9 July 1989 to 10 July 1990. In total, 2364 hours of data were included in the analysis, consisting of data segments as short as 2 hours.

Each of the chosen data segments was averaged with a bin size of 20 minutes and the data collated into periods covering the four seasons. Diurnal curves were then generated by combining all the data segments available for each season. A simple average of the data in each time bin was used to derive the diurnal curves for the meteorological parameters. The electric field however, demanded a more complex form of averaging in order to remove the significant variability in the DC offsets of the various data segments. The electric field diurnal curves were reconstructed from averages of the differences between consecutive 20 minute values. The discontinuities occasionally apparent between the 24 UT and 00 UT values are due to the preference in the selection process for choosing 00 UT start times and 24 UT finish times.

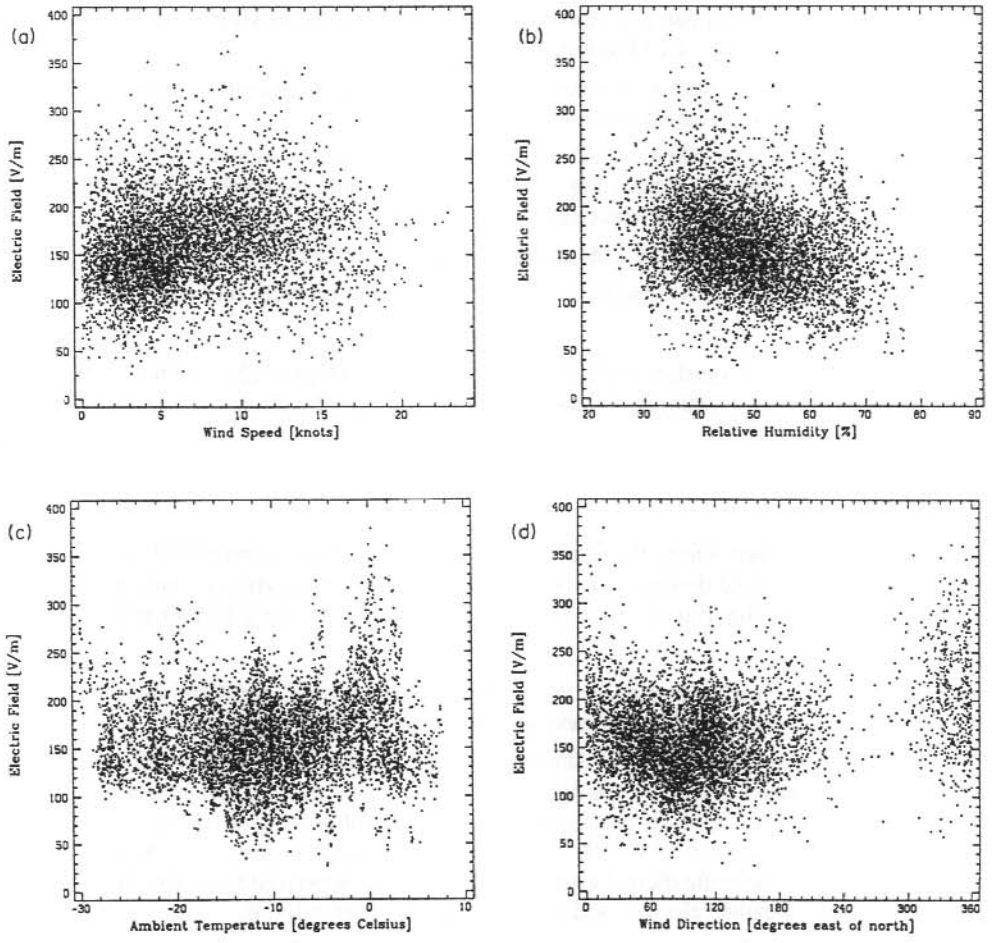

Figure 12. The 20-min. electric field averages 'scatter' plotted against the associated averages of: (a) wind speed, (b) relative humidity, (c) temperature, (d) wind direction.

Figure 11 shows the diurnal variations for the electric field, wind speed, humidity and temperature calculated for the four seasons. The error bars plotted are +/- twice the standard error of the parameters averaged. It is important to remember that the results presented here are from an initial analysis of subjectively selected data.

18.5 FURTHER POSSIBLE METEOROLOGICAL INFLUENCES

The 'fair weather' data set described above was further examined for evidence of any local influences which might remain. Figure 12 shows scatter plots of the 20 minute electric field averages, versus the associated averages of the wind speed, relative humidity, temperature and wind direction respectively.

1. The weak correlation apparent in the wind speed plot (Figure 12a) yields a linear best fit of: E [electric field (V m^{-1})] = 1.9 S [speed (knots)] + 145.

2. The weak correlation apparent in the humidity plot (Figure 12b) yields a linear best fit of: E [electric field (V m^{-1})] = -1.2 H [humidity (%)] + 214.

3. The plot of the electric field versus temperature (Figure 12c) shows an excess of high electric field values associated with temperatures around 0°C.

4. Very few values below 100 V m^{-1} are recorded for temperatures below -20°C. This may be an indication that these low values are associated with cloud, as lower temperatures in the Antarctic are generally associated with clear skies.

5. The wind direction plot (Figure 12d) shows no major correlation.

6. A similar comparison of the electric field and atmospheric pressure (not included) shows no apparent correlation.

The weak correlations of the electric field with the wind speed (Figure 12a) and humidity (Figure 12b) are insignificant in accounting for the diurnal variations in the electric field curves (Figures 11a–d).

18.6 DISCUSSION

As has been indicated previously, the results presented here are from an initial look at subjectively selected data. Before final diurnal 'fair weather' electric field curves are presented for the Davis site, we propose that the 'fair weather' data set be subjected to these further reductions and checks.

1. Electric field data recorded when the temperature is between -3°C and +3°C will be discarded from the data set on the basis of the temperature association shown in Figure 11c.

2. Davis station 3-hourly meteorological information of 'visibility' and 'total cloud cover' will be obtained for the period covered by the data set. Periods when the visibility is less than normal will be excluded from the data set because of the possibility of drifting or falling snow affecting the data as indicated in Section 18.3.4. The 3-hourly 'total cloud cover' data will be used to determine whether an accurate diurnal electric field curve can be derived from 'cloudy times' data. If not, then the 'fair weather' electric field data set will be further reduced.

Once a final 'fair weather' data set has been selected following the investigations outlined above, seasonal diurnal electric field variations will be determined. An auroral activity parameter will

then be used to split the data and determine if a magnetospheric influence is apparent in the ground-measured vertical electric field at Davis. Finally, the consistency of the results obtained will be investigated by extending the analysis to the full data set available since March 1988.

18.7 ACKNOWLEDGMENTS

The collection of the Davis electric field data for 1989 was the responsibility of Dr Russell McLoughlin. Meteorological information which was not recorded directly in association with the electric field data was supplied by the Bureau of Meteorology. The manufacture of research instrumentation and the maintenance of a remote observatory facility requires concerted effort from many people. To those who assisted in ensuring the collection of these data, out thanks.

REFERENCES

Burke, H.K. *and* Few, A.A. (1978). Direct measurements of the atmospheric conduction current. *Journal of Geophysical Research 83*:3093 – 3098.

Park, C.G. (1976). Solar magnetic effects on the vertical atmospheric electric field at Vostok, Antarctica. *Geophysical Research Letters 3*:475 – 479.

19. IONISATION BELOW 55 KM IN THE ANTARCTIC MESOSPHERE

H.A. von Biel

Department of Physics
University of Canterbury
Christchurch
New Zealand

ABSTRACT

The characteristics of a thin layer of ionisation occasionally observable during the Antarctic summer months at heights between 40 km and 55 km, are described. The results presented pertain to data collected over five consecutive years since 1987 from a 2.9 MHz partial reflection program operated at Scott Base.

The maximum density of the layer is most frequently found to be in the vicinity of 600 cm^{-3}, which is sufficiently low to rule out ionisation by energetic protons, while photo-ionisation would produce a layer of nearly twice the observed thickness of about 12 km. It is shown that ionisation by relativistic electrons might well account for the production of this ionisation.

19.1 INTRODUCTION

At the 1988 SCAR Meeting in Hobart, and more recently at the 1990 SCAR Meeting in Sao Paulo, Brazil, some of the results from the Canterbury University partial reflection program at Scott Base were presented. These results indicated that significant ionisation could occasionally be detected in the height interval between 40 and 60 km.

The partial reflection experiment was first performed by Gardener and Pawsey (1953), and details on more recent improvements to the experimental technique can be found in a number of papers (e.g. Belrose and Burke 1964, von Biel 1976). A skeleton description of the operating principles is as follows.

Back scattered radiowave energy at 2.9 MHz from irregularities in the D region are analysed to yield the differential absorption and the differential phase between the magneto-ionic wave components. These data are interpreted in terms of the electron density per unit volume at a given scattering height.

It should be noted that ionisation can only be computed for a given scattering height when an echo is received from that height and when the back scattered magneto-ionic wave components suffer unequal absorption. These conditions are quite frequently satisfied at scattering heights ranging from 40 to 60 km in the mesophere at Scott Base (von Biel 1989), and suggest that a layer of ionisation occasionally exits in that height interval.

The results presented in this paper were obtained over the five year time interval from January 1987 to January 1992, and the purpose of the present paper is to update the earlier results, as well

as to investigate the most likely mechanism that might be responsible for the observed phenomenon.

19.2 RESULTS

Figure 1 shows a 'normal' electron density profile as well as a profile which exhibits the ionisation layer with its maximum density at 48 km. The latter was computed from data collected at Scott Base on 27 December 1989, at 1500 hours (UT). The three-hour magnetic K index, which commonly has a value between 2 and 4, was 6 at that time and was, therefore, considerably larger than is normally observed. Also shown in this illustration is a parabolic approximation to the layer which exhibits a maximum electron density N_{max} at a height H_{max}. The thickness of this layer at heights that correspond to 0.5 N_{max} is designated as ΔH and in this case amounts to 12 km. Figure 2 shows the distribution of values for ΔH obtained from nearly 3000 observations of the ionisation layer during the 5 year interval. From this figure it is apparent that the layer thickness is between 10 km and 14 km for nearly 60% of the observed cases. The distribution of values for the maximum density N_{max} of the layer is shown for the same time interval in Figure 3. Although this distribution shows a fairly broad peak in the range from 400 cm^{-3} to 800 cm^{-3}, it should be remembered that the partial reflection technique yields electron densities values which can readily differ from the true value by a factor of two.

Figure 4 shows the distribution of values for the height H_{max} at which the maximum density N_{max} occurs. Data for the five consecutive years are presented as separate plots in order to show

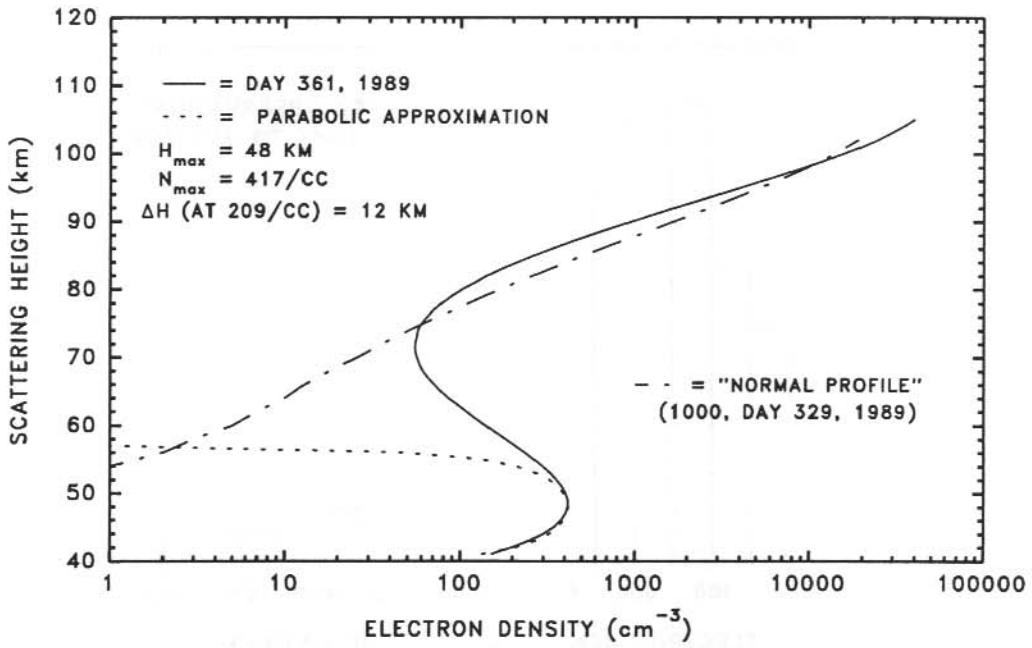

Figure 1. Electron density profile and the parabolic approximation of the layer.

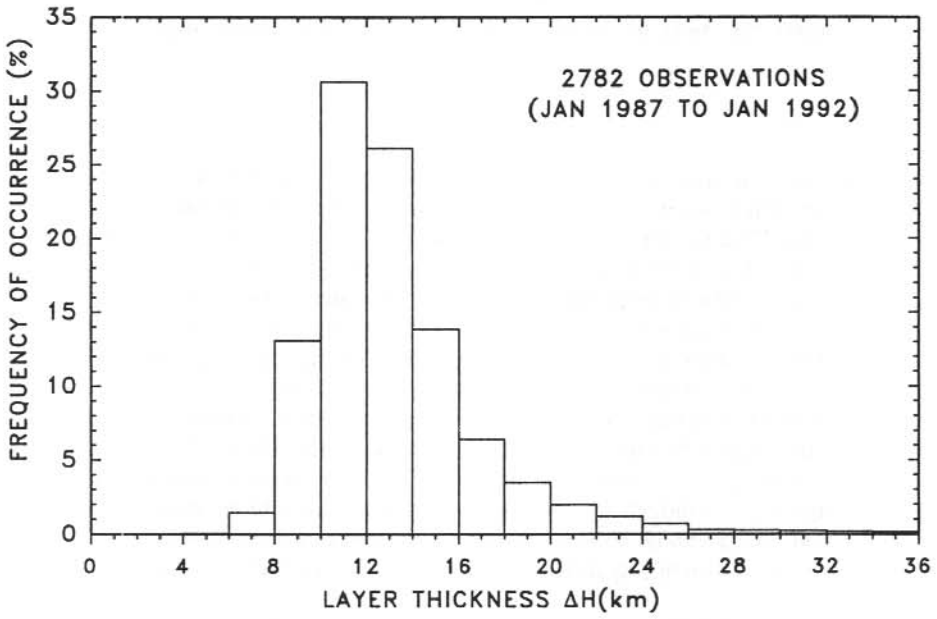

Figure 2. Distribution of the layer thickness ΔH at the half-maximum density.

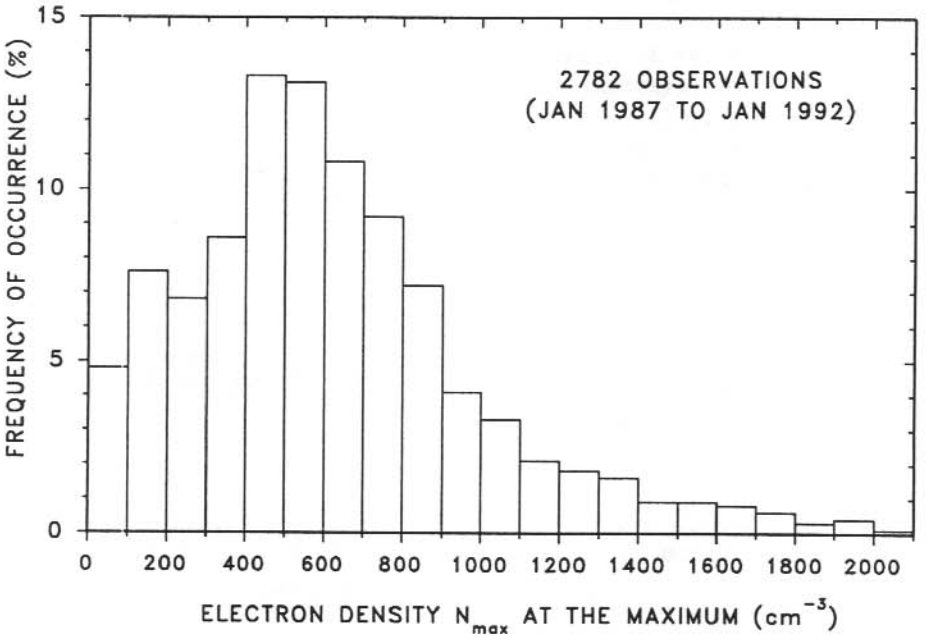

Figure 3. Distribution of the maximum electron density N_{max} of the layer.

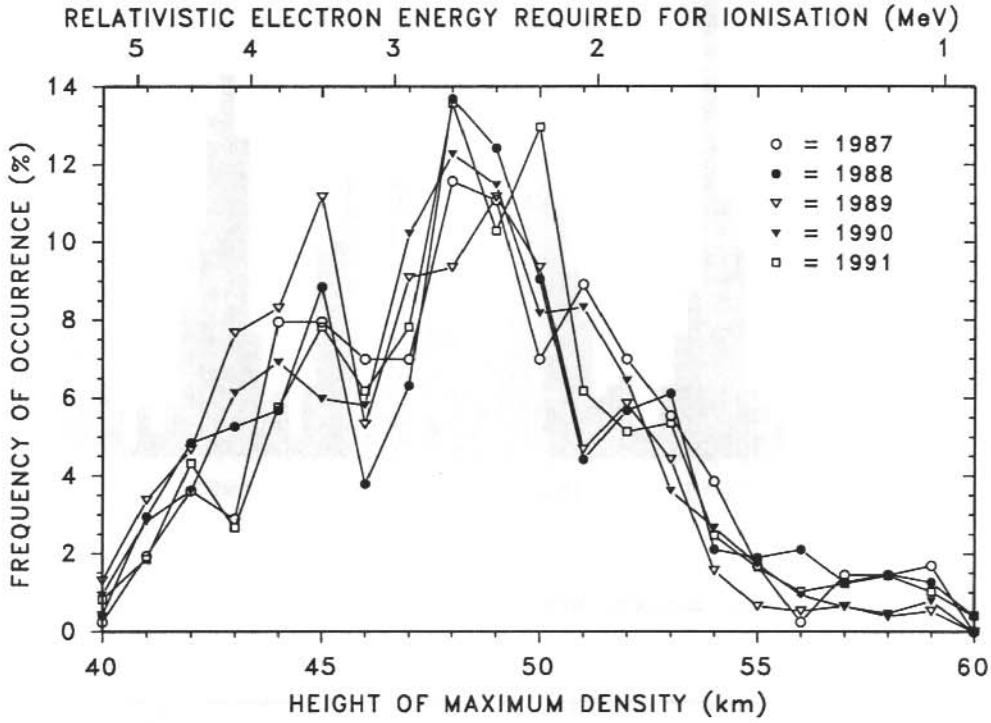

Figure 4. Distribution of the height of maximum density H_{max}.

their remarkable similarity. A second horizontal scale was added to this figure to indicate the energy required by mono-energetic electrons, normally incident upon the atmosphere, for maximum ion pair production at that particular height. Figure 4 should be valuable in assessing the energy spectrum of the particles that might be responsible for the observed ionisation.

Monthly mean values of occurrence of the ionisation layer are shown in Figure 5, and there can be little doubt that the phenomenon is most frequently observable during the austral summer months. The probability of observing the ionisation layer on a daily basis is plotted as a function of local time in Figure 6. Also shown in this figure are the approximate times of local magnetic noon and midnight and a curve which represents the sum of the mean value and the first three Fourier components of the data. This composite curve appears to fit the actual distribution quite well. When the data are sorted according to the solar zenith angle at the time of the occurrence, a remarkable result is obtained as shown in Figure 7. From Figure 7 it is apparent that by far the greatest number of occurrences of the ionisation are observed for zenith angles between approximately 77° and 83°. The zenith angle distribution for data that do not exhibit the low altitude ionisation are also shown in this illustration and should serve as a means for comparison.

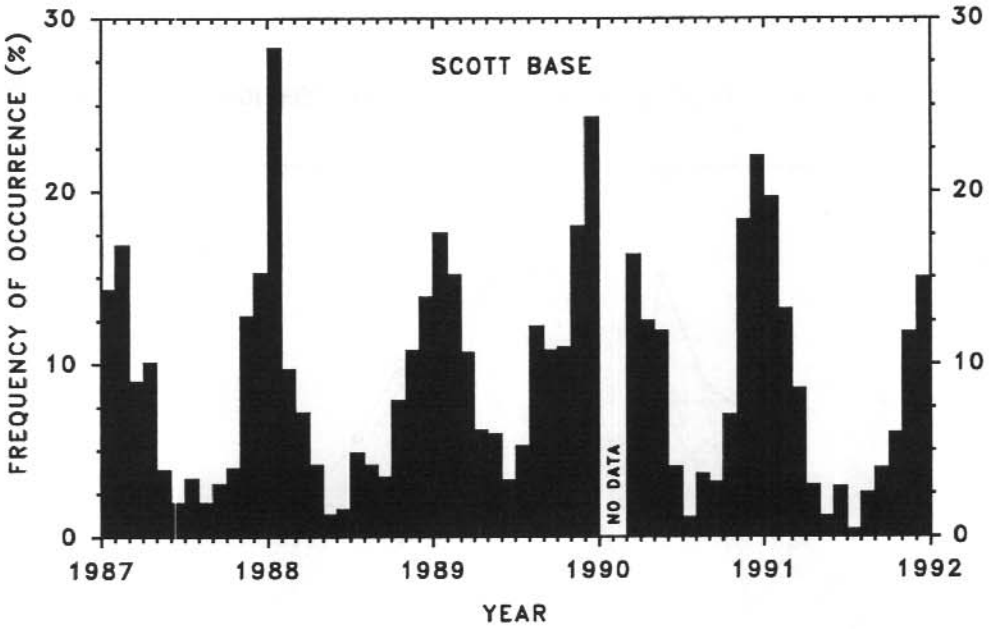

Figure 5. Monthly mean values of occurrence.

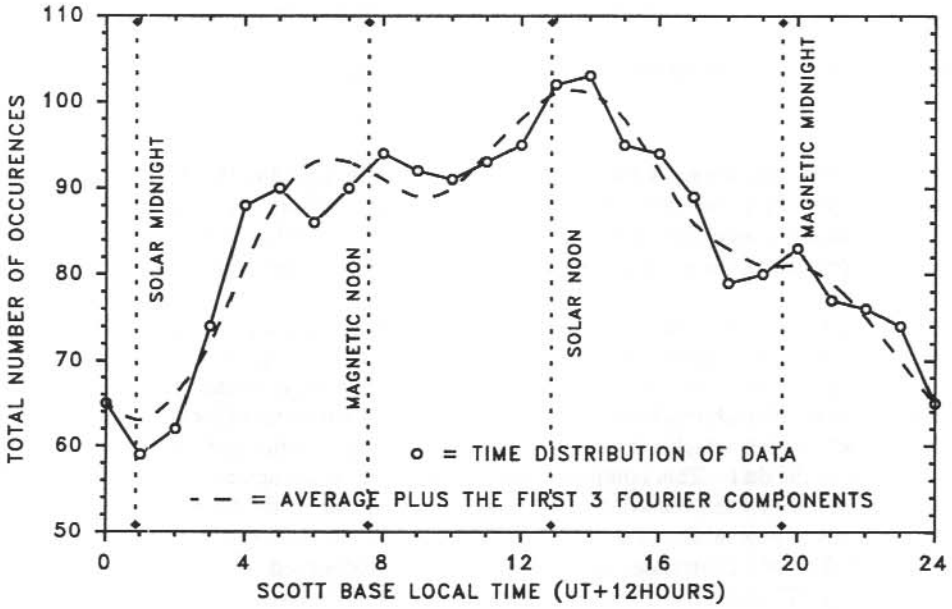

Figure 6. Time distribution of occurrences.

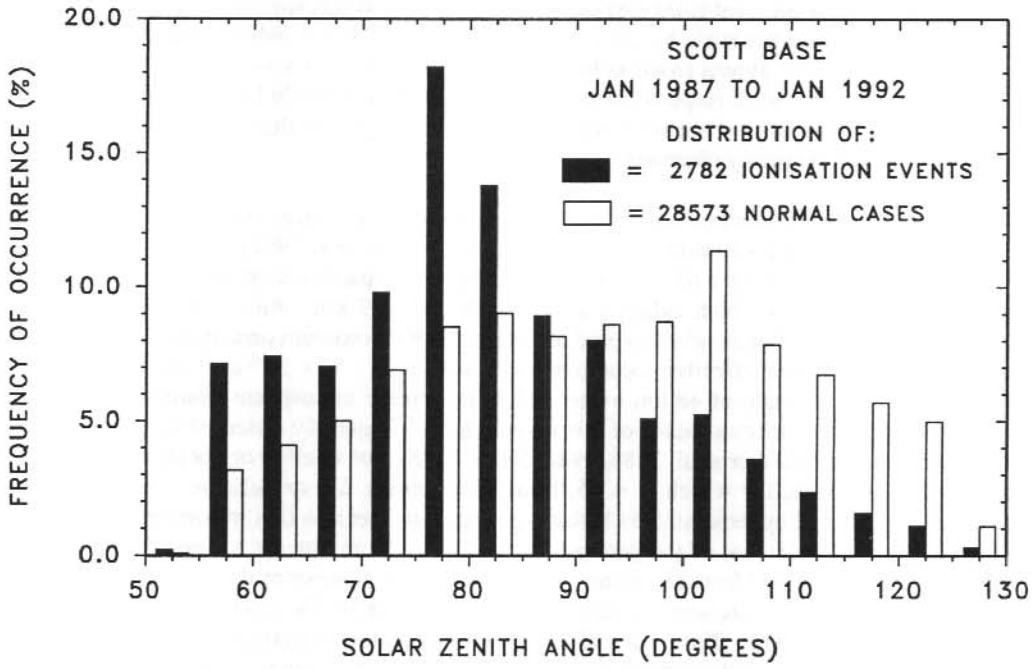

Figure 7. Probability of observing the layer at a given solar zenith angle.

19.3 DISCUSSION

One of the most frequent questions raised in connection with the observation of the anomalous ionisation concerns its life-time. To answer this question presents a problem because experimental data are collected for only 12 minutes of every hour, and although these data will confirm whether or not the layer was present during the data collection time, it could have come into existence at the termination of the previous experiment, and it could continue to exist up to the beginning of the next hourly experiment. The net result is an uncertainty about 2 hours. This uncertainty can be reduced considerably by considering sequential occurrences of the layer. An example of such a sequence of events is shown in Figure 8. When such data are used to calculate the probability that a certain layer life-time will be exceeded, then the graph shown in Figure 9 is obtained, from which one may conclude that the 'time constant' of the observed phenomenon is probably about 72 minutes, but it might be as long as 2 hours.

Finally there remains the question regarding the mechanism that might be responsible for the ionisation. Figure 10 shows the energy requirements for photons, electrons, and protons in order to ionize the atmosphere at a given height (Thorne 1980). If photons were responsible for the

ionisation, then a characteristic Chapman layer would be expected which should exhibit a half width ΔH somewhere between 2 and 3 atmospheric scale heights, depending on whether recombination or attachment is the predominant ionisation loss mechanism. During the summer months at Scott Base the scale height is about 9 km, and the expected half-width of the layer would then have to be almost twice as big as the observed value of about 10 to 12 km. On the other hand, if protons were responsible for the ionisation, then it would be expected (Reid 1974) that the maximum density of the layer would be substantially greater than about 600 cm^{-3}, which is the value most frequently observed.

That leaves relativistic electrons as the source of ionisation. The extent to which mono-energetic electron fluxes produce ionisation is shown in Figure 11 (von Biel 1992). Figure 12 shows the ion-pair production rate for 2.67 MeV electrons along with a parabolic approximation which has its peak at 48 km and which exhibits a half-width ΔH of 9 km. An electron flux of about 1500 cm^{-2} sec^{-1} would be required to produce a layer with a maximum density of 500 cm^{-3}. This estimate is based on an 'effective recombination constant' of 3.54×10^{-4} cm^3 sec^{-1} (Adams and Masley 1965) at a height of 48 km in the Antarctic summer atmosphere (Barnett and Corney 1985). Relativistic electron fluxes of this magnitude are frequently observed by geostationary satellites at L = 6.6 (Baker et al. 1986, 1987, Nagai 1988), but whether or not these results also apply to Scott Base, for which L = 35, remains a subject for speculation. An interesting observation reported by these authors is that the relativistic electron flux maximises about 4 to 5 days after an enhancement of the geomagnetic activity. In an attempt to see whether similar results could be obtained from the partial reflection data, the number of daily occurrences of the layer for a given epoch date were correlated with the mean daily AK index at Scott Base for ± 15 days from the epoch date. The results of this epoch correlation analysis are shown in Figure 13 and appear to indicate that the correlation maximises a few days on either side of the epoch dates.

19.4 CONCLUSION

The material presented in this paper provides additional evidence that a layer of ionisation is frequently present in the Antarctic mesophere over Scott Base. The data further indicate that the phenomenon observed is recurring year after year with a maximum probability of occurrence during the Antarctic summer, and that the layer thickness, as well as the height and maximum density, does not vary greatly from one year to the next.

If the ionisation were caused by relativistic electrons as was suggested by Aikin (1989, private communication) then there should be a correlation between the magnetic K index and the occurrence of the layer. The data appear to show such a correlation. It should be noted, however, that at times when large values of magnetic K index are observed the total absorption is frequently also very large, and the resulting experimental data are often unusable. The inference that the occurrence of ionisation is correlated with the magnetic K index should, therefore, be treated with caution.

Although it appears quite possible that relativistic electrons might be responsible for the observed ionisation layer, it is puzzling why such particle fluxes should exhibit any pronounced seasonal dependence, which is not characteristic of relativistic electrons detected by satellites. Also the large occurrence frequency of the layer at a solar zenith angle near 80° appears to suggest that the observed phenomenon is linked to solar emission of one form or another rather than particle

precipitation. It is hoped that the proposed VLF experiments to be conducted near Scott Base during the coming season will provide answers to some of these remaining questions.

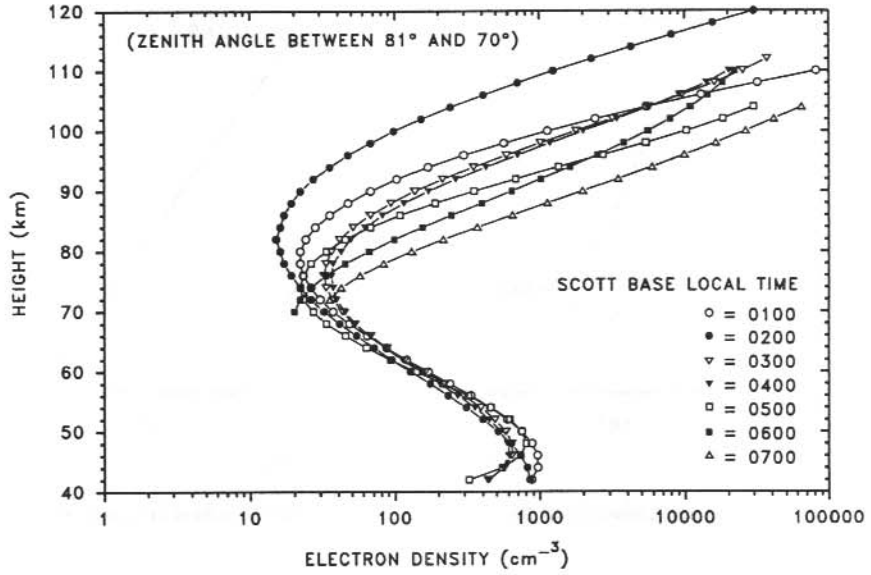

Figure 8. Composite of seven sequential electron density profiles (Day 015, 1984).

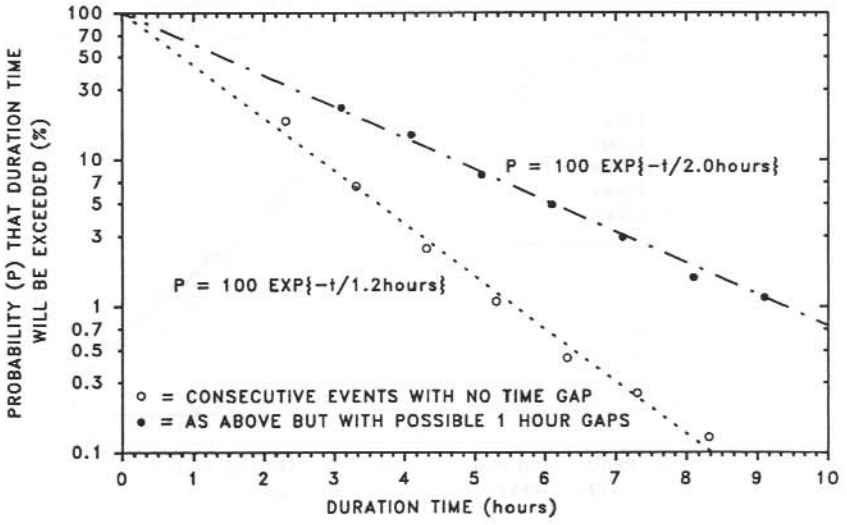

Figure 9. The probable duration of events.

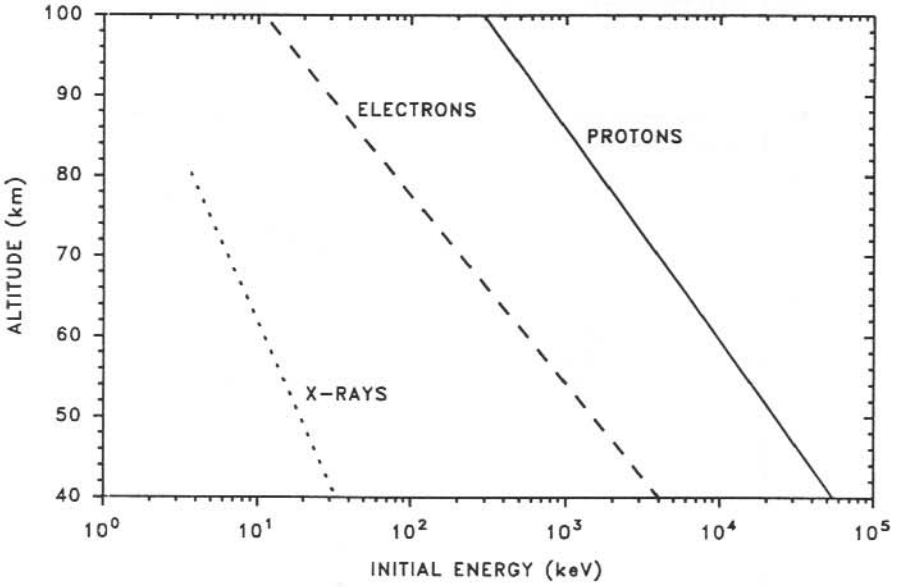

Figure 10. Nominal penetration depth for vertically incident particles as a function of particle energy (Thorne 1980).

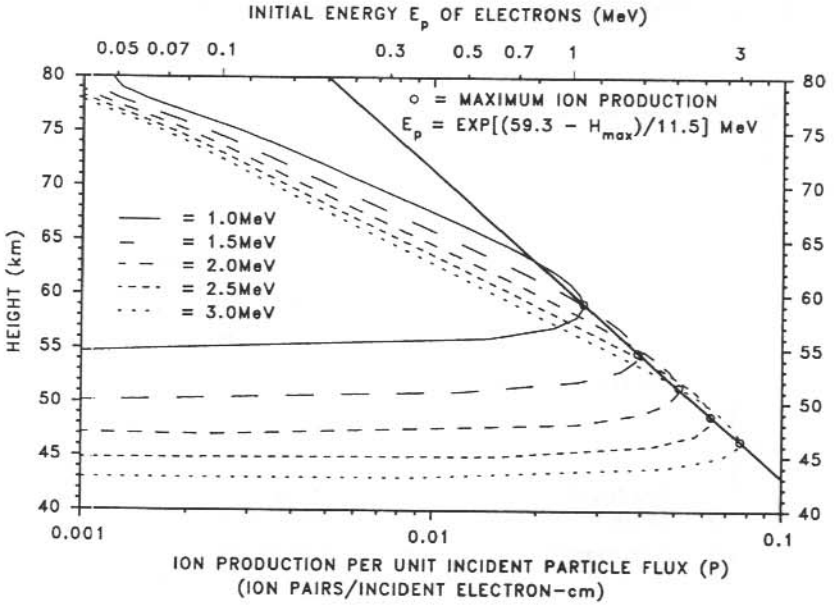

Figure 11. Ionisation by mono-energetic relativistic electrons normally incident upon the atmosphere.

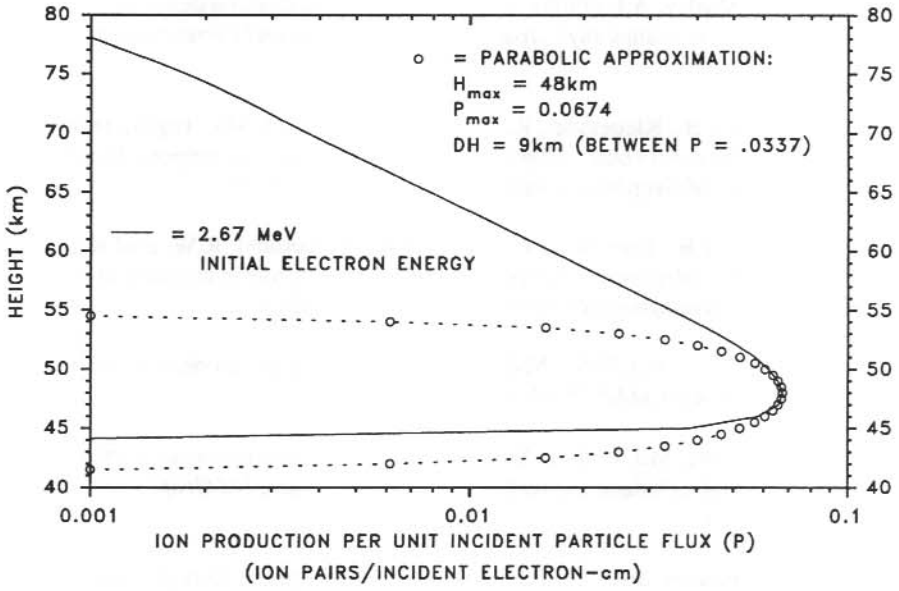

Figure 12. Parabolic approximation to ionisation production by 2.67 MeV electrons.

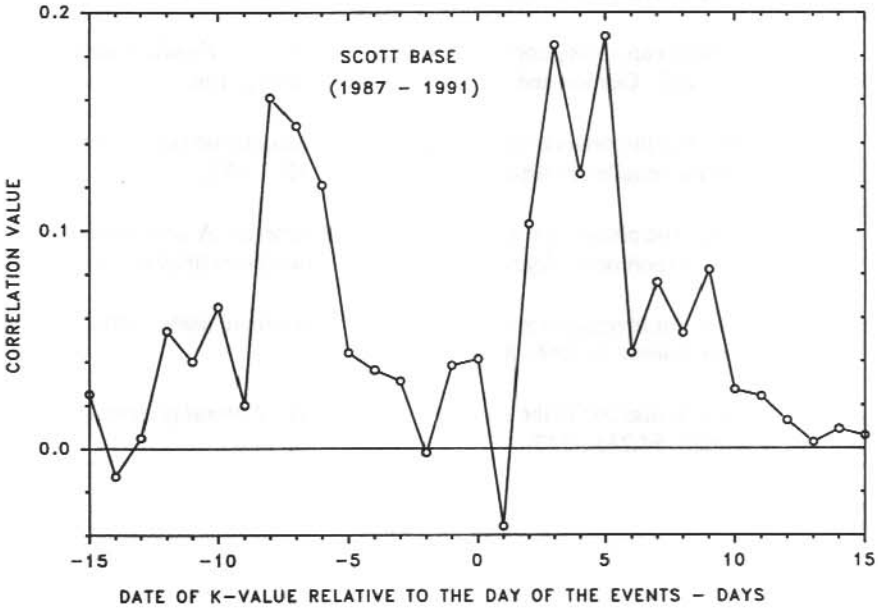

Figure 13. Correlation between the total number of daily occurrences and the 24-hour K index.

REFERENCES

Adams, G.W. *and* Masley, A.J. (1965). Production rates and electron densities in the lower ionosphere due to cosmic rays. *Journal of Atmospheric and Terrestrial Physics 27*:289 – 298.

Baker, D.N., Blake, J.B., Klebesadel, R.W. *and* Higbie, P.R. (1986). Highly relativistic electrons in the earth's outer magnetosphere. 1. Lifetimes and temporal history 1979 – 1984. *Journal of Geophysical Research 91 (A4)*:4265 – 4276.

Baker, D.N., Blake, J.B., Gorney, D.J., Higbie, P.R., Kelbesadel, R.W. *and* King, J.H. (1987). Highly relativistic magentospheric electrons: A role in coupling to the middle atmosphere. *Geophysical Research Letters 14*:1027 – 1030.

Barnett, J.J. *and* Corney, M. (1985). Middle atmosphere reference model derived from satellite data. *Handbook for MAP 16*:47 – 85.

Belrose, J.S. *and* Burke, M.J. (1964). Study of the lower ionosphere using partial reflections. 1. Experimental technique and methods of analysis. *Journal of Geophysical Research 69*:2799 – 2818.

Gardner, F.F. *and* Pawsey, J.L. (1953). A study of the ionospheric D-region using partial reflections. *Journal of Atmospheric and Terrestrial Physics 3*:321 – 344.

Nagai, T. (1988). 'Space weather forecast': Prediction of relativistic electron intensity at synchronous orbit. *Geophysical Research Letters 15(5)*:425 – 428.

Reid, G.C. (1974). Polar cap absorption – observations and theory. *Fundamentals of Cosmic Physics 1*:167 – 202. Gordon and Breach Science Publishers Ltd.

Thorne, R.M. (1980). The importance of energetic particle precipitation on the chemical composition of the middle atmosphere. *Pageoph 118*:128 – 151.

von Biel, H.A. (1976). The phase-switched correlation polarimeter – A new approach to the partial reflection experiment. *Journal of Atmospheric and Terrestrial Physics 39*:769 – 778.

von Biel, H.A. (1989). An investigation of the Antarctic mesosphere using partial reflections. *Planetary Space Science 37*:889 – 897.

von Biel, H.A. (1992). Ionisation in the Antarctic stratosphere. *Journal of Atmospheric and Terrestrial Physics 54*:235 – 242.

20. TIME CONSTANTS OF THE D-REGION

G.B. Burns[1] and D.J. Partridge[2]

[1] Auroral and Space Physics
Antarctic Division
Kingston Tasmania 7050
Australia

[2] Department of Physics
University of Tasmania
Hobart Tasmania 7000
Australia

ABSTRACT

A fast response riometer with a 5 MHz bandwidth and giving a resolution of 0.02 dB was used to measure cosmic noise absorption (CNA) pulsations during a pulsating aurora event. Comparisons of the CNA pulsations with optical intensities of the N_2^+ 1NG (0, 1) band were used to infer 'ionospheric time constants' in the range 2 – 10 s.

The time constants derived are weakly related to the absolute level of absorption at 30.9 MHz throughout the event. Lower time constants are generally measured at times of higher absorption.

Using reasonable approximations to the altitude and width of the absorption layer, and some recently published (Hargreaves and Devlin 1990) measurements of the effective recombination rate and specific absorption (dB km^{-1} per electron density), an attempt was made to balance the measurements of total absorption and the inferred time constants. The variable results obtained are most likely related to variations in the average energy of the precipitating auroral electrons (and thus variations in the altitude of the absorption layer) during the event.

By incorporating a means of estimating the average and total energy of the incident auroral particles, the method of analysis used here may provide a means to measure the height profile and seasonal variation of the D-region effective recombination coefficient.

20.1 INSTRUMENTATION AND DATA

Measurements of CNA pulsations, associated optical auroral fluctuations, and the background level of absorption were made during a pulsating auroral event at Macquarie Island (54.5°S 159.0°E, geographic coordinates; 64.3°S magnetic latitude). A wide-angle, zenith-oriented photometer was used to measure the time varying optical intensity of the N_2^+ 1NG (0, 1) band emission. A fast-response riometer with a 5 MHz bandwidth (30 MHz – 35 MHz) measured the cosmic noise pulsations. A standard, 30.9 MHz, riometer measured the background absorption levels. The instrumentation has well matched, but not identical, 'fields-of-view' (see Figure 1).

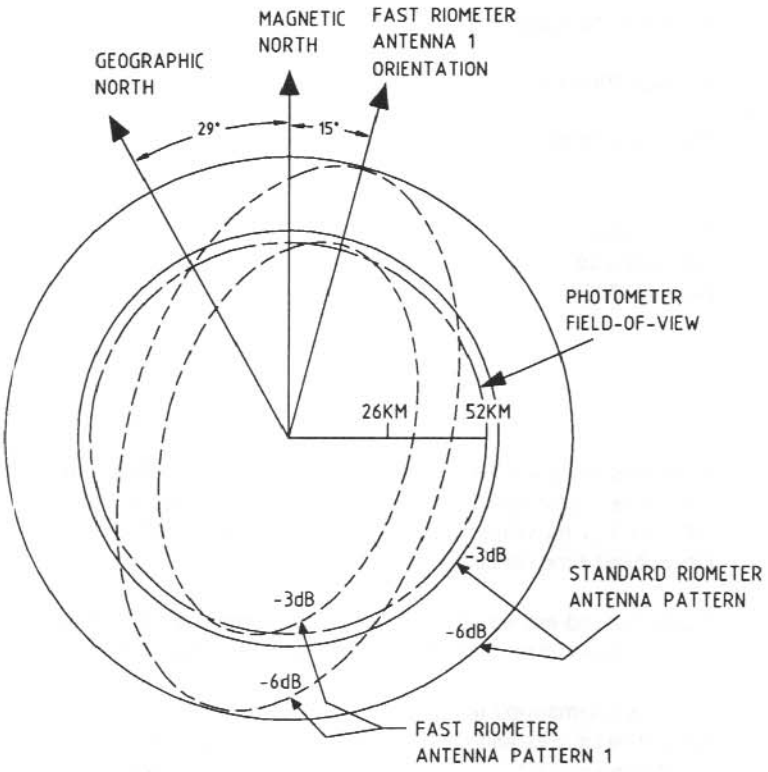

Figure 1. The orientations and fields-of-view of the photometer, standard riometer and fast response riometer at Macquarie Island. The distance measurements assume an altitude of 100 km. The contours of a second fast response riometer antenna are at right angles to those displayed above. Signals from the two antennae are added to give the fast response riometer an increased signal-to-noise response.

The photometer and fast riometer data were collected digitally at 10 Hz, but averaged to 2 Hz for this analysis. The standard riometer data is available only on chart, recorded at 6 cm hr^{-1}.

The event reported covers the interval from 1410–1630 UT, corresponding to 0150–0410 Magnetic Local Time, on 27 April 1985.

20.2 ANALYSIS AND RESULTS

For small fluctuations, ΔN, the ionospheric rate equation

$$\frac{dN}{dt} = \frac{q}{(1+\lambda)} - \alpha N^2 \qquad (1)$$

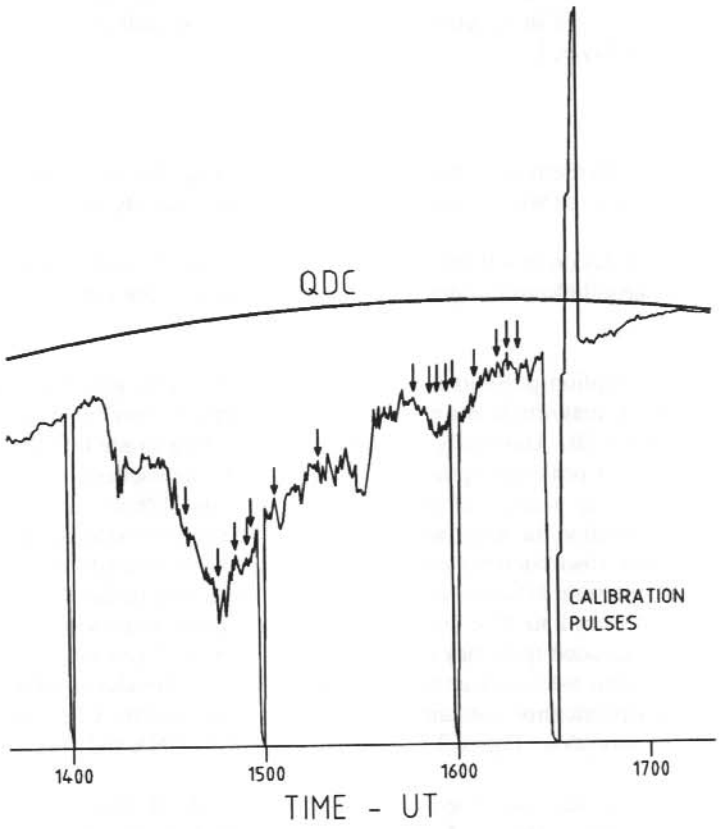

Figure 2. The standard riometer chart record for the interval 1400 UT to 1700 UT, 27 April 1985. A quiet day curve (QDC) is drawn on the diagram and the times for which ionospheric time constants were evaluated are indicated.

(where N is the electron density, q is the production rate of ions per unit volume, λ is the ratio of negative ions to electrons and α is the effective recombination rate of the electrons)

reduces to

$$\Delta N = (\Delta N)_0 \, e^{-t/2\alpha N_0} \qquad (2)$$

implying an 'ionospheric time constant', τ, given by

$$\tau = \frac{1}{2\alpha N} \qquad (3)$$

(Ratcliffe 1960).

For a frequency above 30 MHz, and for a thin absorption layer, the absorption, A (in dB), is proportional to the product of the electron density, N, the electron collision frequency, v, and the width of the absorption layer, h.

$$A\ (dB) \propto Nvh \qquad (4)$$

If the energy of the incident precipitation remains constant for the time interval of the approximation, the absorption will be proportional to the electron density at the peak of the layer.

The N_2^+ 1NG band emission at 428 nm, which results from an allowed transition of a species directly excited by auroral electron impact, is proportional to the time varying ionisation rate, q (Omholt 1971, P. 25).

The cosmic noise absorption pulsations measured during the event generally varied between 0.05 dB to 0.25 dB in magnitude on a background absorption level that generally ranged between 0.5 dB and 4.0 dB. Unusually large pulsations, of magnitude 0.9 dB, were however recorded near the 5.4 dB peak absorption time of the event. Ionospheric time constants were determined by convolving a range of time constants with the 428 nm optical intensity data (proportional to the ionisation function), and selecting the time constant that best approximated the measured cosmic noise absorption pulsations. It was possible to estimate the ionospheric time constants for seventeen time intervals ranging from 30 s to 2 min in duration. The measured time constants ranged from 2 to 10 s. Figure 2 shows the section of the standard riometer chart for the event. The estimated quiet day curve (QDC) is overlayed and the intervals for which ionospheric time constants were measured are indicated. Table 1 includes the time interval of the fit, the estimated ionospheric time constant, the level of absorption of the CNA pulsations and the background level of absorption. Figure 3 shows selections of the CNA and optical pulsation data.

The ionospheric time constants calculated are weakly related to the absolute level of absorption as measured by the standard riometer (see Figure 4). Lower ionospheric time constants are generally measured at times of higher absorption. The relationship comes from the dependence of the background absorption level and the ionospheric time constant on the electron density (see equations 3 and 4). The weak nature of the relationship indicates that other parameters are varying between the time intervals for which the ionospheric time constants could be derived.

A superposed epoch analysis of the '2 s time constant' CNA pulsations (Figure 5), shows an under-estimation in the amount of absorption by the fitted exponential at the peak of the absorption, and longer duration, lower amplitude, negative residuals (corresponding to an over-estimation of the amount of absorption by the fitted exponential) away from the time of the peak absorption. This may be explained if the first order correction to our 'thin absorbing layer' assumption is that there is a range of time constants associated with α and N varying across the absorption layer. The addition of exponentials with a range of time constants would result in a combined function which initially decayed more quickly and then more slowly than, an exponential 'best fitted' to it.

Table 1. The time intervals for which ionospheric time constants were evaluated, the values obtained, the level of absorption of the pulsations, the background level of absorption and the implied variation in a published value of the effective recombination coefficient, α, for the assumptions detailed in the text.

Time Interval	τ (seconds)	dB of CNA pulses	Background level dB	Implied α (90km) variation
14:35:45 – 14:36:40	6	0.25	2.54	2.02
14:47:55 – 14:50:00	2	0.75	5.42	1.44
14:51:35 – 14:52:40	2	0.90	3.97	1.05
14:56:40 – 14:57:15	4	0.24	3.93	2.09
14:57:20 – 14:58:10	4	0.22	3.66	1.94
15:04:00 – 15:05:00	2	0.25	2.70	0.71
15:18:00 – 15:18:30	3	0.12	1.88	0.75
15:46:20 – 15:47:20	3	0.08	1.05	0.42
15:52:30 – 15:53:15	8	0.15	1.42	1.51
15:55:25 – 15:56:15	5	0.24	1.53	1.01
15:56:25 – 15:57:00	5	0.22	1.55	1.01
15:57:25 – 15:57:55	4	0.27	1.50	0.80
15:58:00 – 15:59:20	5	0.20	1.50	1.00
16:05:10 – 16:06:40	5	0.17	1.03	0.69
16:11:55 – 16:12:35	8	0.15	0.69	0.73
16:15:30 – 16:16:05	4	0.08	0.69	0.36
16:16:15 – 16:16:55	10	0.22	0.52	0.69

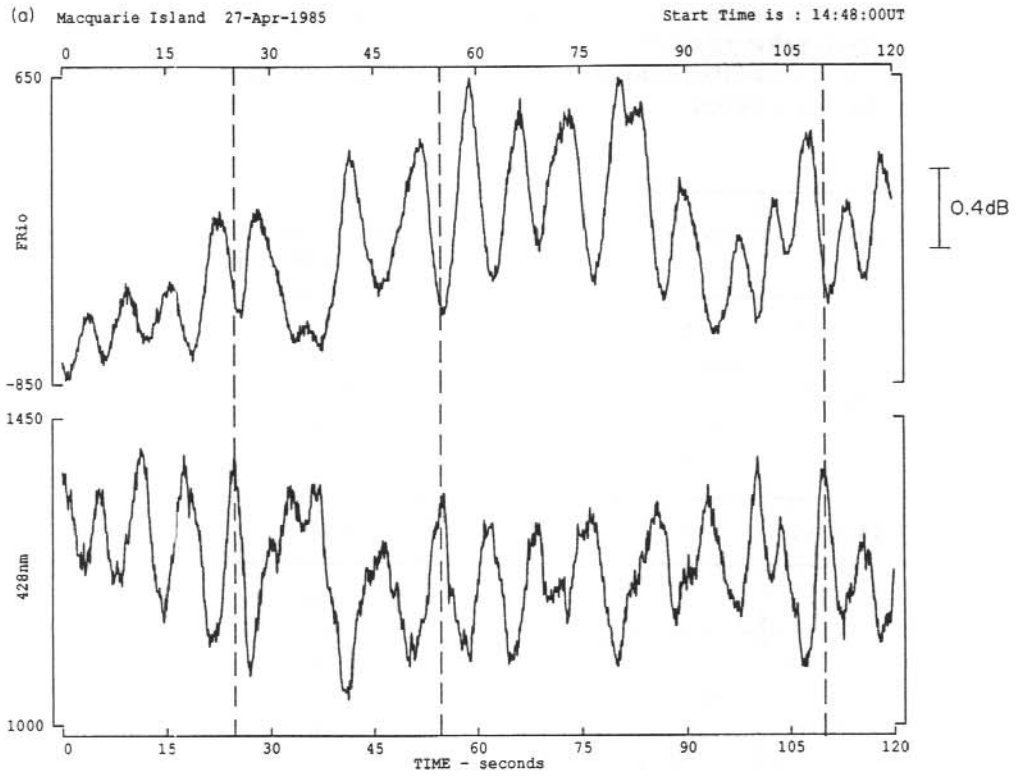

Figure 3. Examples of the data analysed. The dashed lines help with determining the time alignment for the optical (428 nm) and the CNA (FRio) pulsations.

(a) 1448-1450 UT, 27 April 1985.
For this interval the 'ionospheric time constant ' is 2 seconds. The background absorption level decreases from 5.4 to 5.2 dB across the interval, and the CNA pulsations are less than 0.8 dB in magnitude. These were among the largest, fastest, CNA pulsations of the interval analysed.

(b) 1555-1557 UT, 27 April 1985
Includes intervals for which the 'ionospheric time constant' is 5 seconds. The background absorption level increases from 1.4 to 1.5 dB across the interval, and the CNA pulsations are approximately 0.2 dB in magnitude. These absorption magnitudes, both for background levels and for the absorption pulsations, are typical for the event.

(c) 1611:20-1613:20 UT, 27 April 1985
This example includes the interval for which an 8 second 'ionospheric time constant' was calculated. The background absorption level decreases from 0.8 to 0.7 dB across the interval presented, and the level of the CNA pulsations are approximately 0.15 dB.

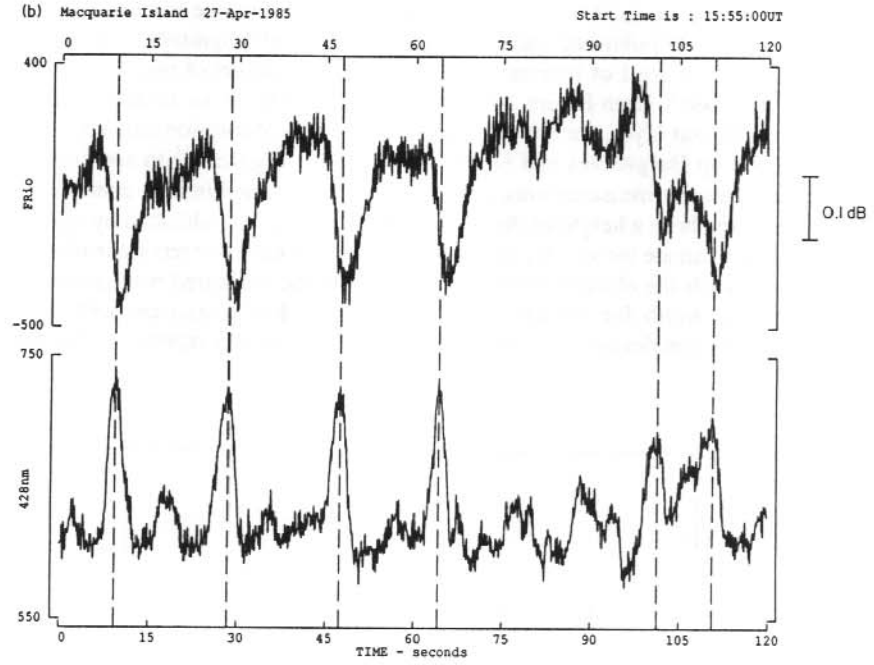
(b) Macquarie Island 27-Apr-1985
Start Time is : 15:55:00UT
0 15 30 45 60 75 90 105 120
400
FRio
-500
750
428nm
550
0.1 dB
TIME - seconds

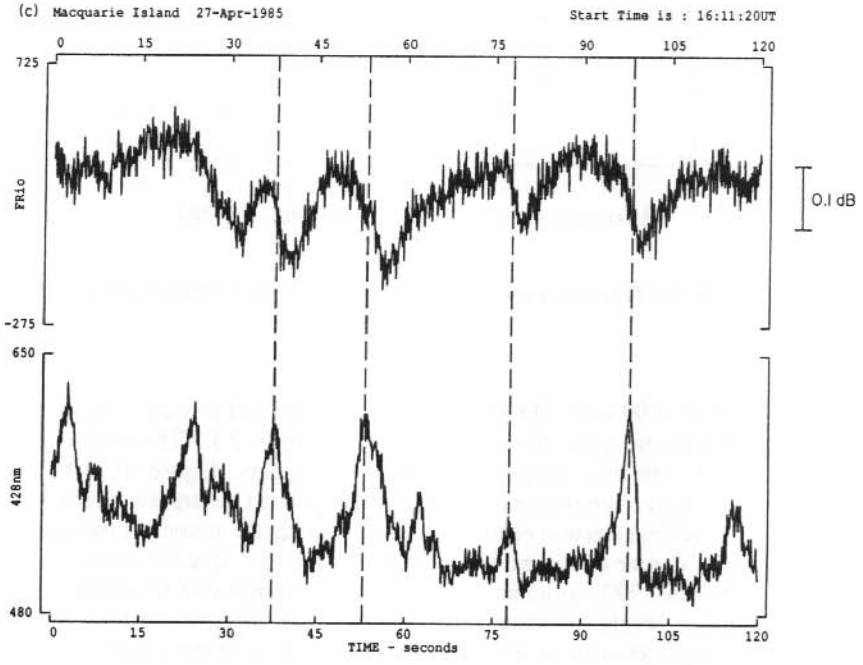
(c) Macquarie Island 27-Apr-1985
Start Time is : 16:11:20UT
0 15 30 45 60 75 90 105 120
725
FRio
-275
650
428nm
480
0.1 dB
TIME - seconds

There is a wide range of variability in the published values of the effective recombination coefficient. The range of published values exceeds one order of magnitude at 90 km (10^{-7} to 3×10^{-6} cm^3 sec^{-1}, from Figure 1 of Penman et al. 1979) and two orders of magnitude at 80 km (2×10^{-7} to 2×10^{-5} cm^3 sec^{-1}, from Figure 1 of Penman et al. 1979). If we assume an altitude and a width for the absorption layer, we can use curves of specific absorption (dB km^{-1} per electron density) published by Hargreaves and Devlin (1990) (their Figure 15) to see how closely the ionospheric time constant measurements match the effective recombination coefficient, α, at the chosen altitude. We chose a height of 90 km, which for the curves published by Hargreaves and Devlin (1990) is the altitude for which a minimum value of the effective recombination coefficient, α, is required to match the electron density inferred from the measured background absorption level. We chose a width for the absorption layer of 15 km, consistent with the EISCAT measurements of electron densities and the specific absorption values reported by Hargreaves and Devlin (1990).

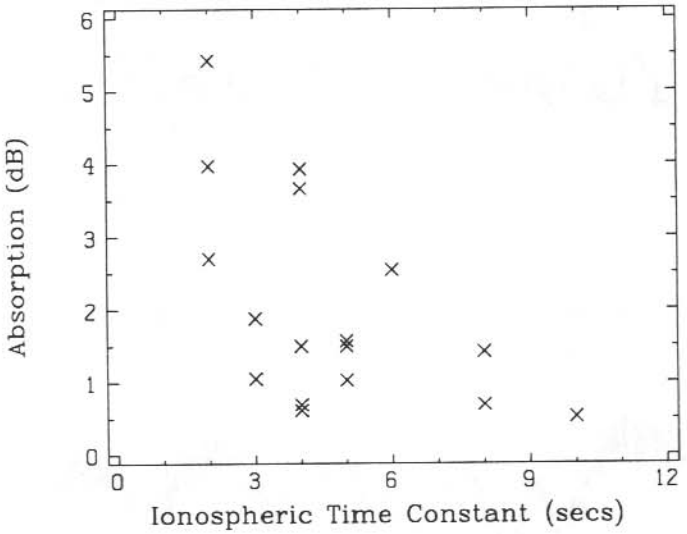

Figure 4. A plot of the background level of absorption at 30.9 MHz against the ionospheric time constant.

The factor by which α at 90 km (5.3×10^{-7} cm^3 sec^{-1}) is required to vary in order to match our measurements, with all the assumptions, ranges from 0.36 to 2.1. The ratios calculated are positively correlated with the background level of absorption (Figure 6). The most likely explanation for this positive correlation is that higher background absorption levels are associated with higher average incident electron energies. This may lower the altitude of the absorption layer below 90 km where higher α values are required (using the specific absorption curves of Hargreaves and Devlin 1990) to balance the measured ionospheric time constants with the background absorption levels. Within the limits of the assumptions we must make with our present data set, the measured time constants are consistent with the effective recombination coefficient at 90 km published by Hargreaves and Devlin (1990).

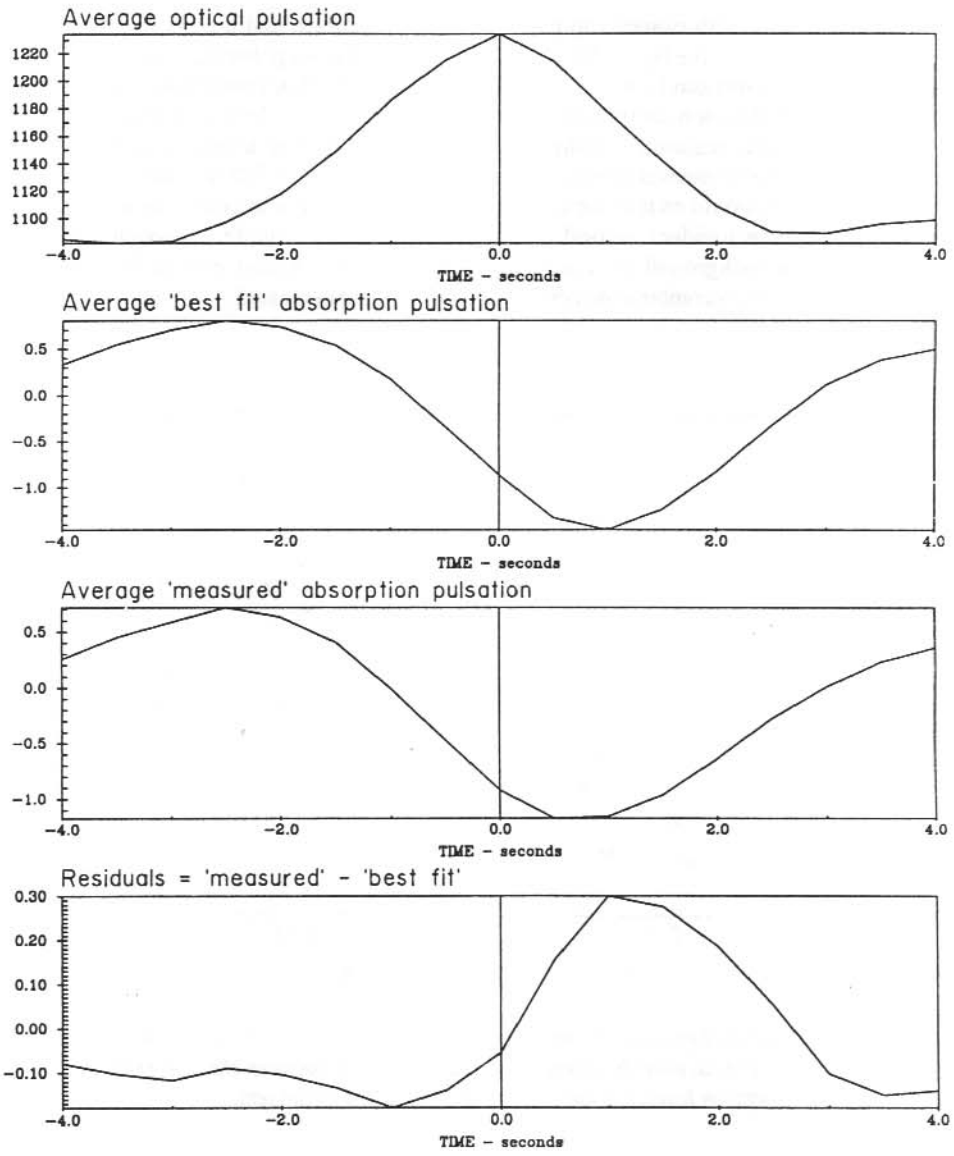

Figure 5. A superposed epoch analysis of the '2 s time constant' noise absorption pulsations. The epochs are centred on the peaks of the associated optical pulsations. Shown are the average 428 nm pulse, the average 'best fit' absorption pulse (generated from convolving the optical pulsations with the 2 s ionospheric time constant), the average 'measured' CNA pulsation and the residuals (calculated as the difference between the 'measured' and 'best fit' absorption pulsations).

20.3 DISCUSSION

By using a wide bandwidth riometer to measure CNA pulsations, and a photometer for optical intensity measurements of the N_2^+ (1NG) auroral emissions during pulsating aurora, estimates of ionospheric time constants can be made. In order to make a significant contribution to estimations of the effective recombination coefficient, further information on the electron density profile at the time of measurement is required. Within the constraints of present available instrumentation, absolute auroral intensity measurements of the auroral green line at 558 nm and the N_2^+ (1NG) (0,1) band at 428 nm would enable the ordering of the estimated time constants in terms of the average energy of the incident auroral electrons, and thus in altitude. In conjunction with measurements of the background level of absorption, the electron density may be inferred and the variation of the effective recombination coefficient with altitude estimated.

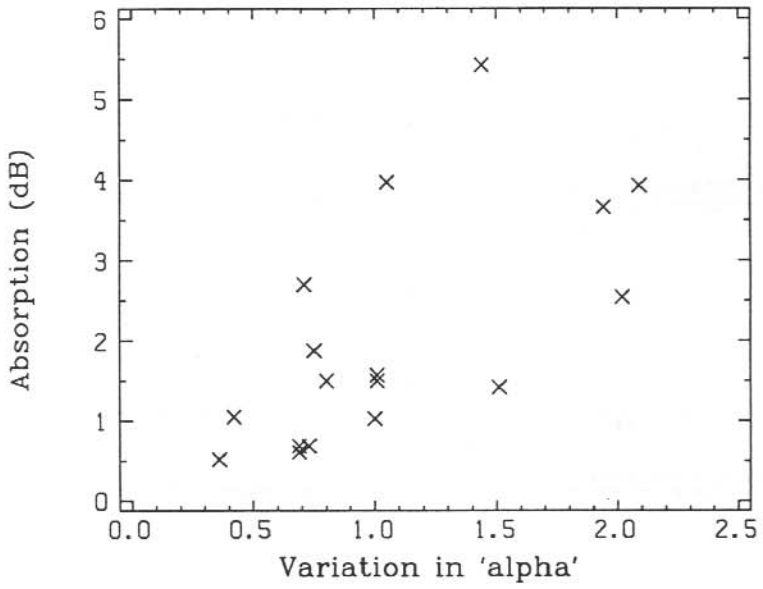

Figure 6. A plot of the background absorption level against the factor by which the effective recombination coefficient, α, must be altered to achieve balance between the ionospheric time constant and the absorption level, for the assumption indicated in the text.

20.4 ACKNOWLEDGMENTS

Mr Mike Craven and Mr David Barrett were responsible for the collection of the data at Macquarie Island in 1985. The manufacture of research instrumentation and the maintenance of a remote observatory facility requires the concerted effort of many people. To those who assisted with the collection of these data, our thanks.

REFERENCES

Hargreaves, J.K. *and* Devlin, T. (1990). Morning sector electron precipitation events observed by incoherent scatter radar. *Journal of Atmospheric and Terrestrial Physics 52*:193 – 203.

Omholt, A. (1971). *The optical aurora*. Springer-Verlag.

Penman, J.M., Hargreaves, J.K. *and* McIlwain, C.E. (1979). The relation between 10 to 80 keV electron precipitation observed at geosynchronous orbit and auroral radio absorption observed with riometers. *Planetary and Space Science 27*:445 – 451.

Ratcliffe, J.A. (1960). *Physics of the Upper Atmosphere*. Academic Press, New York.

21. ELECTROMAGNETIC ION CYCLOTRON WAVE OBSERVATIONS NEAR THE PLASMAPAUSE BY THE CRRES SPACECRAFT

B.J Fraser[1], H.J. Singer[2], W.J. Hughes[3], J.R.Wygant[4] and R.R. Anderson[5]

[1] Department of Physics
University of Newcastle
Newcastle NSW 2308
Australia

[2] Geophysics Directorate/GPSG
Phillips Laboratory
Hanscom AFB MA 01731 USA

[3] Centre for Space Physics
Boston University
MA 02215 USA

[4] Space Science Laboratory
University of California
Berkeley CA 94720 USA

[5] Department of Physics and Astronomy
University of Iowa
Iowa City IA 52242 USA

ABSTRACT

Electromagnetic ion cyclotron waves (ICW) observed by the AFGL fluxgate magnetometer on the elliptically orbiting Combined Release/Radiation Effects Satellite (CRRES) satellite (apogee 6.3 Re) are seen to occur inside, on, and outside the plasmapause identified by the Iowa/AFGL plasma wave experiment. Wave data over the 19–07 MLT interval have been analysed and a comparison will be made between the pre- and post-midnight ICW events. Propagation characteristics and implications relating to source mechanisms will be discussed with respect to individual event spectra and polarisation parameters.

21.1 CRRES OBSERVATIONS

The suggestion that electromagnetic ion cyclotron (EMIC) waves may be favourably generated in the region of the plasmapause has been known for some twenty-five years. The free energy for wave growth is provided by anisotropic energetic proton distributions in the 10–100 KeV range (Cornwall 1965, Liemohn 1967) and wave growth may occur preferentially near the plasmapause (Kozyra et al. 1984). Such a situation could occur at the plasmapause where a change in the cold plasma density by up to two orders of magnitude is seen. It is therefore of interest to make simultaneous observations of the cold plasma density near the plasmapause and EMIC wave events in order to study amplitude and spectral characteristics. Such results have been reported

using limited data at synchronous orbit from GEOS-1 and 2, ATS-6 and over radial paths by ISEE-1 and 2, DE-1 and AMPTE/CCE. Following from these studies the recently launched Combined Release and Radiation Effects Satellite (CRRES) spacecraft orbit is ideal for studying EMIC waves near the plasmapause and preliminary results are presented in this paper.

CRRES was launched on 25 July 1990 into an elliptical orbit of period 9 hours 52 minutes, with apogee 6.3 R_E, perigee 350 km and inclination 18.2° and ceased operation on 12 October 1991. Instrumentation of interest to the present EMIC wave study include the AFGL triaxial fluxgate magnetometer (Singer et al. 1992) and the University of Iowa/AFGL plasma wave experiment (PWE) (Anderson et al. 1992). The magnetometer has a Nyquist frequency of 8 Hz and a minimum detectable signal of ~0.5 nT in the high gain mode. Typically the high gain mode is used at altitudes of >2 R_E. CRRES has a spin period of ~30 s and the spin axis is directed to within ±15° of the sun direction.

Figure 1 illustrates the dynamic spectra of an EMIC wave event recorded on 1 September 1990. The top panel shows the event at L = 3.6 – 4 and a frequency of 3.2 – 3.8 Hz, is about 17 minutes in duration and seen in the early morning hours at 0330 – 0400 MLT. The total wave power transverse to the ambient magnetic field is plotted here and this greatly exceeds the field aligned wave power indicating that this is essentially a parallel propagating transverse wave event. Wave polarisation (not shown) is left-hand throughout the events, as expected for waves near the equator and above the He^+ cyclotron frequency. The lower panel shows the dynamic spectra observed by the PWE instruments over the complete orbit 92. The PWE provides cold electron density data through the observation of the upper hybrid resonance frequency (f_{uhr}) and the electron plasma frequency (f_{pe}) (Gurnett and Inan 1988). The PWE measures the electric and magnetic wave fields over the frequency range 5 Hz – 400 kHz using two electric dipole antennae and a search coil magnetometer. Only the lower spectra covering 0.1 – 400 kHz are of interest here and the electron density profile is represented by the plasma frequency with $N_e = f_{pe}^2/80.6$. Consequently, the electron density profile across the CRRES orbit can be seen in the $f_{pe} \sim f_{uhr}$ emission lines in the PWE frequency spectra. The plasmapause on the outbound pass is seen at L = 3.4 and 1615 UT and on the inbound pass at L = 4.1 and 2350 UT. Thus the EMIC wave event commences about 0.2 R_E outside the plasmapause in the lower density plasma trough region where the electron density N_e ~30 cm^{-3}. These properties are typical for waves seen in the vicinity of the plasmapause in the post midnight sector.

A preliminary statistical analysis of EMIC waves seen by CRRES from 25 October 1990 to 30 March 1991 covering the local time interval from 07 MLT to 21 MLT has been undertaken. There is a data gap from 14 December 1990 to January 1991, when the magnetometer was turned off or the spacecraft was duty cycling. Over the intervals analysed, 29 post-midnight events and 14 pre-midnight events were observed. Statistics on an event basis have been compiled for the following parameters; event start and stop times (UT and MLT), wave amplitude, power, frequency and bandwidth, L value range, magnetic latitude, associated plasmapause location, and electron density at the time of the event. The three panels in Figure 2 illustrate some of the statistical results. The top panel, a plot of event mean frequency against L value, shows that the higher frequency events are seen at low L while lower frequency events are seen out to L = 8.7 the limit of the coverage. The mean equatorial He^+ cyclotron frequency associated with the events is also shown. Wave events are about equally distributed above and below this frequency.

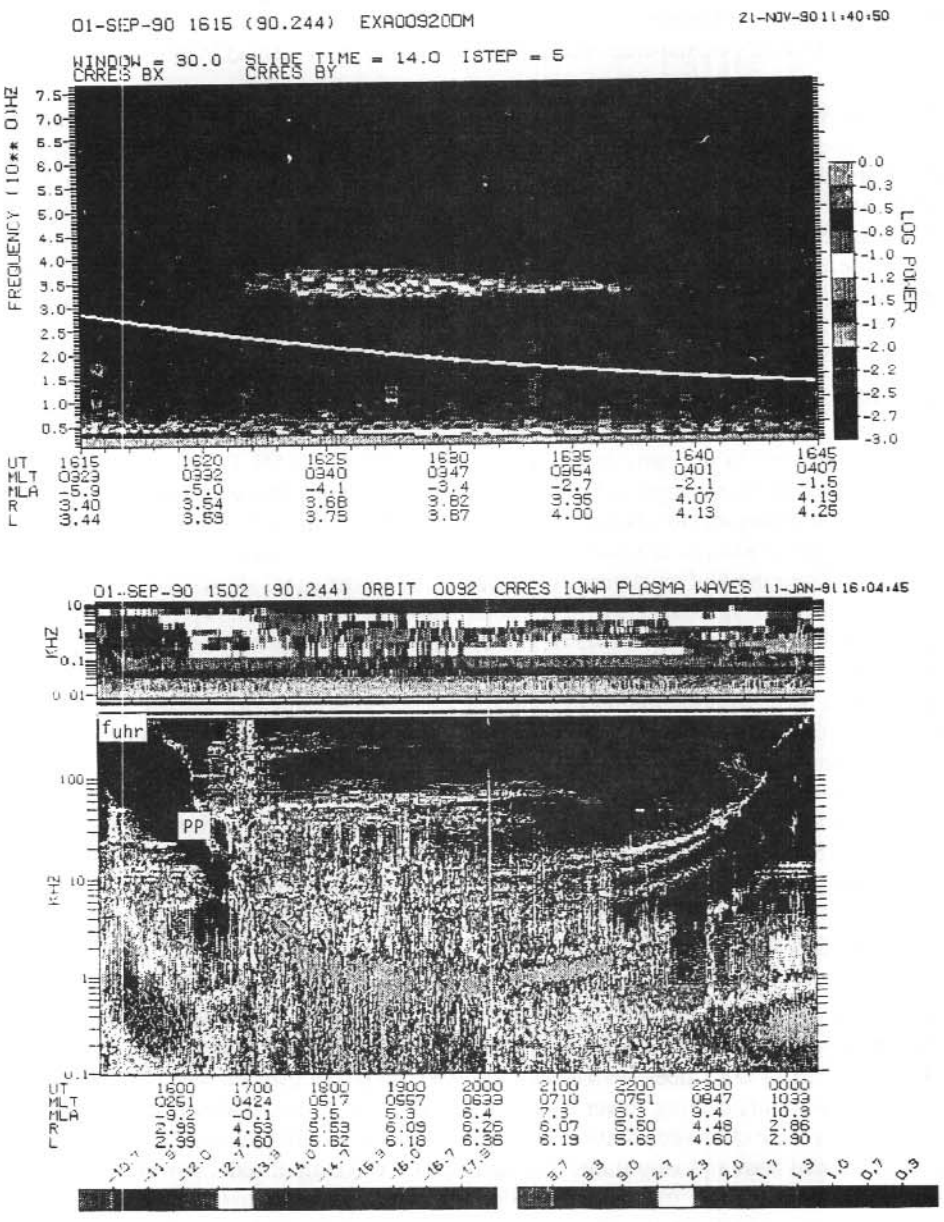

Figure 1. Top: Ion cyclotron wave (EMIC) event in the post-midnight sector. The curve is the local He^+ cyclotron frequency. Bottom: The upper hybrid resonance on the Iowa PWE electric field spectra. The plasmapause location is the steep gradient pp.

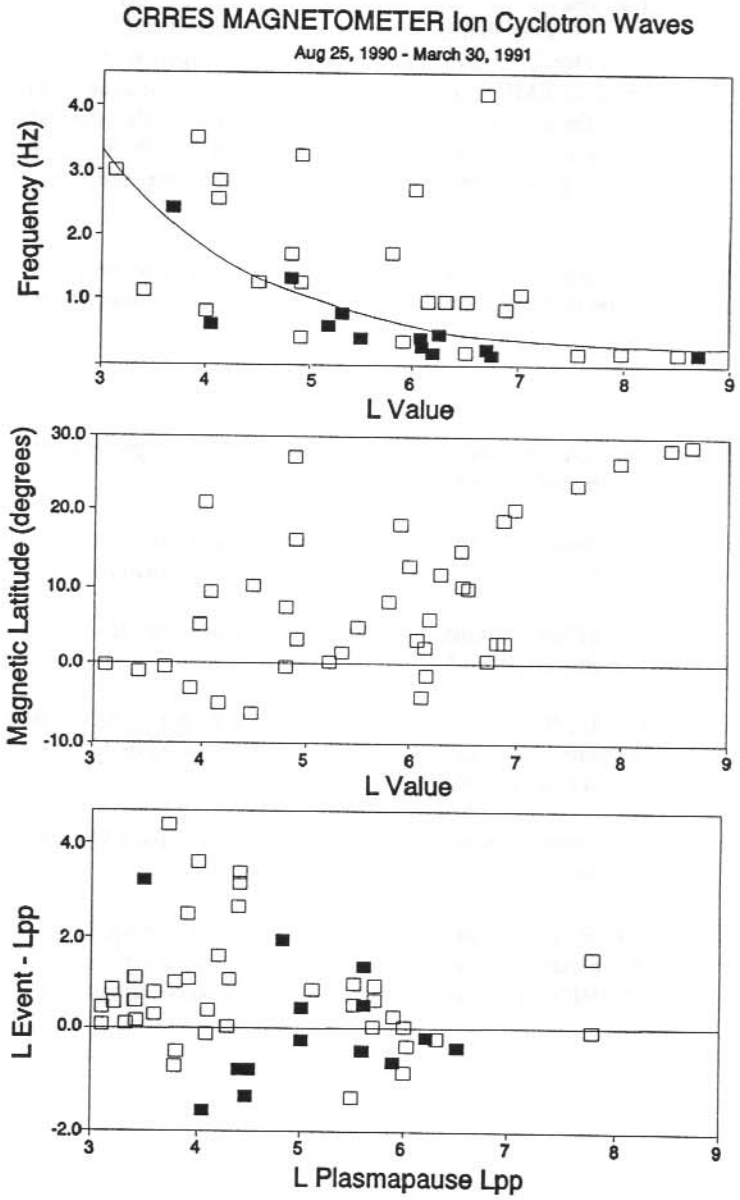

Figure 2. Top: Distribution of wave frequency with L value. The curve is the equatorial He^+ cyclotron frequency. Middle: Distribution of wave location with latitude and L value. Bottom: Location of EMIC sources with respect to the plasmapause, negative values for (L event − L pp) are in the plasmasphere, positive values are outside the plasmapause.

CRRES has the ability to observe waves at latitudes up to about 30° off the equator. From the second panel in Figure 2 it is seen that EMIC waves are observed over the full latitude range covered. The lack of points for L >7 and MLAT <20° is a consequence of the CRRES orbit and does not imply an absence of EMIC waves over this region of the magnetosphere. The third panel in Figure 2 illustrates the location of wave events with respect to the plasmapause. The pre-midnight events, although a small sample, appear to be seen both inside and outside the plasmapause, while in the post-midnight sector more events are seen on or outside the plasmapause at L = 3.4.

Plans for future studies include an extension of the statistical data set for the study of EMIC wave properties and the inclusion of electric field data in individual event analysis in order to calculate the wave Poynting vector.

REFERENCES

Anderson, R.R., Gurnett, D.A. *and* Odem, D.L. (1992). The CRRES plasma wave experiment. *Journal of Spacecraft and Rockets*.

Cornwall, J.M. (1965). Cyclotron instabilities and electromagnetic emission in the ultra low frequency and very low frequency ranges. *Journal of Geophysical Research 70*:61 – 69.

Gurnett, D.A. *and* Inan, I. (1988). Plasma wave observations with the DE-1 spacecraft. *Reviews of Geophysics 26*:285 – 316.

Kozyra, J.U., Cravens, T.E., Nagy, A.F., Fontheim, E.G. *and* Ong, R.S.B. (1984). Effects of energetic ions on electromagnetic ion cyclotron wave generation in the plasma pause region. *Journal of Geophysical Research 89*:2217 – 2234.

Liemohn, H.B. (1967). Cyclotron-resonance amplification of VLF and UHF whistlers. *Journal of Geophysical Research 72*:39 – 55.

Singer, H.J., Sullivan, W.P., Anderson, P., Mozer, F., Harvey, P., Wygant, J. *and* McNeill, W. (1992). Fluxgate magnetometer instrument on the combined release and radiation effects satellite (CRRES). *Journal of Spacecraft and Rockets*. (In press).

22. THE UNPRECEDENTED SEQUENCE OF GROUND LEVEL ENHANCEMENTS DURING THE RECENT SOLAR MAXIMUM

M.L. Duldig[1], J.E. Humble[2] and M.B.M. Bendoricchio[2]

[1] Cosmic Ray Section
Antarctic Division
Kingston Tasmania 7050
Australia

[2] Physics Department
University of Tasmania
Hobart Tasmania 7001
Australia

ABSTRACT

An uprecedented sequence of Ground Level Enhancements (GLE) was observed world-wide during the recent solar maximum including the largest such event (29 September 1989) since 1956.

An introduction to the ground based detection of low energy cosmic rays is presented. Features of a number of recent GLE are presented with emphasis on the large 29 September 1989 event and improved modelling of the 22 October 1989 event.

22.1 INTRODUCTION

Cosmic rays are fully ionised nuclei of very high energy ($10^9 - 10^{20}$ eV) which bombard the earth almost isotropically. They have an abundance distribution similar to neutral matter in the galaxy (~90% protons) and are principally of non-solar system origin. The energy spectrum follows a power law of slope -2.6 and the acceleration mechanisms by which the particles gain their energy are poorly understood, particularly at the very highest energies.

On rare occasions a solar flare will accelerate protons to sufficiently high energies to allow these particles to propagate along the solar magnetic field lines to the earth and be detected as a sharp increase in the ground based counting rate of cosmic ray detectors. Such events are known as Ground Level Enhancements (GLE) and there have been 52 recorded since reliable records began in the 1940s.

Although the average rate of occurrence of GLE is about one per year, there have been significant periods when no GLE have been recorded. The longest of these 'gaps' was from November 1949 to February 1956. The recent sequence of GLE was preceded by a 'gap' of almost 5.5 years. The frequency of GLE is also loosely correlated with solar activity (Figure 1) although Nagashima et al. (1991) propose that no GLE can occur at the peak of the solar activity cycle whilst the solar magnetic field is in the process of reversing.

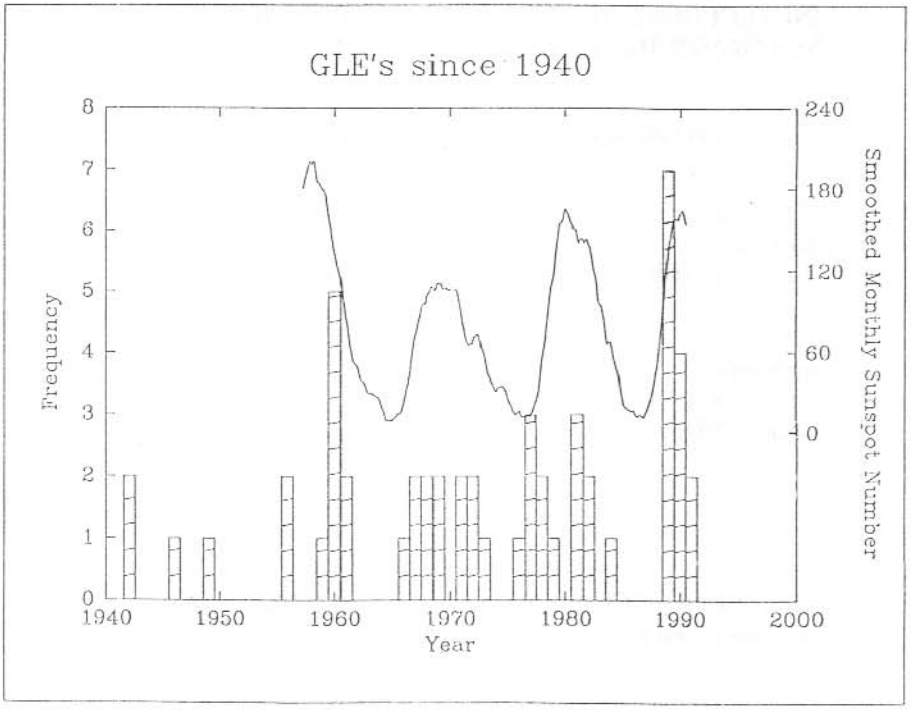

Figure 1. The frequency of GLE plotted together with smoothed monthly sunspot number (solid line) showing the loose correlation between GLE occurrence and solar activity.

The largest GLE ever recorded was on 23 February 1956 and reached a peak 45 times the usual cosmic ray background level. Typical GLE peak levels range from ~5% – 40% above background with very few exceeding 100%.

There were 13 GLE in the period July 1989 – July 1991 corresponding to the most recent maximum in the solar sunspot cycle. Such a high frequency of events is unprecedented.

In this paper we briefly discuss the propagation of GLE particles from the sun to the earth and their detection by ground based systems. We then present an overview of the 13 recent GLE and finally present a more detailed analysis of features of two of the events, namely those of 29 September and 22 October 1989.

22.2 GROUND LEVEL ENHANCEMENT PROPAGATION TO EARTH

Solar flares and other magnetic phenomena at the sun may give rise to a GLE. The acceleration of charged particles to energies sufficiently high to be detected by ground based cosmic ray detectors is poorly understood and several mechanisms have been proposed and are hotly debated.

Propagation of these particles to the earth is more readily explained. The solar magnetic field is 'frozen' into the solar wind plasma which flows radially outward from the sun. Coupled with the 27-day rotation of the sun, the field near the solar equator forms an Archimedian spiral structure and a field line connecting the earth to the sun typically emanates from the sun at a longitude ~60°W of the sun-earth line (footpoint) and intersects the earth at ~45° as shown in Figure 2. This field line, linking the sun to the earth, is referred to as the 'garden hose' field line.

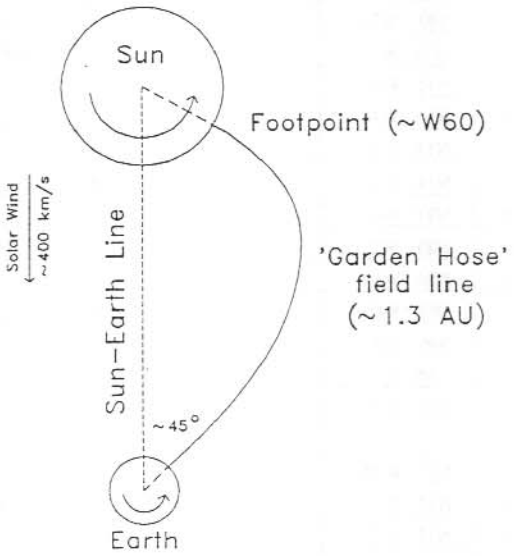

Figure 2. Schematic representation of the typical field line connection between the sun and earth (garden hose) along which GLE particles propagate most easily.

Charged particles gyrate around magnetic field lines as they propagate along them. Therefore, particles accelerated at the sun near to the footpoint of the garden hose field line will propagate easily to the earth. Particles accelerated some distance from the footpoint must cross field lines before they can propagate to the earth along the garden hose.

The direction of the garden hose field line at the earth and its footpoint at the sun vary considerably, both being strongly dependent on interplanetary conditions. In particular, variations in the solar wind speed and disturbance of the field by shocks will have significant effects on the large scale field structure. There is, however, a strong tendency for the solar active region responsible for a GLE to be located at westward solar longitudes. Of the seven GLE clearly attributed to an eastern source longitude, only three were positioned farther east than 15°.

Table 1 gives details of all known GLE prior to the present solar cycle.

Table 1. GLE prior to the present solar cycle with details of associated solar flares and maximum ground level response. For a complete list of references see Bendoricchio (1991).

		Parent Flare			GLE Maximum	
Event	Date	Location	Start (UT)	Max (UT)	%	Location
1	28/02/42	N07 E04			600	
2	07/03/42	N07 W90			750	
3	25/07/46	N22 E15	1615	1640	1100	
4	19/11/49	S03 W72	1029	1033	2000	
5	23/02/56	N24 W74	0331	0342	4554	Leeds
6	31/08/56	N15 E15	1226	1243	8	Chicago
7	17/07/59	N16 W31	2114	2132	10	Resolute Bay
8	04/05/60	N13 W90	1000	1016	290	Churchill
9	03/09/60	N18 E88	0037	0108	4	Mawson
10	12/11/60	N27 W04	1315	1330	135	Thule
11	15/11/60	N25 W35	0207	0221	160	Mawson
12	20/11/60	N26 W113	2017	2020	8	McMurdo
13	18/07/61	S07 W59	0920	1005	24	Thule
14	20/07/61	S06 W90	1553		4	Ottawa
15	07/07/66	N35 W48	2025	0040	3	Kerguelen
16	28/01/67	N22 W154				
17	28/01/67				21	McMurdo
18	29/09/68	N17 W15	1618	1623	2	Thule
19	18/11/68	N21 W87	1017	1035	14	Goose Bay
20	25/02/69	N13 W37	0900	0913	15	Goose Bay
21	30/03/69	N19 W110			9	Sanae
22	24/01/71	N16 W49	2314	2316	26	McMurdo
23	01/09/71	S12 W130			16	Dumont D'urville
24	04/08/72	N14 E34	0621	0635	23	South Pole
25	07/08/72	N14 W36	1505	1520	6	Inuvik
26	29/04/73	N14 W73	2056	2100	3	
27	30/04/76	S08 W46	1839	2048	4	
28	19/09/77	N08 W57	0955	1030	2	
29	24/09/77	N10 W120		0554	6	
30	22/11/77	N24 W40	0945	0959	25	
31	07/05/78	N22 W66			125	Apatity
32	23/09/78	N35 W50	0947	0959	8	
33	21/08/79	N17 W40	0615	0616	9	Goose Bay
34	10/04/81	N07 W35	1632			
35	10/05/81	N05 W74	0715			
36	12/10/81	S17 E32	0615			
37	26/11/82	S11 W89	0232			
38	07/12/82	S19 W86	2341		62	Kerguelen
39	16/02/84	W122			95	Goose Bay

22.3 EFFECT OF THE EARTH'S MAGNETIC FIELD

On reaching the earth, particles encounter the geomagnetic field. In traversing the field the particles undergo an energy dependent deflection of their trajectories. As a result it is necessary to model the 'viewing cone' of cosmic ray telescopes. This involves calculating the particle arrival directions outside the magnetic field that have access to the telescope field of view using models of the earth's magnetic field. In the past this has only been possible for undisturbed geomagnetic field models. Recent improvements in our understanding of the structure of the disturbed geomagnetic field has allowed us to take into account these deformations and dramatically improve the accuracy of the 'viewing cone' calculations (Kobel 1989). This is important because the presence of a GLE invariably means that the sun is in an active state and, as a result, the influence of the solar wind and shocks are likely to have caused magnetically disturbed conditions at the earth.

A second aspect of the particle trajectory deflection is that the minimum energy a particle must have to gain access to a ground based telescope is dependent on the location of that telescope on the earth's surface. This minimum energy is termed the 'cut-off' of the site and can be as high at 15 GeV for equatorial observatories. At mid-latitudes the cut-off reduces to a few GeV and at polar sites to virtually zero. There is a weaker dependence of the cut-off on longitude. Additionally the particles lose energy in penetrating the atmosphere; at sea level this amounts to ~0.5 GeV. The observations of GLE at multiple sites, with varying cut-offs, allows the determination of the direction of arrival of the event, the distribution about this arrival direction or anisotropy and the spectrum of the event. Furthermore, the absence of a response to a GLE at higher cut-off energy observatories gives an estimate of the maximum particle energies involved in the event.

22.4 PARTICLE INTERACTIONS IN THE ATMOSPHERE

As discussed above, particles with sufficient energy will eventually reach the earth's atmosphere. Within the upper levels of the atmosphere, above ~125 mb pressure level, these incident cosmic ray particles collide with atmospheric nuclei. Prior to the collision the particles are referred to as primary cosmic rays. The ensuing collision and nuclear interaction produces secondary particles through one of three characteristic processes. The process which takes place is dependent on the primary particle energy. Figure 3 shows the various cascade processes in the atmosphere. At energies above ~1000 GeV an 'air shower' of gamma rays and pair production/annihilation results. This may be detected at the surface through the arrival of a 'wave front' of electrons over a large area or from the emission of Cherenkov radiation as the air shower propagates deeper into the atmosphere. At energies of ~10 – 1000 GeV the nuclear interaction of the primary cosmic ray will produce a pion which subsequently decays into a muon. The muon may be detected at, or below, ground level with radiation detectors such as plastic scintillators and proportional counters. At the lowest energies capable of penetrating the atmosphere (~0.2 – 50 GeV) a nucleonic cascade results in the production of high energy neutrons. These neutrons are detected at ground level by a neutron monitor.

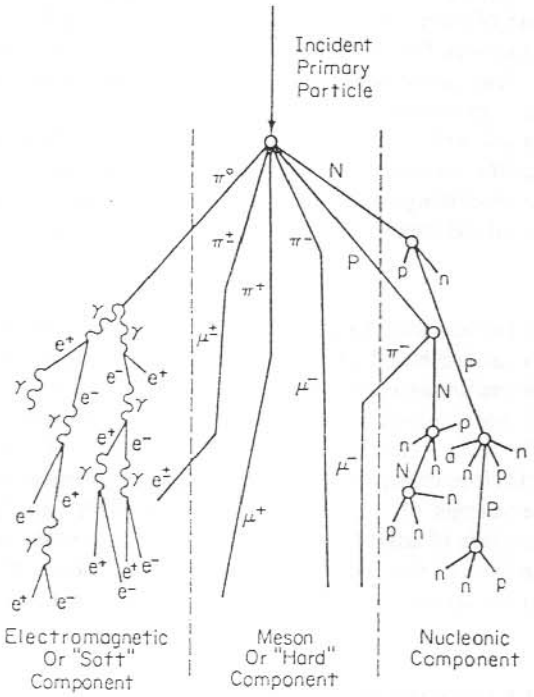

Figure 3. Principal interaction pathways of secondary particles following a primary cosmic ray interaction in the atmosphere. N and P are high energy nucleons; n, p are disintegration nucleons; o are atomic nuclei of the atmosphere.

22.5 NEUTRON MONITOR

Modern cosmic ray neutron monitors comprise large boron-trifluoride gas-filled counters surrounded by a polyethylene sheath and lead castings, the whole structure being enclosed by further polyethylene. High energy neutrons strike the lead causing a disintegration of some lead nuclei and producing an average of ten neutrons of lower energy which are scattered by the polyethylene and enter the detector counters. The inner polyethylene sheath reduces the number of other products from the initial interaction entering the counters. Within the counters the lower energy neutrons are able to interact with the boron nuclei as follows:

$$B^{10} + n \rightarrow Li^{7} + He^{4}$$

The lithium and helium ions (the latter are simply alpha particles) carry about 2.5 MeV energy for each event and it is the deposition of this energy in the counter which produces a detectable pulse on the anode wire. By its very nature this technique is non-directional, however the field of view of such detectors is approximately vertical. There is a well established decrease in efficiency with increasing zenith angle. This is due to the increasing atmospheric depth that particles must traverse as the zenith angle increases and is included in calculations of the viewing cone of the telescope system. A complete description of neutron monitors can be found in Hatton (1971).

22.6 MODELLING GLE

Techniques for modelling the dynamic behaviour of GLE throughout their development are not presently available. It is possible, however, to analyse the particle flux and distribution on an instantaneous basis following a standard technique (Shea and Smart 1982, Humble et al. 1991a, Humble et al. 1991b). The response to the increase of numerous telescopes worldwide are modelled to determine a best fit spectrum and spatial distribution of the particles arriving from the sun. The model for the telescope response is of the form

$$I = \sum_{P_c}^{\infty} J_a(\alpha, P).\ S(P).\ G(\alpha).\ dP$$

where I is the recorded percentage increase at the time
P is the particle momentum (in GV)
P_c is the minimum accessible momentum or cut-off for that telescope
α is the pitch angle of the particles
J_a is the interplanetary differential flux
S is the specific yield function of the telescope
and G is the pitch angle distribution of the arriving particles.

The specific yield function includes two components, the neutron monitor yield function (Lockwood et al. 1974), which gives the monitor response to particles arriving at the top of the atmosphere above the detector, and the telescope cones of viewing described above. The use of the particle momentum rather than energy relates to particle deflection in a magnetic field which is directly proportional to the momentum.

22.7 THE RECENT SEQUENCE OF GLE

Table 2 shows details of the sequence of GLE observed during the maximum of solar cycle 22 (July 1989 – June 1991). Several features of note are apparent. Firstly, the frequency of GLE occurrence around solar cycle 22 maximum is unprecedented. Of the 52 known GLE since 1942 a quarter of them were within this two year interval. Such a clustering of events has not been recorded previously. Secondly, the GLE on 29 September 1989 is the largest in the space exploration era and only exceeded in intensity by two events in the late 1940s and the largest event recorded on 23 February 1956. Thirdly, the three October 1989 GLE were all associated with the same active solar region. This was also true for the four GLE in May 1990. Multiple GLE from a single active region, though not unknown, are quite rare and two such multiply active regions within months of each other have only been observed once before. Analysis of the 19 October 1989 GLE by Shea et al. (1991) led to a proposal that a 'precursor' in the GLE time profile was a

result of solar neutrons decaying at the 'garden hose' field line and then propagating to the earth. This event also showed evidence of direct solar neutrons arriving at the earth. Another noteworthy point is that the fluence of the three associated October 1989 events was greater than the combined fluence of all other GLE in the present solar cycle.

Table 2. Summary of the sequence of GLE of the present solar cycle including details of the associated solar flares and the maximum response recorded at ground level.

		Parent Flare			GLE Maximum	
Event	Date	Location	Start (UT)	Max (UT)	%	Location
40	25/07/89	N25 W84	0839	0843	3	Goose Bay
41	16/08/89	S18 W84	0108	0117	13	Mawson
42	29/09/89	W105	1047	1133	372	Inuvik
43	19/10/89	S27 E10	1229	1255	47	Mawson
44	22/10/89	S27 W31	1708	1757	182	McMurdo
45	24/10/89	S30 W57	1736	1831	90	Thule
46	15/11/89	N11 W26	0638	0705	2	Deep River
47	21/05/90	N35 W36	2212	2217	11	Ottawa
48	24/05/90	N33 W78	2046	2049	11	Ottawa
49	26/05/90	W104			12	Thule
50	28/05/90	W130				
51	11/06/91				25	Mawson
52	15/06/91					

Data from *Solar Geophysical Data* - Part II, Nos. 545-555, Swinson and Shea (1990) and Humble et al. (1990)

22.8 29 SEPTEMBER 1989 GLE

The 29 September 1989 GLE was the first such event to be detected by all detectors in the present Australian neutron monitor network, which stretches from Mawson, Antarctica to Darwin in the tropics. To gain access to the Darwin monitor the energy of the solar accelerated particles must have extended to at least 15 GeV. Furthermore, surface muon detectors at Hobart and Mawson also observed the increase, confirming the high energy nature of the event. No increases were seen at either site by the underground telescopes. Previously, only the 23 February 1956 GLE had resulted in muon detection of solar particles at these observatories (Fenton et al. 1956).

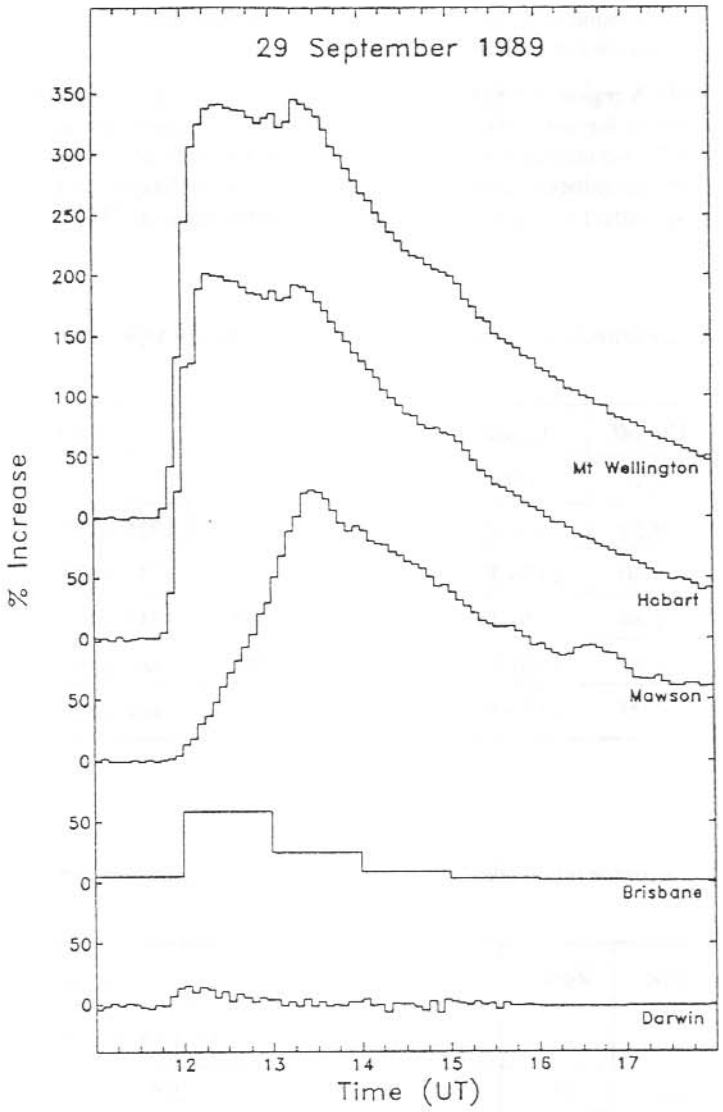

Figure 4. 29 September 1989 GLE as observed by the Australian neutron monitor network. Problems with the recording system at Brisbane meant that only hourly data were available from that station.

Table 3 gives details of the Australian neutron monitors and the times of onset and maximum response to the enhancement whilst Figure 4 shows the time profile from these stations. Note that problems with the recording electronics at Brisbane required data recovery from a chart record.

Table 4 gives the hourly muon telescope responses for the Hobart and Mawson observatories. Data on shorter timescales are not available for these instruments.

The solar region (NOAA region 5698) believed responsible for this event had rotated to ~15° behind the western limb of the sun (~105°W). The NOAA/GOES-7 spacecraft observed an X-ray event onset at 1047 UT and lasting 4 hours. The maximum intensity of X9.8 at 1133 UT was accompanied by a loop prominence system seen in H_α and discrete frequency radio bursts. At 8800 MHz the commencement was at 1120 UT and reached a maximum at 1137 UT.

Table 3. The Australian neutron monitor and their responses to the 29 September 1989 GLE.

Station	Cut-off	Onset	First Max		Second Max	
	GV	UT	UT	%	UT	%
Mawson	0.20	1154-55	not seen		1325-1330	230
Mt Wellington	1.80	1146-47	1225-1230	342	1315-1320	344
Hobart	1.84	1146-47	1215-1230	300	1315-1320	291
Brisbane	6.99	1150-55	1205-1220	79	not seen	
Darwin	14.09	1150-55	1155-1215	13	not seen	

Table 4. Hobart and Mawson muon telescope responses to the 29 September 1989 GLE.

Station	Telescope	Zenith	Az	Threshold	Increase %	
				GV	1200-1300 UT	1300-1400 UT
Mawson	Surface	42	N	~3	2.5	1.7
		42	S	~3	2.5	1.7
		62	N	5	1.3	1.3
		62	S	5	1.5	1.3
	Underground	24	N	10	not seen	not seen
		40	SW	11	not seen	not seen
Hobart	Surface	0	V	2.5	28.0	8.4
	Underground	0	V	10	not seen	not seen

The solar region (NOAA region 5698) believed responsible for this event had rotated to ~15° behind the western limb of the sun (~105°W). The NOAA/GOES-7 spacecraft observed an X-ray event onset at 1047 UT and lasting 4 hours. The maximum intensity of X9.8 at 1133 UT was accompanied by a loop prominence system seen in H_α and discrete frequency radio bursts. At 8800 MHz the commencement was at 1120 UT and reached a maximum at 1137 UT.

In Figure 5 the asymptotic directions of view of the Australian network neutron monitors are shown assuming an undisturbed geomagnetic field. The analysis of this event using the disturbed magnetic field appropriate to the time of the event (Kp ~2+) is presently being undertaken and will be reported elsewhere.

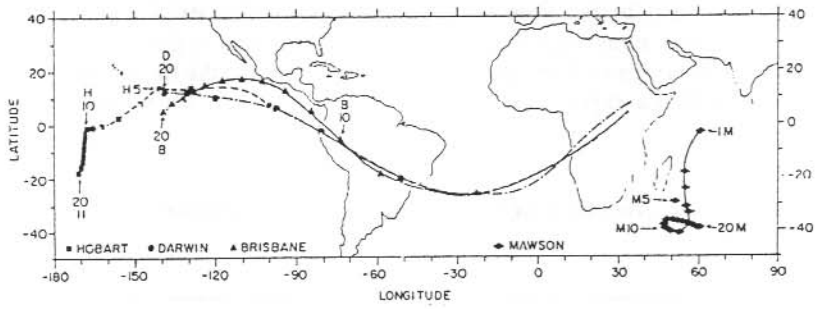

Figure 5. Viewing cones of the five Australian neutron monitor stations. Hobart and Mt Wellington have identical viewing cones and are not repeated.

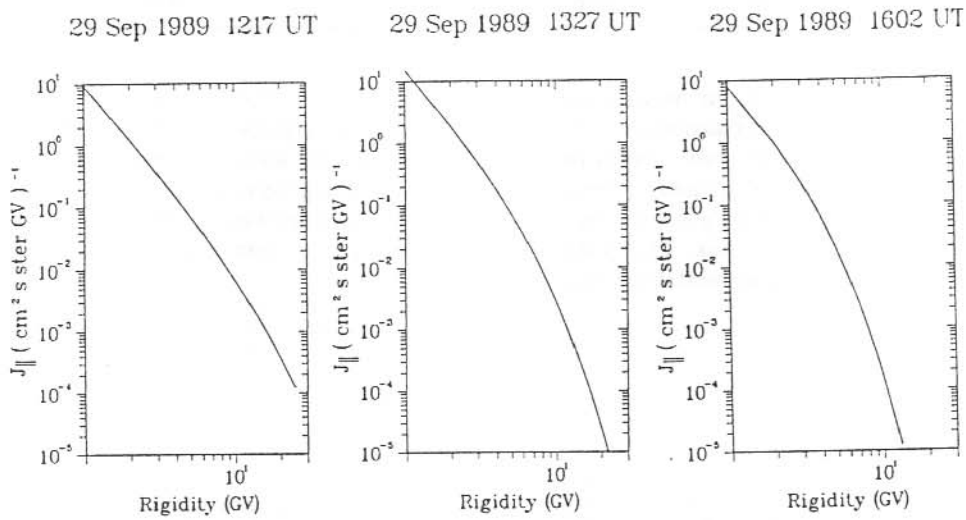

Figure 6. Spectral fits to the first maximum (left), second maximum (centre) and decay phase (right) of the 29 September 1989 GLE.

It is clear from Figure 4 that the event has complex structures with two maxima, the first seen by all stations except Mawson and the second not seen by the low latitude stations Brisbane and Darwin. The event was therefore analysed at the times of each maximum and during the decay phase.

The initial apparent 'source' direction was westward of the nominal 'garden hose' direction but we do not have knowledge of the actual interplanetary magnetic field as IMP-8 was in the geomagnetic tail at the time. The event was also significantly anisotropic.

In Figure 6 the derived spectra for the two maxima and during the decay phase are shown. It is clear that the spectrum was initially quite hard and softened throughout the event. Figure 7 shows the derived pitch angle distribution of the arriving particles during the first maximum and decay phases. The spectrum may be described in terms of the particle flux arriving parallel to apparent source direction $J_{\parallel}$ or as an average integrated over the full pitch angle distribution J_{av}. The spectra are summarised in Table 5 and are quoted as power laws in the range 1 to 2 GV together with the rate of power law exponent steepening, $\delta\gamma$, above 2 GV. J is in units of $(cm^2\ s\ ster\ GV)^{-1}$.

Table 5. Spectra resulting from the analysis of Australian neutron monitor data for 29 September 1989.

Time	$J_{\parallel}$	J_{av}	γ	$\delta\gamma$ per GV(>2 GV)
1217 UT (1st max)	9.30	5.54	-2.9	-0.1
1330 UT (2nd max)	15.21	10.05	-3.0	-0.3
1600 UT (decline)	10.26	7.52	-3.0	-0.9

In modelling this event the Mawson response is due to particles propagating in the 'reverse' direction whilst the other stations observe 'forward' propagating particles. It is clear that the time of the first maximum is dominated by the higher rigidity particles whilst the lower rigidity flux reaches its maximum at the time of the second peak. In modelling the response at Darwin to the high energy maximum a significant fraction of the detected particles were found to have arrived from non-vertical directions. This is consistent with the large variation in geomagnetic cut-off between vertical and westward directions at Darwin.

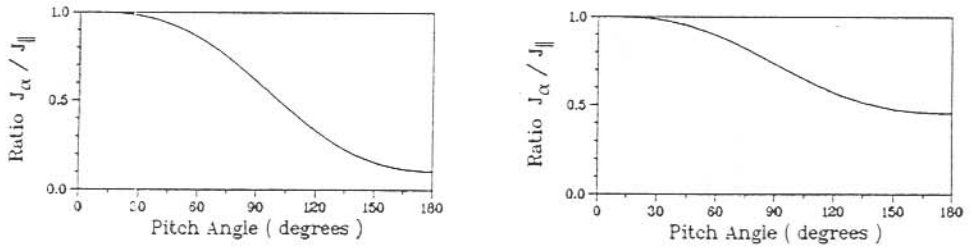

Figure 7. Pitch angle distribution fits to the first maximum (left) and decay phase (right) of the 29 September 1989 GLE.

22.9 22 OCTOBER 1989 GLE

The GLE of 22 October 1989 is quite different in structure from the 29 September 1989 event just described. It was the second of three GLE which have been associated with the same solar active region, namely NOAA/USAF Region 5747. A coincident X-ray event commenced at 1708 UT, lasted four hours and was accompanied by H_α emission. Radio emission at frequencies of 245 MHz - 15400 MHz commenced at ~1730 UT. These associated emissions are summarised in Table 6.

The GLE was observed at many stations in the world wide neutron monitor network but a 'precursor' peak was observed at only five stations. These observations are shown in Figure 8.

The main GLE increase is shown in more detail in Figure 9 for several widely dispersed stations. It is clear that the event is quite complex with several significant peaks implying multiple particle injections or varying particle acceleration either at the solar source or in propagation to the earth. The main increase is being modelled at present and results will be reported elsewhere.

The sharp 'precursor' event has been modelled as described earlier in this paper. Initial efforts to model the 'precursor' with an undisturbed geomagnetic field were unsuccessful and no satisfactory fit could be derived. The geomagnetic field was, however, highly disturbed at this time with $K_p = 5+$. Figure 10 shows the effect on the viewing cones of the four stations in this disturbed magnetic state. As before, Hobart and Mt Wellington have identical viewing cones; only Hobart is shown.

Table 6. Details of the solar flare emissions associated with the 22 October 1989 GLE.

Frequency	Onset	Maximum	End
	(UT)	(UT)	(UT)
1-8 Å X-ray	1708	1757	2108
H_α	1708	1757	2108
245 MHz	1734	1738	1841
410	1735	1751	1852
610	1731	1746	1915
1415	1732	1824	2019
2695	1731	1818	2019
4995	1731	1801	2013
8800	1732	1801	1956
15400	1732	1801	2023

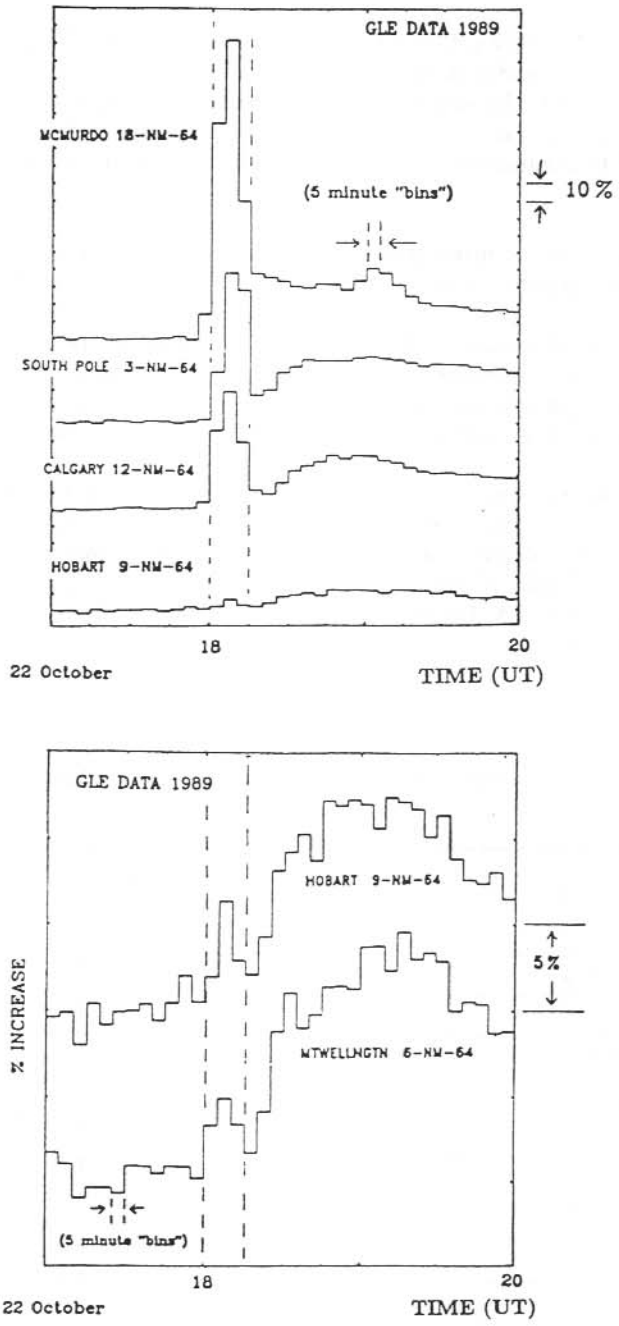

Figure 8 (a). 22 October 1989 'precursor' observations at McMurdo, South Pole, Calgary and Hobart. (b). Enlarged view as seen at Hobart and Mt Wellington.

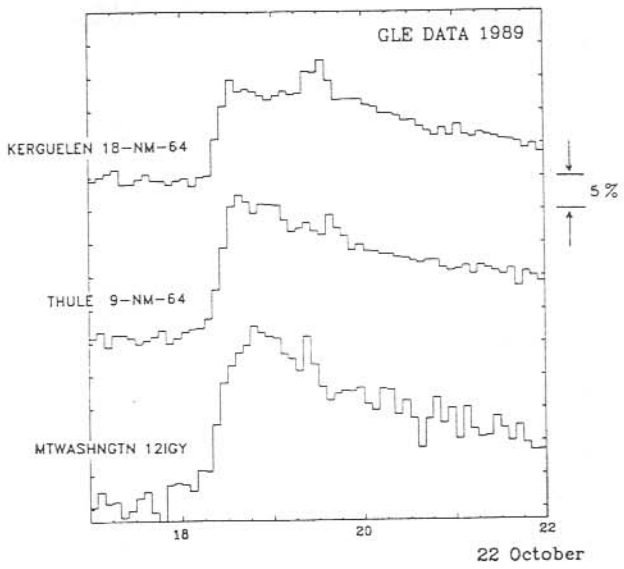

Figure 9. 22 October 1989 GLE as seen at Kerguelen, Thule and Mt Washington. The 'precursor' is absent at these stations.

Taking account of the disturbed geomagnetic conditions it was possible to obtain an excellent fit to the arriving particle distribution. The spectrum was found to be very steep and was best described by

$$J_{||} = 47.78P^{-8.55}$$

with a constant spectral slope. The pitch angle distribution was found to be extremely anisotropic as shown in Figure 11.

This is the first time that it has been shown to be essential to include geomagnetic disturbance parameters in the GLE modelling to obtain satisfactory parameters for an event.

The cause of this very highly anisotropic 'precursor' with its unusually steep spectrum in unclear. As no direct solar neutrons were observed at earth it is unlikely that the event was due to decaying of neutrons on the 'garden hose' field line with subsequent propagation to earth. No information on the interplanetary magnetic field is available for this event, again because IMP-8 was in the magnetotail, but the apparent source direction of -20°, 265° was very close to the sub-solar point of -11°, 271°. This source direction is a long way from the nominal 'garden hose' direction some 45° westward of the sub-solar point. Although we have no interplanetary field data for the event, it is known from IMP-8 measurements that a fast solar wind (>700 km s^{-1}) stream was present on 20 and 21 October and may well have continued until the time of the event. Such high speed streams will tend to flatten the curve in the 'garden hose' field line and move the field line direction at earth closer to the sun-earth line. It seems likely that the 'precursor' event involved an unusual particle injection/acceleration at the sun and further studies are continuing.

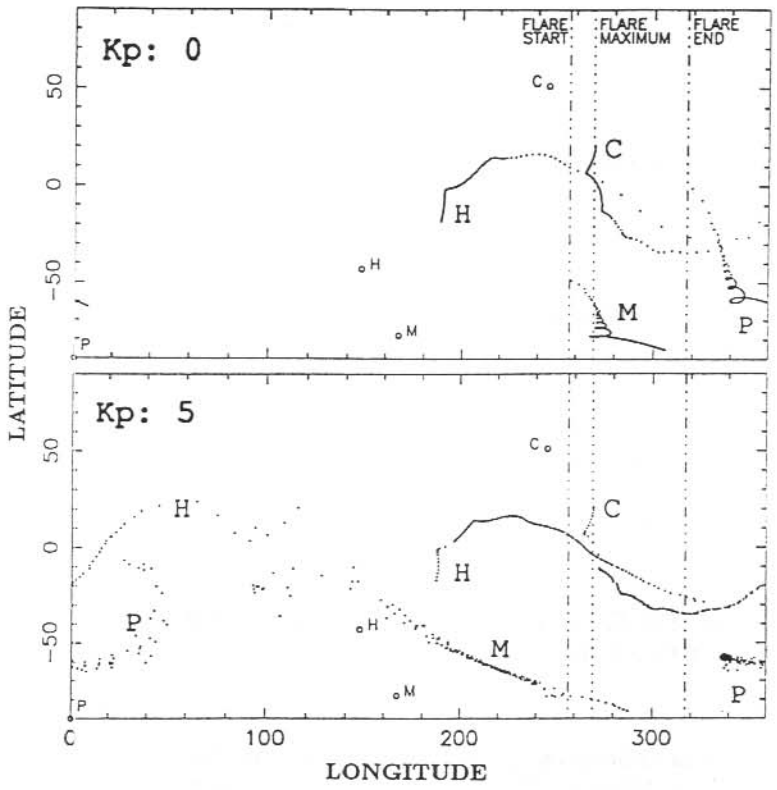

Figure 10. Comparison of the viewing cones for undisturbed (Kp = 0, top) and disturbed (Kp = 5, bottom) geomagnetic conditions [H = Hobart, C = Calgary, P = South Pole, M = McMurdo].

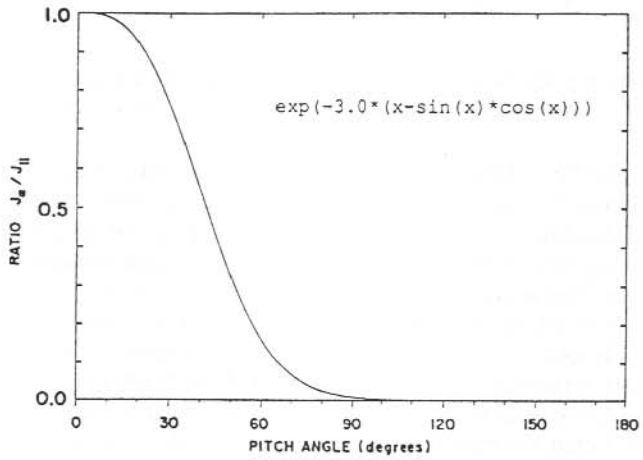

Figure 11. Pitch angle distribution fit to the 'precursor' of 22 October 1989 GLE at 1805 UT.

22.10 CONCLUSION

The derivation of accurate descriptive parameters for the structure of GLE particle distributions give important insights into and set limits on particle acceleration mechanisms at the sun. It is clear from the present ongoing study that disturbed geomagnetic conditions must be included in the analysis of GLE and it is likely that many conclusions from earlier studies will need to be reconsidered. With the recent development of techniques to account for geomagnetic disturbance effects on the viewing cones of neutron monitors there is a need for all previous analyses of GLE to be reconsidered. For those GLE where disturbed conditions existed (the majority) reanalysis of the data should be undertaken. It is also important to consider the same effects in past and present studies of Forbush decreases. Conclusions about shock propagation in the interplanetary magnetic field near the earth and shock interaction with energetic particles (>1 GeV) may need to be modified following such reanalysis.

The two GLE highlighted in this paper indicate that present understanding of the acceleration and propagation of high energy particles is still in its infancy. Present theoretical models are too simplistic to account for the complex structures observed, and reanalysis of GLE will help to advance our understanding of acceleration and propagation phenomena.

REFERENCES

Bendoricchio, M.B.M. (1991). *The 22 October 1989 ground level enhancement.* Honours Thesis, University of Tasmania.

Fenton, A.G., McCracken, K.G., Parsons, N. *and* Trost, P.A. (1956). Cosmic ray increase observed at high southern latitudes on February 23, 1956. *Nature 177*:1173 – 1174.

Hatton, C.J. (1971). The neutron monitor. *In: Progress in Elementary Particle and Cosmic Ray Physics*, Vol. XX, Chapter 1. Pp. 1 – 100.

Humble, J.E., Duldig, M.L., Fenton, A.G. *and* Fenton, K.B. (1990). Australian observations of the 16 August 1989 ground level event. *Proceedings of the 21st International Cosmic Ray Conference, Adelaide 5*:164 – 166.

Humble, J.E., Duldig, M.L., Smart, D.F. *and* Shea, M.A. (1991a). Detection of 0.5–15 GeV solar protons on 29 September 1989 at Australian stations. *Geophysical Research Letters 18*:737 – 740.

Humble, J.E., Duldig, M.L., Smart, D.F. *and* Shea, M.A. (1991b). The 29 September 1989 solar cosmic ray event as observed by Australian stations. *Proceedings of the 22nd International Cosmic Ray Conference, Dublin 3*:109 – 112.

Kobel, E. (1989). *Bestimmung der grenzsteifigkeiten und der asymptotichen richtungen der kosmichen strahlung für das solare protonenereignis vom 7./8. Dezember 1982 unter berücksichtigung der einflüsse der gestörten erdmagnetosphäre.* M.Sc. Thesis, University of Bern.

Lockwood, J.A., Webber, W.R. *and* Hsieh, L. (1974). Solar flare proton rigidity spectra deduced from cosmic ray neutron observations. *Journal of Geophysical Research 79*:4149 – 4155.

Nagashima, K., Sakakibara, S. *and* Morishita, I. (1991). Quiescence of GLE-producible solar proton eruptions during the transient phase of heliomagnetic polarity reversal near the solar-activity-maximum period. *Journal of Geomagnetism and Geoelectricity 43*:685 – 689.

Shea, M.A. *and* Smart, D.F. (1982). Possible evidence for a rigidity-dependant release of relativisitic protons from the solar corona. *Space Science Reviews 32*:251 – 271.

Shea, M.A., Smart, D.F., Wilson, M.D. *and* Flückiger, E.D. (1991). Possible ground-level measurements of solar decay protons during the 19 October 1989 solar cosmic ray events. *Geophysical Research Letters 18*:829 – 832.

Swinson, D.B. *and* Shea, M.A. (1990). The September 29, 1989 ground-level event observed at high rigidity. *Geophysical Research Letters 17*:1073 – 1075.

23. THE COSMIC RAY DIURNAL VARIATION NEAR THE HELIOSPHERIC CURRENT SHEET

J.L. Cramp[1], M.L. Duldig[2] and J.E. Humble[1]

[1] Physics Department
University of Tasmania
Hobart Tasmania 7001
Australia

[2] Cosmic Ray Section
Antarctic Division
Kingston Tasmania 7050
Australia

ABSTRACT

The proximity of the Heliospheric Current Sheet (HCS) may affect the modulation of cosmic rays. Duldig and Humble (1990) have previously reported that during many periods of enhanced diurnal variation (DV) at least one sector boundary crossing occurred. Here we investigate the variations in the DV with changing distance between the HCS and the earth. We have used both 1D and 3D models to estimate the HCS distance. Significant correlations have been found with the 1D model. The results and models are discussed.

23.1 INTRODUCTION

The heliospheric current sheet (HCS) is present at the solar magnetic equator where the magnetic field lines are drawn away from the sun by the solar wind. Near solar minimum the HCS forms a nearly flat sheet in interplanetary space but as solar activity increases the HCS becomes wavy. At solar maximum it may extend nearly to the poles (Svalgaard and Wilcox 1976, Wilcox et al. 1980).

When the HCS is wavy the earth is sometimes above and at other times below the surface. The result of this is the observation, at earth, of an apparent sector structure in the solar magnetic field. The field is oppositely directed in adjacent sectors, being alternately toward and away from the sun.

Cosmic ray particles tend to co-rotate with the solar magnetic field, sweeping past the earth at about 400 km/s. This results in a diurnal variation (DV) in intensity observed at earth due to a Doppler effect (Ahluwalia and Dessler 1962). This variation is harmonically analysed and represented as the sum of three sinusoids. Each harmonic can be represented as a vector on a harmonic dial and cartesian components a and b are found.

Periods of enhanced DV have been observed by both surface and underground detectors, (Swinson and Saito 1986, Humble et al. 1989 and references therein) where the amplitude of the variation may be 2 – 5 times the mean amplitude. Various mechanisms have been suggested but

Humble et al. (1989) were not satisfied that any of these models fully explained all events. They noted that at least one sector boundary crossing occurred during many of the events they observed. Swinson et al. (1981) also related the occurrence of enhanced DV to the sector structure of the interplanetary field.

23.2 ONE DIMENSIONAL MODEL

23.2.1 *Distance approximation*

As the HCS sweeps past the earth the distance to a sector boundary crossing can be approximated by counting the number of days before or after its arrival. It is therefore possible to obtain an approximation to the distance between the earth and the HCS by calculating the number of days to the nearest sector boundary crossing. This represents the distance to the HCS around the earth's orbit and, for a slowly varying HCS, should give a reasonable approximation to the actual distance to the HCS.

Consider the HCS to be smooth and symmetrical about the centre of a sector. When the earth is at a sector boundary crossing the distance to the HCS is zero. As the field structure sweeps past the earth the number of days to the nearest sector boundary crossing increases until the middle of the sector is reached. At this point the earth is furthest from the HCS. As long as the maximum latitudinal extent of the HCS does not change greatly the distance approximations for different sectors will be comparable. It is therefore necessary to restrict the length of time over which comparisons are made.

During times when the shape of the HCS is irregular or when there are multiple current sheets, as is common at solar maximum (Hoeksema et al. 1983), this calculation clearly does not represent the distance to the HCS. It may, however, be expected to give good results at solar minimum.

Sector boundary crossings can be identified as changes in the radial magnetic field direction from one day to the next, or occurrences of mixed field direction. Interplanetary field direction data include a measurement of the radial field direction for each day. The data employed are the standard set used by the Hobart cosmic ray group. The set has been compiled from various sources by J.E. Humble and D.B. Swinson. By identifying the position of sector boundary crossings, the number of days since a sector boundary crossing and the number of days until the next one can be calculated for each day. The smaller of these two numbers is taken as the number of days to the nearest sector boundary crossing.

23.2.2 *Analysis*

There are two possible ways of finding the average amplitude of the DV for a set of data. The scalar average is simply the average over all amplitudes:

$$\langle \text{amp} \rangle = \frac{\sum_{i=1}^{N} \text{amp}(i)}{N},$$

where N is the number of days.

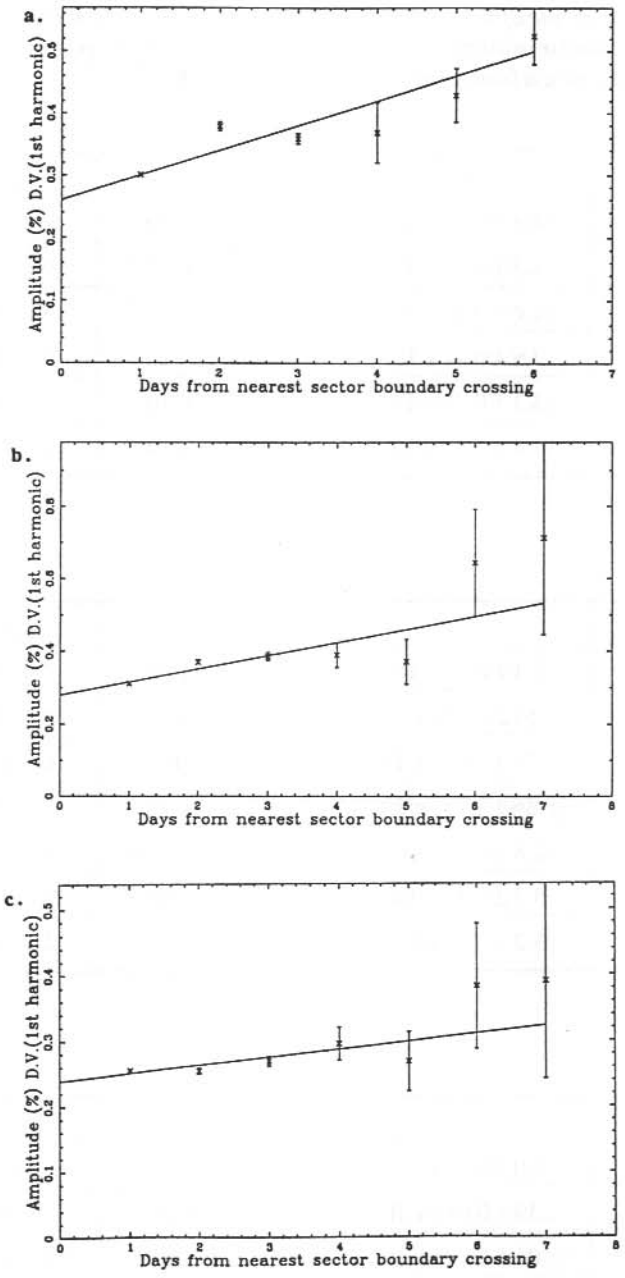

Figure 1. Scalar averages of amplitude of diurnal variation plotted against the number of days to nearest sector boundary crossing, for (a) Mawson, (b) Mt Wellington and (c) Darwin neutron monitor data 1978 – 79.

Table 1. Coefficients of line of best fit (y = mx+c) for (a) Mawson, (b) Mt Wellington and (c) Darwin neutron data for available periods between 1970 and 1985. p is the probability that a random sample would have a better correlation with the fitted line.

(a)

Period	c	m	p
1974 – 75	$(2.8 \pm 0.1) \times 10^{-1}$	$(1.2 \pm 0.4) \times 10^{-2}$	3×10^{-3}
1976 – 77	$(2.3 \pm 0.1) \times 10^{-1}$	$(3.8 \pm 0.5) \times 10^{-2}$	9×10^{-9}
1978 – 79	$(2.6 \pm 0.1) \times 10^{-1}$	$(4.0 \pm 0.5) \times 10^{-2}$	5×10^{-9}
1980 – 81	$(2.9 \pm 0.1) \times 10^{-1}$	$(2.3 \pm 0.5) \times 10^{-2}$	1×10^{-5}
1982 – 83	$(3.1 \pm 0.2) \times 10^{-1}$	$(2.7 \pm 0.5) \times 10^{-2}$	3×10^{-6}
1984 – 85	$(3.4 \pm 0.1) \times 10^{-1}$	$(1.4 \pm 0.4) \times 10^{-2}$	2×10^{-4}

(b)

Period	c	m	p
1970 – 71	$(3.1 \pm 0.1) \times 10^{-1}$	$(1.4 \pm 0.4) \times 10^{-1}$	2×10^{-3}
1972 – 73	$(2.57 \pm 0.07) \times 10^{-1}$	$(1.0 \pm 0.3) \times 10^{-2}$	5×10^{-3}
1974 – 75	$(2.71 \pm 0.08) \times 10^{-1}$	$(2 \pm 3) \times 10^{-3}$	6×10^{-1}
1976 – 77	$(1.86 \pm 0.07) \times 10^{-1}$	$(3.0 \pm 0.3) \times 10^{-2}$	1×10^{-9}
1978 – 79	$(2.8 \pm 0.1) \times 10^{-1}$	$(3.6 \pm 0.6) \times 10^{-2}$	4×10^{-9}
1980 – 81	$(3.2 \pm 0.1) \times 10^{-1}$	$(1.3 \pm 0.5) \times 10^{-2}$	5×10^{-3}
1982 – 83	$(3.2 \pm 0.1) \times 10^{-1}$	$(1.7 \pm 0.3) \times 10^{-2}$	2×10^{-3}

(c)

Period	c	m	p
1977	$(2.0 \pm 0.3) \times 10^{-1}$	$(3.0 \pm 0.2) \times 10^{-2}$	0.1
1978 – 79	$(2.39 \pm 0.08) \times 10^{-1}$	$(1.2 \pm 0.3) \times 10^{-2}$	3×10^{-4}
1980 – 81	$(2.01 \pm 0.08) \times 10^{-1}$	$(2.0 \pm 0.4) \times 10^{-2}$	2×10^{-8}
1982 – 83	$(1.47 \pm 0.07) \times 10^{-1}$	$(1.6 \pm 0.2) \times 10^{-2}$	1×10^{-8}
1984 – 85	$(1.83 \pm 0.09) \times 10^{-1}$	$(1.1 \pm 0.2) \times 10^{-2}$	8×10^{-3}

A vector average may be obtained by first averaging the a and b components of the diurnal vectors to obtain $\langle a \rangle$ and $\langle b \rangle$:

$$\langle a \rangle = \frac{\sum_{i=1}^{N} a(i)}{N}, \qquad \langle b \rangle = \frac{\sum_{i=1}^{N} b(i)}{N}$$

The vector average of amplitude is then given by

$$\langle amp \rangle = \sqrt{\langle a \rangle^2 + \langle b \rangle^2}$$

23.2.3 *Analysis using a scalar average of amplitude*

As there is a known change in the DV over the period of a solar cycle (~11 years), it is necessary to consider data over a sufficiently short period that the results will not be affected by such a change. It is also important to ensure that the maximum latitudinal extent of the HCS does not change significantly during the chosen time period. On the other hand, the statistical significance of results increases when more data are used so there must be a compromise between these factors in choosing the periods over which analysis should be performed. In general, periods of two consecutive years were chosen.

Data from Mawson, Mt Wellington and Darwin neutron monitors were used in the study. Scalar averages of the amplitude of the first harmonic of the DV were calculated for days of equivalent distance from the nearest sector boundary crossing. Example plots are shown in Figure 1. The error bars represent the 1σ RMS errors in the mean of the data averaged to obtain each point. Most of the plots displayed linear characteristics, with a positive slope. A least squares fit of straight lines was made to the data.

Results for Mawson, Mt Wellington and Darwin neutron monitor data are shown in Table 1 (a), (b) and (c) respectively. The fitted line is given as

$$y = mx + c$$

and errors in c and m are shown, along with the probability, p, of randomness of the fit. The errors in c and m are calculated from the standard deviations of the data used to calculate c and m. The rejection criteria in the analysis were based on the residuals, in units of standard deviation, between the cosmic ray data and the sum of the fitted harmonics. All days for which the maximum residual was $>5\sigma$ were rejected. This means that intensity variations such as Ground Level Enhancements and Forbush Decreases were removed.

23.2.4 *Analysis using a vector average of amplitude*

Analysis using the vector average of the amplitudes of the first harmonic of the DV was also undertaken. The data were again processed in two year intervals. The resulting plots for Mawson, Mt Wellington and Darwin neutron monitor data for 1978–79 are shown in Figure 2.

Unlike the scalar average of the amplitude, there appears to be no definite correlation which can be applied to these plots. Only a few plots show linear tendencies.

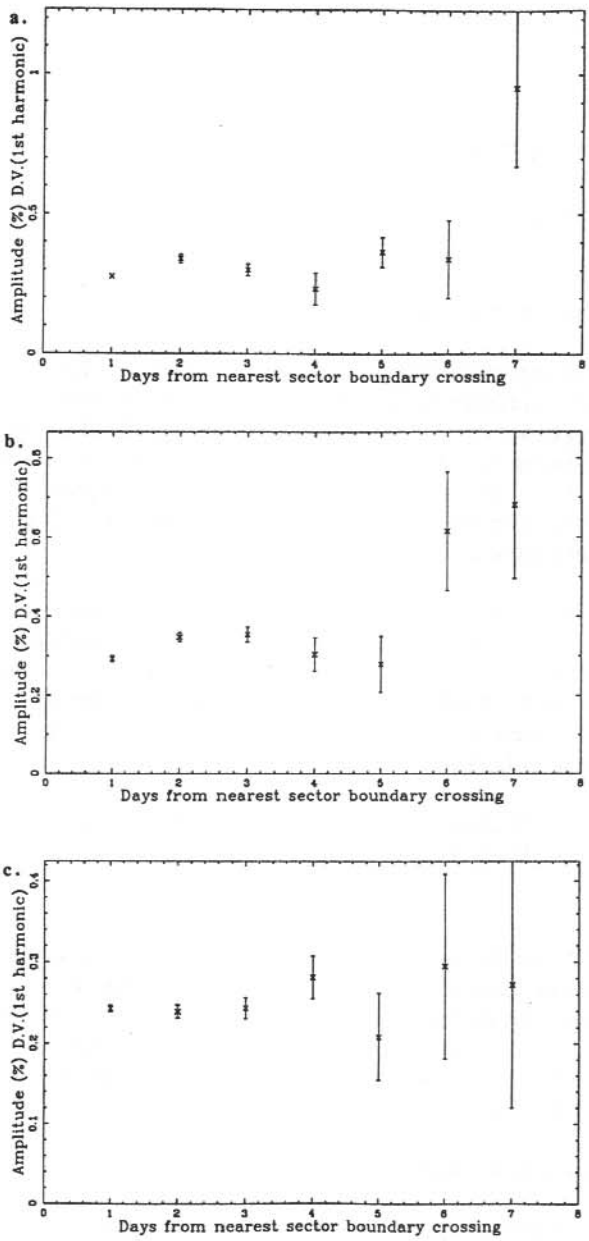

Figure 2. Vector averages of amplitude of DV plotted against the number of days to the nearest sector boundary crossing for (a) Mawson, (b) Mt Wellington and (c) Darwin neutron monitor data 1978–79.

23.3 THREE DIMENSIONAL MODEL

It may be possible to improve the correlations observed between the distance to the HCS and amplitude of the DV by construction of a three dimensional model of the HCS and calculating the distance from its nearest point to earth.

23.3.1 *Modelling the HCS*

If we assume that the HCS on the solar surface can be described by a function $f(\theta, \phi) = 0$, it can be shown (Appendix A) that for a coordinate system (r, θ, ϕ) in which the sun rotates with angular velocity Ω and the radial solar wind speed is V, the form of the equation is

$$f(t) = \theta - \frac{\pi}{2} - \alpha \sin\left(\frac{1}{2}n\phi + \frac{r\Omega}{V} - \frac{1}{2}\Omega t\right) = 0 \qquad (1)$$

for an n-sector HCS, where α, the tilt angle of the dipole of the solar magnetic field, is small.

To generalise this for larger tilt angles, an harmonic expansion is used and the equation becomes

$$\theta_{ns}(t) = \frac{\pi}{2} - \sum_{i=1}^{6}\Big[\, \beta_{2i-1} \sin\left(i[\phi - \Omega t] + \frac{r\Omega}{V}\right) + \beta_{2i}\cos\left(i[\phi - \Omega t] + \frac{r\Omega}{V}\right)\Big] + \beta_{13}t + \beta_{14} \qquad (2)$$

Therefore if we have some information about the heliolatitude of the HCS over a period of time, we can fit this function to the data, determining the 14 parameters β_i.

Modelling of the HCS near the sun is possible using Zeeman observations to construct the structure on a spherical source surface (Hoeksema et al. 1982, 1983). Propagation is then assumed to be with the solar wind. Daily calculations of the heliolatitudinal displacement of the HCS from earth produced by this model were available (J.T. Hoeksema, private communication) for the period 1977 – 1988.

Using these data and the position of the earth in heliocentric coordinates, the heliolatitude of the HCS can be calculated. This forms a data set to which equation (2) can be fitted. This was done by a method of singular value decomposition. The distance between the earth and the nearest point on the HCS was then calculated numerically.

23.3.2 *Comparison of DV amplitude with distance to HCS*

Plots of DV amplitude against the distance to the nearest point on the HCS were produced. A typical plot is shown in Figure 3.

Amplitudes were also 'binned' into ranges of distance from the HCS. Both scalar and vector averages were used as described in Section 23.2. Figure 4 is an example of the results with scalar averages. The average amplitude is shown above the largest distance in the 'bin'. Figure 5

shows the same data analysed using vector averages. No consistent correlations were found for either case.

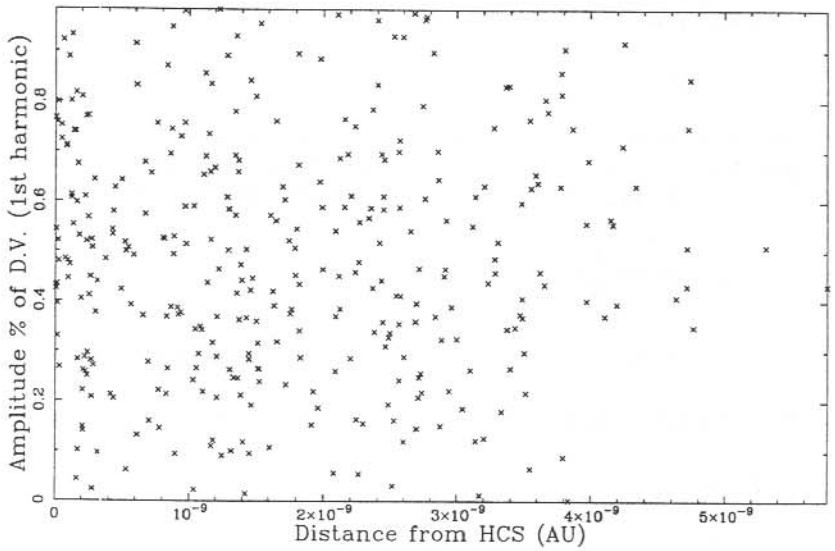

Figure 3. Amplitude of the DV (Mawson neutron monitor data 1978) plotted against the calculated distance to the HCS.

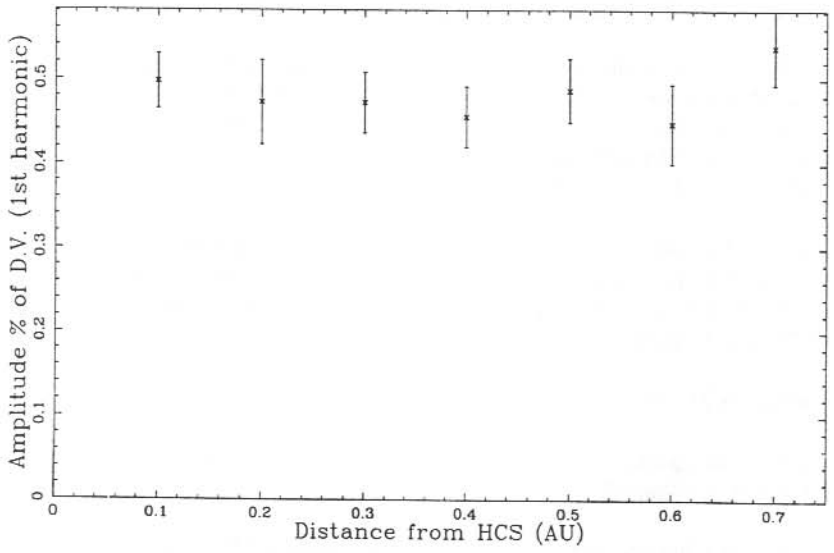

Figure 4. Scalar average of amplitude of the DV plotted against the calculated distance to the HCS for Mawson neutron monitor data of 1978.

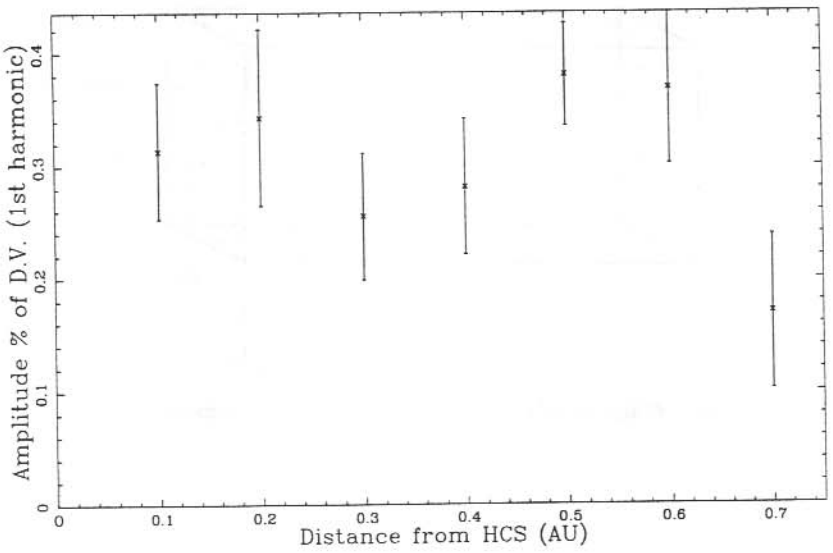

Figure 5. Vector average of amplitude of the DV plotted against the calculated distance to the HCS for Mawson neutron monitor data of 1978.

23.4 DISCUSSION AND POSSIBLE EXPLANATION

It is generally accepted that a cosmic ray density gradient exists perpendicular to the solar magnetic equator (i.e. the HCS). There is some speculation as to the form of the gradient but observations by Badruddin et al. (1985) indicate that there is a maximum in cosmic ray intensity at the HCS, decreasing on either side. We now investigate the effect of this gradient upon the DV.

Consider N particles in a box with sides of length X, dy, dz. Let the number density of the particles be a function of x, i.e. $\rho = \rho(x)$. Now,

$$N = \left[\int_0^X \rho(x)dx \right] dydz$$

Let the average speed of the particles in the x direction be w_x.

Consider the particles to have an additional streaming velocity V in the positive x direction, as illustrated in Figure 6.

The flux of particles through the plane dy, dz in the positive and negative x directions will be given by j_+ and j_- respectively, where

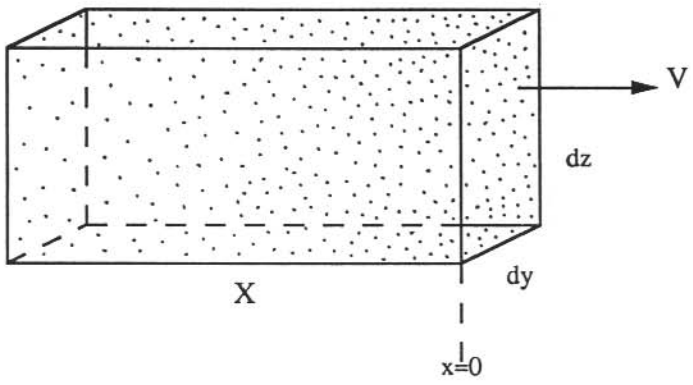

Figure 6. Particles with average speed w_x in the x direction and a streaming velocity of V as shown.

$$j_+ = \frac{v_{x+}}{X}\,\frac{\int_{-X}^{0}\rho(x)dx}{dt} \quad \text{and} \quad j_- = \frac{v_{x-}}{X}\,\frac{\int_{0}^{X}\rho(x)dx}{dt},$$

v_{x+}, v_{x-} are the average speeds of particles in the positive and negative x directions respectively.

$$v_{x+} = w_x + V, \quad v_{x-} = w_x - V$$

Now consider the particles to be cosmic rays streaming past the earth. The average flux of particles is

$$\langle j \rangle = \frac{j_+ - j_-}{2}$$

and the difference between the fluxes in the positive and negative directions as a fraction of the average flux is

$$\Delta j = \frac{j_+ - j_-}{\langle j \rangle} = \frac{2(j_+ - j_-)}{j_+ + j_-}$$

Let us consider a sinusoidal density profile, reaching its maximum at the HCS. In this case

$$\rho(x) = \rho_0\left(\cos\left(\frac{\pi x}{13.5}\right) + n\right)$$

where n is a constant which may be adjusted to give the required intensity variation. The factor $\pi/13.5$ allows x to be measured in days, with the positive half of the cosine function spanning about half a solar rotation, i.e. one sector of a 2-sector structure.

Badruddin et al. (1985) measured the change in intensity near sector boundary crossings for several stations and found it to vary by less than 1%. Taking n to be 250 gives a variation of 0.8%.

A 10 GV proton has gyroradius of ~0.06 AU so X = 1 (≡ 0.23 AU, the tangential distance the HCS has moved with respect to the earth in 1 day) or 4 gyroradii is sufficient to ensure that the particle is modulated by the region of interest. Therefore if a sector boundary crossing occurs at x = 0, we can integrate for X = 1 giving

$$j_+ = \rho_0(w_x + V)\left[250 - \frac{13.5}{\pi}\sin\left(\frac{\pi}{13.5}\right)\right]$$

$$j_- = \rho_0(w_x - V)\left[250 - \frac{13.5}{\pi}\sin\left(\frac{\pi}{13.5}\right)\right]$$

i.e. $j_+ = (w_x + V)j_0$ and $j_- = (w_x - V)j_0$

where $j_0 = \rho_0\left[250 - \frac{13.5}{\pi}\sin\left(\frac{\pi}{13.5}\right)\right]$

Calculating Δj from j_+ and j_- gives

$$\Delta j = \frac{2(j_+ - j_-)}{j_+ + j_-} = \frac{2V}{w_x}$$

As the earth rotates, this flux difference will produce a DV with amplitude $100\Delta j\%$. V is the co-rotation velocity of particles at R = 1 AU.

i.e. $$V = \frac{2\pi R}{T} = \frac{2\pi \times 1.496 \times 10^{11}}{27 \times 86400} \approx 4 \times 10^5 \text{ m/s}$$

It can be shown that the average speed of particles in both the positive and negative directions is half their average speed. Cosmic ray particles travel at relativistic speeds and so for a 10 GV proton

$$w_x = \frac{1}{2}c$$

As w_x is relativistic we must be careful when adding the streaming velocity. Since the streaming velocity, V, is small compared with c, relativistic calculations make very little difference and it is sufficient to proceed non-relativistically.

Using the values for V and w_x calculated above we can find the amplitude of the DV

$$\Delta j = \frac{2V}{w_x} = \frac{2\times 4\times 10^5}{\frac{1}{2}\times 3\times 10^8}$$

$\therefore$ amp $\approx 0.53\%$

Let us now consider the case when the earth is not at a sector boundary crossing. If we let the 'distance' to the sector boundary crossing be four days then the density profile is given by

$$\rho(x) = \rho_0\left[\cos\left(\frac{\pi(x-4)}{13.5}\right) + n\right]$$

Calculating the flux difference as a fraction of the average flux we have

$$\Delta j = \frac{2(w_x+V)s_1 - 2(w_x-V)s_2}{(w_x+V)s_1 + (w_x-V)s_2}$$

where $$s_1 = \left[250 + \frac{13.5}{\pi}\left(\sin\frac{4\pi}{13.5} - \sin\frac{5\pi}{13.5}\right)\right]$$

and $$s_2 = \left[250 + \frac{13.5}{\pi}\left(\sin\frac{3\pi}{13.5} - \sin\frac{4\pi}{13.5}\right)\right]$$

This gives amp $\approx 0.61\%$

In order to compare this with the results given earlier, let us assume a linear relationship. Thus the slope of the line is

$$m = \frac{0.61 - 0.53}{4} \approx 2.0\times 10^{-2}$$

which is of the same order of magnitude as the observed values.

The approximations used here limit this method to prediction of a general trend. It has been assumed that the density gradient only occurs in one dimension. In fact the radial density gradient is well established and azimuthal gradients related to the HCS structure are also possible. These would result in amplitude variations which were not necessarily in phase with the average DV.

This prediction is in agreement with the correlation observed between the scalar average of amplitude and the one dimensional distance to the HCS. The lack of any correlation with the three dimensional distance remains to be resolved. It could be that the observed relationship is dependent only upon the distance from the HCS along the ecliptic plane, since this is the distance measured by the one dimensional method. However there is no apparent physical reason for this

to be so. Alternatively, it is possible that the 3D modelling does not produce as accurate a measure of the distance to the HCS.

Figure 7 illustrates two occasions when the predicted shape of the HCS does not correspond with the field measured at earth. It can be seen that for the period covered by Figure 7(a), the model predicts sector boundary crossings 1 – 2 days earlier than those observed from the measured field data. Although the sector boundary crossings are predicted fairly well in the first part of Figure 7(b), the measured field shows a brief crossing into a toward sector around days 53 and 54 while the model predicts that the HCS does not reach the heliolatitude of the earth.

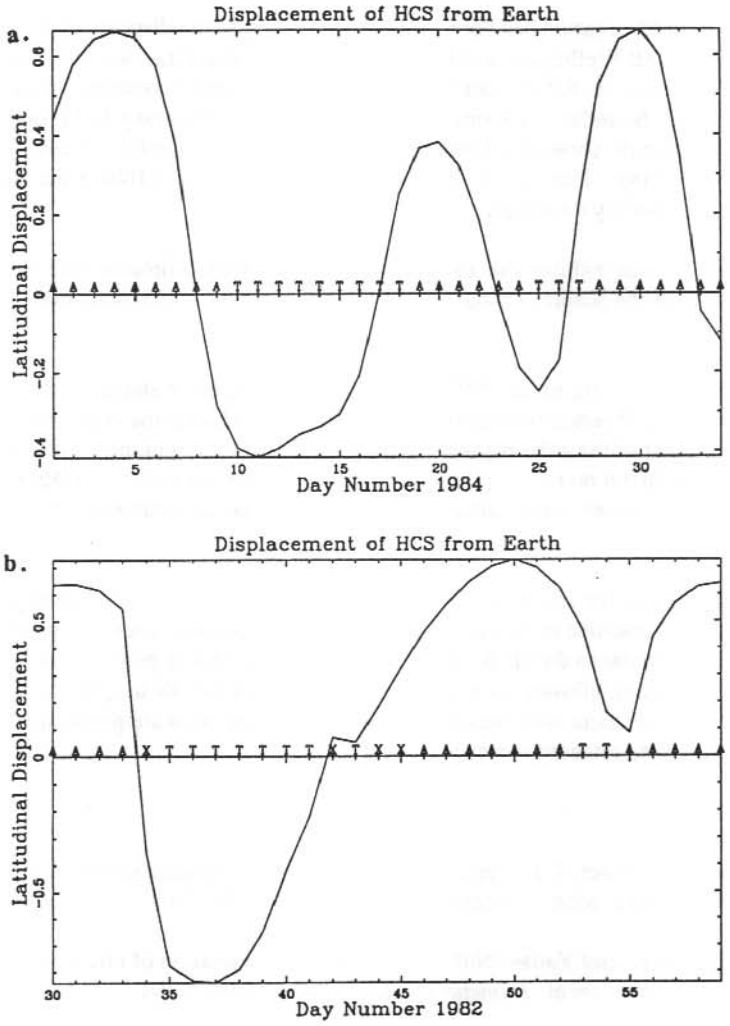

Figure 7. Comparison of the predicted HCS shape with the measured field direction at earth for days (a) 1 – 34 1984 and (b) 30 – 60 1982.

It appears that the model for the HCS predicts its general shape but it is not always an accurate representation, particularly near sector boundary crossings. There are some assumptions in Hoeksema's model which do not hold for all situations. In particular the assumptions of a constant solar wind speed and the absence of electric currents in the solar corona. The second assumption is used because Zeeman observations of the solar surface do not allow measurements of electric currents. It is also possible that the HCS may change in shape during the 5 day transit time from the source surface to earth, although it is unlikely that this would fully account for the discrepancies.

23.5 CONCLUSION

The cosmic ray diurnal variation has been analysed according to the distance of the earth from the HCS using Mawson, Mt Wellington and Darwin neutron monitor data. A one dimensional model used to find approximations for the earth to HCS distance involved counting the number of days to the nearest sector boundary crossing identified from interplanetary field data. The scalar average of the amplitude showed a linear relationship with the number of days to the nearest sector boundary crossing. The slope is found to be between 0.01 and 0.04% per day, increasing away from sector boundary crossings.

Vector averages do not exhibit the same relationship. This indicates that the mechanism producing changes in the scalar average results in an anisotropy which does not have a constant phase.

A functional model (Duldig et al. 1990) was used to predict the shape of the HCS in three dimensions using data obtained from a model by Hoeksema (Hoeksema et al. 1982, 1983) which involved measurement of the solar magnetic field by Zeeman observations. Distance calculations from this model displayed no relationship with either the scalar or vector averages of amplitude. It appears that this 3D model is not sufficiently accurate to provide a suitable measure of the earth to HCS distance.

A possible explanation for the observed correlation between the scalar averages of the DV amplitude and the 1D distance to the HCS has been found by consideration of a gradient in cosmic ray intensity perpendicular to the HCS. Approximation of the flux of particles on the evening and morning sides of the earth allowed an estimate of the effect on the DV amplitude. This was found to be in reasonable agreement with the observed trend. A more accurate prediction would require modelling of the density gradient in three dimensions.

REFERENCES

Ahluwalia, H.S. *and* Dessler, A.J. (1962). Diurnal variation of cosmic radiation intensity produced by a solar wind. *Planetary Space Science 9*:195 – 210.

Badruddin, Yadav, R.S. *and* Yadav, N.R. (1985). Intensity variation of cosmic rays near the heliospheric current sheet. *Planetary Space Science 33*:191 – 201.

Duldig, M.L., Baker, C.P. *and* Humble, J.E. (1990). Intensity waves and the neutral sheet structure. *Proceedings of the 21st International Cosmic Ray Conference, Adelaide 6*:291 – 294.

Duldig, M.L. *and* Humble, J.E. (1990). Enhanced cosmic ray diurnal variations in Mawson and Hobart neutron monitor and underground data records. *Proceedings of the Astronomical Society of Australia 8*:268 – 271.

Hoeksema, J.T., Wilcox, J.M. *and* Scherrer, P.H. (1982). Structure of the heliospheric current sheet in the early portion of sunspot cycle 21. *Journal of Geophysical Research 87*:10331 – 10338.

Hoeksema, J.T., Wilcox, J.M. *and* Scherrer, P.H. (1983). The structure of the heliospheric current sheet: 1978–1982. *Journal of Geophysical Research 88*:9910 – 9918.

Humble, J.E., Duldig, M.L., Fenton, K.B. *and* Fenton, A.G. (1989). Cosmic ray enhanced diurnal variations – neutron monitor and underground observations. In: Conde, M. *and* Beggs, H. (Eds). *ANARE Research Notes Number 69*. Pp. 155 – 168.

Svalgaard, L. *and* Wilcox, J.M., (1976). Structure of the extended solar magnetic field and the sunspot cycle variation in cosmic ray intensity. *Nature 262*:766 – 768.

Swinson, D.B., Saito, T. *and* Mori, S. (1981). Enhanced cosmic ray anisotropies and the extended solar magneic field. *Journal of Geophysical Research 86*:8845 – 8851.

Swinson, D.B. *and* Saito, T. (1986). Recurrence of periods of enhanced cosmic ray solar diurnal variation associated with a two-sector structure. *Journal of Geophysical Research 91*:13675 – 13768.

Wilcox, J.M., Hoeksema, J.T. *and* Scherrer, P.H. (1980). Origin of the warped heliospheric current sheet. *Science 209*:603 – 605.

APPENDIX A

MODELLING THE HCS

The following derivation is based on earlier modelling by Duldig et al. (1990).

First consider an inertial, heliocentric coordinate system (r, θ, ϕ).

At the sun, the HCS is the line joining all points where the radial magnetic field strength is zero. Let this be represented by a function

$$f(\theta,\phi) = 0, \quad r = R_S \tag{1A}$$

Let the angular velocity of the sun be Ω and the solar wind speed be V. The direction of the solar wind flow is radial, hence

$$\mathbf{V} = V\hat{\mathbf{r}}$$

The solar wind carries the magnetic structure radially away from the sun, hence if $\Omega = 0$, the HCS satisfies the equation

$$f(\theta,\phi) = 0$$

for any value of $r > R_S$

Now consider a frame of reference (r', θ', ϕ') rotating with the sun at an angular velocity $\Omega > 0$. In a small interval of time dt, the solar wind will carry the HCS radially out to a distance

$$dr' = Vdt$$

At the same time, the rotating reference frame will have rotated through an angle

$$d\phi' = \Omega dt$$

hence

$$\frac{d\phi'}{dr'} = \frac{\Omega}{V}$$

Integrating from R_S to r' gives

$$\phi' = \frac{(r' - R_S)\Omega}{V}$$

We now generalise equation (1A) to obtain an equation for the HCS for all $r > R_S$, in the rotating frame of reference

$$f\left(\theta, \phi + \frac{(r' - R_S)\Omega}{V}\right) = 0$$

($\theta = \theta'$, $r = r'$ since the sun is only rotating in ϕ)

however we are not interested in the situation close to the sun so $r \gg R_S$ and this becomes

$$f\left(\theta, \phi + \frac{r\Omega}{V}\right) = 0 \qquad (2A)$$

Returning to the inertial heliocentric coordinate system, we now wish to represent the HCS for any $r \gg R_S$, given $\Omega > 0$. An observer in this frame will view the rotation period of the sun as τ_S where

$$\Omega = 2\pi/\tau_S$$

and any point fixed with respect to the sun will be seen to vary as Ωt. Therefore equation (2A) for the HCS now becomes

$$f\left(\theta, \phi + \frac{r\Omega}{V} - \Omega t\right) = 0 \qquad (3A)$$

CALCULATING THE FORM OF f

A two sector HCS follows directly from a simple tilted dipole model of the solar magnetic field, as illustrated in Figure 1a, with tilt angle α.

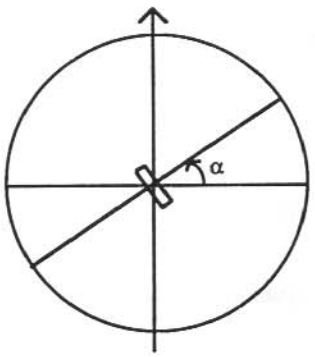

Figure 1a. The sun as a tilted dipole. A 2-sector HCS is simply the plane perpendicular to the dipole as illustrated.

On the surface of the sun, the HCS is the locus of points lying in the plane perpendicular to the dipole direction, where the radial magnetic field goes to zero. If $\alpha = 0$, the HCS coincides with the solar equator.

In a cartesian coordinate system centred on the sun with the z axis coinciding with the rotation axis, the projection of this locus on to the yz plane is shown in Figure 2a.

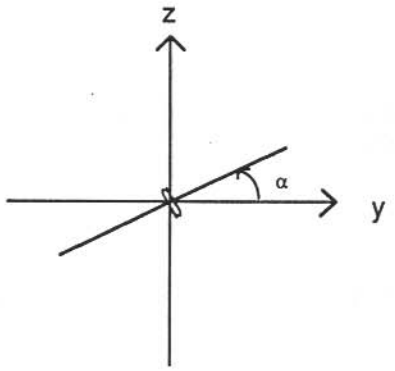

Figure 2a. Projection of the HCS at the sun onto the yz plane of a cartesian system centred on the sun with the z axis along the rotation axis.

The locus of points then satisfies the equation

$$z = (\tan\alpha)y \qquad (4A)$$

Using the usual transformations into polar coordinates (4A) becomes

$$r\cos\theta = (\tan\alpha)\, r\sin\theta\sin\phi$$

$$\cos\theta/\sin\theta = (\tan\alpha)\sin\phi$$

$$\tan\left(\frac{\pi}{2}-\theta\right) = (\tan\alpha)\sin\phi$$

$$\theta = \frac{\pi}{2} - \tan^{-1}((\tan\alpha)\sin\phi)$$

or $$f(\theta, \phi) = \theta - \frac{\pi}{2} + \tan^{-1}((\tan\alpha)\sin\phi) = 0$$

From equation (2A) we know that for $r \gg R_S$ we must replace ϕ by $\phi' + r\Omega/V$ hence

$$\theta' = \frac{\pi}{2} - \tan^{-1}\left((\tan\alpha)\sin\left(\phi' + \frac{r\Omega}{V}\right)\right).$$

Now in the inertial, heliocentric frame we have by (3A)

$$\theta(t) = \frac{\pi}{2} - \tan^{-1}\left((\tan\alpha)\sin\left(\phi + \frac{r\Omega}{V} - \Omega t\right)\right).$$

For small values of α, $\tan\alpha \approx \alpha$.

Now $-\alpha < \left(\frac{\pi}{2} - \theta\right) < \alpha$, so for small α we have

$$\tan\left(\frac{\pi}{2} - \theta\right) \approx \frac{\pi}{2} - \theta .$$

The equation for a two sector HCS simplifies to

$$\theta(t) \approx \frac{\pi}{2} - \alpha\sin\left(\phi + \frac{r\Omega}{V} - \Omega t\right), \qquad \text{for small } \alpha.$$

GENERALISATION TO AN N-SECTOR HCS

First let us consider a 4-sector HCS. In this case, $\lambda = \pi/2 - \theta$ reaches $+\alpha$ twice during each revolution. A 4-sector structure satisfies

$$\theta(t) = \frac{\pi}{2} - \alpha\sin\left(2\phi + \frac{r\Omega}{V} - 2\Omega t\right), \qquad \text{for small } \alpha.$$

Similarly an n-sector HCS satisfies

$$\theta(t) = \frac{\pi}{2} - \alpha\sin\left(\frac{n}{2}\phi + \frac{r\Omega}{V} - \frac{n}{2}\Omega t\right), \qquad \text{for small } \alpha.$$

The approximation that α is small is not a realistic assumption since towards solar maximum the HCS extends nearly to the poles. We therefore need to generalise the equation further. This is done by considering an harmonic expansion.

HARMONIC GENERALISATION

We need to find an equation for an HCS of arbitrary shape. In this case the tilt angle is no longer defined, so we consider the maximum latitudinal extent of the HCS instead. (In a simple 2- or 4-sector HCS the maximum latitudinal extent is the same as the tilt angle.)

The ϕ dependence of the generalised harmonic equation will be the same as that derived above, thus we have

$$\theta_{ns}(t) = \frac{\pi}{2} - \sum_{i=1}^{6}\Big[\, \beta_{2i-1}\sin\left(i[\phi - \Omega t] + \frac{r\Omega}{V}\right) + \beta_{2i}\cos\left(i[\phi - \Omega t] + \frac{r\Omega}{V}\right)\Big] + \beta_{13}t + \beta_{14}$$

The last two terms allow for a linear offset from the equator. This model requires the determination of 14 parameters (β_i) to obtain the best fit to the HCS.

24. HELIOSPHERIC MODULATION MODELS OF HIGH-ENERGY COSMIC RAYS: THEORY vs OBSERVATION AT 1 AU

C.P. Baker[1], J.E. Humble[1] and M.L. Duldig[2]

[1] Physics Department
University of Tasmania
Hobart Tasmania 7001
Australia

[2] Cosmic Ray Section
Antarctic Division
Kingston Tasmania 7050
Australia

ABSTRACT

The intensity of galactic cosmic rays in the solar system can be determined theoretically by solving the standard cosmic ray transport equation. Numerical solutions are presented for cosmic rays in the energy range 10^9 to 10^{10} eV. Comparisons are made between the calculated radial gradient of cosmic rays at earth and that inferred by terrestrial based neutron monitors. This comparison shows a discrepancy between theory and observation by up to a factor of 5. The radial gradient is inferred from observations of the 'north/south anisotropy'. A method of observing this anisotropy at these and slightly higher energies, and inferring the radial gradient using the cosmic ray detectors at Mawson, Antarctica, is given. Possible inadequacies of the model are also discussed.

24.1 INTRODUCTION

Galactic cosmic rays are high energy charged particles. It is known that they originate from regions external to our own solar system, however their precise origin is still unknown. They include electrons and fully ionised atomic nuclei roughly in the same galactic abundances as their neutral counterparts. Hence most (~90%) of the positively charged cosmic rays are protons. Galactic cosmic rays are characterised by their extremely high kinetic energies. The energies of those cosmic rays that reach the earth range from the order of 10^8 eV to 10^{20} eV (eV = electron volt) per particle. From observations of very high energy cosmic rays it appears that they are essentially isotropically distributed in the galaxy (see Berezinskii et al. 1990 for a review of the properties of galactic cosmic rays). As they enter our solar system, their paths are altered and re-distributed by the solar wind (V_{sw}) and the solar magnetic field (B_*). This region, where V_{sw} and B_* have a greater effect than the background galactic field, is termed the 'heliosphere'. The heliosphere is shown schematically in Figure 1. At the boundary of the heliosphere V_{sw} drops to effectively zero and B_* merges with the background galactic magnetic field.

By observing galactic cosmic rays using both spacecraft and terrestrial based particle detectors and modelling their interaction with B_* and V_{sw} we can gain both a better understanding of

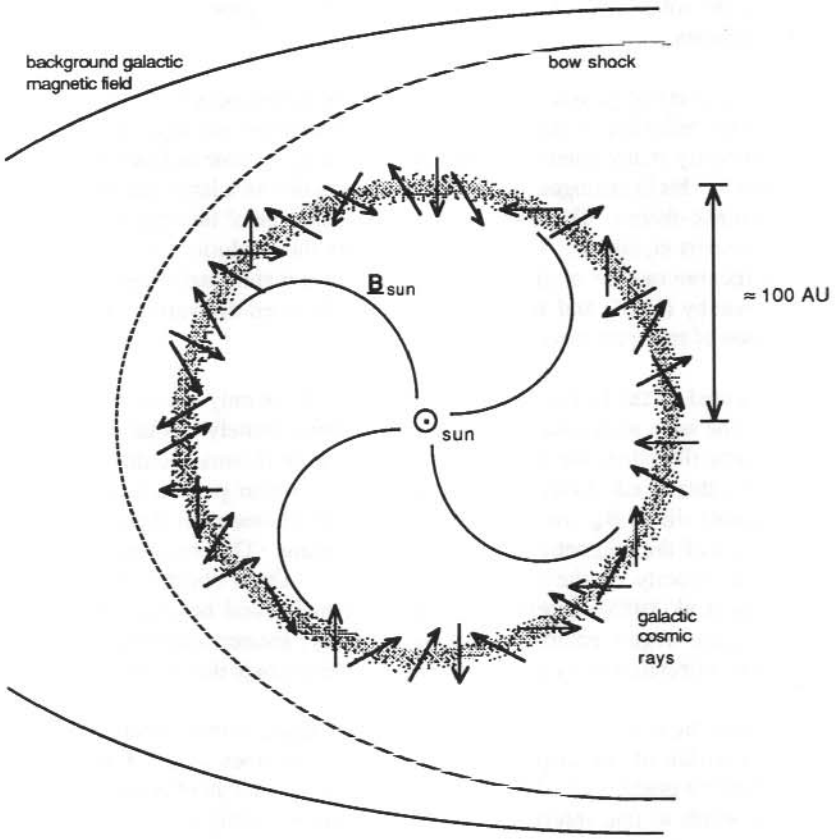

Figure 1. The heliosphere is defined as the region where the sun's magnetic field dominates the background galactic magnetic field. At the boundary of the heliosphere, it appears that the distribution of galactic cosmic rays is essentially isotropic. The boundary is shown here as a 'fuzzy' region roughly 100 AU (astronomical units) from the sun. The actual distance of the boundary from the sun is not well known and most likely varies throughout the solar-cycle.

interplanetary fields and solar processes and an appreciation of the radiation properties of these particles in space.

The path of a single cosmic ray particle as it enters the heliosphere is affected by four main processes. These processes are directly related to V_{sw} and B_* which can be written as ($\langle B_* \rangle + \delta B_*$) where $\langle B_* \rangle$ is the large-scale average magnetic field and δB_* is the average magnitude of the small-scale random fluctuations in B_* caused by solar disturbances. These disturbances include, for example, flares and coronal mass ejections. The cosmic ray particles undergo large-scale gradient and curvature drift due to $\langle B_* \rangle$. They are scattered in pitch-angle due to the small-scale turbulence in B_*. The amount of scattering is characterised by a 'diffusion' timescale which is related to δB_*. The particles undergo energy changes by the process of Fermi-acceleration and

they are convected by the solar wind. The combined effect of these processes describes the total 'modulation' of the particles.

Because of the large numbers of galactic cosmic rays in space it is impossible to attempt to keep track of every possible individual particle as it travels through the heliosphere. Instead, the galactic cosmic ray intensity at any point in the heliosphere at a given time is described in terms of a distribution function f. This is analogous to describing the motion of a large number of particles of a gas in terms of kinetic-theory. The spatial and time dependence of this distribution function is governed by a 'transport equation'. This equation relates the evolution of f to the physical parameters which affect the motion of the galactic cosmic rays mentioned above. See Gleeson and Webb (1980), Quenby (1984) and Jokipii (1971) for a detailed derivation of the transport equation and discussion of transport theory in general.

Modelling f is complicated by the fact that both B_* and V_{sw} are not only spatially dependent but also time dependent. The large scale solar magnetic field is approximately dipolar near the surface of the sun. The magnetic field lines are 'frozen' into the solar wind plasma and drawn out into the heliosphere radially by this wind. Over an (on average) eleven year period, in phase with the sunspot cycle, the dipole tilt of B_* on the source surface increases until there is a complete reversal in the direction of the magnetic field at solar maximum. This periodic change in B_* affects the bulk drift velocity of the cosmic ray particles. On a shorter timescale, solar disturbances (Burlaga et al. 1985) increase the turbulence in B_* and hence cause more local scattering of the particles. Again analogous to kinetic theory, greater scattering of individual particles corresponds to a decrease in the rate of diffusion of the particle distribution.

In the following section the transport equation is described, along with a standard method for solving this equation within the heliosphere. Section 24.3 describes a 'test' for the model – namely a comparison of the predictions of the model for the radial gradient of cosmic ray intensity in the vicinity of the earth to that inferred through observations using ground-based particle detectors. Predictions given in Section 24.4 show a substantial discrepancy between the model and observations. Possible reasons for these differences are discussed in Section 24.5. Finally a method for determining this radial gradient, based on previous work by Yasue (1980) and using data collected by the cosmic ray detectors at Mawson, Antarctica, is given.

24.2 TRANSPORT THEORY

The cosmic ray distribution function $f = f(\mathbf{x},p,t)$ is a five-dimensional scalar function of space $\mathbf{x} = \mathbf{x}(r,\theta,\phi)$, momentum p (magnitude only) and time t. The usual definition of f is such that there exists $p^2 f\, d^3\mathbf{x}\, dp$ particles with momentum in the range p to p+dp in a spatial region $d^3\mathbf{x}$ about $\mathbf{x}$ at time t. With this definition, the differential intensity of particles is

$$j(\mathbf{x},p,t) \;\alpha\; p^2 f(\mathbf{x},p,t)$$

and the integral intensity is

$$I(\mathbf{x},t) \;\alpha\; \int_0^\infty j(\mathbf{x},p,t)\, dp$$

Using arguments of particle continuity and energy conservation in phase-space, it can be shown (Jokipii et al. 1977, Jokipii and Kopriva 1979 and references therein) that f satisfies the partial differential equation:

$$\frac{\partial f}{\partial t} = \nabla \bullet (\mathbf{K} \bullet \nabla f) - (V_D + V_{SW}) \bullet \nabla f + \frac{1}{3}(\nabla \bullet V_{SW}) p \frac{\partial f}{\partial p}$$

This is know as the 'transport equation' and is a parabolic type partial differential equation, being second-order in space coordinates and first-order in time. The terms in the equation are:

K = diffusion tensor. A 3 x 3 matrix whose terms include the diffusion coefficients parallel and perpendicular to the magnetic field. These coefficients are functions of the turbulence δB_* of the field;

V_D = drift velocity. This describes the total effect of the gradient and curvature drifts of the distribution of particles and is a function of the average field $<B_*>$;

V_{SW} = solar wind speed. As a first approximation, the solar wind speed is radial in direction and has a magnitude around 400 km s^{-1}. The adiabatic energy loss of particles is related to the divergence of the solar-wind.

As no analytical solution exists for the general transport equation, numerical techniques are employed to solve for f under pre-specified (and generally idealised) heliospheric conditions. Stable numerical codes used in solving multidimensional partial differential equations are generally very computationally intensive. Solutions given by Kota and Jokipii (1991a, 1991b) are the only examples of three-space dimensional time-dependent solutions for f. Other authors have solved f in one or two space dimensions or time-independent three space dimensions (Kadokura and Nishida 1986, Potgieter and Moraal 1985, Perko and Fisk 1983, Kota and Jokipii 1983). These solutions are generally given for particle energies below about 5 GeV and the value of f in the vicinity of the earth (at 1 AU from the sun) has not been well-specified (Kota 1990). We have solved the time-dependent transport equation in two-space dimensions and time $f = f(r, \theta, p, t)$ in a spherical coordinate system centred on the sun. Here r is the radius dimension and θ the polar-angle or co-latitude. Hence we assume azimuthal symmetry. This approximates the configuration of the heliosphere at solar minimum where B_* near the surface of the sun (at the 'source' surface of the magnetic field) is dipolar and aligned with the rotation axis of the sun.

The transport equation is written as a difference equation and solved for $f = f_t(z, \theta, p, t)$ on a three-dimensional grid (i, j, k) for i = 1...I, j = 1...J, k = 1...M where I, J, M are respectively the number of gridpoints in the radial, polar-angle and momentum coordinate. z is a transformation of the radial coordinate r where:

$$r_i = r_{min} + \varepsilon \tan z_i$$

for constant ε. This transformation gives closer spaced gridpoints in the radial direction for small r, whilst keeping a constant grid increment for the z-variable. The gridpoint (i, j, k) represents the point $(z, \theta, \ln(p))$ where:

$$z = i\,\Delta z + z_{min}$$

$$\theta = j\,\Delta\theta$$

$$\ln(p) = k\,\Delta(\ln(p)) + p_{min}$$

and (Δz, $\Delta\theta$, $\Delta\ln(p)$) are the constant grid-increments. It is assumed that all the cosmic ray particles are protons and therefore particle mass and charge are constant. Initial and boundary conditions are specified for f at time $t = 0$. f is then solved for all points (i, j, k) for $t = \Delta t$. The distribution function is then solved at all points for incrementing timesteps of Δt using the solution at the previous timestep as the initial condition for the current timestep. The iteration continues until the solution becomes sufficiently steady-state. The boundary conditions are:

$$f(i = I, j, k) = \text{assumed galactic spectrum } (\forall\, j,\, k)$$

$$\left.\frac{\partial f}{\partial\theta}\right|_{j=1,J} = 0$$

$$\left.\frac{\partial f}{\partial \ln(p)}\right|_{k=1} = \left.\frac{\partial f}{\partial \ln(p)}\right|_{k=2} \quad \text{and} \quad \left.\frac{\partial f}{\partial \ln(p)}\right|_{k=M} = \left.\frac{\partial f}{\partial \ln(p)}\right|_{k=M-1}$$

We tested a number of different inner boundary conditions for f(i=1, j, k) and these will be discussed in Section 24.4.

Writing the transport equation as a finite difference equation in the specified coordinate system in two space dimensions gives

$$\frac{\delta f}{\delta t} = \left(L_z + L_\theta + L_p\right) f$$

where

$$L_z = A_{zz}\frac{\delta^2}{\delta z^2} + A_z\frac{\delta}{\delta z}$$

$$L_\theta = A_{\theta\theta}\frac{\delta^2}{\delta\theta^2} + A_\theta\frac{\delta}{\delta\theta}$$

$$L_p = A_p\frac{\delta}{\delta \ln(p)}$$

are difference operators, and

$$A_{zz} = A_{zz}(z,\theta,p) = \left(\frac{\cos^2 z}{\varepsilon}\right)^2 K_{rr}$$

$$A_z = A_z(z,\theta,p) = \left(\frac{2K_{rr}}{r} + \frac{\partial K_{rr}}{\partial r} - V_{SW}(r) - (V_D)_r\right)\cdot\left(\frac{\cos^2 z}{\varepsilon}\right)$$

$$+ K_{rr}\cdot\left(\frac{\cos^2 z}{\varepsilon}\right)\cdot\left(\frac{-\sin(2z)}{\varepsilon}\right)$$

$$A_{\theta\theta} = A_{\theta\theta}(z,\theta,p) = \frac{K_{\theta\theta}}{r^2}$$

$$A_\theta = A_\theta(z,\theta,p) = \frac{1}{r^2}\frac{\cos\theta}{\sin\theta}K_{\theta\theta} + \frac{1}{r^2}\frac{\partial K_{\theta\theta}}{\partial\theta} - \frac{1}{r}(V_D)_\theta$$

$$A_p = A_p(z) = \frac{1}{3}\left(\frac{2V_{sw}(r)}{r} + \frac{\partial V_{sw}(r)}{\partial r}\right)$$

are the coefficients of the difference equation.

$$\frac{\delta}{\delta z}, \frac{\delta^2}{\delta z^2} \cdots$$

are difference operators. For example, acting on an interior point $f_{i,j,k}$,

$$\frac{\delta}{\delta z}\left(f_{i,j,k}\right) = \frac{f_{i+1,j,k} - f_{i-1,j,k}}{\Delta z}$$

is a central difference operator. At the boundary, the operators must become one-sided.

The non-zero terms in the diffusion tensor are

$$K_{rr} = K_{\|}\cos^2\psi + K_{\perp}\sin^2\psi$$
$$K_{\theta\theta} = K_{\perp}$$

where

$$\tan\psi = \frac{r\Omega\sin\theta}{V_{sw}}$$

and Ω is the solar rotation rate. $K_{\|}$ and $K_{\perp}$ are the diffusion coefficients parallel and perpendicular to the magnetic field direction. The drift velocity (Isenberg and Jokipii 1979) is given in terms of the mean solar magnetic field $\mathbf{B}_{sun}$ as

$$V_D = \frac{pv}{3q}\,\nabla\times\left(\frac{\mathbf{B}_{sun}}{B^2}\right) \qquad \left(B = |\mathbf{B}_{sun}|\right)$$

where v is the particle speed, q is the charge and $\mathbf{B}_{sun}$ is a standard Parker spiral solar magnetic field (Figure 1) modified at the poles according to Jokipii and Kota (1989).

The difference equation is solved on the three-dimensional grid using two methods, namely the alternating-direction-implicit (ADI) and the Local-One-Dimensional-Implicit (LOD) techniques. Both schemes are fully described in Lapidus and Pinder (1982).

24.3 INNER BOUNDARY SOLUTION AND THE NORTH/SOUTH ANISOTROPY

We are interested in comparing the predictions of the model for the intensity distribution of particles at 1 AU to that observed by ground-based particle detectors, namely neutron monitors and muon detectors. 'North/South (N/S) anisotropy' analysis (Yasue 1980, Bieber and Pomerantz 1986) is one of only a few methods whereby direct comparisons can be made between the model and ground-based observation. From spacecraft measurements (Fillius 1989) and model predictions, we know that there exists a positive radial gradient g_r of cosmic rays near the heliographic equator. That is, there exists a smaller number of cosmic ray particles on the sunward side of the earth. Figures 2a and 2b show the typical gyro-paths of these particles in the 'towards' and 'away' field configuration. Because the solar wind drags out the magnetic field radially, the earth can be in one of two field configurations. Either the radial component of the field is pointing toward the sun or the radial component is pointing away from the sun. The boundary between these two regions forms a discontinuity in the field direction and is termed the 'neutral sheet'. At solar minimum, the neutral sheet simply corresponds to the heliographic equator. Toward solar maximum the situation becomes more complicated and the boundary between the two regimes becomes warped (Hoeksema et al. 1983). At any one time however, the earth is in only one of these two magnetic configurations (or passing from one to the other). The earth passes from one regime to the other and back again every full or half rotation of the sun. As seen in Figure 2, the effect of this radial gradient in space is to produce an observable latitudinal variation at earth. This gradient, or anisotropy, is given by

$$\xi_{NS} = \pm \frac{I_N - I_S}{I_N + I_S}$$

where I_N is the intensity of particles along the north pole and I_S is the intensity along the south pole. The $\pm$ sign depends on whether the earth is in a toward or away sector.

In terms of transport theory, the anisotropy vector is given by

$$\xi = \frac{3S}{4\pi v p^2 f}$$

where S is the vector which describes the streaming of cosmic rays. In heliographic coordinates:

$$\xi_{NS} = \xi_\theta \Big|_{\theta=\frac{\pi}{2},\, r=1AU}$$

i.e. the N/S anisotropy vector is the component of the general anisotropy vector along the polar angle θ at the position of the earth. From expressions of S given in Forman and Gleeson (1975), it can be shown that

$$\xi_\theta = \frac{-3}{v}\left(\frac{pv}{3qB}\, g_r \sin\psi + \frac{K_\perp}{r}\, g_\theta\right)$$

where

$$g_r = \frac{1}{f}\frac{\partial f}{\partial r}$$

is the radial gradient and

$$g_\theta = \frac{1}{f}\frac{\partial f}{\partial \theta}$$

is the latitudinal gradient of cosmic rays. Hence from this theoretical expression it can be seen that the N/S anisotropy can be explained by the existence of a radial gradient (first term) and perpendicular diffusion driven by a latitudinal gradient (second term). This second term is generally neglected on the basis of it being much smaller in magnitude than the first (Bieber and Pomerantz 1986). Hence the N/S anisotropy can be written in terms of the radial gradient as:

$$\xi_{NS} = \xi_\theta\Big|_{\theta=\frac{\pi}{2},\, r=1AU} = -\frac{p}{qB}\, g_r \sin\psi = -r_g \cdot g_r \cdot \sin\psi$$

where r_g is the (energy dependent) gyroradius of the particles. It is clear from this equation that a direct measurement of ξ_{NS} using terrestrial-based particle detectors gives us a measure of g_r as a function of energy. Table 1 summarises measurements of the radial gradient from observational data.

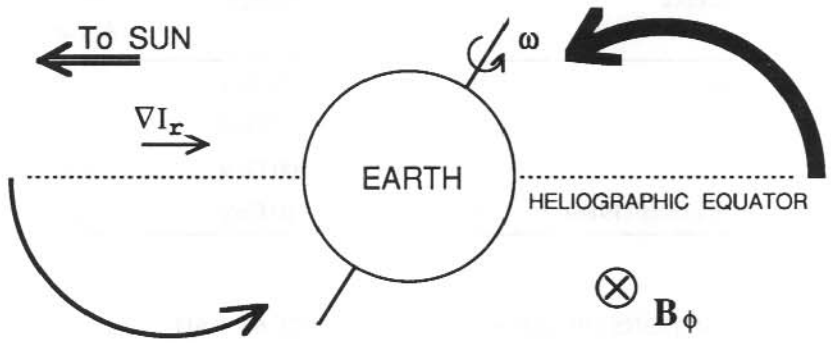

Figure 2a. Typical gyro-paths of particles in a 'TOWARD' field configuration are schematically shown. Note that the gyro-radii of galactic cosmic ray particles are much larger than the scale of the earth. The azimuthal component of the sun's magnetic field is directed into the page. The radial component is toward the sun. The radial gradient of cosmic rays along the heliographic equator causes more particles to be observed in the northern hemisphere due to particle gyration around the azimuthal component of the solar field.

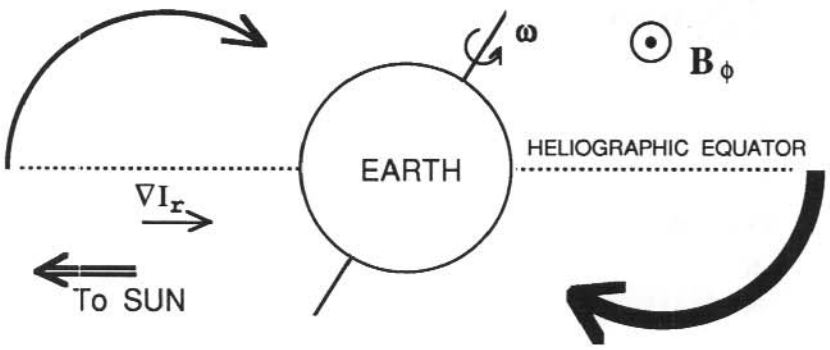

Figure 2b. Typical gyro-paths of particles in an 'AWAY' field configuration are schematically shown. Note that the gyro-radii of galactic cosmic ray particles are much larger than the scale of the earth. The azimuthal component of the sun's magnetic field is directed out of page. The radial component is away from the sun. The radial gradient of cosmic rays along the heliographic equator causes more particles to be observed in the southern hemisphere due to particle gyration around the azimuthal component of the solar field.

*Table 1. Values of the radial gradient g_r at the position of the earth. (*values range from 1 to 3% during a solar cycle).*

Reference	Years	Energy	g_r (% AU^{-1}) At Earth
Yasue (1980)	1969 – 73	5 GeV	5
		10 GeV	3
		100 GeV	0.6
Beiber & Pomerantz (1986)	1961 – 83	~10 GeV	1 to 3*

24.4 MODEL PREDICTIONS OF THE RADIAL GRADIENT AT 1 AU

On the scale of the heliosphere, where the outer boundary is of the order of 100 AU from the sun, the position of the earth (at 1 AU) is very near the inner boundary of the heliographic coordinate system. It turns out that the predicted gradient of cosmic rays at 1 AU depends significantly on the choice we make for the inner boundary condition when solving the transport equation. Table 2 lists the values of the integral radial gradient solution of the model using the specified inner boundary condition.

Table 2. Values of the predicted radial gradient of cosmic rays calculated from the model using the specified boundary conditions. The values are the integral of g_r for particles with energy between 1 and 10 GeV.

Inner-boundary condition	Integrating algorithm used	Integral gradient (% AU^{-1})
Absorbing boundary	LOD	22
Floating boundary	LOD	18
"	ADI	8
Inner boundary='power law'	LOD	14
No net radial streaming (S_r=0)	LOD	17
"	ADI	8

The 'absorbing' inner-boundary condition corresponds to $f(r = r_{min}, \theta, p) = 0 \ \forall \ (\theta, p)$. This condition has been used by other authors (e.g. Kadokura and Nishida 1986, Potgieter 1984) and corresponds to the sun acting as a 'sink' of galactic cosmic rays.

The 'floating' inner-boundary condition corresponds to setting

$$\left.\frac{\partial f}{\partial r}\right|_{r=r_{min}} = \left.\frac{\partial f}{\partial r}\right|_{r=r_{min}+\Delta r}$$

That is, the second derivative of f at the inner-boundary goes to zero. This condition ensures that f changes smoothly with r as $r \rightarrow r_{min}$.

The 'power-law' inner-boundary condition assumes that, as at the outer-boundary, the distribution function at the inner-boundary follows a power law in energy E. This will not be the case for low energy particles (less than say 500 MeV) but is likely to be more accurate as E increases. It can be shown (Appendix A) that if the distribution function at the inner boundary follows a power law:

$$f(r = r_{min}, \theta, E) = f_I \, E^{-\gamma_1}$$

and the function at the outer boundary follows

$$f(r = r_{max}, \theta, E) = f_O \, E^{-\gamma_0}$$

where f_I and f_O are constants, then the two are related via

$$f(r = r_{min}, \theta, E) = f(r = r_{max}, \theta, E) \cdot \left(\frac{E}{E_\infty}\right)^{\gamma_0 - \gamma_1}$$

where E_∞ corresponds to the energy above which no measurable heliospheric modulation occurs. By assuming an isotropic distribution at the outer-boundary and measuring γ_0 (~4.6) from observations of very high energy cosmic rays (Berezinskii et al. 1990), we can determine the distribution at the inner boundary as a function of (γ_1, E_∞). The problem, in practice, is that this pair must be arbitrarily chosen. The value of (γ_1, E_∞) used for the result in Table 2 was (4.5, 200 GeV). Significantly lower values of the integral radial gradient at 1 AU could not be found using other pairs of (γ_1, E_∞).

The 'no-net radial streaming' inner-boundary condition corresponds to the radial component of the streaming vector $\mathbf{S}_r$ going to zero at $r = r_{min}$. This is physically equivalent to there being no net flow of galactic cosmic rays in or out of the sun.

24.5 DISCUSSION OF RESULTS

From Table 2 it is clear that not only is the prediction of g_r at 1 AU dependent on the inner boundary condition we choose for our model, but it also depends on the type of integrating algorithm we use (LOD vs ADI). Figure 3 is a plot of f vs r ($\theta = \pi/2$) for a range of energies between 1 and 10 GeV. The integrating algorithm is LOD and the boundary condition is $S_r = 0$. The radial gradient of f increases significantly below ~5 AU. Figure 4 is the same plot using the ADI algorithm. This run also included a 'termination shock' in the solar wind speed at $r = 60$ AU where V_{SW} becomes sub-sonic and then decreases in speed as r^{-2}. The value of the radial gradient near the inner boundary (less than ~10 AU) is not measurably affected by the presence of this shock. The radial gradient still increases sharply below ~3 AU. This sharp decrease in the number of galactic cosmic rays near the inner boundary is not seen in spacecraft data measuring lower energy particles (Fillius 1989). It seems implausible that high energy particles should be affected more by the heliomagnetic field than low energy particles.

We have investigated possible causes of the discrepancy between the model and observation but as yet can not find a definitive explanation for the problem. The large difference between ADI vs LOD methods strongly suggests that the problem is numerical in nature. Numerical inaccuracy arises primarily through (a) unstable code due to computer round-off error, and (b) inconsistency between the partial differential equation and its numerical representation – namely the finite difference equation. Von Neumann analysis (Lapidus and Pinder 1982) can show whether the finite difference equation is numerically unstable through computer round-off error. Because the coefficients of the second derivatives in our finite difference equation are positive-definite it follows from Von Neumann analysis that the finite difference representation of the transport equation is numerically stable. Inconsistency on the other hand is directly related to the step-size of the three-dimensional grid over which we obtain our solution. We have doubled the number of gridpoints in the radius coordinate for both ADI and LOD methods and there was no significant change in the solution. We can therefore safely rule out inconsistency as the problem. A further cause of numerical inaccuracy, namely artificial viscosity (Roache 1972), is currently being investigated to see what effect it may have on the predictions of the cosmic ray intensity near the inner boundary.

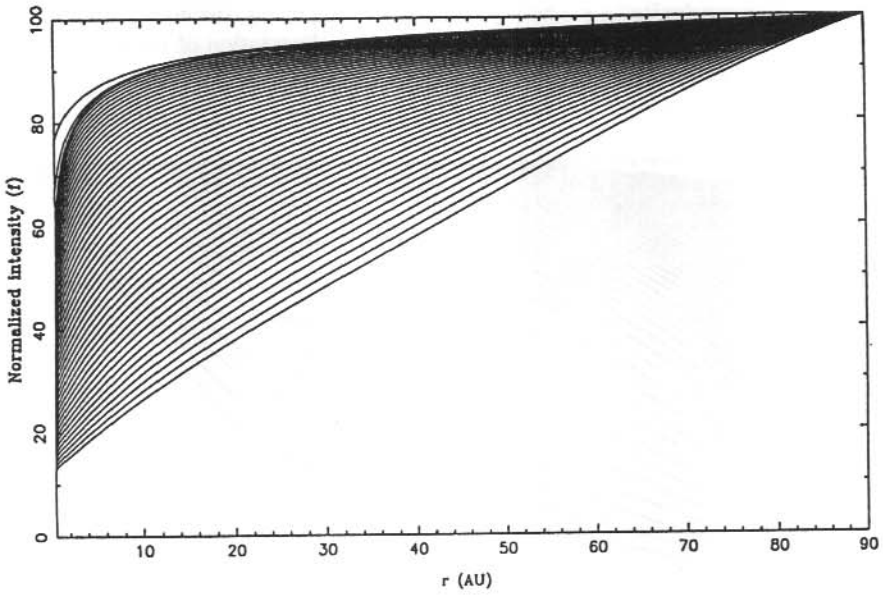

Figure 3. The distribution f plotted as a function of radius along the heliographic equator. The traces are for energies in logarithmic intervals from ~1 GeV (bottom trace) to ~10 GeV (top trace). The integrating algorithm used was LOD and the inner boundary condition was $S_r = 0$.

The distribution of f(**x**, p, t) is, as expected, sensitive to our choice of the functional dependence of the diffusion tensor **K** on **x** and p. An analysis of the variation of the distribution function with changing functional dependence of **K** was undertaken, however no significant improvements to the spatial distribution of g_r was found by using functions of **K** other than the standard form (Potgieter 1984):

$$K_{\parallel} \propto p^{\alpha} \cdot \left(\frac{B_{\oplus}}{B}\right)^{\eta} \cdot \beta \qquad \alpha \in (1,2), \quad \eta \in \left(\tfrac{1}{2},1\right)$$

$$K_{\perp} \approx \mu \cdot K_{\parallel} \qquad \mu \in (0.01,\ 0.1)$$

where $B_{\oplus}$ is the magnitude of the magnetic field at earth and β is the ratio of the particle speed to the speed of light. It is true however that there still does not exist a generally accepted definitive spatial and energy dependence of **K** and the problem of high radial gradients in the models at 1 AU may be partially due to a lack of understanding of this parameter.

There are very few independent determinations of g_r at 1 AU from measurements of the N/S anisotropy. Both results in Table 1 used the neutron monitors at Thule, Greenland and McMurdo, Antarctica for their analyses. Problems of calibration arise when trying to compare absolute intensities between two telescopes at completely separate sites – mainly due to local environmental effects on the cosmic rays. It is for this reason, along with using independent

telescope data, that we devised a method for calculating ξ_{NS} using cosmic ray detectors from the single site at Mawson, Antarctica (see Duldig 1990 for a description of these detectors). This method is discussed in the following section.

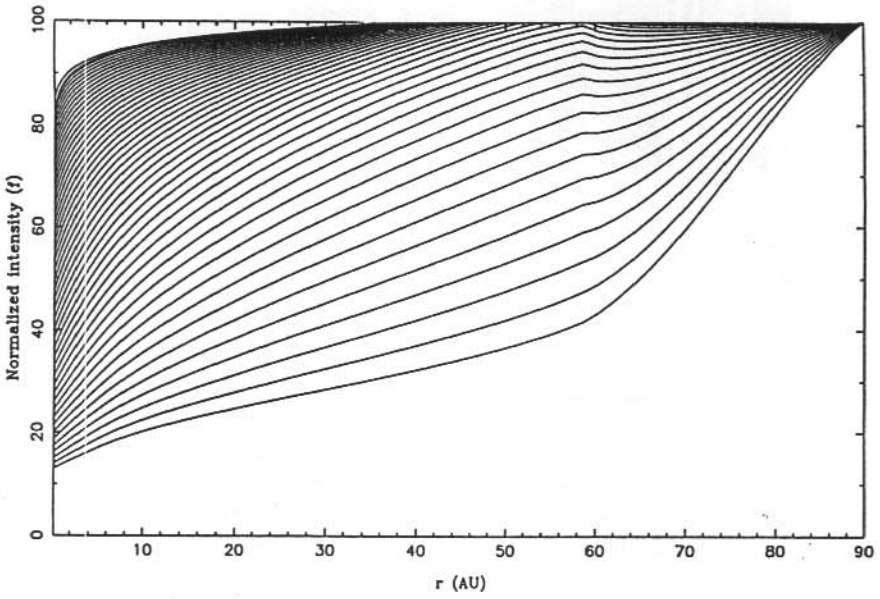

Figure 4. The same plot as in Figure 3 except that (a) the integrating algorithm was ADI and (b) a shock in the solar wind speed was included at 60 AU. Both plots are normalised to the differential intensity at the boundary of the heliosphere which, in these calculations, was chosen to be 90 AU.

24.6 N/S ANISOTROPY MEASUREMENTS

This technique is based on the analysis of Yasue (1980) which we incorporate below. According to the formalism developed by Nagashima (1971) for describing an axis-symmetric anisotropy of cosmic ray intensity I in space, we can write the anisotropy as

$$\frac{\delta I}{I}(\chi,P) = F(\chi)\cdot G(P)$$

where we can expand $F(\chi)$ as a series of Legendre polynomials. Here G(P) is the energy, or 'rigidity', dependence of the anisotropy and χ is the angle from the symmetry axis. P denotes rigidity which is the relativistic momentum per unit charge. In the case of the N/S anisotropy, $F(\chi)$ can be approximated by $\eta\cdot\cos\chi$ where the symmetry axis is perpendicular to the heliographic equator. Consider Figure 5 in which **R** is a vector along the symmetry axis of the anisotropy with magnitude η. As the earth rotates, this N/S anisotropy will give rise to a constant

increase/decrease (depending on the sign of η) in the count rate of a particle-detector due to that component of **R** along the earth's rotation axis (R_Z), together with a sidereal daily variation of intensity due to the components of **R** perpendicular to the rotation axis ($R_x + R_y$). That is,

$$R_x = \eta \sin\theta_R \cos\alpha_R$$
$$R_y = \eta \sin\theta_R \sin\alpha_R$$
$$R_z = \eta \cos\theta_R$$

where

$$\alpha_R = \frac{2\pi}{24} t_{(hours)}$$

The magnitude of the anisotropy is

$$|\xi_{NS}| = \eta \cdot G(P)$$

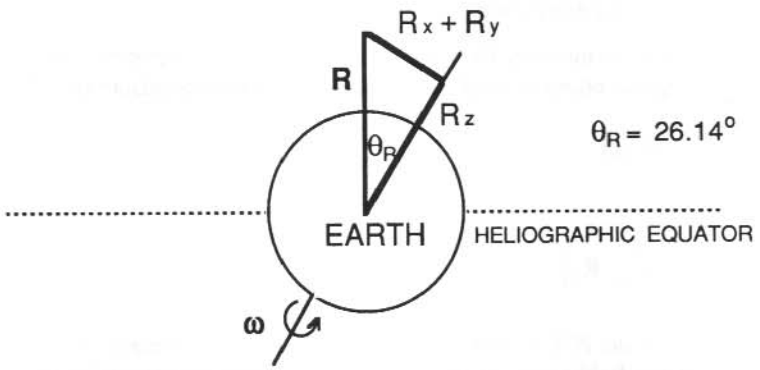

*Figure 5. Components of the vector **R** which is aligned with the symmetry-axis of the N/S anisotropy.*

Terrestrial based particle detectors do not directly observe galactic cosmic ray particles. The paths of these 'primary' particles are bent by the earth's magnetic field. They then interact with nuclei in the atmosphere to produce 'secondary' particles (neutrons, muons...) which are physically detected (Sandstrom 1965). Nagashima (1971) describes the relationship between the observed intensity variation of the secondary particles to the intensity variation of the primary particles in space through so-called 'coupling-coefficients'. These coefficients are unique to each particular particle detector and are a function of the geographic location of the detector, its size, orientation and the amount of absorbing material between it and free-space. Tables of coupling coefficients are given by Fujimoto et al. (1984) and for the Mawson telescopes by Baker (1988). It can be shown that the observed fractional variation **D**, of count-rate in the particle detectors, due to the space variation **R** is related through the coupling coefficients c_1^0, c_1^1, s_1^1 via:

$$\begin{pmatrix} D_x \\ D_y \\ D_z \end{pmatrix} = \begin{pmatrix} c_1^1 & s_1^1 & 0 \\ -s_1^1 & c_1^1 & 0 \\ 0 & 0 & c_1^0 \end{pmatrix} \cdot \begin{pmatrix} R_x \\ R_y \\ R_z \end{pmatrix}$$

The functional dependence of G(P) is chosen to be

$$G(P) = (P)^{\gamma} \qquad (P \leq P_u)$$

for parameters (γ, P_u). The coupling coefficients are tabulated as functions of γ and P_u. Of interest to us is the magnitude of the anisotropy in space $\eta \cdot G(P)$. η is obtained via

$$\eta = \frac{R_z}{\cos\theta_R} = \frac{D_z}{c_1^0 \cos\theta_R}$$

and hence for a chosen set (γ, P_u), a determination of R_z is sufficient to uniquely specify η. This is convenient because we can use daily-averages of intensity recorded by the particle detectors and effectively ignore the $R_x + R_y$ term, which averages to zero over one complete (sidereal) day. What follows is a method for determining R_z.

Let I_m be the average daily intensity for telescope m. Let J_m be the average daily intensity for telescope m neglecting that component of the intensity due to the N/S anisotropy. Then

$$I_m = J_m \left(1 \pm D_{z,m}\right)$$

or

$$I_m = J_m \left(1 \pm c_{1,m}^0 R_z\right)$$

Note from Figure 2 that the N/S anisotropy changes sign – but not magnitude – when moving from a 'toward' magnetic field sector to an 'away' sector. Hence the reason for the $\pm$ sign in the above formulae. Comparing two telescopes m and n, define a normalisation factor between them $A_{m,n}$ such that

$$J_m = A_{m,n} J_n \qquad \left(A_{m,m} = 1,\ A_{n,m} = A_{m,n}^{-1}\right)$$

Averaging data over an equal number of 'towards' and 'away' days, we would find that

$$< I_m > = J_m \qquad (\text{hence } A_{m,n} = < I_m > / < I_n >)$$

In a 'towards' sector

$$I_m = J_m \left(1 + c_{1,m}^0 R_z\right)$$

and in an 'away' sector

$$I_m = J_m \left(1 - c^0_{1,m} R_z\right)$$

and

$$(I_m - A_{m,n} I_n) = \pm J_m (c^0_{1,m} - c^0_{1,n}) \cdot R_z$$

or equivalently

$$\left(\frac{I_m}{J_m} - \frac{I_n}{J_n}\right)$$

$$= \pm\left(c^0_1,m - c^0_1\right) R_z$$

R_z can be calculated from this formula by regressing the intensity data with the coupling coefficients over a number of pairs of detectors (m,n). The energy dependence of the anisotropy can be found simultaneously by varying the coupling coefficients (which are a function of the energy spectrum of the anisotropy) and finding the 'best-fit' regression over the parameters γ and P_u.

Periods when other transient variations are present need to be excluded from the above analysis. Such variations include Forbush decreases (Sandstrom 1965) and enhanced diurnal variations (Duldig and Humble 1990). In addition, times when the earth is near a sector boundary crossing should also be excluded since there will be a mixing of particles coming from both sector regimes at the same time.

Analysis of the data collected by the Mawson muon telescopes for the N/S anisotropy using this technique is being undertaken.

24.7 SUMMARY

This paper has served as a progress report for a project that is part of an on-going collaboration between the cosmic ray sections at the University of Tasmania and the Australian Antarctic Division. It is clear that there is a major discrepancy between the observational measurement of the gradient of galactic cosmic ray particles in the vicinity of the earth and the corresponding gradient predicted by a standard numerical model of cosmic ray transport in the heliosphere. This discrepancy has yet to be resolved. By using data collected by the muon particle detectors at Mawson, it will be possible to obtain an independent measurement of the gradient. If the measurement agrees with other observational data cited in this paper, then it is clear that the most likely cause of the ambiguity between theory and observation is that the standard numerical model for galactic cosmic ray transport is inadequate at energies above a few GeV, in the vicinity of the earth. It would then be likely that either (a) the inner boundary condition is ill-defined, or (b) the numerical integrating procedure is inaccurate. Both these possibilities are under further investigation.

24.8 ACKNOWLEDGMENT

Mr Baker wishes to acknowledge Mr Damian Hall (University of Tasmania) for his contribution to discussions on the development of the N/S anisotropy analysis technique.

REFERENCES

Baker, C.P. (1988). *Coupling Coefficients for Muon Telescopes*. Honours Thesis, University of Tasmania, Australia.

Bieber, J.W. *and* Pomerantz, M.A. (1986). Solar cycle variation of cosmic ray north-south anisotropy and radial gradient. *Astrophysical Journal 303*:843–848.

Berezinskii, V.S., Bulanov, S.V., Dogiel, V.A., Ginzburg, V.L. *and* Ptuskin, V.S. (1990). *Astrophysics of Cosmic Rays*. North-Holland Publishing Co., Amsterdam.

Burlaga, L.F., McDonald, F.B., Goldstein, M.L. *and* Lazarus, A.J. (1985). Cosmic ray modulation and turbulent interaction regions near 11 AU. *Journal of Geophysical Research 90*:12027–12039.

Duldig, M.L. (1990). The Mawson automatic cosmic ray observatory (MACRO). *Proceedings of the 21st International Cosmic Ray Conference, Adelaide 7*:288–291.

Duldig, M.L. *and* Humble, J.E. (1990). Enhanced cosmic ray diurnal variations in Mawson and Hobart neutron monitor and underground data records. *Proceedings of the Astronomical Society of Australia 8*:268–273.

Fillius, W. (1989). Cosmic ray gradients in the heliosphere. *Advances in Space Research 9*:209–219.

Forman, M.A. *and* Gleeson, L.J. (1975). Cosmic ray streaming and anisotropies. *Astrophysics and Space Science 32*:77–94.

Fujimoto, K., Inoue, A., Murakami, K. *and* Nagashima, K. (1984). *Report 9, Cosmic Ray Research Laboratory*. Nagoya University, Nagoya, Japan.

Gleeson, L.J. *and* Webb, G.M. (1980). The propagation of cosmic rays in the interplanetary region (the theory). *Fundamentals of Cosmic Physics 6*:187–312.

Hoeksema, J.T., Wilcox, J.M. *and* Scherrer, P.H. (1983). The structure of the heliospheric current sheet: 1978–1982. *Journal of Geophysical Research 88*:9910–9918.

Isenberg, P.A. *and* Jokipii, J.R. (1979). Gradient and curvature drifts in magnetic fields with arbitrary spatial variation. *Astrophysical Journal 234*:746–752.

Jokipii, J.R. (1971). Propagation of cosmic rays in the solar wind. *Reviews of Geophysics and Space Physics 9*:27–87.

Jokipii, J.R., Levy, E.H. *and* Hubbard, W.B. (1977). Effects of particle drift on cosmic ray transport. I. General properties, application to solar modulation. *Astrophysical Journal 213*:861 – 868.

Jokipii, J.R. *and* Kopriva, D.A. (1979). Effects of particle drift on cosmic rays III. Numerical models of galactic cosmic ray modulation. *Astrophysical Journal 234*:384 – 392.

Jokipii, J.R. *and* Kota, J. (1989). The polar heliospheric magnetic field. *Geophysical Research Letters 16*:1 – 4.

Kadokura, A. *and* Nishida, A. (1986). Numerical modeling of the 22-year variation of the cosmic ray intensity and anisotropy. *Journal of Geophysical Research 91*:1 – 11.

Kota, J. (1990). Diffusion, drifts and modulation of galactic cosmic rays in the heliosphere. In: Grzedzielski,S. *and* Page, D.E. (Eds). *Physics of the Outer Heliosphere*. Pergamon Press. Pp. 119 – 131.

Kota, J. *and* Jokipii, J.R. (1983). Effects of drift on the transport of cosmic rays VI. A three-dimensional model including diffusion. *Astrophysical Journal 265*:573 – 581.

Kota, J. *and* Jokipii, J.R. (1991a). Solar wind streams and galactic cosmic rays: Results from a three-dimensional simulation. *Proceedings of the 22nd International Cosmic Ray Conference, Dublin 3*:533 – 536.

Kota, J. *and* Jokipii, J.R. (1991b). The role of co-rotating interaction regions in cosmic ray modulation. *Geophysical Research Letters 18*:1797 – 1800.

Lapidus, L. *and* Pinder, G.F. (1982). *Numerical Solutions of Partial Differential Equations in Science and Engineering*. John Wiley & Sons.

Nagashima, K. (1971). Three-dimensional cosmic ray anisotropy in interplanetary space. Part 1 – Formulation of cosmic ray daily variation produced by axis-symmetric anisotropy. *Report of Ionospheric and Space Research in Japan 25*:189 – 211.

Perko, J.S. *and* Fisk, L.A. (1983). Solar modulation of galactic cosmic rays 5. Time-dependent modulation. *Journal of Geophysical Research 88*:9033–9036.

Potgieter, M.S. (1984). *The Modulation of Galactic Cosmic Rays as Described by a Three-dimensional Drift Model*. Ph.D. Thesis. Potchefstroom University, South Africa.

Potgieter, M.S. *and* Moraal, H. (1985). A drift model for the modulation of galactic cosmic rays. *Astrophysical Journal 294*:425 – 440.

Quenby, J.J. (1984). The theory of cosmic ray modulation. *Space Science Reviews 37*:201 – 267.

Roache, P.J. (1972). On artificial viscosity. *Journal of Computational Physics* *10*:169 – 184.

Sandstrom, A.E. (1965). *Cosmic Ray Physics*. North Holland Publishing Co., Amsterdam.

Yasue, S. (1980). North-south anisotropy and radial density gradient of galactic cosmic rays. *Journal of Geomagnetism and Geoelectricity 32*:617 – 635.

APPENDIX A

POWER LAW RELATIONSHIP for INNER-BOUNDARY CONDITION.

Assume the distribution function at the inner and outer boundary is a function only of energy E and follows a power-law in E:

$$f(r = r_{min}, \theta, E) = f_I E^{-\gamma_1} \quad \text{at the inner - boundary } (\forall\theta)$$

and $$(r = r_{max}, \theta, E) = f_O E^{-\gamma_0} \quad \text{at the outer - boundary } (\forall\theta)$$

where f_I and f_o are constants. Let

$$X(E) = \frac{f(r = r_{min}, \theta, E)}{f(r = r_{max}, \theta, E)} \leq 1.0 \ \forall E$$

be the ratio between the distribution at the inner boundary to that at the outer boundary at the same energy. As $E \rightarrow E_\infty$, $X(E) \rightarrow 1.0$. That is, we define E_∞ to be that energy above which no measurable modulation occurs in the heliomagnetic field and the distribution functions at the inner and outer boundary are identical. Then

$$f(r = r_{min}, \theta, E) = X(E) \cdot f(r = r_{max}, \theta, E)$$

where

$$X(E) = \frac{f_I}{f_O} E^{\gamma_0 - \gamma_1}$$

but

$$X(E_\infty) = \frac{f_I}{f_O} E_\infty^{\gamma_0 - \gamma_1} = 1.0$$

therefore

$$X(E) = E_\infty^{\gamma_1 - \gamma_0} \cdot E^{\gamma_0 - \gamma_1}$$

and

$$f(r = r_{min}, \theta, E) = f(r = r_{max}, \theta, E) \cdot \left(\frac{E}{E_\infty}\right)^{\gamma_0 - \gamma_1}$$

25. A COMPARATIVE STUDY OF SOLAR MODULATION PROCESSES AS RECORDED BY SOUTHERN LATITUDE COSMIC RAY TELESCOPES

D.L. Hall[1], M.L. Duldig[2] and J.E. Humble[1]

[1] Physics Department
University of Tasmania
Hobart Tasmania 7001
Australia

[2] Cosmic Ray Section
Antarctic Division
Kingston Tasmania 7050
Australia

ABSTRACT

In an effort to obtain a greater understanding of the magnetic structure of the heliosphere and the associated mechanisms responsible for the modulation of high energy cosmic ray particles, the solar anisotropies measured at a number of southern observatories will be studied. Specifically, long-term variations over solar magnetic cycles in the anisotropies measured by underground and surface muon telescopes and neutron monitors will be studied and results from different latitude stations and energy ranges compared. Also, long-term variations in the absolute intensity of cosmic rays will be studied as another related modulation. An introduction to this research project is presented.

25.1 INTRODUCTION

Primary cosmic rays are almost isotropically distributed in space. Secondary cosmic ray particles produced by nuclear interactions at the top of the earth's atmosphere between incoming primary particles and atmospheric nuclei can be divided into three components. These are the electromagnetic (soft) component, meson (hard) component and the nucleonic component (Figure 1).

All the secondary particles are the result of a nuclear disintegration; the most common nucleon being the neutron and the most common meson being the pion. The neutral pion decays into 2 photons producing an electron-photon cascade, while the positive and negative pions decay into muons of the same charge. The muons (being relativistic) are able to survive a length-contracted journey to sea level if their energy is greater than about 2 GeV, and thus be recorded.

Variations in atmospheric parameters such as sea level pressure, temperature of the pion production level and height of the muon production level can vary the number of particles detected at sea level for a constant primary flux.

After atmospheric and geomagnetic effects are accounted for, a small solar diurnal variation in the intensity still remains. The time of maximum of this approximately sinusoidal variation is at about

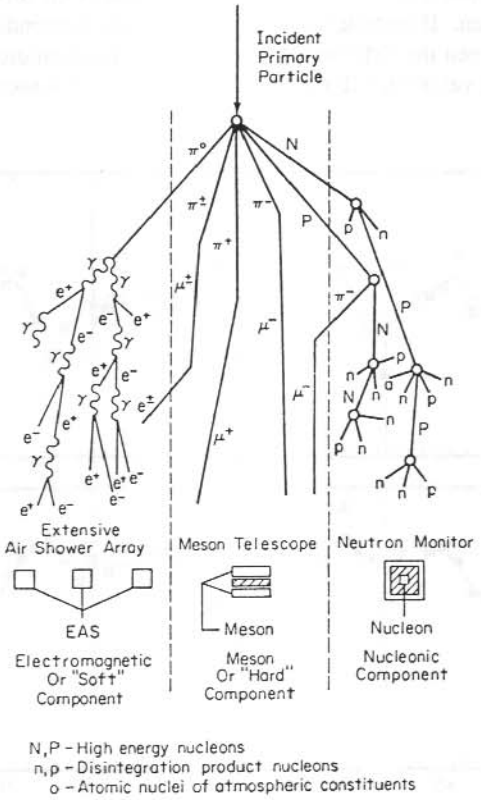

Figure 1. Components of the secondary radiation (Pomerantz 1971).

1800 hours local time and the amplitude (depending on the energy of the particles and location ofthe telescope) can be between 0.1 and 0.5 percent of the daily mean intensity recorded by a telescope. Both the amplitude and phase show cyclic behaviour (Figure 2) with periods about 11 years (sunspot cycle) and about 22 years (solar magnetic cycle) respectively (Bieber and Chen 1991a).

The solar diurnal anisotropy is due to a balance in the outward convection of particles in the solar wind and the inward and perpendicular diffusion of particles and perpendicular gradient and curvature drifts of particles in the heliosphere due to the interplanetary magnetic field (IMF) (Forman and Gleeson 1975). The result is a distribution that corotates with the IMF and leads to the anisotropy as seen by a stationary observer on earth. Drifts depend on the direction of the IMF. Therefore, on a scale larger than the particle gyroradius (Isenberg and Jokipii 1979) these drifts can be represented by a product between the number density gradients and a unit vector in the direction of the magnetic field. Due to a neutral heliospheric current sheet in the vicinity of the

solar equator produced by the IMF and the solar wind, the earth spends some of its time in regions where the IMF is directed towards the sun and the rest of the time in regions with the IMF directed away from the sun. If particle density gradients exist perpendicular to the solar equator then cross products between the IMF and the gradients will contribute to the overall azimuthal streaming and the diurnal variation will change (Swinson 1969, Swinson et al. 1991).

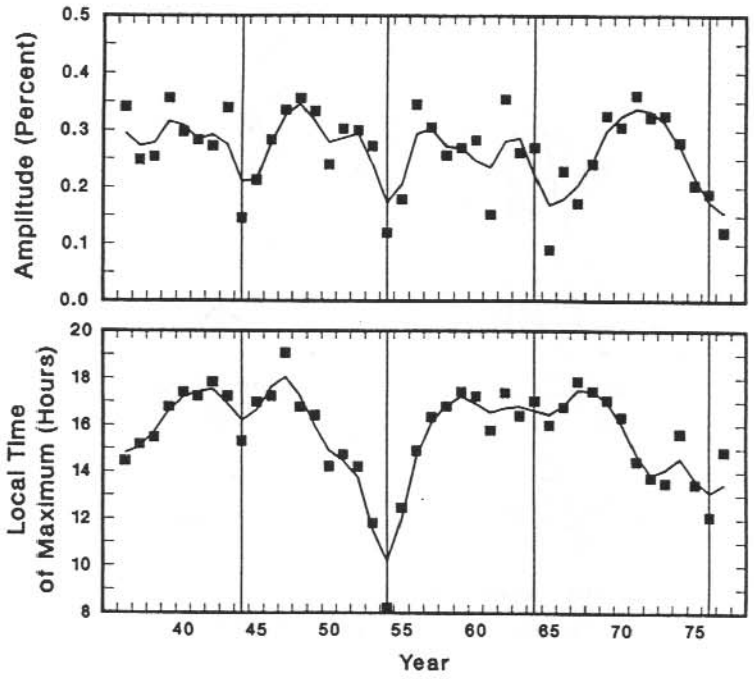

Figure 2. Cyclic behaviour of the solar diurnal variation (Bieber and Chen 1991a).

Another observation of cosmic ray intensity that is related to solar modulation is the variation in the intensity of particles over long time periods. The intensity is seen to be anti-correlated with sunspot number. The sunspot number is related to magnetic activity so we can say that the intensity is related to the solar magnetic cycle (Figure 3).

Obviously an understanding of the diurnal variation and other solar modulations will lead to further information about the IMF and propagation and gradients of particles in the heliosphere.

This paper is essentially an introduction to a new research project, although some preliminary results are presented. In the following sections we introduce the reader to the concepts that lead to solar modulation of the galactic cosmic ray distribution and then review some of the more recent observations of these modulations. We then discuss what data we shall use in our new study and briefly present some preliminary results from the data. It is hoped that this will give the reader an

insight into how we intend to obtain new information about the heliosphere and galactic cosmic ray particles.

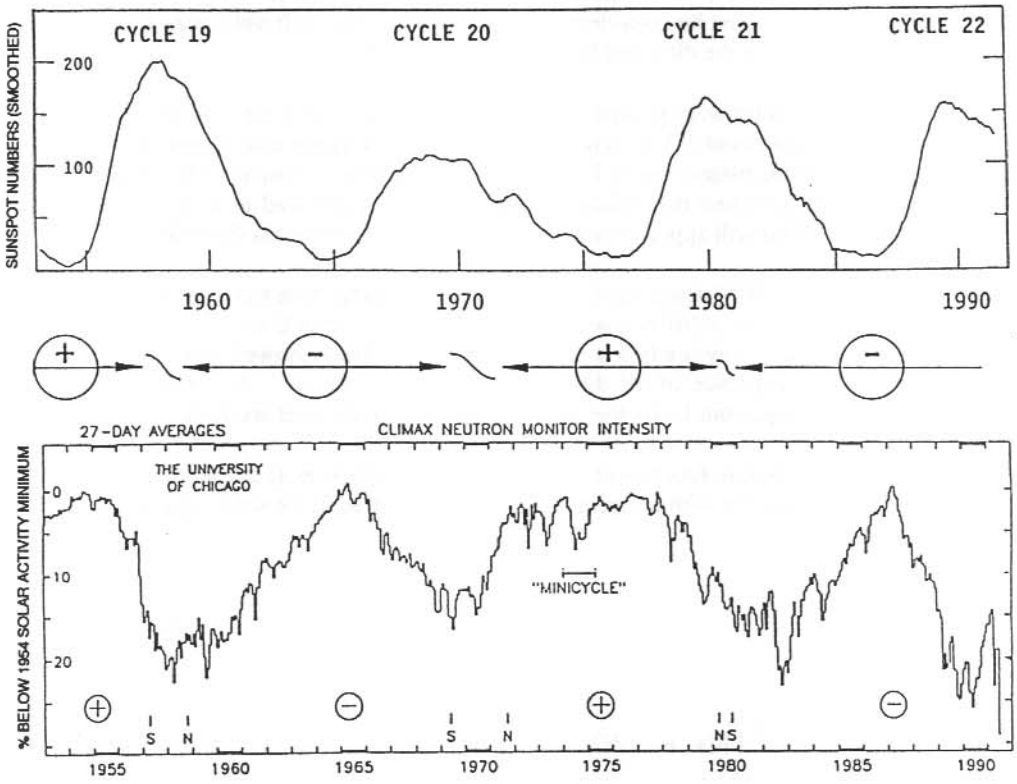

Figure 3. Long term variation of cosmic ray intensity. The top panel shows the sunspot number for the last 4 solar cycles and this can be seen to be anti-correlated with the cosmic ray intensity (bottom panel) as recorded by the Climax neutron monitor. The shape of the intensity profiles can be seen to be correlated with the magnetic polarity of the sun as indicated by the middle pane.

25.2 THEORY OF COSMIC RAY SOLAR MODULATION

Primary cosmic ray particles are high energy nuclei and exist in roughly the same relative abundances as their corresponding galactic atomic elements. Thus most of the primary particles are protons.

The heliosphere is the region of space where the interplanetary magnetic field of the sun dominates the galactic magnetic field. Outside the heliosphere, in the local inter-stellar region the distribution of galactic particles is considered almost isotropic in space and time. Due to random motion and collisions these particles cross the boundary and enter the heliosphere. They will

gyrate around the IMF but due to small scale irregularities in the IMF the particles are scattered from their gyro-orbits. The overall motion of the particles will be seen as diffusion from the boundary towards the sun. Along their diffusive journey the particles will also undergo gradient and curvature drifts in the IMF according to first order orbit theory. The bulk motion of the collection of particles must be considered when looking at the drift velocities because of the irregularities which cause the diffusion (Isenberg and Jokipii 1979).

The sun also emits a solar wind plasma radially from its surface with the IMF 'frozen' into it. If the velocity of the solar wind is **V** with respect to a heliocentric coordinate system then an electric field **E** is induced in the plasma where $\mathbf{E} = -\mathbf{V} \times \mathbf{B}$. The radially flowing plasma will collide with the cosmic ray particles and the induced electric field will also lead to an $\mathbf{E} \times \mathbf{B}$ drift in the particles' velocity. This will appear as a convection of particles outwards from the sun.

Forman and Gleeson (1975) determined the equations describing these motions of the particles in the heliosphere in terms of a differential number density of particles U and a streaming vector S. The streaming vector is physically a directional intensity. They showed that the solar diurnal anisotropy is a consequence of all the above transport processes. A quick summary and explanation of these equations is in order to assist the reader in the later sections.

If $F(\mathbf{x}, \mathbf{p}, t)$ is a distribution function of particles such that $p^2F(\mathbf{x}, \mathbf{p}, t)\, d^3x\, dp\, d\Omega$ is the number of particles in a volume d^3x with momentum **p** to **p** + d**p** centred in the solid angle $d\Omega$ then it can be shown that

$$\frac{\partial U}{\partial t} + \nabla \cdot \mathbf{S} = 0 \qquad (1)$$

where

$$U(\mathbf{x}, p, t) = p^2 \int_{4\pi} F(\mathbf{x}, \mathbf{p}, t)\, d\Omega$$

and S is the streaming vector:

$$\mathbf{S}(\mathbf{x}, p, t) = CU\mathbf{V} - \kappa\left(\frac{\partial U}{\partial r}\right)_{\parallel} - \frac{\kappa}{1+(\omega\tau)^2}\left(\frac{\partial U}{\partial r}\right)_{\perp} - \frac{\omega\tau\kappa}{1+(\omega\tau)^2}\left[\frac{\partial U}{\partial r} \times \hat{\mathbf{B}}\right] \qquad (2)$$

and

- ω = Gyrofrequency of the particles orbit
- τ = collision period of the particles
- κ = (isotropic) diffusion coefficient
- C = Comptron-Getting factor
- U = number density

The first term of equation (2) describes the outward convection of the particles by the solar wind with velocity **V** and **E** x **B** drift velocity, the second term describes parallel diffusion, the third describes perpendicular diffusion and the fourth involves the gradient and curvature drifts. Parallel and perpendicular directions are related to the direction of the IMF (Figure 4).

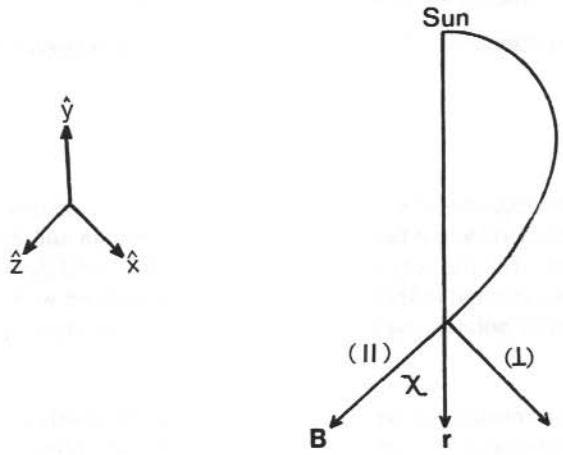

*Figure 4. Parallel (//) and perpendicular (⊥) directions related to the interplanetary magnetic field (**B**). χ is the angle between the **B** and the radial direction (**r**) from the sun.*

Writing equation (2) in terms of a diffusion tensor

$$S = CUV - \underline{\underline{\kappa}}\cdot(\nabla U), \quad \underline{\underline{\kappa}} = \begin{pmatrix} \kappa_\perp & \kappa_T & 0 \\ -\kappa_T & \kappa_\perp & 0 \\ 0 & 0 & \kappa_\parallel \end{pmatrix} \tag{3}$$

where $\kappa_\perp$, $\kappa_\parallel$, are respectively the perpendicular and parallel diffusion coefficients and the off-diagonal elements are related to gradient and curvature drifts, then

$$\frac{\partial U}{\partial t} = -\nabla\cdot\left(CUV - \underline{\underline{\kappa}}\cdot\nabla U\right) \tag{4}$$

Equation (4) is a standard time dependent diffusion equation. If we note that

$$\left(\frac{\partial U}{\partial t}\right)^D = +\nabla\cdot(\kappa\cdot\nabla U)$$
$$= +\nabla\cdot\left(\underline{\underline{\kappa}}^S\cdot\nabla U\right) + \left(\nabla\cdot\underline{\underline{\kappa}}^A\right)(\nabla U)$$
$$= +\nabla\cdot\left(\underline{\underline{\kappa}}^S\cdot\nabla U\right) + V_D\cdot\nabla U$$

where $\underline{\underline{\kappa}}^S$ and $\underline{\underline{\kappa}}^A$ refer to $\underline{\underline{\kappa}}$ being split into symmetric and antisymmetric tensors) then equation (4) is a transport equation explicitly representing the convection, diffusion and drifts mentioned earlier. The combined effect of these processes is known as modulation of the galactic particles and the distribution of particles is now slightly anisotropic. Vector addition of the components in

equation (3) shows that the streaming of particles can be azimuthal and since the drifts are related to the IMF then this azimuthal streaming will corotate with the sun.

Since the streaming is representative of anisotropy, we define the anisotropy vector in terms of the streaming vector:

$$\xi = \frac{3S}{VU}$$

This anisotropy, and consequently the temporal dependence of the distribution function, will obviously depend on many different factors including IMF strength and direction, solar wind speed and particle energy. The intensity at earth of these particles could then be expected to vary with the parameters of the sun and indeed does vary in a way correlated with the 11 and 22 years solar sunspot and magnetic polarity cycles. (For a review of these observations see Flückiger 1991).

Due to the earth's 24 hour rotation period a detector on earth is effectively mounted on a circular pedestal which rotates through 360° of space in a day while recording the flux of particles streaming into its view. An azimuthal anisotropy in space would therefore be seen as a variation of intensity in time, with a maximum at the local time corresponding to the detector looking as directly as possible into the streaming vector. This is called the solar diurnal variation. The solar diurnal variation shows the solar modulation of primary particles and the amplitude and phase of this variation (when put into a vector form) can be related to the magnitude and direction of the streaming vector. This vector can be further related to the drifts and gradients of the particles in the heliosphere via equations (1) to (4). Long term observations of these processes will then offer accurate and important constraints on the theories of particle transport.

The day to day diurnal variation will scatter due to counting statistics (Humble 1971) and other transient modulation phenomena, so daily vectors averaged over months or years must be used in order to obtain significant information. Yearly averaged vectors (i.e. vectors obtained using an entire year's data) are convenient as they will not contain contributions from sidereal or other variable components in solar time which average to zero on this timescale. These vectors represent the streaming of particles (on average) over the year. Therefore vectors from year to year can be compared. Information about number density gradients and parameters such as mean free paths (Swinson et al. 1986, 1991; Bieber and Chen 1991a; Chen et al. 1991) can be obtained and thus incorporated into the theories. Theories which do include the particle drifts (e.g. Jokipii 1984) predict transport in the heliosphere that is dependent on the polarity of the solar field. Specifically, when the IMF is directed away from the sun in the northern hemisphere (this state of magnetic polarity is denoted qA >0), one prediction is that the net flow of particles into the heliosphere is via the poles producing a minimum in particle density at the helioequator (producing a bidirectional latitudinal number density gradient). When the polarity of the solar field is reversed (qA <0) the particle transport is predicted to be predominantly along the thin neutral current sheet separating the opposite magnetic polarity hemispheres. Hence an oppositely directed bidirectional latitude gradient and a larger radial gradient are predicted than for qA >0. Although long term studies reveal that the amplitude and phase of the solar diurnal variation do indeed vary with a period of 11 and 22 years respectively (Pomerantz and Duggal 1971, Bieber and Chen 1991a) the success of drift theories is still questioned (Bieber and Pomerantz 1986).

Obviously more observations and analysis of the solar diurnal variation and thus particle gradients and other associated transport parameters can only be advantageous to the pursuit of knowledge about the heliosphere.

25.3 TERRESTRIAL EFFECTS

25.3.1 *Geomagnetic field effects*

Once a primary particle enters the earth's magnetosphere its direction of motion will be altered as it gyrates around the earth's magnetic field lines. Secondary particles travel such short distances that they are not noticeably affected by the geomagnetic field, but particles detected at one location on earth with a certain arrival direction are invariably due to primaries that entered the magnetosphere from another direction. This original direction of travel is termed the particle's 'asymptotic direction of approach'.

Also, particles need greater energy (or magnetic rigidity) to reach equatorial regions since they must cross magnetic field lines to gain access. At any given latitude, part of the spectrum of particles is consequently cut-off from detection below a 'cut-off' rigidity. There is also a smaller cut-off rigidity effect due to the longitude of particle detection because the geomagnetic field is offset from and inclined relative to the rotation axis.

In effect, this means that the field of view of a cosmic ray telescope is not the same as its geometrical pointing direction. Therefore we define the asymptotic cone of acceptance of a telescope as the solid angle containing the asymptotic directions of approach of all particles capable of reaching the telescope (Humble 1971). The asymptotic cone of acceptance is a function of particle energy, geographic longitude and latitude, detector response to secondaries and the varying geomagnetic field. Due to detectors (of different types or having different axial directions) having different asymptotic cones of acceptance (even if they are at the same location) an anisotropy measured by two telescopes may be registered with different times of maximum and with different amplitudes (Rao et al. 1963). Coupling coefficients are used to relate the variation seen at earth by different telescopes to the actual anisotropy in free space (Yasue et al. 1982, Fujimoto et al. 1984, Baker 1988).

If we measure the solar diurnal variation with a particular telescope to have an amplitude A^G and a phase ϕ^G then the corresponding variation in the absence of the geomagnetic field would have amplitude A^F and phase ϕ^F where

$$A^F = \frac{A^G}{\delta A}, \quad \phi^F = \phi^G + \delta\phi$$

We call these A^F and ϕ^F the free space variation parameters and δA and $\delta\phi$ are derived from the coupling coefficients for the diurnal anisotropy for that particular telescope.

25.3.2 *Atmospheric effects*

In the introduction we noted that the secondary particles detected by ground based instruments can be divided into 3 components. This paper will only be concerned with the nucleon and meson components corresponding to primary rigidities (momentum per unit charge) of between 1 and

500 GV (energies about 1.5 to 500 Gev). The most common detected secondaries are neutrons and muons.

If the air pressure increases then more secondaries will interact with the atmosphere due to the increased depth of absorbing matter and will not survive to be detected. This is the pressure effect. If the height of the muon production layer (approximately the height corresponding to 100 – 150 millibars of air pressure) increases due to thermal expansion of the atmosphere then the muons have a larger distance to travel to ground level and more muons will decay to electrons and positrons and subsequently not be detected. This is called the negative temperature effect. If the temperature of the mean pion production level (approximately the 120 mb level of air pressure) increases then the density of the atmosphere decreases and the probability for negatively charged pions to be captured by atmospheric nuclei decreases. This is called the positive temperature effect as the number of detected muons will rise (due to the larger number of pions that survive to decay to muons) as the temperature increases.

Correction for these 3 effects need to be made when considering cosmic ray data from surface muon telescopes. All cosmic ray observations include effects of pressure fluctuations. Naturally, neutron monitor records are not affected by the two temperature effects. If one has enough atmospheric data then corrections for the atmospheric effects can be obtained using ordinary regression analysis (Fenton et al. 1961).

25.4 DATA ACQUISITION

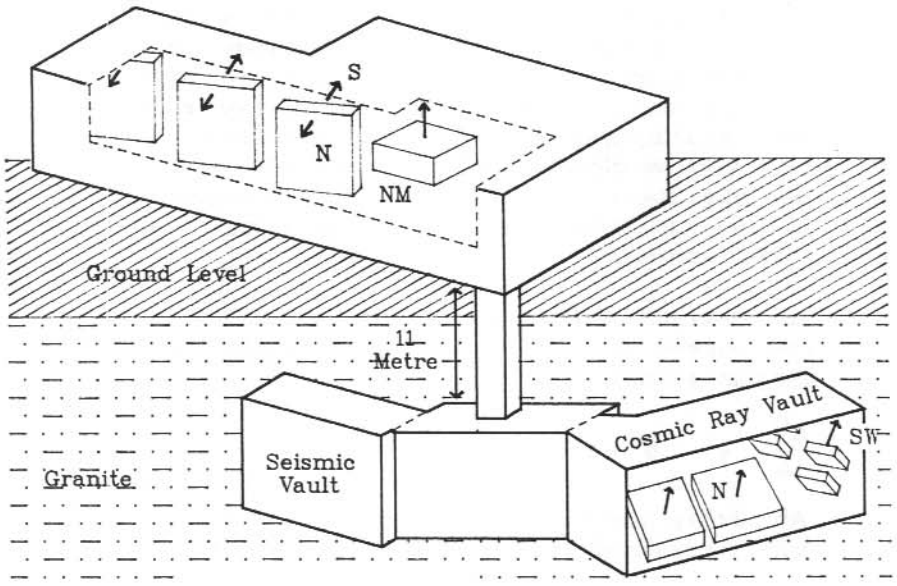

Figure 5. Schematic of the Mawson Automated Cosmic Ray Observatory (MACRO) showing the placement of the neutron monitor (NM), surface north and south pointing muon telescopes (S, N), the underground north pointing telescope (N) and the underground south-west pointing telescope (SW).

Table 1. Various cosmic ray telescopes and their locations

Station	Geographic Latitude	Geographic Longitude	Telescope	Zenith Angle	R_e(GV)	R_{med} (GV)
Cambridge	43°S	147°	U/G Muon	0° V	≈10	184
				43° N	≈10	195
Hobart	43°S	147°	Surface Muon	0° V	1.9	50
Mt Wellington	43°S	147°	Neutron Monitor	–	1.9	15
Mawson	68°S	63°	U/G Muon	24° N	10	164
				40° SW	11	188
			Surface Muon	74° N	≈10	150
			pre-1987	74° S	≈10	150
			Surface Muon	61° S	5	106
			since 1987	61° N	5	106
				45° S	3	72
				45° N	3	72
			Neutron Monitor	–	1.9*	15

* R_e is the 'effective' minimum rigidity a particle must have to be detected by an instrument. R_e is determined by the total amount of atmosphere (and rock in the case of an underground telescope) that particles must pass through. On the earth's surface, at high latitudes, R_e is usually greater than the magnetic cut-off rigidity R_c which for Mawson is 0.2 GV.

The University of Tasmania and the Australian Antarctic Division have a series of cosmic ray observatories in the southern hemisphere. In this study, neutron monitors and surface and underground muon telescopes from both Hobart and Mawson will be used giving information over a large range of primary rigidities (1 GV to 500 GV) (Table 1).

The coupling coefficients of all these detectors are known (Yasue et al. 1982, Fujimoto et al. 1984, Baker 1988) but before any major analyses can be applied to the surface muon data the corrections for the temperature effects must be calculated. Coefficients for the various atmospheric corrections are currently being determined.

What makes the geographical location of Mawson so attractive is that it is reasonably close to the rotation axis of the earth and the south magnetic pole. Telescopes have thus been aligned to: look along the rotation axis (practically no diurnal variation); look along the field lines (no energy dependent deflection of particles); look across the field lines (maximum energy dependent deflection) and; look simultaneously into the opposite temporal hemisphere by viewing over the

rotation axis. This site also allows the heliosphere at 1 A.U. to be viewed from the equatorial to the most southern heliolatitudes (Figures 5 and 6) and variations will have their temporal and energy responses recorded for a wide range of parameters from a single site (Duldig 1990).

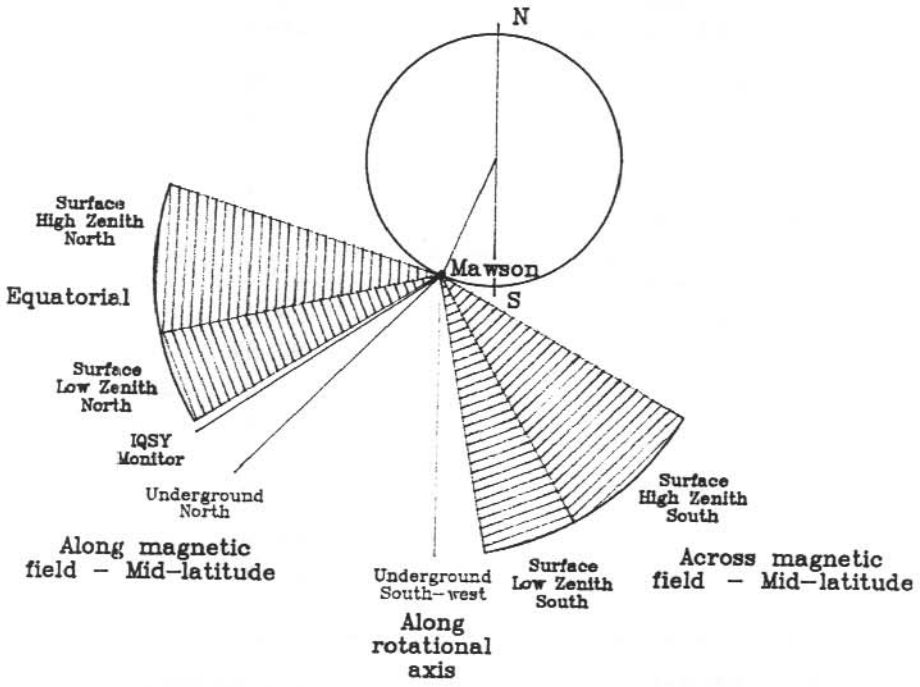

Figure 6. Viewing directions of the muon telescopes at Mawson.

25.5 POSSIBLE PROJECT AVENUES

Many authors (Swinson et al. 1986, 1991; Bieber and Chen 1991a; Chen et al. 1991) have studied the long term variations of the solar diurnal variation in order to gain information about particle density gradients and associated transport parameters. Most analyses are performed by using cosmic ray data separated according to the direction of the IMF in the vicinity of the earth, being either towards or away from the sun. This is done primarily because the reversal of the IMF direction will alter the drifts of the particles, changing some of the components that lead to the diurnal anisotropy.

Bieber and Chen (1991a) used the transport equations described above plus solar data from the IMP-8 satellite to derive information about the latitudinal and radial gradients and scattering mean free paths of cosmic rays. Their analysis used mainly neutron monitor data. They conclude that the bidirectional latitudinal gradient reverses with a change in solar magnetic polarity. This agrees with the modern drift theory. In an update of their 1991 publication (Bieber and Chen 1991b)

they conclude that the radial gradient is not solar polarity dependent but that the parallel mean free path is. These observations suggest inadequacies in drift theories.

Conversely, Swinson et al. (1991) devised a model to explain the apparently observed unidirectional latitude gradient in terms of asymmetric solar modulation and a bidirectional latitude gradient that is not magnetic polarity dependent.

The majority of observations employed for these types of analyses have been obtained from northern hemisphere telescopes, usually neutron monitors. Southern hemisphere observations and similar analyses at the same and higher primary energies may help to provide new insight into modulation theories.

Another feature of solar modulation directly observable at earth is the long term variation in the intensity of particles averaged over a solar rotation period. This has long been known to be correlated with the sun's 22 year magnetic polarity cycle (Simpson 1989). Drift models predict the correct shape of the intensity profile over the years. Lopate and Simpson (1991) studied the low energy particle intensity (0.02 – 1.5 GeV) using spacecraft observations and concluded that the onset time of enhanced modulation of intensity around solar minimum was influenced by the particle energy, i.e. particles of higher energy were modulated before particles with lower energy. They observed the time lag in the modulation onset for the solar minima of 1965 and 1987 but not for 1954 or 1977. A model was devised that incorporated the warp of the neutral current sheet.

A similar study using particle data of much higher energy (i.e. 1 – 500 GeV) would be most interesting. Investigations into the mechanisms responsible for this modulation and time lag would be valuable for further development of modulation theories.

25.6 PRELIMINARY RESULTS

Figure 7 shows the solar diurnal variation (not corrected for geomagnetic effects) at Hobart and Mawson as recorded over the last 33 and 17 years respectively. The solid lines are a 3 point moving average. Eleven and 22 year cycles in the amplitudes and phases (respectively) are evident and these data will be used to obtain information about particle density gradients.

25.7 SUMMARY

This paper was written with two main objectives in mind. It is intended to introduce the reader to the nature of cosmic ray modulation in the heliosphere. Secondly, by reviewing the more recent observations and theories about solar modulation of galactic cosmic rays in the heliosphere we hope to give the reader an insight into the motivation that has led to this research project.

Studying the long term variations in the average intensity and the diurnal variation of cosmic ray particles can help us to obtain a greater understanding of the structure of the heliosphere and its modulating mechanisms. At the University of Tasmania and the Australian Antarctic Division data are available to undertake this project. These southern hemisphere observations should offer new information about the mechanisms responsible for the solar modulation of galactic cosmic ray particles.

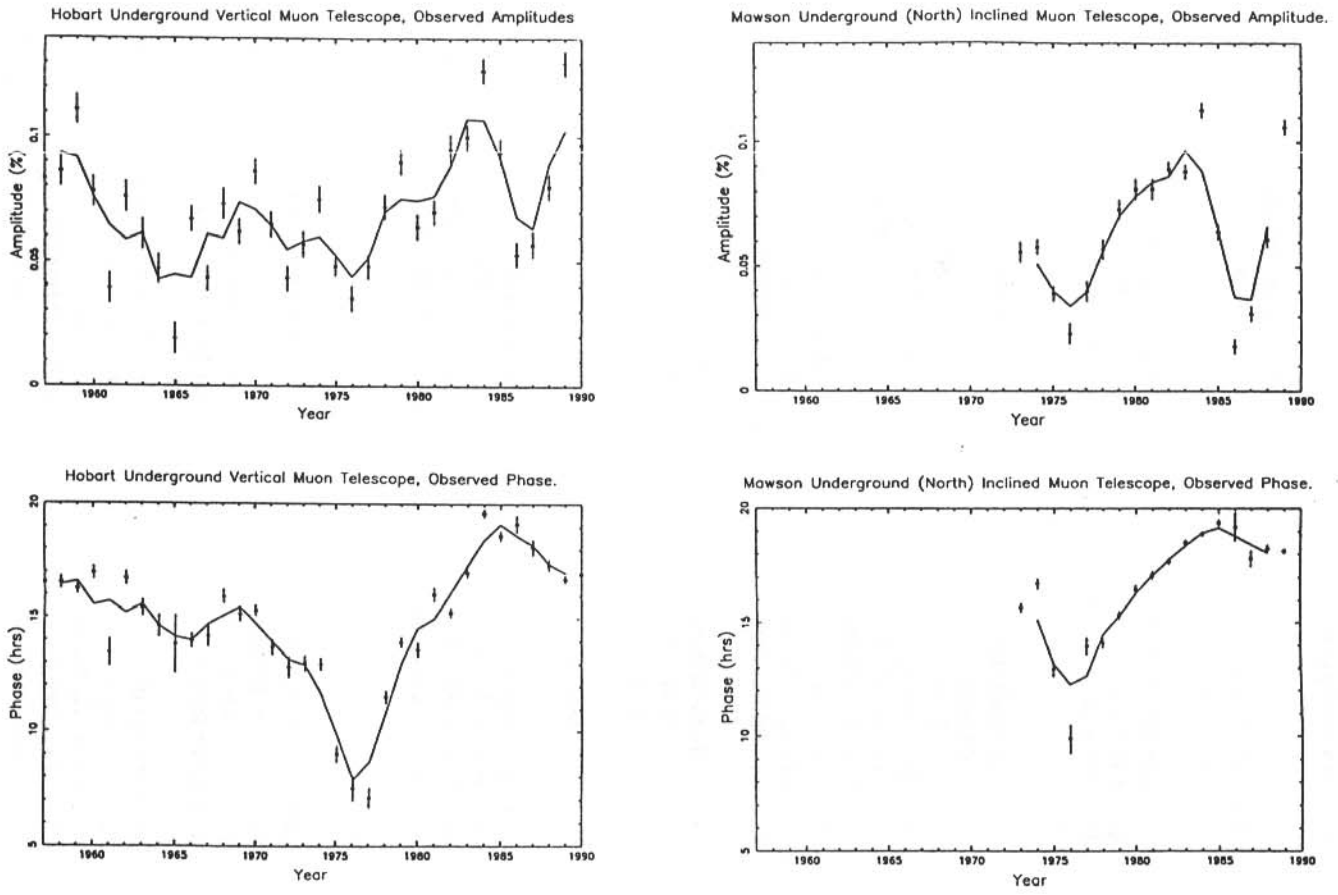

Figure 7. Amplitude and phase of the diurnal variation as observed by the Hobart underground vertical muon telescope, and the Mawson underground north pointing telescope.

25.8 ACKNOWLEDGMENT

D.L. Hall wishes to thank Mr C.P. Baker for many helpful discussions on transport theory.

REFERENCES

Baker, C.P. (1988). *Coupling coefficients for muon telescopes*. Honours Thesis, University of Tasmania, Australia.

Bieber, J.W. *and* Chen, J. (1991a). Cosmic ray diurnal anisotropy, 1936–1988: implications for drift and modulation theories. *The Astrophysics Journal 372*:301 – 313.

Bieber, J.W. *and* Chen, J. (1991b). Solar magnetic cycle variation of cosmic ray gradients and scattering mean free path. *Proceedings of the 22nd International Cosmic Ray Conference, Dublin 3*:525 – 528.

Bieber, J.W. *and* Pomerantz, M.A. (1986). Solar cycle variation of cosmic ray north-south anisotropy and radial gradient. *The Astrophysics Journal 303*:843 – 848.

Chen, J., Bieber, J.W. *and* Pomerantz, M.A. (1991). Cosmic ray uni-directional latitude gradient: Evidence for north-south asymmetric solar modulation. *Journal of Geophysical Research 96*:11569 – 11585.

Duldig, M.L. (1990). The Mawson automatic cosmic ray observatory (MACRO). *Proceedings of the 21st International Cosmic Ray Conference, Adelaide 7*:288 – 291.

Fenton, A.G., Jacklyn, R.M. *and* Taylor, R.B. (1961). Cosmic ray observations at 42 m.w.e. underground at Hobart. *Il Nuovo Cimento XXII N2*:3985 – 3996.

Flückiger, E.O. (1991). Solar and terrestrial modulation. *Proceedings of the 22nd International Cosmic Ray Conference, Dublin 5*:273 – 292.

Forman, M.A. *and* Gleeson, L.J. (1975). Cosmic ray streaming and anisotropies. *Astrophysics and Space Science 32*:77 – 94.

Fujimoto, K., Inoue, A., Murakami, K. *and* Nagashima, K. (1984). Coupling coefficients of cosmic ray daily variations for meson telescopes. *Cosmic Ray Research Laboratory Report No.9*. Nagoya, Japan.

Humble, J.E. (1971). *Diurnal and transient cosmic ray variations*. Ph.D. Thesis, University of Tasmania.

Isenberg, P.A. *and* Jokipii, J.R. (1979). Gradient and curvature drifts in magnetic fields with arbitrary spatial variation. *The Astrophysical Journal 234*:746 – 752.

Jokipii, J.R. (1984). The effects of heliospheric magnetic structure on the modulation of galactic cosmic rays. *Proceedings of the International Symposium on Cosmic Ray Modulation in the Heliosphere*. Pp. 27 – 38.

Lopate, C. *and* Simpson, J.A. (1991). The physics of cosmic ray modulation: Heliospheric propagation during the 1987 minimum. *Journal of Geophysical Research 96(2)*: 15877 – 15898.

Pomerantz, M.A. (1971). *Cosmic Rays*. Van Nostrand-Reinhold.

Pomerantz, M.A. *and* Duggal, S.P. (1971), The cosmic ray solar diurnal anisotropy. *Space Science Reviews 12*:75 – 130.

Rao, U.R., McCracken, K.G. *and* Venkatesan, D. (1963). Asymptotic cones of acceptance and their use in the study of the daily variation of cosmic radiation. *Journal of Geophysical Research 68*:345 – 369.

Sandstrom, A.E. (1965) *Cosmic Ray Physics*. North Holland.

Simpson, J.A. (1989). Evolution of our knowledge of the heliosphere. *Advanced Space Research 9(4)*:5 – 20.

Swinson, D.B. (1969). Sidereal cosmic ray diurnal variations. *Journal of Geophysical Research 74*:5591 – 5598.

Swinson, D.B., Humble, J.E., Shea, M.A. *and* Smart, D.F. (1986). Solar activity asymmetries and their possible effect on the high energy cosmic ray perpendicular gradient. *Advanced Space Research 9(4)*:221 – 224.

Swinson, D.B., Humble, J.E., Shea, M.A. *and* Smart, D.F. (1991). Latitudinal cosmic ray gradients: their relation to solar activity asymmetry. *Journal of Geophysical Research 96*:1757 – 1765.

Yasue, S., Mori, S., Sakakibara, S. *and* Nagashima, K. (1982). Coupling coefficients of cosmic ray daily variations for neutron monitor stations. *Cosmic Ray Research Laboratory Report No. 7*. Nagoya, Japan.

26. TWO HEMISPHERE OBSERVATIONS OF THE NORTH-SOUTH SIDEREAL ASYMMETRY AT 1 TeV

J.E. Humble[1], A.G. Fenton[1], K.B. Fenton[1], M.L. Duldig[2], S. Mori[3], S. Yasue[3], K. Munakata[3], K. Chino[3], M. Furuhata[3], Y. Shiozaki[3], S. Akahane[3], Z. Fujii[4] and I. Morishita[5]

[1] University of Tasmania
Hobart Tasmania 7001
Australia

[2] Cosmic Ray Section
Antarctic Division
Kingston Tasmania 7050
Australia

[3] Shinshu University
Matsumoto 390
Japan

[4] Nagoya University
Nagoya 464
Japan

[5] Asahi University
Motosu-gun 501–02
Japan

ABSTRACT

A new underground muon telescope system has been recently installed at Liapootah, central Tasmania in an hydro-electric power scheme access tunnel at a depth of 150 mwe. The telescope system comprises two 20 m^2 layers of 1 m^2 scintillation detectors. Data from the new system will be used in conjunction with similar data from the Matsushiro observatory in Japan to investigate the galactic sidereal anisotropy in the rigidity range ~300 – 1000 GV. Significant results should be achieved after 5 years data collection. The new telescope system is described.

26.1 INTRODUCTION

Ground level cosmic ray detectors invariably observe small amplitude diurnal variations in the incident cosmic-ray flux. At primary particle rigidities less than about 100 GV (the precise value varies with the solar cycle (Humble 1971, Ahluwalia and Riker 1987) this variation is clearly related to the modulation of primary cosmic rays by various mechanisms within the heliosphere (Hall et al. 1992 and references therein). The diurnal variation at these energies therefore appears primarily in solar time.

At higher energies, however, the gyro-radii of the primary cosmic rays in the interplanetary magnetic field are sufficiently large that the particles are little affected by transient variations in the magnetic field. Particles of these energies should therefore carry information about their bulk direction of motion in interstellar space in the region of the heliosphere.

The existence of orderly interstellar magnetic fields is likely to result in preferential bulk drift of cosmic rays along the direction of the field. A detector sequentially scanning different directions in space would therefore be expected to see apparent changes in flux as the viewing direction changes. For an earth-bound detector such a change would produce a regular variation in sidereal time.

26.2 SIDEREAL TIME VARIATIONS IN COSMIC RAYS

Unfortunately, the mere observation of a sidereal variation in sidereal time does not itself confirm the existence of an anisotropic cosmic ray flux at the heliopause (the boundary of the heliosphere). In any data which contains a diurnal variation in solar time, and which is also exposed to an annual variation in intensity, a 'spurious' sidereal variation will be found, caused by modulation of the 365 cycle/yr solar diurnal variation by the 1 cycle/yr annual variation. The modulation produces sidebands with frequencies 366 cycle/yr (sidereal time) and 364 cycle/yr. The latter, called the 'anti-sidereal' variation, can be used in some circumstances to help to distinguish between genuine and spurious variations in sidereal time.

The University of Tasmania cosmic ray group instituted a high energy observing program in 1957, in a disused railway tunnel near Cambridge, Tasmania. The station, which operates at a median rigidity of ~100 GV, is not entirely clear of solar influences, and consequently in 1972 the group commissioned a small installation at Poatina, Tasmania, in a corner of a deep underground power station. This station, which is still in operation, has a median rigidity of 1 TV, well above the highest rigidity which could be expected to undergo significant solar system modulation. A significant sidereal diurnal variation was found.

Table 1. Some characteristics of the Sakashita telescopes. (After Ueno et al. 1985).

	Viewing Latitude	Median Rigidity
NN	77°N	595 GV
N	73°N	400
V	36°N	300
E	35°N	380
W	18°N	440
S	5°S	390
SS	23°S	540

In 1978, observations of the sidereal diurnal anisotropy were started at Sakashita, Japan, using multi-directional muon telescopes with median rigidities in the range (depending on the direction of viewing) of 330 to 600 GV. The telescopes have median latitudes of viewing ranging from 73°N to 23°S, and the results over the six year period 1978–1983 clearly suggest that the amplitude of the variation increases as the median direction of viewing moves southward (Ueno et al. 1985). Figure 1 and Table 1 are from their paper. The cosmic ray group at Shinshu University, Matsumoto, Japan have obtained similar results from a deeper underground (vertical depth 200 mwe) observatory at Matsushiro (Mori et al. 1991a).

Observations made solely in the one hemisphere cannot unambiguously distinguish between a sin (η) and a sin(2η) dependence on co-latitude η (Jacklyn 1970) so in 1987 the Shinshu University group suggested that observations similar to their own should be made from a Tasmanian observatory. The end result of this suggestion was the installation, in December 1991, of a new underground observatory at Liapootah (42.32°S, 146.47°E) in central Tasmania.

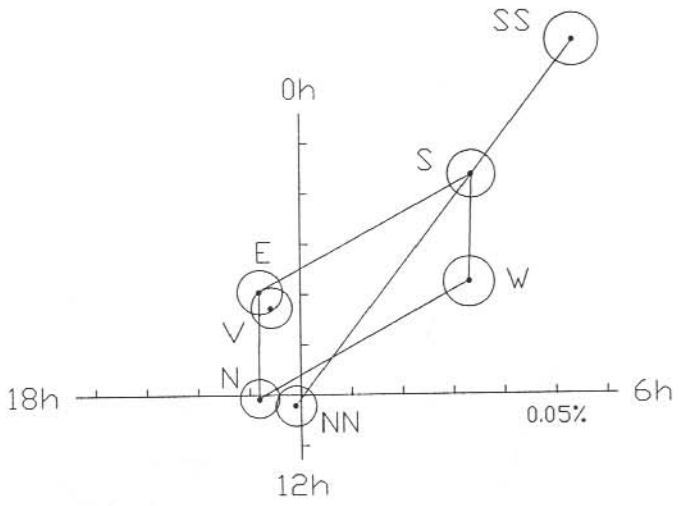

Figure 1. Mean observed sidereal diurnal variation, Sakashita, Japan 1978–1983, depth 80 mwe. (After Ueno et al. 1985).

26.3 THE LIAPOOTAH OBSERVATORY

The new observatory is installed in an access adit which forms an extension of a 6.4 km tunnel dug by the Tasmanian Hydro-Electric Commission in the 1940s to carry water from the Liapootah storage dam to the Liapootah power station. Adits, originally constructed for access and spoil removal purposes, exist at each end of the main tunnel and are now required only for emergency access should a rock-fall occur. The observatory is located approximately 90 m in from the open end of the northern adit, under a rock depth of about 150 mwe, and is mounted on sledges against

the possibility that urgent access to the main tunnel might be required by heavy machinery. In this unlikely event the sledge mounted telescopes and electronics can be quickly and easily removed from the adit.

The equipment consists of forty 1 m^2 scintillator detectors, provided by Shinshu University, mounted in two layers each of 20 m^2. The output of each detector is recorded, and directional information comes from coincidence of suitable pairs of detectors between the layers. The adit is aligned 24° west of north and it is not, therefore, possible to use the conventional rectangular arrangement of detectors. The actual arrangement is shown in Figure 2.

This configuration permits recording of cosmic rays arriving with vertical (V), north, south, east and west zenith angles 30° (N, S, E, W) and 49° (2N, 2E, 2S, 2W) as well as a NE, SE, SW and NW at a zenith angle of 39°. The count rates decrease with increasing zenith angle due not only to the additional absorber traversed but also due to the smaller effective area of detector available at the larger angles. The absorption effect varies with direction due to the topography of the ground above the detector.

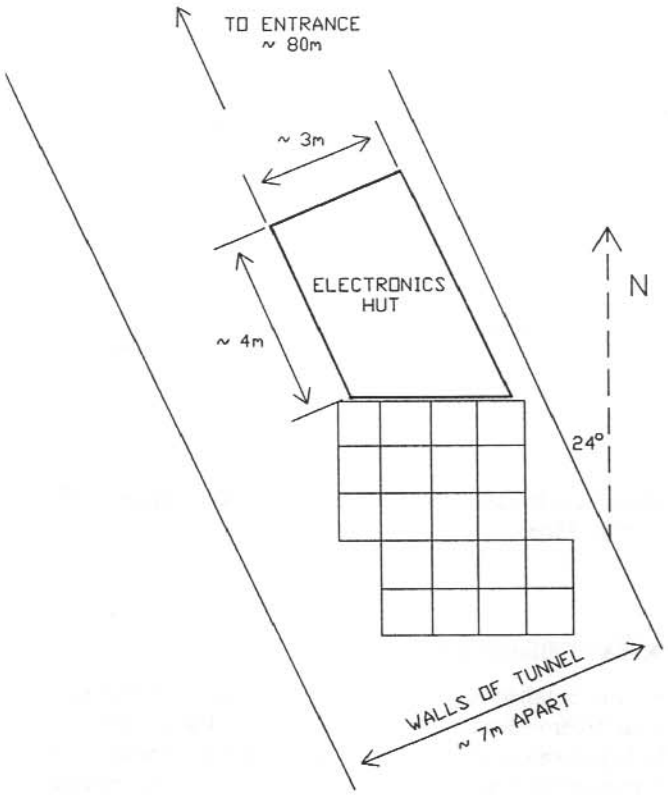

Figure 2. Layout of Liapootah observatory.

Figure 3, redrawn from Mori et al. 1991b, shows the estimated mean directions of viewing of the Liapootah observatory. The northward looking directions overlap the southern-most directions observed from Matsushiro and should thus allow any local effects which might be present to be clearly distinguished and then eliminated from the data.

Accumulation of sufficient data for a statistically reliable result will take about five years. It is hoped, however, that suggestive results will be available after operation for about one year.

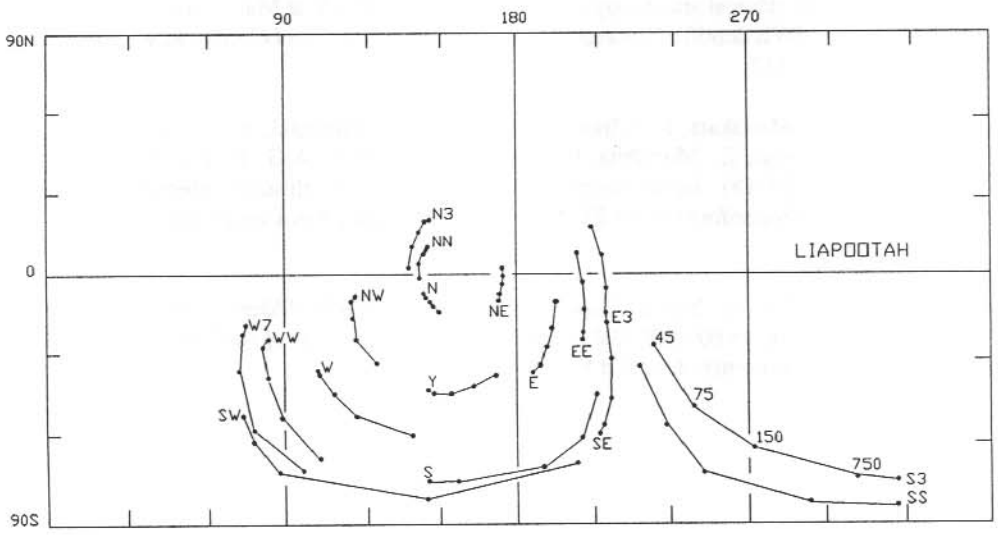

Figure 3. Directions of viewing of Liapootah detectors. (After Mori et al. 1991b).

26.4 ACKNOWLEDGMENTS

This project is supported by grants from the Australian Research Council and the Japanese Ministry of Education, Science and Culture. We gratefully acknowlege the help received from the Tasmanian Hydro-Electric Commission.

REFERENCES

Ahluwalia, H.S. *and* Riker, J.F. (1987). Secular changes in the upper cut-off rigidity of the solar diurnal anisotropy of cosmic rays. *Planetary and Space Science 35*:39 – 43.

Hall, D.L., Duldig, M.L. *and* Humble. H.E. (1992). A comparative study of solar modulation processes as recorded by southern latitude cosmic ray telescopes. In: Burns, G.B. *and* Duldig, M.L. (Eds). *ANARE Research Notes Number 88*. Australian Antarctic Division.

Humble, J.E. (1971). Rigidity spectrum of the cosmic ray solar diurnal variation. *Proceedings of the 12th International Cosmic Ray Conference, Hobart* 2:612–617.

Jacklyn, R.M. (1970). Studies of the sidereal daily variation of Cosmic Ray intensity, with particular reference to observations at 40 mwe underground. *ANARE Scientific Reports, Series C(II) Cosmic Rays, Number 114*. Antarctic Division, Melbourne.

Mori, S., Yasue, S., Munakata, K., Chino, K., Akahane, S. *and* Furuhata, M. (1991a). Observation of sidereal anisotropy of cosmic rays at ~10^{12} eV at Matsushiro underground station (220 MWE depth). *Proceedings of the 22nd International Cosmic Ray Conference, Dublin* 2:109–112.

Mori, S., Yasue, S., Munakata, K., Chino, K., Furuhata, M., Shiozaki, Y., Yokota, Y., Akahane, S., Fujii, Z., Morishita, I., Humble, J.E., Fenton, A.G., Fenton, K.B. *and* Duldig, M.L. (1991b). Japan-Australia observation of the north south sidereal asymmetry at ~10^{12} eV. *Proceedings of the 22nd International Cosmic Ray Conference, Dublin* 2:720–723.

Ueno, H., Fujii, Z., Mori, S., Yasue, S. *and* Nagashima, K. (1985). Sidereal anisotropies in the median rigidity range 60–600 GV in 1978–1983. *Proceedings of the 19th International Cosmic Ray Conference, La Jolla* 5:35-38

27. ANTARCTIC ASTRONOMY – INTRODUCTION AND SUMMARY OF INTERNATIONAL DEVELOPMENTS AFFECTING AUSTRALIA

P.R. Gillingham

Anglo-Australian Observatory
Coonabarabran NSW 2357
Australia

ABSTRACT

The extremely dry and cold atmosphere above the highest part of the Antarctic plateau presents opportunities for astronomical observations at infrared (IR) and mm wavelengths substantially better than from anywhere else on earth. Contrary to the popular conception of Antarctica, the climate high on the plateau features low wind speeds, mostly clear skies and relatively little snow fall. Many nations have already done astronomical work in Antarctica, some producing very good science, and in the last few years there has been a substantial quickening of interest. Several US institutions have collaborated to set up a Center for Astrophysical Research in Antarctica and this group has plans for greatly increasing the power of IR and mm instruments at the South Pole. A new international observatory sited for optimum astronomical performance has also been proposed. Australian and French astronomers, meeting in 1991 to discuss future collaboration, placed developments in Antarctica as their highest priority and a follow-up meeting on this topic will be held in 1992. At its triennial General Assembly in 1991, the International Astronomical Union adopted a resolution urging the establishment of an international high altitude observatory in Antarctica and set up a Working Group to encourage this.

27.1 INTRODUCTION

It is prophetic that the Australian $100 note features Douglas Mawson and Antarctica on one side, John Tebbutt and astronomy on the other. The next decade should see a blending of these two fields, in each of which Australia already has an enviable reputation, to produce valuable new scientific results. In this and the following papers, we shall explain why astronomers are becoming so interested in Antarctica and why we believe that Antarctic astronomy offers a particularly fruitful and appropriate field for Australian science.

Figure 1 shows some of Antarctica's key features from an astronomer's point of view. It is the high plateau and particularly its highest part, reaching nearly 4300 m altitude, that especially excites interest. Whereas the coastal sites, exemplified by the Australian stations at Mawson, Davis and Casey, suffer extremely high winds and much cloud, the high interior is very different. This is largely due to the systematic pattern of air flow that persists over much of the continent. Far from the ocean, surface winds are almost entirely the result of air, being cooled by the ground, flowing downhill. The velocities increase until, near the coast, they are very high. But near Dome A, the wind speeds are very low and the air flow is predominantly a slow settling from the stratosphere.

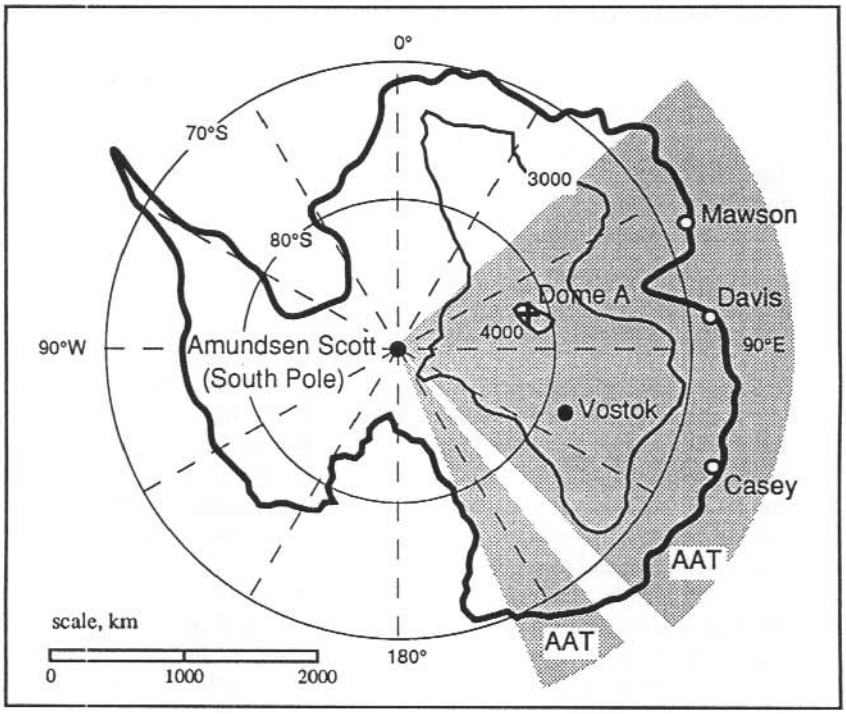

Figure 1. Antarctic stations, sites of special astronomical interest, Australian Antarctic Territory (AAT) and contours at 3000 and 4000 m altitude.

The outstanding attractions of a very high Antarctic site to astronomers working at wavelengths from the near-IR to a few mm results from the very dry, tenuous and cold atmosphere. Over much of this wavelength range, the main source of absorption in the earth's atmosphere is water vapour; at Dome A, the water vapour typically should be less than one tenth as great as at the best high altitude temperate sites (e.g. the summit of Mauna Kea on the island of Hawaii). The extremely low temperatures, down to below -80°C in winter, lead to very beneficial reductions in the thermal radiation from the atmosphere and telescope that is the major hindrance to detecting faint celestial sources, even at wavelengths where the atmosphere does transmit well. Note that nearly all the plateau above 3500 m altitude is in Australian Antarctic Territory.

27.2 ANTARCTICA'S CLIMATIC AND GEOGRAPHICAL ATTRACTIONS

Of the high inland sites, most work has been done at the South Pole where the USA operates the Amundsen-Scott base. The altitude there is about 2800 m. For the 18 year period 1957–75, the highest wind speed recorded was 24 m/s and there were many months for which the maximum was less than 15 m/s. The highest manned base, Vostok, at about 3500 m, has lower winds (a year round average of 5.1 m/s, with a very consistent direction) and less cloud (0 to 2/10 cloud

for 61% of summer and 56% of winter observations, with 80% of the cloud being high cirrus). The year round average air temperature at Vostok is -55.3°C while it is -49.3°C at Amundsen-Scott (Burdyuzha 1992). Dome A, at 4300 m, will have more favourable wind speeds and cloud cover and lower temperatures than either the South Pole or Vostok.

Continuous observations for several days can be crucial in observing some time-dependent phenomena. For the more typical astrophysical observations for which time variations are not of interest, continuous access is still desirable, especially for observing very faint objects, when many consecutive hours may be needed to accumulate the required signal to noise ratio. The sky is astronomically dark (i.e. the solar zenith distance is greater than 108°) round the clock at mid-winter for latitudes south of -84.5° and nautically dark (solar ZD >102°) south of -78.5°.

For some relatively rare and short-lived events (such as bright super-novae) within a particular range of celestial positions, an Antarctic site could be the only one on earth from which the phenomenon was observable at a reasonable altitude in a dark sky. Importantly, this applies to the region of the Large Magellanic Cloud.

27.3 PLANS FOR MAJOR OBSERVING FACILITIES IN ANTARCTICA

Over the last few decades, many nations have made astronomical observations of one kind or another from Antarctica. The most notable scientific results have come from studies of seismological oscillations of the sun and from mm wavelength measurements of the uniformity of the cosmic background radiation. In the last few years, technological advances in astronomical detectors, especially the advent of very sensitive IR arrays, have pushed the performance of these detectors close to that theoretically attainable. Concurrently, several projects to build much larger optical telescopes have begun and one, the 10 m diameter Keck telescope on Mauna Kea, is nearing completion. Once these new telescopes are operational, one of the few ways to substantially improve sensitivity will be to exploit sites which give better transmission and lower background. Space, including the moon, offers ideal performance but placing telescopes of even modest aperture and therefore restricted (diffraction-limited) resolution into orbit or on the moon is very expensive. The Antarctic offers many of the attractions of space at a small fraction of the cost, especially for very large aperture instruments.

The most comprehensive set of projects currently planned are those under the aegis of the new NSF financed Center for Astrophysical Research in Antarctica (CARA) with its base at Yerkes Observatory, Wisconsin. Members include several US universities and a couple of industrial corporations. Their currently planned research includes the following projects (Harper and Bally 1992):

1. Antarctic Sub-millimetre Telescope and Remote Observatory (ASTRO) will use a 1.7 m diameter telescope to survey the galactic plane, the galactic centre, and the magellanic clouds at wavelengths of 609 μm and 650 μm;

2. The Cosmic Background Radiation Anisotropy (COBRA) experiment will search for and map anisotropies in the cosmic background radiation on angular scales ranging from 15 arcmin to 20° at sufficient sensitivity to place stringent constraints on current theories of the origin of the universe;

3. South Pole Infrared Explorer (SPIREX) will use a near-IR telescope and IR array detectors to explore the potential of the Antarctic Plateau as an IR site and to make deep 2.4 μm continuum

surveys for faint sources including primeval galaxies, brown dwarf stars and dust-obscured objects in regions of star formation.

CARA researchers and collaborating astronomers from the United States and other countries will conduct experiments to measure environmental parameters including sky brightness, atmospheric transmission and seeing. They will also discuss and develop plans for more powerful telescopes which could be built in the future at the South Pole or other Antarctic sites.

Another important US initiative (Lynch 1989, 1992) has been the proposal for a new international base sited for optimum astronomical performance (at Dome A). Such a base, at an altitude above 4000 m and having a winter time pressure altitude equivalent to over 5000 m, would probably require pressurised living and working enclosures. It would then closely emulate a base on the moon and would provide very valuable logistic, scientific and political lessons on the path to an international lunar observatory. At its biennial meeting in 1990, the ICSU Scientific Committee for Antarctic Research (SCAR) adopted a resolution recommending serious international consideration be given to establishing such a station. At its meeting in June 1992, a session specifically to discuss astrophysical plans is scheduled.

27.4 INTERNATIONAL COLLABORATION INVOLVING AUSTRALIA

Following a meeting on Antarctic Astronomy at its General Assembly in 1991, the International Astronomical Union (IAU) passed a resolution 'encouraging international development of Antarctic astronomy' and created a Working Group (chaired by the author) 'to encourage international cooperation in site testing and in designing and constructing new Antarctic astronomical facilities'.

As part of a bi-national colloquium sponsored by the Australian Department of Industry, Technology and Commerce to encourage future scientific collaboration, French and Australian astronomers met in Sydney in April 1991. They rated cooperation in Antarctic astronomy as their first priority and recommended that a workshop specifically on this topic be held in 1992. This is to occur in Paris in May. A probable field of early collaboration is in developing critical tests of site quality, especially of seeing, to quantify the gains achievable in Antarctica and to help choose the very best site (Gillingham 1992). The director of CARA has indicated that they are very willing to provide logistic support for operating test equipment, developed by an Australian-French collaboration, at the Amundsen-Scott base. Good contact has also been established with Russian astronomers, who, following the 1991 IAU General Assembly, formed an Antarctic working group within their astronomical society. This contact is likely to lead to collaborative site-testing at Vostok.

A first meeting of some potential members of the IAU Working Group on Antarctic astronomy will be held in conjunction with the French-Australian meeting in May 1992.

An application has been made to the Australian Research Council for a grant to cover an initial investigation of the best ways for Australia to contribute to developing Antarctic astronomy, concentrating on the questions of how best to test site quality. The nominated chief investigators are at University of NSW, Anglo-Australian Observatory and Australian Defence Force Academy and the University of NSW would administer the grant.

27.5 CONCLUSION

In this decade and, even more so, in the 21st century, Antarctic observatories are likely to contribute very significantly to the advancement of astrophysical science. With our proximity to Antarctica, our long experience there in engineering and research, our strengths in astronomy and the technology of its instrumentation, and our claim to all that part of the Antarctic plateau most suited to astronomy, we in Australia should commit ourselves to playing a leading role in this very promising new field.

REFERENCES

Burdyuzha, V. (1992). Soviet Experience at Vostok and Plans for Antarctic Astronomy. *Highlights of Astronomy as presented at the 21st General Assembly of the International Astrophysics Union.*

Gillingham, P.R. (1992) Super seeing from the Australian Antarctic Territory. In: Burns, G.B. *and* Duldig, M.L. (Eds). *ANARE Research Notes Number 88.* Australian Antarctic Division.

Harper, D.A. *and* Bally, J. (1992). CARA – The Center for Astrophysical Research in Antarctica. *Highlights of Astronomy as presented at the 21st General Assembly of the International Astronomical Union.*

Lynch, J.T. (1989). A proposal for an International Station in Antarctica. *American Institute of Physics Conference Proceedings 198, Astrophysics in Antarctica.*

Lynch, J.T. (1992). An International Research Station in Antarctica. *Highlights of Astronomy as presented at the 21st General Assembly of the International Astronomical Union.*

28. SUPER SEEING FROM THE AUSTRALIAN ANTARCTIC TERRITORY?

P.R. Gillingham

Anglo-Australian Observatory
Coonabarabran NSW 2357
Australia

ABSTRACT

Seeing, the degradation of resolution due to the earth's atmosphere, is a crucial factor in determining the performance of ground-based telescopes. This degradation is predominantly the result of thermal inhomogeneity of the air, to which a substantial contribution arises from the diurnal cycle of solar heating. In most of Antarctica the diurnal variation in temperature is negligible throughout winter, so good seeing can be expected on this account. Above the highest point of the Antarctic plateau the predominant air flow is a slow settling from the stratosphere which should promote extraordinarily uniform optical quality. Unfortunately, the lower boundary layer in which a strong inverse temperature gradient develops, especially in winter, is likely often to degrade what might otherwise be unprecedented seeing. Critical tests are needed to measure this degradation and determine whether it can be circumvented by mounting a telescope on a higher pier than usual.

28.1 THE IMPORTANCE TO ASTRONOMY OF GOOD SEEING

For astronomy at wavelengths from the near-infrared (IR) up to a few mm, it is clear that high Antarctic sites, with their very dry cold atmosphere, offer the potential of enormous gains in sensitivity. Another important attraction at a very high altitude Antarctic site may be better angular resolution, i.e. better seeing, than from anywhere else on the Earth's surface. Seeing is a measure of the distortion suffered by an initially plane wavefront propagating through the earth's atmosphere. The distortions of most significance are due to refractive index inhomogeneity on a scale from about 1 cm up to a few metres and the refractive index variations are predominantly due to air temperature variations.

For telescopes larger than about 20 cm diameter for the visible and about 1 m for the near-IR, the image resolution at even the best sites currently in use is always degraded to some extent by seeing; in the visible, these sites yield images with a median full width half maximum about 0.6 arsec. For many critical astronomical observations, the figure of merit in deciding the sensitivity of a telescope is its collecting area divided by the area into which it concentrates a star image. So the inverse of the seeing diameter is generally as significant a measure of performance as the diameter of a telescope's mirror. For some observations, high angular resolution is crucial to obtaining the desired scientific result; in these cases good seeing is the most critical requirement of all.

28.2 FACTORS AFFECTING SEEING IN ANTARCTICA

At most observatory sites, diurnal temperature variation is a major cause of seeing degradation, both in the free atmosphere and, especially for large instruments, in the immediate vicinity of the telescope. In Antarctica, at least during the dark months, systematic diurnal variation in temperature is negligible, so seeing will not suffer on this account. The Antarctic atmospheric circulation pattern centres on the highest point of the plateau, where the predominant airflow is a slow settling to feed the very consistent downward-flowing surface winds. This should promote extraordinarily stable and uniform optical quality in the upper atmosphere above this highest point (Dome A). The thinness of the air above Dome A (which is at an altitude equivalent in pressure to above 5000 m) will also contribute to good seeing.

There have been few measurements of seeing reported from high altitude Antarctic sites – just some visual observations from the South Pole, which is at about 2800 m (Harvey 1989, 1991). These have not been remarkably good but most have been in daytime (i.e. summer) and have been made from small telescopes a few metres at most above the snow. Near-ground effects can dominate seeing degradation at many observing sites – hence the elevation of telescopes on piers and towers – but this is especially likely in Antarctica. There the ground cools well below the bulk air temperature, setting up a strong inverse air temperature gradient in the lower several to many tens of metres. In winter, the gradient can reach 0.1°C/m or more. Stirring of this boundary layer leads to large air temperature variations near the surface from hour to hour and, presumably, to significant thermal inhomogeneity which must degrade seeing.

28.3 MEASUREMENT OF ANTARCTICA'S SEEING POTENTIAL

Crucial uncertainties which must be resolved before we will know whether 'super seeing' is economically attainable from Antarctica are the quality of seeing from above the boundary layer and the height to which a telescope must be raised to avoid significant seeing degradation by this layer. Part of the program of the US Center for Astrophysical Research in Antarctica (CARA) is to measure seeing at the South Pole more quantitatively than in the past. It is important (a) that this program be extended to include measurements which will resolve the uncertainties just mentioned and (b) that, as soon as appropriate techniques for doing this are proved at the Pole, the same measurements be made at higher altitude sites. Initial moves have been made towards setting up a collaboration to this end, involving CARA, a few Australian institutions, and a group at the University of Nice, who have relevant experience in site testing for seeing (e.g. Vernin and Azouit 1990) as well as experience in building optical instruments for operation at the South Pole (for solar seismology). Encouraging contact has also been made with Soviet astronomers, which should lead to seeing tests being made at the Soviet Antarctic station, Vostok, currently the highest, manned, inland base.

28.4 INSTRUMENTATION TO CAPITALISE ON SUPER ANTARCTIC SEEING

In the wavelength range from 2.27 to 2.45 μm, which is free of atmospheric emission lines, the thermal radiance from the atmosphere is very steeply dependent on temperature, such that Antarctic sites offer about one hundred fold reduction compared with sites at 0°C. Because of these and other factors (Burton et al. 1992) there is enormous potential for Antarctic telescopes working in this wavelength range. At 2.4 μm, the diffraction limited resolution (the Airy disc radius) of a 3 metre diameter telescope is 0.2 arsec. So with a telescope of this size or larger,

seeing which frequently allowed close to diffraction-limited performance would further enhance the near-IR sensitivity gain and deliver very high resolution indeed. As argued above, there are good reasons to think such seeing will be attainable at a very high Antarctic site but it may be necessary to mount the telescope higher above the terrain than is usual on mountain-top sites.

REFERENCES

Burton, M.G., Allen, D.A. *and* McGregor, P.J. (1992). The potential of near-infrared astronomy in Antarctica. In: Burns, G.B. *and* Duldig, M.L.(Eds). *ANARE Research Notes Number 88*. Australian Antarctic Division.

Harvey, J. (1989). Solar observing conditions at the South Pole. In: Mullan, D.J., Pomerantz, M.A. *and* Stanley, T. (Eds). Astrophysics in Antarctica. *American Institute of Physics Conference Proceedings 198*.

Harvey, J. (1991). Daytime astronomical observing conditions at South Pole. *Highlights of Astronomy as presented at the XXIst General Assembly of the IAU*.

Vernin, J. *and* Azouit, M. (1990). SCIDAR measurements during LASSCA. In: Sarazin, M. (Ed.). *Site testing for the VLT, the La Silla seeing campaign. ESO Report No. 60.*

29. THE POTENTIAL OF NEAR-INFRARED ASTRONOMY IN ANTARCTICA

M.G. Burton[1], D.A. Allen[1], P.J. McGregor[2]

[1] Anglo Australian Observatory
Epping Laboratory
Epping NSW 2121
Australia

[2] Mt Stromlo and Siding Springs Observatories
The Australian National University
Weston Creek ACT 2611
Australia

ABSTRACT

The highest part of the Antarctic Plateau (Dome A) holds the promise of providing a superlative site for near-infrared (IR) astronomy and, in particular, for observations in the 2.27 – 2.45 μm waveband. This is a result of the intense cold, which reduces the thermal background by 6 magnitudes compared to a mid-latitude site, the absence of OH airglow emission between these wavelengths and the minimum in the zodiacal emission which occurs in the near-IR. The prospects exist for the darkest site for astronomy at any wavelength, anywhere in the inner solar system. Some possible scientific projects to exploit this potential, particularly deep cosmological surveys, are outlined.

29.1 INTRODUCTION

During the past few years it has become increasingly evident that the Antarctic plateau may be the best site on the planet for astronomical observations at infrared (IR), sub-mm and mm wavelengths. This is a result of the combination of high altitude, extreme cold and low water vapour content of the atmosphere. The 'seeing', or atmospheric-turbulence-limited resolution, may also be exceptional. Research groups from a number of countries have now conducted astronomical experiments from the South Pole, mainly focusing on the research areas of the microwave background and cosmic rays, and their experiences confirm the general expectations that Antarctica may provide an exceptional site for astronomy. In this paper we discuss the scientific potential of the Antarctic plateau for near-IR astronomy, and some of the plans that are being made to exploit it. There are fundamental astrophysical problems which might only be tackled from Antarctica. Other papers in this volume discuss the prospects for Antarctic astronomy at other wavelengths (see Gillingham 1992, Smith 1992, Storey and Hyland 1992).

29.2 NEAR-IR ASTRONOMY

IR astronomy can loosely be described as encompassing all observations spanning the wavelength range from 1 μm to 1 mm, and is subdivided into several regimes resulting from differences in detector capability and observational difficulty with wavelength. The near-IR regime covers the 1 – 5 μm waveband, and several factors conspire to make it an integral part of astronomy. First

is the cosmological redshift, whereby distant (and therefore young) objects in the universe recede from us at ever greater speeds and thus have their radiation Doppler shifted into IR wavelengths. Second, the extinction of light waves passing through interstellar material is vastly reduced in the IR compared to the optical, a factor of 10 between 5500Å and 2.2 μm. Hence we are able to peer into and through the numerous dark clouds of dust and gas that lie along the plane of our galaxy. We can witness star formation, which otherwise would be hidden from us, and explore the dynamic and often violent interstellar medium through the many atomic and molecular emission lines that are radiated in these wavelengths. Third, the exponential leading edge of the blackbody function, that moderates most astronomical emission mechanisms. Many types of object are intrinsically cool and radiate only in the IR and most of the photon energy of the universe is emitted in the IR. Figure 1 illustrates some of these points by showing the blackbody emission from a 300 K source and a 10 000 K body subject to 100 magnitudes of visual extinction.

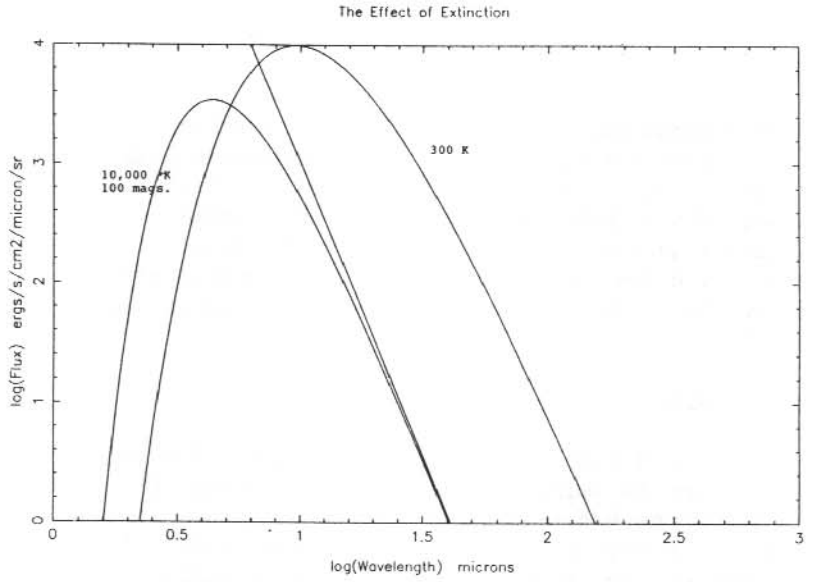

Figure 1. The Blackbody emission flux from sources at 300 K (right-hand curve) and at 10 000 K (left-hand curve) but subjected to 100 magnitudes of visual extinction (and divided by a factor of 1000). Also shown is the intrinsic (unextinguished) emission from the 10 000 K body. The figure illustrates that both cool bodies and heavily reddened objects are observable only at IR wavelengths.

29.3 SENSITIVITY LIMITATIONS IN IR ASTRONOMY

Three factors have been limiting the achievements of IR astronomy, as compared to the optical. These are:

1. Inferior technology
2. Poor atmospheric transmission
3. High thermal background

The first of these restrictions is now, however, receding. In the past five years, in what has been dubbed the 'infrared revolution', two dimensional array-format near-IR detectors, the equivalent of CCDs used in the optical, have replaced single element detectors and led to improvements of 10^3 to 10^4 in observational efficiencies. Although there still remains another order of magnitude improvement to equilibrate with the optical, it is realistic to expect that within the next decade IR arrays will be comparable in capability to optical CCDs. We are thus free to pursue the other two factors that limit performance.

The best IR observatories in the world are on high, dry mountain top sites, where the low water vapour content improves the atmospheric transparency over a lower altitude site and the low temperature reduces the IR thermal background radiation from both atmosphere and telescope. On the Antarctic plateau these gains are multiplied still further. Near-IR ($1-5$ μm) wavelengths lie on the Wien side of the blackbody radiation spectrum emitted by the earth. The decrease in temperature in Antarctica from a mid-latitude site results in an enormous decrease in the background. This is illustrated in Figure 2, which compares the blackbody emission fluxes in the near-IR at 273 K and 210 K, representative of a mountain top site, such as Mauna Kea, and the South Pole, respectively. The drop in the thermal emission from the sky in Antarctica is over two orders of magnitude over much of the near-IR spectrum. At longer wavelengths, although the drop in background levels are not so dramatic, the very low water vapour density over the Antarctic plateau considerably improves the atmospheric transparency, even opening some new 'windows' which are opaque at other observing sites (Smith 1992, Storey and Highland 1992).

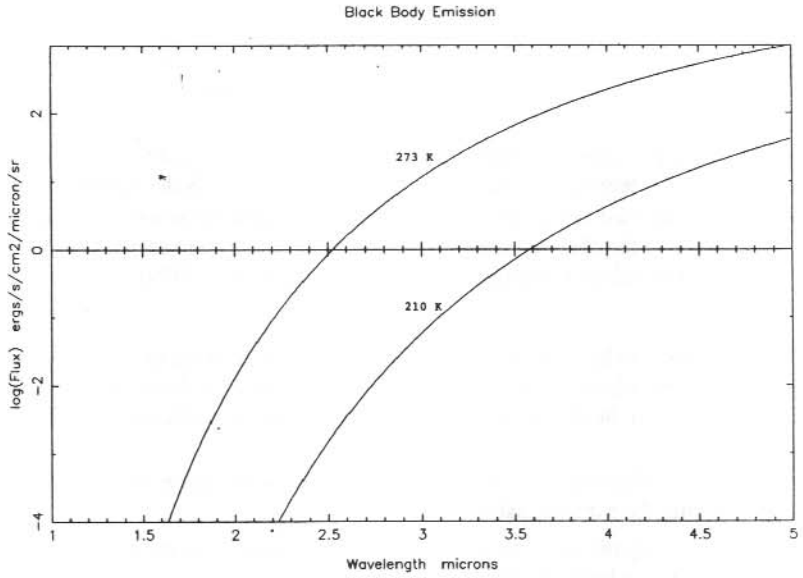

Figure 2. Blackbody emission fluxes in the near-IR ($1-5$ μm) regime for an atmosphere at 273 K (upper curve) and 210 K (lower curve), illustrating the relative thermal backgrounds at Mauna Kea and the South Pole.

In the near-IR, sensitivity is limited by a combination of airglow emission from OH radicals at altitudes of 80 – 90 km and thermal emission from the telescope and atmosphere. As demonstrated above, a small decrease in the ambient temperature results in a large decrease in the thermal background. Ultimately, if these could be reduced, we would be limited by the zodiacal emission (scattered and thermally re-emitted sunlight off solar system dust). This itself is at a minimum in the near-IR (Figure 3). Furthermore, and fortuitously, the 2.27 to 2.45 μm region is devoid of airglow emission. Model calculations (Figure 4) indicate that at the South Pole, with an air temperature of -60°C, the background is reduced by a factor of 220 from Mauna Kea, the best observing site currently in use, to a level close to the zodiacal emission itself. Even larger reductions can be expected above 4000 m, at the highest point on the Antarctic plateau (Dome A), where the temperature may drop to -90°C. The Antarctic plateau may therefore provide a site with as dark a sky background as can be found anywhere within the inner solar system.

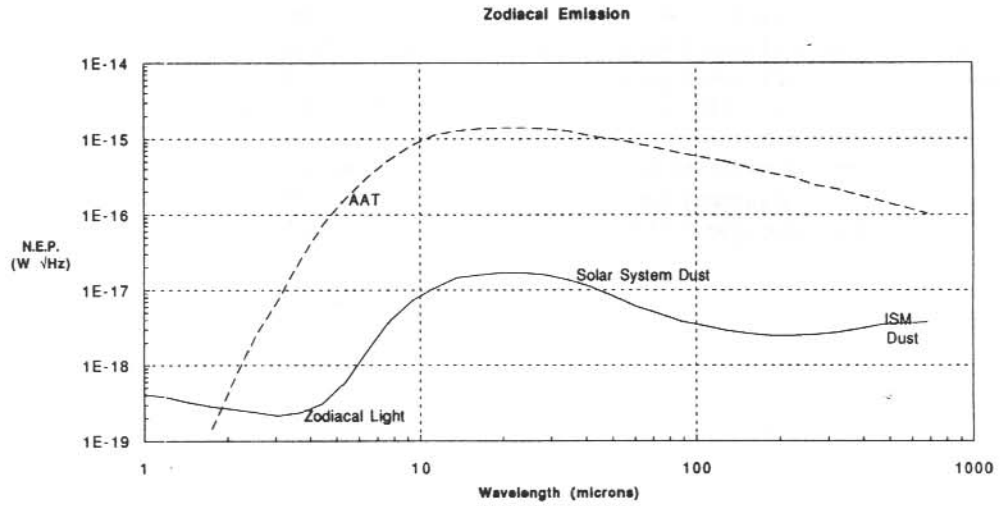

Figure 3. The Zodiacal emission in the IR, comprised of scattered sunlight off interplanetary dust in the optical and near-IR, thermal emission from interplanetary dust in the mid-IR, and thermal emission from interstellar dust in the far-IR. The minimum occurs in the near-IR regime. Also shown, for comparison, is the thermal emission from a 300 K site, representative of the background at Anglo Australian Telescope. (Adapted from Lee et al. 1990).

The reduced background can be translated into significant improvements in observing efficiencies. For a background limited observation between 2.27 and 2.45 μm, a decrease of a factor 220 in background corresponds to the following gains for a telescope in Antarctica compared to Mauna Kea (Harper 1989):

1. With the same size telescope and integration time, to observing a source 2.9 magnitudes fainter in Antarctica with the same signal-to-noise ratio;

2. To achieve the same signal-to-noise ratio on the same source, with the same integration time, requires a telescope 15 times larger in diameter on Mauna Kea;

3. With the same size telescope, to achieve the same signal-to-noise ratio on the same object, requires an integration time 220 times longer on Mauna Kea.

In other words, for such observations a 1 m telescope in Antarctica is equivalent to a 15 m telescope on Mauna Kea, with a price vastly smaller! A 1 m class telescope can be constructed from kit form, whereas building a 15 m class telescope is at the very limits of current technological capability.

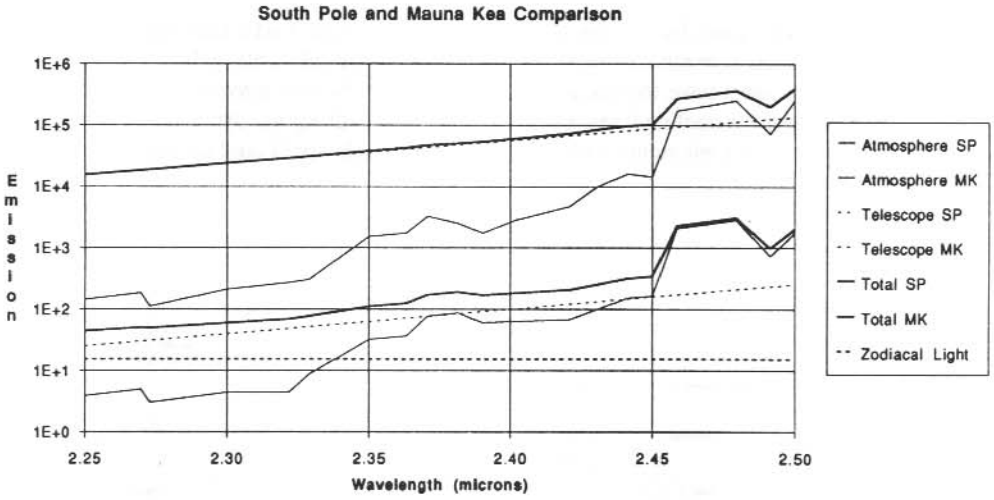

Figure 4. Comparison of the background at the South Pole (lower curves) and Mauna Kea (upper curves) in the 2.25 – 2.50 μm region. Contributions from the atmosphere are shown as thin solid lines, from the telescope as thin dashed lines and from the zodiacal light as a thick dashed line. The total background at each site is shown by the thick solid line. At the South Pole the background is close to the fundamental limit set by the zodiacal emission. (Adapted from Lubin 1988 and Harper 1989).

For the very deepest observations there is an additional and perhaps even more important gain. The ultimate sensitivity achievable depends on how accurately it is possible to flatfield the data in order to measure a signal which is a tiny fraction of the sky background. Practical experience shows that this is about 0.1% of the background level. In this case an Antarctic telescope will enjoy an advantage in signal-to-noise ratio directly proportional to the decrease in background, an improvement in limiting flux density of some 5.9 magnitudes. This has significant implications for cosmological surveys.

29.4 SCIENCE PROJECTS

Several key problems in cosmology, star formation, the physics of the interstellar medium and the galactic centre might be addressed by high sensitivity observations from the Antarctic plateau. Despite great strides in our understanding of the universe in the past few decades, major questions remain unanswered. How did galaxies form from an initially smooth and expanding primordial gas and when? How do stars actually form and what is the mass spectrum and formation rate? What is the role of the interstellar medium in regulating this process? Is there a massive black

hole at the centre of our galaxy? Significant progress can be made on these issues through observations at IR wavelengths from the Antarctic plateau. Some example projects which can be tackled are described below.

29.4.1 *Early Star Formation in Galaxies*

How did the first stars form from a gas of only hydrogen, helium and a little lithium? Without dust and metals the usual mechanisms of star formation observed in our galaxy cannot operate. Molecular hydrogen must have formed at some point and the heat of gravitational contraction be radiated away through its cooling lines, mainly at mid-IR wavelengths. After the first generation of stars formed and heavy elements built up, collapsing clouds could cool through fine structure

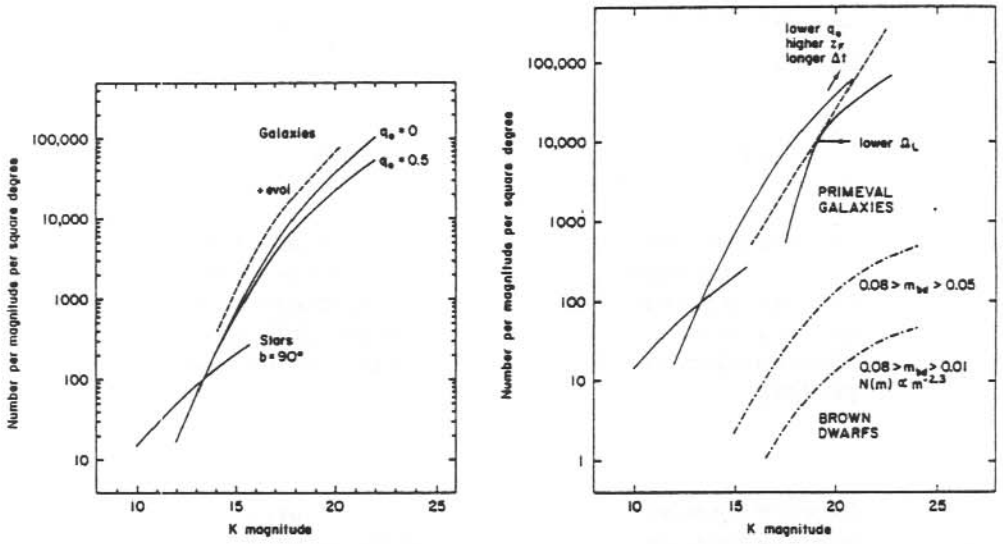

Figure 5. (a) Left. A predicted number-magnitude relation at K (2.2 μm) for stars and galaxies, as would be observed at high galactic latitude, based on K-corrections determined at low redshift and for two different cosmological models. The number counts are dominated by galaxies in the faint IR sky. For an equivalent survey, a sensitivity gain of nearly 3 magnitudes will be achieved from the Antarctic Plateau compared to Mauna Kea.

(b) Right. As for (a), but also including possible populations of brown dwarf stars and high-redshift proto-galaxies. The curves for brown dwarfs represent the field populations for different mass ranges which will account for the local 'missing mass'. The dashed line for proto-galaxies represents a locus along which plausible luminosity functions will slide depending on model parameters. The very deepest surveys might reach limits 0.1% of the sky level, or 7.5 magnitudes fainter than the K = 13 magnitudes per square arcsec background of Mauna Kea. On the Antarctic plateau the background is reduced a further 6 magnitudes at K. (Both figures from Lilly and Cowie 1987.)

lines of elements such as O and C^+, emitted at far-IR wavelengths. For redshifts in the range z = 3 – 10, where Galaxy formation probably occurred, the peak of mean stellar spectrum can be observed at near-IR wavelengths. Deep near-IR surveys are required to search for and detect these proto-galaxies.

Figure 5(a) (Lilly and Cowie 1987) shows a prediction of the number-magnitude relation at K (2.2 μm) for stars and galaxies for a field at high galactic latitude, extrapolated from measurements at shorter wavelengths and lower sensitivity. Galaxies will clearly dominate any faint survey. Assuming a sensitivity improvement of 2.9 magnitudes over a similar survey conducted from Mauna Kea, as discussed above (i.e. with the same size telescope and integration times), an order of magnitude more sources will be detected for the same effort.

For the very deepest survey of a small region we may expect to do even better. A practical limit to such a survey is 0.1% of the sky background, which for Mauna Kea, where the background is K = 13 magnitudes per square arcsec, corresponds to K~20.5. On the Antarctic plateau, if we are able to achieve such a limit, this would take us down by a factor of 220, to K~26.5! In Figure 5(b) (Lilly and Cowie) are shown the same number-magnitude relation predictions but this time including contributions from possible brown dwarf stars, postulated to account for the 'missing mass', and from high-redshift proto-galaxies. It is clear that with these sensitivity levels, not only are the prospects of discovering orders of magnitude more proto-galaxies than from Mauna Kea excellent but that a significant number of brown dwarfs would be detected too, if they exist. The brown dwarf yield for a similar survey from Mauna Kea is too low to result in a significant chance of detection.

29.4.2 *Formation of Stars and Planets*

Some of the nearest and richest star forming regions lie in the southern sky and their embedded stars are only observable at IR wavelengths. In the near-IR the extinction is at most a few magnitudes to such regions and the sensitivity high enough that a complete population census of the cluster membership of several nearby star forming regions, such as Rho Ophiuchus and R Coronae Australis, can be undertaken to determine the distribution and range in mass of the young stars. The strongest lines from shocked and fluorescent molecular hydrogen, which trace the energetic activity associated with young stellar objects, are also emitted near 2.4 μm.

29.4.3 *The Galactic Centre*

The study of the stars at the centre of our galaxy is the domain of IR astronomy, as they are totally obscured by intervening gas and dust in the visible. The stars are readily apparent by 2.4 μm, but the region is so crowded at the highest spatial resolutions achieved that we still do not know what lies at the very centre of our galaxy. With the prospects of super-seeing, combined with high sensitivity at 2.4 μm, we may hope to understand the nature of the galactic nucleus.

29.5 CURRENT PLANS

A number of countries have expressed interest in Antarctic astronomy and undertaken exploratory experiments. The most developed plans come from the Center for Astrophysical Research in Antarctica (CARA) in the USA, which has been funded and has initial plans for three telescopes at the South Pole; a sub-millimetre telescope, a cosmic background microwave detector, and a

near-IR telescope. The latter, the South Pole Infrared Explorer (SPIREX), is a 60 cm transportable telescope which will be used with a near-IR array camera and spectrometer and is designed to exploit the minimum of zodiacal emission in 2.27 – 2.45 μm window. There are only proto-designs at present, however, for a 2 m-class telescope, which also offers the potential of benefitting from 'super-seeing', as well as from the low background in the near-IR and yet remains relatively simple to construct.

29.6 SUMMARY

The combination of extreme cold and minimal atmospheric water vapour content mean that the summit of the Antarctic plateau (Dome A) might prove to be the preeminent site on the earth for astronomical observations across the entire IR and sub-mm wavebands with superior atmospheric transparency and reduced background to any other site on the earth. The thermal background in the near-IR is reduced by over two orders of magnitude from mid-latitude sites like Mauna Kea. In particular, in the 2.27 – 2.45 μm regime, devoid of atmospheric airglow emission, observations will be limited only by the natural zodiacal background which is itself at a minimum in this region. Thus, the background against which observations must be made is at a minimum for a site anywhere within the inner solar system. This offers us an unprecedented window to peer out upon the universe and pursue fundamental astrophysical problems in star formation and cosmology.

REFERENCES

Harper, D.A. (1989). Infrared astronomy in Antarctica. In: Mullan, D.J., Pomerantz, M.A. *and* Stanev, T. (Eds). Astrophysics in Antarctica. *American Institute of Physics Conference Proceedings 1988*. Pp. 123 – 129.

Lee., T.J., Hawarden, T.G., Thronson, H.A., Mountain, C.M., Davies, J.K. *and* Longair, M.S. (1990). Radiatively cooled telescopes for infrared space astronomy. *Proceedings of the 24th Liege International Astrophysical Colloquium, July 1990, ESA SP 314*:373 – 379.

Lilly, S.J. *and* Cowie, L.L. (1987). Deep infrared surveys. In: Wynn-Williams, C.G. *and* Becklin, E.E. (Eds). *Infrared Astronomy with Arrays*. Pp. 473 – 482.

Lubin, D. (1988). Masters Thesis. University of Chicago.

30. THE POTENTIAL FOR MID-INFRARED ASTRONOMY FROM ANTARCTICA

C.H. Smith

Department of Physics
University College
Australian Defence Force Academy
Canberra ACT 2600
Australia

ABSTRACT

The Antarctic plateau, with its very dry and cold atmosphere, presents a number of advantages for astronomy in the thermal infrared region. With atmospheric temperatures 60 – 80° below zero, the thermal background drops by a factor of 5, compared with the best currently available observatory sites (e.g. Mauna Kea). More importantly however, the extremely low precipitable water vapour content in the Antarctic atmosphere (200 – 600 μm) means that the accessible region of the spectrum extends virtually all the way to 60 μm, compared with the almost complete cut-off at 22 μm for currently available observing sites. While the potential gains are significant, there are also some potential drawbacks, such as ice 'haze'. It is essential that site testing begin as soon as possible to determine the reality of the benefits from siting a telescope in Antarctica.

30.1 INTRODUCTION

For astronomical purposes the infrared (IR) spectral regime (1 – 500 μm) is generally divided into three parts:

Near-IR	1 – 5 μm
Mid-IR	5 – 60 μm
Far-IR	60 – 500 μm

This paper discusses some of the problems and possible solutions that are particular to the mid-IR.

The mid-IR is also called the thermal-IR, as it sits at the peak of the Planck function for a room temperature black body. Unfortunately, this makes the mid-IR one of the least sensitive spectral regions in which we can work, as the thermal background is higher here than any other part of the spectrum. In fact, if it wasn't for a host of interesting and important astrophysical phenomena which manifest themselves in the mid-IR we may not bother trying to use this spectral region at all. By way of an example, the astronomical sources that we observe are generally orders of magnitude fainter than the background due to the 'warm sky' and telescope.

The high background however, is not the only problem that besets us. The mid-IR (as are the near- and far-IR) is further sub-divided by atmospheric transparency effects, or atmospheric windows. At low altitude (< 2000 m) terrestrial observing sites, only the region from 8 – 13 μm is workable but from better sites (>2000 m) the region from 16 – 22 μm is also accessible.

These 'windows' are largely defined by the transparency (or rather, lack of it) of atmospheric CO_2 and H_2O, although other atmospheric gases also play their part. CO_2 is fairly uniformly distributed throughout the atmosphere and has a scale height of about 6 km. H_2O however, resides mainly in the lower regions of the atmosphere, and has a scale height of around 2 km. There is not much that can be done about CO_2 absorption other than observe from above the atmosphere with space-bourne observatories such as IRAS, ISO and SIRTF. There are, however, some less expensive solutions to the water vapour problems.

So, the two major factors which limit ground based mid-IR astronomy at present are:

(a) the thermal background and
(b) the atmospheric transparency.

Mid-IR astronomy from Antarctica offers improvements in both of these areas.

30.2 THERMAL BACKGROUND

In a modern IR (photo conducting) array detector, the noise photocurrent (i_n), per beam, is defined as:

$$i_n = \left[NR^2 + 2G\left(i_s + i_{bg} + i_{dc}\right)T \right]^{1/2} \quad e^- / s \qquad (1)$$

where i_s = signal photocurrent
i_{bg} = background photocurrent
i_{dc} = dark current
NR = read noise
G = photoconductive gain
T = temperature

The factor of 2 arises from both generation and recombination photo-electron noise in the detector.

We calculate the signal (photocurrent) as:

$$i_s = \frac{\eta G \tau A F_\lambda}{\hbar} \frac{\Delta\lambda}{\lambda} \quad e^- / s \qquad (2)$$

where η = detector quantum efficiency
τ = transmission by sky, telescope and instrument
A = telescope collecting area
F_λ = incident flux
$\Delta\lambda$ = band width
λ = observation average wavelength

and using typical numbers at a 4 m telescope this signal current is around 10^4 e^-/s.

The photocurrent due to the background is

$$i_{bg} = \frac{\eta\, G\, \varepsilon\, B(\lambda,T)\, A\, \Omega}{\hbar}\ \frac{\Delta\lambda}{\lambda}\ \ e^- / s \qquad (3)$$

where ε = emissivity of sky and telescope
Ω = beamsize solid angle
$B(\lambda,T)$ = Planck function for λ, T

The emissivity of sky and telescope is typically about 15% and i_{bg} amounts to $10^9 - 10^{10}$ e^-/s at 10 μm and T ≅ 273K.

In the mid-IR the read noise and dark current are generally negligible compared with the background i.e. a few 100 – 1000 e^-/s: this is also true of the signal photocurrent. The system noise is therefore dominated by photon shot noise from the sky background.

So, ignoring i_s, i_{dc} and NR the system noise reduces to:

$$i_n = \left[2\, G\, i_{bg}\, T\right]^{1/2}\ \ e^- / s \qquad (4)$$

and substituting for i_{bg} gives:

$$i_n = G\left[\frac{2\, T\, \eta\, \varepsilon\, B\,(\lambda,T)\, A\, \Omega}{\hbar}\ \frac{\Delta\lambda}{\lambda}\right]^{1/2}\ \ e^- / s \qquad (5)$$

The noise is clearly a maximum in the mid-IR as $B(\lambda,T)$ peaks here, for a room temperature blackbody. Given our estimates of i_s and i_{bg}, the typical signal is around 10^{-5} of the background.

A further problem with modern IR array detectors is that the detector well depth is generally limited to 10^5 – 10^7 e^-/s and so with an i_{bg} of 10^{10} e^-/s we must read the array between 10^3 and 10^5 times per second in a broad band imaging mode. These detectors (with formats typically 128^2 or 256^2) have around 16000 and 65000 elements and so we need to be able to read individual pixels at around $1.6 \times 10^7 - 6.5 \times 10^9$ per second to avoid well saturation and this requires some fast readout electronics. This is only a technical problem and is already being resolved but the fast read rate can lead to non-negligible values for the read noise.

Another problem is that most mid-IR detectors show a non-white noise component in their noise, the origin of which is still a mystery, although carrier bunching and current noise at edge contacts have been suggested as possibilities. This introduces a component of noise that is proportional to the background, at least in high background conditions. Going to a lower background does help to reduce this effect.

Generally then, most mid-IR detectors fall short of being background limited by a factor of between 2 and 4, even though the general misconception is that the mid-IR is background limited. However, these last two problems are not fundamental and detector development and refinement

is continuing. By the time a telescope is constructed in Antarctica these problems will hopefully have been resolved and any reduction in the thermal background will be fully utilised.

Ideally, to minimise noise, we would put telescopes in space where there is no thermal background from the sky and we could cryogenically cool the telescope. This however, is difficult and expensive for any reasonable size telescope and the lifetime of a cryogenically cooled telescope is always limited (e.g. IRAS, ISO, SIRTF). Next best are stratospheric aircraft, which get to heights of around 12 km above the earth and precipitable water vapour of 7 μm (e.g. KAO and SOFIA), although these observatories also suffer many of the problems of space bourne telescopes, such as size, limited duration and expense. At the proposed observatory site in Antarctica, with an altitude of over 4000 m and telescope/sky temperatures of around 210–220 K there is a significant reduction in the thermal background at 10 μm (factor of 5), although this is not quite the spectacular gain available in the near-IR. Table 1 shows the ratio of background flux at 273 and 213 K at a number of infrared wavelengths. Also indicated is the reduction of limiting flux commensurate with the reduced background at the lower temperature.

Table 1. Effect of temperature on thermal background.

Wavelength (mm)	2.4	5	10	20	40	60
B(l, 273 K)/B(l, 213 K)	480	20	4.4	2.2	1.6	1.2
Reduction in limiting flux	22	4.5	2	1.5	1.25	1.1

Clearly there will be some gains (a factor of ~2 in S/N) at 10 μm but at wavelengths longer than 10 μm the reduction in thermal background becomes less significant. While these gains are valuable we would need to build a rather large (> 4 m) telescope in Antarctica to compete with the modern 8 and 10 m class telescopes being proposed and constructed elsewhere.

One potentially serious problem for mid-IR astronomy with an Antarctic telescope is the possible presence of ice haze, i.e. any suspended icy crystals, which cause observed phenomena such as sun haloes and sun dogs. If such icy crystals have optical depths of as little as 1% then the sky/telescope background (nominally 10%) increases by ~10%. While this increase may not seem catastrophic in itself, it represents something like 1000 times the limiting flux and any temporal or spatial structure in the haze/cirrus could easily negate the gains derived from the cold site. At present however, we do not have any firm data on the frequency or composition of the ice haze and so we clearly have a need for some proper site testing at the proposed observatory site before any informed decision can be made about the suitability of the Antarctic for mid-IR astronomy.

30.3 ATMOSPHERIC TRANSPARENCY

Thermal background is not the only factor and it is in atmospheric transparency that Antarctica wins out over any other terrestrial observatory. As noted previously, the main culprits in reducing atmospheric transparency are CO_2 and H_2O and there is little we can do about CO_2 from ground based observatories. We can however, beat down the effects of water vapour by going to a high, cold site. High to get above the water vapour and cold to minimise the amount of precipitable water vapour in the remaining atmosphere.

At the proposed observatory site in Antarctica (Dome A) the altitude is >4000 m, and the temperature is around -60°C. Under these conditions the precipitable water vapour (PWV) drops to around 500 μm in the Antarctic summer and 250 μm in winter, compared with ~2 mm on a

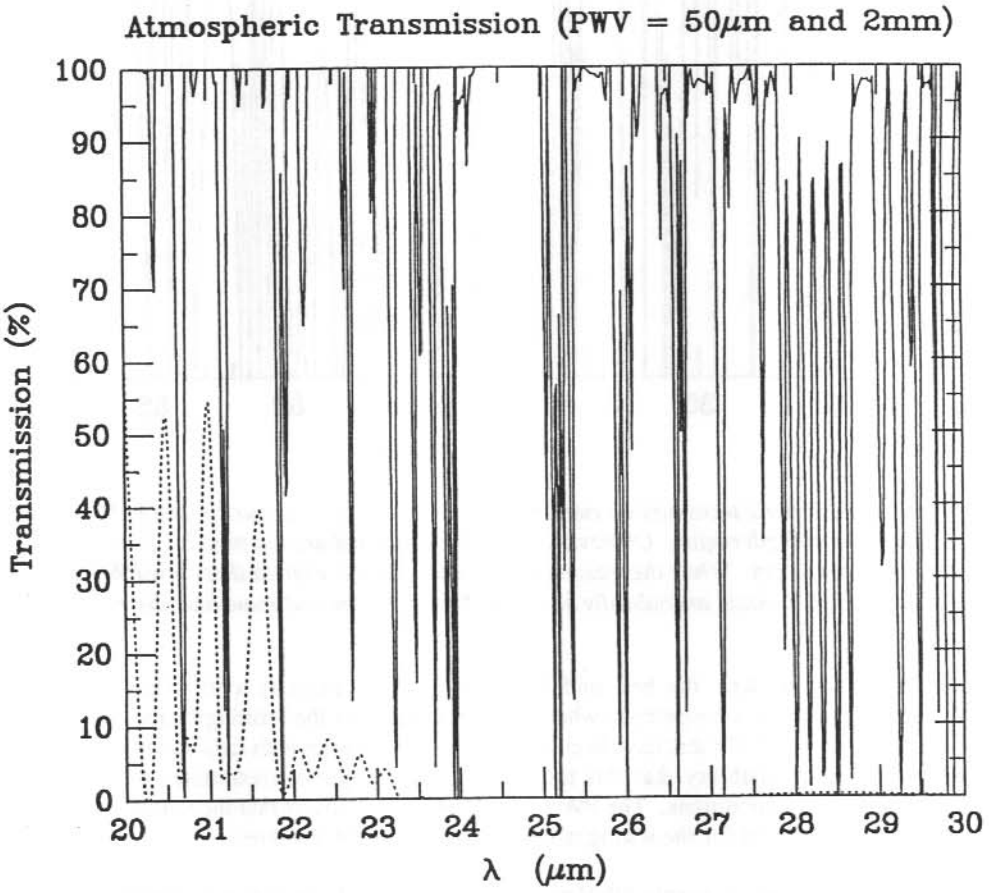

Figure 1. Atmospheric transmission curves for precipitable water vapour content of 50 μm (solid line) and 2 mm (dotted line) in the 20–30 μm wavelength region. Fifty μm PWV represents a 'good' day in Antarctica, and 2 mm PWV represents a 'good' day at a site like Mauna Kea. The improved transmission under Antarctic conditions is dramatic.

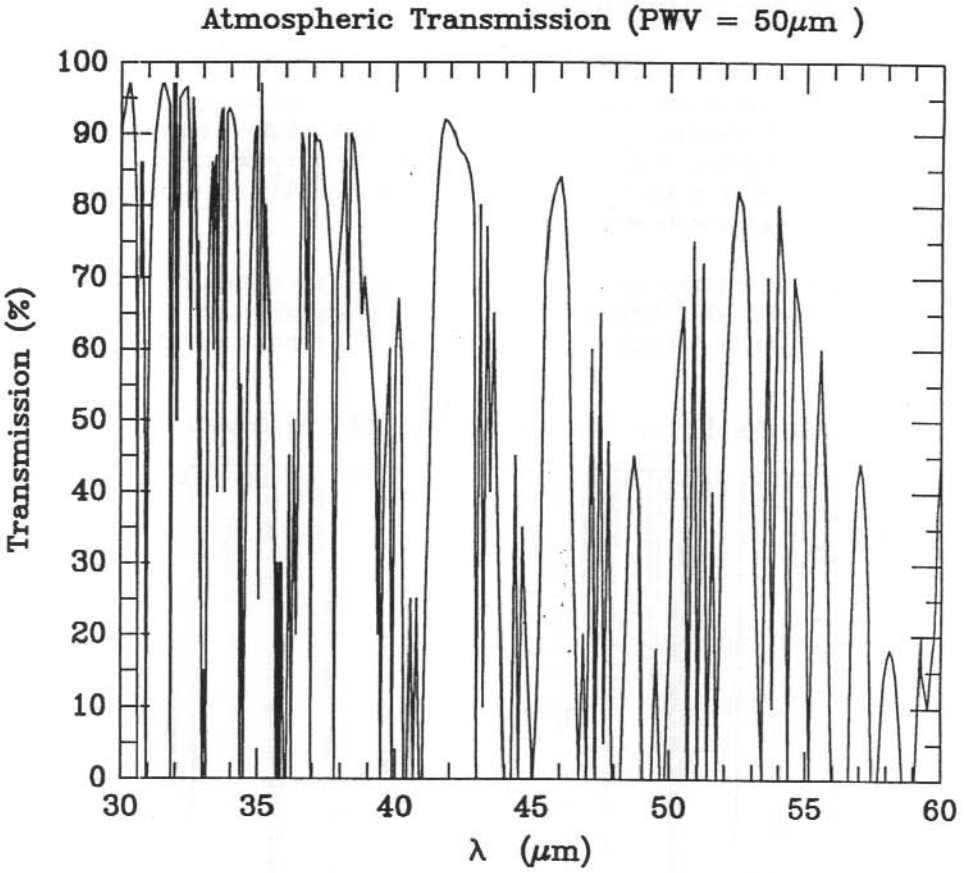

Figure 2. Atmospheric transmission curve for precipitable water vapour content of 50 μm in the 30–60 μm wavelength region. Observations in this waveband are not possible from any other terrestrial observatory. While the transmission is still 'patchy', even at these low PWV levels, this spectral region would undoubtedly be usable for continuum and some line observations.

good day at Mauna Kea, the best mid-IR observing site currently available. This leads to significantly improved transparency wherever water vapour is the limiting factor. Furthermore, the measurements of PWV that have been made in Antarctica were with radiosonde balloons and it seems there is a possibility that this measurement technique overestimates the PWV under Antarctic operating conditions. The PWV may well be even lower that the values adopted here, but again there is a need for site testing to determine the real PWV values.

Based on the currently available PWV estimates, we should be able to achieve photometry and polarimetry right out to 50–60 μm, whereas the previous limit is about 23 μm from Mauna Kea and 13 μm at the Anglo-Australian Telescope. Even in the 8–13 μm region the improved transparency will lead to meaningful spectra with 0.1% accuracy, free from telluric residuals, which is vital when trying to determine the detailed spectral structure.

The most significant gain however, may be in opening up spectral regions with previously unobservable, though important, spectral, atomic, ionic and molecular transition lines. Figures 1 and 2 show calculated atmospheric transmission curves from 20 – 60 μm for PWV of 50 μm and 2 mm. 50 μm PWV is perhaps a little optimistic for Antarctica, but possibly represents a 'good' day, and 2 mm PWV represents a good day at a site like Mauna Kea. Figure 1 clearly shows how the transmission falls rapidly to zero longward of 22 μm at common astronomical sites (i.e. PWV in the mm range), whereas the improved transmission under Antarctic conditions is dramatic. The transmission from 30 – 60 μm is still patchy, even under 'good' conditions, but quite usable for continuum work and line observations provided the desired line falls in one of the 'windows'. Some of the astronomically interesting spectral lines and their observability at various telescope sites are listed in Table 2. Access to these lines via an Antarctic telescope would be most valuable, though it is prudent to remember that all of the listed lines, including the 'No and Maybes' are already observable by the Kuiper Airborne Observatory (KAO), where the precipitable water vapour is around 7 μm. The disadvantages of the KAO of course are the small telescope aperture, the shorter integration times possible and the limited access for Australian astronomers. There is little improvement in transmission between 12 and 22 μm as the lack of transparency in this region is largely attributed to atmospheric CO_2.

Table 2. Observability of some mid-IR spectral lines (AAT = Anglo-Australian Telescope, MKO = Mauna Kea Observatory).

Spectral Line	Wavelength	Observatory Site			
	(μm)	AAT	MKO	Antarctica	
Ar III	9.00	Yes	Yes	Yes	
S IV	10.52	Yes	Yes	Yes	
C IV	11.70	Yes	Yes	Yes	
Ne II	12.81	Yes	Yes	Yes	
Ne III	15.56	No	No	No	(CO_2)
S III	18.71	No	Yes	Yes	
Ne V	24.28	No	No	Yes	
O IV	25.87	No	No	Yes	
S III	33.66	No	No	Yes	
O III	51.81	No	No	Maybe	
N III	57.33	No	No	Maybe	
O I	63.17	No	No	Yes	
H2 S(2) $J = 4 \rightarrow 2$	12.28	Yes	Yes	Yes	
H2 S(1) $J = 3 \rightarrow 1$	17.03	No	Yes	Yes	
H2 S(0) $J = 2 \rightarrow 0$	28.22	No	No	Maybe	

30.4 CONCLUSION

There are significant gains to be made in both reduced thermal background and atmospheric transparency from siting a telescope in the high, cold, dry site of Dome A in Antarctica. If there were a telescope in Antarctica, we could undoubtedly gain good service from it in the mid-IR and probably improve sensitivity by about a factor of 5 when the reduced background and the improved transparency are considered, not to mention the increased spectral coverage and the new lines that this would allow us to observe. There are also some potential losses too and it is imperative that some site testing is commenced as soon as possible to determine whether the suggested gains are real.

Certainly, most of the gains for the mid-IR in Antarctica could also be achieved by a combination of the new generation of large telescopes and KAO/SOFIA airborne observatories, without the serious loss of sky coverage that must occur with an Antarctic based telescope. Of course, Australian astronomers do not have formal access to any of these facilities at present, although participation in such projects should be seriously considered. Nonetheless, an Australian Antarctic telescope, or at least a share in a telescope (with an aperture >2 m), could fulfil most of our requirements for Southern Hemisphere mid-IR astronomy for the next decade.

31. FAR-INFRARED AND SUB-MILLIMETER ASTRONOMY IN ANTARCTICA

J.W.V. Storey[1] and A.R. Hyland[2]

[1] School of Physics
University of NSW
Kensington NSW 2003
Australia

[2] Department of Physics
University College UNSW
A D F A
Campbell, ACT 2600
Australia

ABSTRACT

The wavelength range from 5 to 500 μm is one of the most technologically difficult for astronomers. For this reason, and also because of poor atmospheric transmission, the region has until recently been underexploited relative to, say, the radio and optical regions. To avoid the poor transmission and high emissivity of the atmosphere, astronomers have frequently resorted to balloons, stratospheric aircraft or even satellites to carry out the observations. The high altitude, extremely low temperatures and low humidity of the Antarctic plateau combine to make it potentially the best site on earth for far-infrared and sub-mm astronomy. Indeed, at some wavelengths, it is the only place on earth from which ground-based astronomy is possible. This research note reviews the current status of Antarctic astronomy in the far-infrared and sub-mm, and suggests potential areas for Australian involvement.

31.1 SCIENCE IN THE FAR-IR AND SUB-MM

31.1.1 *Continuum Studies*

The main atmospheric windows in this region are 30, 60, 150, 350 and 1300 μm, almost all of which are good enough for observations from Antarctica. By making broad-band observations at these wavelengths many important issues can be addressed. These include:

(a) Determination of dust masses in galaxies and star formation regions and estimation of A_v

(b) Polarimetry studies of dense clouds to determine magnetic field direction

(c) Determination of the far-infrared wavelength dependence of interstellar extinction

(d) Studies of primordial starlight reprocessed by galactic dust

(e) Cosmic background radiation studies

(f) Mass loss from highly evolved AGB stars

31.1.2 *Spectral Line Studies*

Astrophysically important spectral lines at these wavelengths, which lie in regions where the atmosphere is transparent, arise from:

(a) Atomic and ionic fine structure (e.g. [CI], [CII])
(b) Metal hydrides (e.g. MgH, SH^+, HCl)
(c) Carbon monoxide (J = 1–0, 2–1, 3–2, 4–3, 7–6 .... higher level isotope lines)
(d) Molecular hydrogen
(e) HD
(f) Complex molecules (in the sub-mm)
(g) High density tracers (CS, HCO^+ and HCN)

By making use of these lines to provide density, temperature and dynamical information through their strengths, widths and velocities, important advances can thus be expected in studies of:

(a) Cooling of primordial collapsing clouds
(b) Cooling of early galaxies
(c) Star formation
(d) Structure and composition of the interstellar medium
(e) Planetary formation

In addition, important measurements of stratospheric ozone and other components of earth's atmosphere can be carried out.

31.2 FAR-IR AND SUB-MM TECHNOLOGY

It is in this wavelength region that the techniques of optical astronomy and those of radioastronomy meet. Depending on the application and on the current state of technology, either direct (optical) detection or heterodyne (radio) detection may give the best performance. Figure 1 (Harris 1990) shows diagrammatically the different techniques in use. This is an area of research currently undergoing a revolution in overseas laboratories. The performance of both direct and heterodyne systems has improved by over an order of magnitude in recent years and the way is clear for further major advances.

In Australia, there has so far been only a relatively small effort in developing far-IR and sub-mm instrumentation (or Terahertz Technology, as it is sometime known). An important side benefit of an active Australian Antarctic astronomy program would be the stimulation of THz research both in industry and academia. This could greatly improve Australia's capabilities in an important and rapidly developing area.

31.3 WHY ANTARCTICA?

The best infrared observatories in the world are on high, dry mountain top sites, where the low water vapour content improves the atmospheric transparency and the low temperature reduces the infrared thermal background radiation from both atmosphere and telescope. On the Antarctic plateau these gains are multiplied still further. In addition, in the mid-IR to mm regime, the very

low water vapour density over the Antarctic plateau considerably improves the atmospheric transparency even opening some new 'windows' which are opaque at other observing sites.

On Mauna Kea, Hawaii, the best ground based site now in use, the atmospheric water vapour content is as low as 1 mm of precipitable (ppt) H_2O only about once a week on average. Even then, the atmospheric transmission in the 350 μm window is only about 30% and highly variable making calibration impossible. Measurements at the South Pole indicate an average of 0.2 to 0.5 mm of ppt H_2O, with the best values below 0.1 mm (Bally 1989). At a site above 4000 m elevation, on the highest part of the Antarctic plateau, we expect this to fall as low as 0.05 mm of ppt H_2O. We can therefore expect to make observations in the 350 μm window nearly all the time (Townes and Melnick 1990).

In addition to conditions peculiar to the IR and sub-mm, an Antarctic plateau site offers other advantages over a mid-latitude site:

1. The possibility of continuous monitoring of sources for long periods, as a source will never set. Observations will be possible in both the Antarctic day and night for all but the short end of the IR and optical spectrum.

2. Certain sources, such as the Magellanic Clouds, are poorly placed in the sky during southern winter at mid-latitude sites but will be high in the sky from Antarctica.

3. Significant cost advantages compared to space-based missions, which provide the only alternative for many possible observations, as well as relative ease of servability and maintenance.

The prestige of strong Australian participation in a genuinely international scientific research facility sited in the region claimed as Australian Antarctic Territory should make Antarctic astronomy attractive politically. Looking to the next century, an international Antarctic base will be an ideal precursor to an international space or moon-based observatory, politically, scientifically and logistically.

31.4 INTERNATIONAL PLANS IN IR AND SUB-MM

A number of countries have demonstrated interest in Antarctic astronomy, including Argentina, Germany, France, India, Italy, Japan, Russia, the UK and the USA, as well as Australia. Several of these have undertaken exploratory experiments. The most developed plans come from the Center for Astrophysical Research in Antarctica (CARA) in the USA, which has been funded and has initial plans for three telescopes at the South Pole.

1. The Antarctic Submillimeter Telescope and Remote Observatory (ASTRO); a 1.7 m diameter sub-mm telescope scheduled for permanent installation in late 1993.

2. The Cosmic Background Radiation Anisotropy (COBRA) project; a microwave radiation detector to survey for anisotropies in the cosmic microwave background on angular scales from 15 arcmin to 20°.

3. The South Pole Infrared Explorer (SPIREX); a 60 cm transportable telescope with a near infrared array camera and spectrometer, designed to exploit the minimum of zodiacal emission in the 2.27 – 2.45 μm window.

Beyond these, there are proto-designs for a major observatory, with a 3 m class optical-IR telescope, a 10 m sub-mm dish, a 30 m mm dish, an 8 m class optical telescope and an interferometric array of sub-mm and optical telescopes.

ASTRO is by far the most developed project to date (Stark 1989). ASTRO has a 1.7 m diameter carbon-fibre dish with a surface accuracy of 8 μm rms. All optics are off-axis, leading to high beam efficiency and low sidelobe levels. Beam-switching can be performed without changing the illumination of the primary mirror, thus minimising signal offsets. The principle targets for study will be [CI] at 609 μm and the J = 4→3 transition of CO at 650 μm.

It is clear that the best way for Australia to commence an Antarctic astronomy program is via international collaborations. At present the most likely partners are the USA (through CARA), France and the British Antarctic Survey. Links with the former Soviet Union, who operate a station at Vostok, have been established and Russian astronomers are keen to collaborate. Vostok, at 3500 m altitude, has the best climate of all the existing stations and the Russians have developed overland transport techniques that would be invaluable in establishing any high altitude observatory.

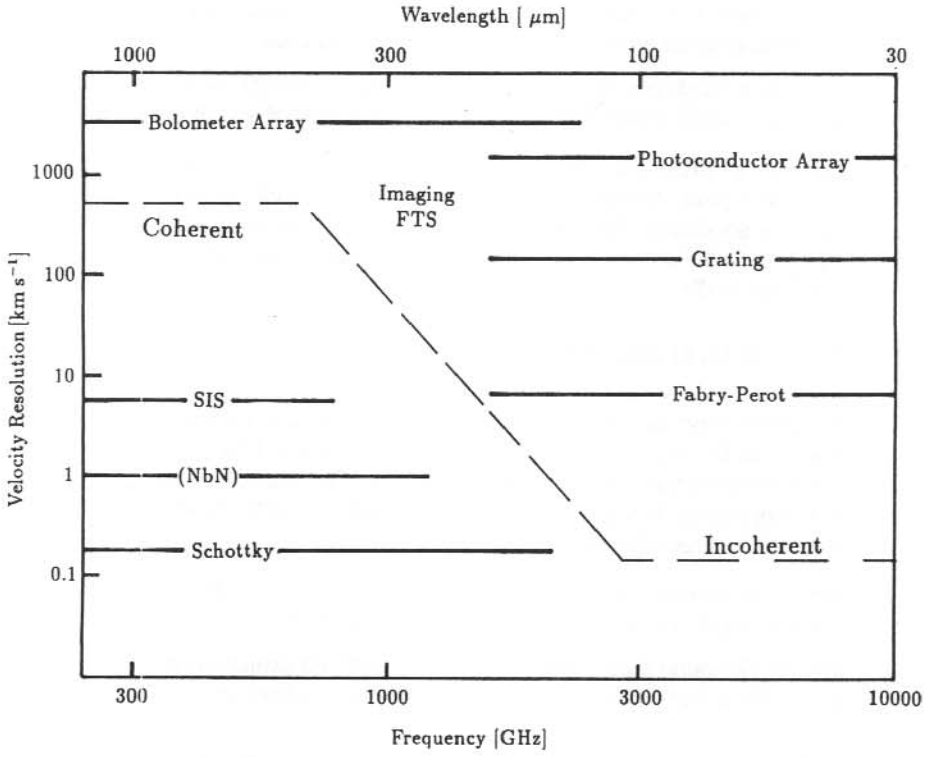

Figure 1. Respresentative overview of appropriate detection techniques as a function of frequency and velocity resolution. The heterodyne receivers are not ranked by resolution, but by total frequency coverage. 'SIS' refers to common Pb and Nb junctions; NbN refers to the developing niobium nitride technology.

31.5 CONCLUSION

It is also clear that simply 'buying into' a share of a facility operated by one of these nations would bring only minimal benefit to Australia. We therefore seek to establish ourselves as an active and technologically equal partner by developing instrumentation for site testing and other research now urgently required. The operation of such a program, particularly if receiving logistical support through the Australian Antarctic Division, would considerably enhance Australia's scientific prestige.

The CARA group are well funded and some of their members have been actively pursuing Antarctic astronomy for several years. If we are not to be left completely behind in what, we believe, is one of the most important current developments in astronomy, we must move quickly along an optimum development path. We should:

1. Establish strong international links, especially with CARA, France and the Vostok operation. (This has already begun, with assistance from DITAC.)

2. Begin collaborative site-testing and survey observations from the Antarctic plateau. This would be done with the logistical support of our international partners and perhaps also with the assistance of the Antarctic Division. The science generated here will not be spectacular, but it is an essential step.

3. Join in the development of a major international observatory to be built on the Australian Antarctic Territory. Given the important advances likely to be made in the far-IR and sub-mm, such an observatory may well include a large sub-mm dish or an array of medium-size telescopes.

REFERENCES

Bally, J. (1989). Astrophysics in Antarctica. In: Mullan, D.J., Pomerantz, M.A. *and* Stanev, T. (Eds). *American Institute of Physics Conference Proceedings 1989*. P. 100.

Harris, A. (1990). *Proceedings of the 29 Liege International Astrophysical Colloquium ESA SP-314*. P. 165.

Stark, A.A. (1989). Astrophysics in Antarctica. In: Mullan, D.J., Pomerantz, M.A. *and* Stanev, T. (Eds). *American Institute of Physics Conference Proceedings 1989*. P. 106.

Townes, C.H. *and* Melnick, G. (1990). Astrophysics in Antarctica. *Publication of the Astronomical Society of the Pacific 102*. P. 357.

32. POSSIBLE COSMIC RAY OBSERVATIONS FROM A MULTI-NATIONAL ANTARCTIC STATION ON DOME A

M.L. Duldig

Cosmic Ray Section
Antarctic Division
Kingston Tasmania 7050
Australia

ABSTRACT

The proposal that a multi-national astrophysical observatory be established on the highest area of the Antarctic ice plateau (Dome A) has centred on the opportunities for optical, infra-red and sub-mm wave astronomy. Such a site could also be used to extend the world-wide cosmic ray observatory network. Suitable cosmic ray experiments for the site are considered. Additionally, possible geomagnetic and upper atmospheric physics measurements from such a site are briefly discussed.

32.1 INTRODUCTION

The Dome A site on the Antarctic ice plateau is located at 67°E, 82.4°S at an altitude of 4270 m. The pressure altitude is even higher, exceeding 5000 m. The location has many unique features which make it a desirable site for cosmic ray observations. A large IQSY neutron monitor at Dome A would be the highest monitor in the world and would have the lowest energy cutoff (both atmospheric and geomagnetic) of any such monitor. This would be invaluable in the study of Ground Level Enhancements (GLE) and Forbush Decreases (FD).

Another advantage of such a site is the possibility of using the ice as a material absorber, of completely determined characteristics, for shallow underground muon observations. All other underground muon observatories suffer from poorly determined overburden with varying densities and rock structures and seasonal changes in water content. A detector buried in the Antarctic ice sheet would have a fully determined absorber depth in all possible directions of view and would be comparable in this respect to previously proposed sub-surface lake and ocean systems.

32.2 NEUTRON MONITOR

The asymptotic cone of response of a neutron monitor located at Dome A is not unique but the energy coverage is significantly different to adjacent cones of view of other instruments. Furthermore, the lowest energy of response, due to atmospheric absorption, would be only several hundred MeV. This would allow the gap in spectral coverage between satellite and ground based instruments to be filled for the first time. Two important needs would be met by such an instrument. Firstly, some apparent inconsistencies between satellite and ground based detector system responses to transient events such as FD and GLE may be resolved. Secondly, access to this spectral 'hole' will help to resolve the problem of poorly determined yield functions for neutron monitors at such energies. Studies of GLE have demonstrated that the yield

functions, based on theoretical calculation of high energy particle interaction in the atmosphere, are not consistent with observations made by high altitude neutron monitors at their lowest energies of response of $\gtrsim 1$ GeV (D.F. Smart, private communication 1992).

Resolution of these two problems using data which fills the spectral 'gap' will lead to deeper insights into the acceleration, scattering and propagation of high energy particles by the solar magnetic fields and associated solar wind plasma during GLE and FD. The complete spectral coverage achieved by the addition of a Dome A monitor will significantly enhance this advance.

32.3 MUON TELESCOPE SYSTEM

Galactic cosmic ray modulation in the heliomagnetosphere at energies above 50 GeV can only be studied by ground based and underground muon telescope systems. In the northern hemisphere there are a number of observatories in Japan, North America, C.I.S. and Europe which give very good latitude and energy coverage necessary for the study of anisotropies generated by solar processes. By contrast the southern hemisphere, particularly viewing southward of 15°S, is only covered by observatories in Tasmania and at Mawson to mid-latitudes, and Mawson alone further south. This coverage is reasonable up to 200 GeV but only the Poatina observatory in Tasmania, viewing to mid-southern latitudes, measures up to 500 GeV, necessary to establish the upper limiting energy of solar modulation (Duldig et al. 1985).

A novel approach to an underground system would be to place a telescope in a simple reinforced building under the ice on the polar plateau. A great advantage of such a system would be the perfectly determined overburden of absorber material.

Underground muon telescope sites suffer from poorly determined overburdens with seasonally varying water content, varying structure with depth and varying density of material including water filled or air filled gaps and fissures. As a result it is difficult to correct for seasonal variations of local origin and to accurately determine energies of response. By contrast an in-ice system would not suffer from any of these difficulties. Furthermore, muon systems could operate at the ambient in-ice temperature of $\approx$ -20°C, minimising the problem of the housing sinking into the ice and changing the depth with time. With no structure extending above the flat surface, snow drift accumulation would not affect this distribution of overburden. The only correction necessary to observational data would be for the very slow accumulation of snow over periods of years to decades which would reduce the count rate and increase the energy of response over long timescales.

Such a system has been designed for the South Pole station (Duldig et al. 1985) but could equally well be placed at the Dome A site. Furthermore, a station specifically established for astrophysical research would be expected to include solar observations throughout the austral summer which could be coordinated with the cosmic ray studies on site.

32.4 AIR SHOWER AND ULTRA-HIGH ENERGY γ-RAY ASTRONOMY

A cosmic ray air shower experiment (TeV – PeV energies) already operates at the South Pole (Finnemore et al. 1991). The atmospheric cascades of electrons produced by very high energy cosmic rays and by ultra-high energy (UHE) γ-rays can be discriminated by the shower structures and by the heavier charged particle content of the shower using muon detectors.

There is no point in reproducing the experiment already operating at the pole, however, the increased altitude at Dome A improves the efficiency of such systems and it may be useful to move the south pole system to Dome A once the station is operational.

32.5 GEOMAGNETIC OBSERVATIONS

The invarient magnetic coordinates (epoch 1988) of the Dome A site are 76.6°S, 46°E. Thus the site is just inside the *average* location of the ionospheric footpoint of the cusp location at local magnetic noon (~1345 UT). The probability of overhead aurora on any day is ~75%. Most commonly the aurorae will be low energy electron precipitation ±3 hours from magnetic noon. They will be principally red in colour, diffuse and of low intensity (500 R to 2 kR). At this latitude the aurorae are not strongly dependent on solar activity but are less likely with increasing activity.

During active substorms, the poleward edge of the auroral oval may move across the site during the auroral break-up phase. When this occurs the aurora will be very active, green-white in appearance and intensities may exceed 100 kR. These aurorae are short in duration, generally lasting less than 1 hour and rarely longer than 2 hours. Although relatively infrequent their occurrence is strongly solar cycle dependent.

Sun-aligned quiet areas of low energy and low intensity may be present at almost any time. These electron precipitations may mark the ionospheric boundaries of plasma convection regions.

The Dome A site, in conjunction with South Pole (74.4°S, 18°E magnetic) and Davis (74.6°S, 102°E), would be valuable for monitoring the passage of the cusp region, the generally accepted principal region of interaction between the solar wind and the geomagnetic field.

Conjugacy studies between Dome A and Godhaven (Greenland) would be an excellent pairing for such high latitudes and would rival the South Pole – Frobisher Bay pairing at similar latitude.

Electric field measurements at a fair weather site such as Dome A may help in setting strict limitations on models of the ionospheric dawn-dusk potential applied by the interaction of the solar wind and the geomagnetic field. Studies are underway at South Pole and Davis to see if this phenomenon gives rise to a measurable surface effect. If it does the addition of such observations at Dome A would extend the possible dawn-dusk temporal coverage of estimates of the polar cap potential magnitude.

32.6 CONCLUSION

The Dome A site would be a valuable addition to the worldwide cosmic ray station network. It would be particularly valuable for the studies of heliospheric modulation and particle interactions in the atmosphere.

Studies of galactic cosmic ray anisotropies, unaffected by the heliomagnetosphere, and UHE γ-ray sources could be improved by moving the present South Pole system to Dome A once a station is established.

Research into geomagnetic phenomena with electric field measurements, auroral and conjugacy observations from the Dome A site will lead to advances in our understanding of the complex interactions between the solar wind and the earth's magnetic field and atmosphere.

32.7 ACKNOWLEDGMENTS

The author wishes to thank Dr Gary Burns for valuable input on the geomagnetic observations possible from the Dome A site.

REFERENCES

Duldig, M.L., Jacklyn, R.M. *and* Pomerantz, M. (1985). A medium rigidity muon experiment for the South Pole station. *Proceedings of the Astronomical Society of Australia 6*:48 – 52.

Finnemore, M., Gaisser, T.K., Perrett, J.C., Petrakis, J., Pomerantz, M.A., Stanev, T.S., van Stekelenborg, J.T.P.M., Hillas, A.M., Johnson, P.A., Lloyd-Evans, J., Smith, N.J.T., Reid, R.J.O. *and* Watson, A.A. (1991). Progress report on the point-source search being made with the South Pole air shower experiment. *Proceedings of the 22nd International Cosmic Ray Conference, Dublin 1*:388 – 391.